MAX-PLANCK-INSTITUT FÜR QUANTENOPTIK

Ultracold quantum gases in three-dimensional optical lattice potentials

Dissertation in the Physics department
of the
Ludwig-Maximilians-Universität München

Markus Greiner

MPQ 283

München, Januar 22, 2003

Max-Planck-Institut für Quantenoptik
85740 Garching, Bundesrepublik Deutschland

Ultracold quantum gases in three-dimensional optical lattice potentials

Dissertation in the Physics department
of the
Ludwig-Maximilians-Universität München

Markus Greiner

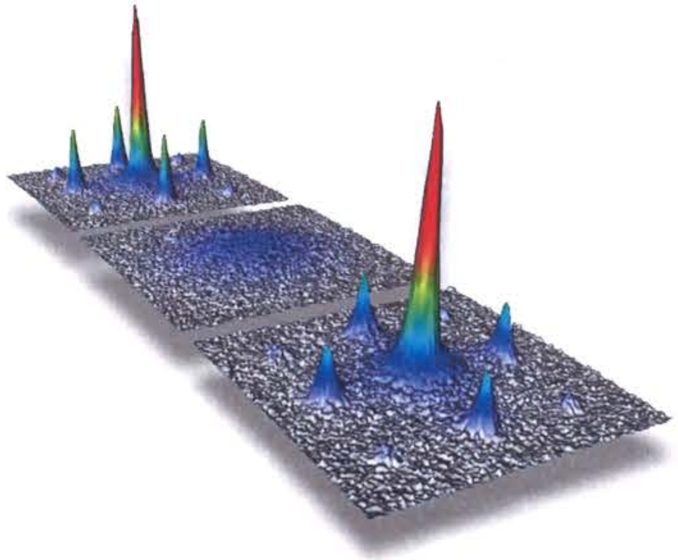

München, January 22, 2003

meiner Familie

Zusammenfassung

In dieser Promotionsarbeit werden Experimente vorgestellt, in denen es gelungen ist, in ein neues Regime der Vielteilchenphysik eines atomaren Quantengases vorzudringen. Ein Bose-Einstein-Kondensat wird in ein dreidimensionales optisches Gitterpotential geladen, das durch interferierende Laserstrahlen gebildet wird. Mit diesem neuartigen Quantensystem konnte ein Quanten-Phasenübergang zwischen einer Superflüssigkeit und einem Mott Isolator realisiert und das Kollabieren und Wiederaufleben eines makroskopischen Materiewellenfeldes beobachtet werden.

Quanten-Phasenübergänge werden durch Quantenfluktuationen getrieben und können daher selbst am absoluten Temperaturnullpunkt auftreten, an dem alle thermischen Fluktuationen ausgefroren sind. Im ersten Teil dieser Arbeit berichte ich über die Beobachtung eines solchen Quanten-Phasenübergangs in einem Bose-Einstein Kondensat mit repulsiver Wechselwirkung, das in einem dreidimensionalen optischen Gitterpotential gespeichert ist. Im superfluiden Grundzustand ist jedes Atom über das gesamte Gitter delokalisiert. Im Mott Isolator Zustand hingegen ist auf jedem Gitterplatz eine konstante Zahl von Atomen lokalisiert. Wir konnten den reversiblen Übergang zwischen diesen beiden Zuständen beobachten und die Lücke im Anregungsspektrum des Mott Isolators nachweisen.

Ein Bose-Einstein Kondensat wird üblicherweise durch ein makroskopisches Materiewellenfeld beschrieben. Diesem "klassischen" Feld liegt bei genauerer Betrachtung jedoch ein quantisiertes Materiewellenfeld zu Grunde. Thema des zweiten Teils dieser Arbeit ist die erstaunliche Dynamik, die ultrakalte Materie aufgrund dieser Quantisierung und der nichtlinearen Wechselwirkung der Atome erfährt. Im Experiment konnten wir ein periodisches Kollabieren und Wiederaufleben des makroskopischen Materiewellenfeldes beobachten. Wir konnten zeigen, daß die Kollisionen zwischen jeweils zwei Atomen lediglich zu einer völlig kohärenten Kollisionsphase im jeweiligen Vielteilchenzustand führen. Die kohärente Kollisionphase ist eine wesentliche Grundlage für verschiedene Vorschläge zur Realisierung eines Quantencomputers.

Mit diesen Experimenten ist es gelungen, in ein neues Gebiet der Physik der ultrakalten Quantengase vorzudringen. Das stark korrelierte System wird durch die Wechselwirkung zwischen den Atomen dominiert und kann daher nicht mehr durch die gängigen Theorien des schwach wechselwirkenden Bosegases beschrieben werden. Durch dieses neuartige Quantensystem eröffnet sich die einzigartige Möglichkeit, in einem ultrakalten atomaren Gas fundamentale Fragen der modernen Festkörperphysik, Atomphysik, Quantenoptik und Quanteninformation zu studieren.

Abstract

In this thesis I report on experiments that enter a new regime in the many body physics of ultracold atomic gases. A Bose-Einstein condensate is loaded into a three-dimensional optical lattice potential formed by a standing wave laser light field. In this novel quantum system we have been able to both realize a quantum phase transition from a superfluid to a Mott insulator, and to observe the collapse and revival of a macroscopic matter wave field.

Quantum phase transitions are driven by quantum fluctuations and occur, even at zero temperature, as the relative strength of two competing energy terms in the underlying Hamiltonian is varied across a critical value. In the first part of this work I report on the observation of such a quantum phase transition in a Bose-Einstein condensate with repulsive interactions, held in a three-dimensional optical lattice potential. In the superfluid ground state, each atom is spread-out over the entire lattice, whereas in the Mott insulating state, exact numbers of atoms are localized at individual lattice sites. We observed the reversible transition between those states and detected the gap in the excitation spectrum of the Mott insulator.

A Bose-Einstein condensate is usually described by a macroscopic matter wave field. However, a quantized field underlies such a "classical" matter wave field of a Bose-Einstein condensate. The striking behavior of ultracold matter due to the field quantization and the nonlinear interactions between the atoms is the focus of the second part of this work. The matter wave field of a Bose-Einstein condensate is observed to undergo a series of collapses and revivals as time evolves. Furthermore, we show that the collisions between individual pairs of atoms lead to a fully coherent collisional phase shift in the corresponding many-particle state, which is a crucial cornerstone of proposed novel quantum computation schemes with neutral atoms.

With these experiments we enter a new field of physics with ultracold quantum gases. In this strongly correlated regime, interactions between atoms dominate the behavior of the many-body system such that it can no longer be described by the usual theories for weakly interacting Bose gases. This novel quantum system offers the unique possibility to experimentally address fundamental questions of modern solid state physics, atomic physics, quantum optics, and quantum information.

Contents

1 Introduction

The realization of Bose-Einstein condensation (BEC) in dilute atomic gases has enabled numerous fascinating experiments in which fundamental quantum mechanics is studied in a macroscopic and accessible system. For example matter wave coherence properties, vortices, and effects of superfluid flow have been explored. In almost all experiments up to now the Bose condensed atoms can be described by a single macroscopic wave function. The dynamics of the weakly interacting condensates is treated in the framework of the Gross Pitaevskii equation and Bogoliubov theory. The fact that a single macroscopic wave function or macroscopic matter wave is sufficient to describe the many body system allows for a very intuitive understanding of the system. Experimentally, the macroscopic wave function can be precisely probed in interference experiments.

From a many body point of view, however, a system described by a macroscopic wave function is the simplest of all possible many body systems. Interaction induced correlations are neglected in such a system or treated as a small perturbation in Bogoliubov theory. Therefore the question arises as to whether one can bring a dilute gas of bosons into the strongly correlated regime, where interaction induced correlations are dominant and the system is too rich and complex to be described by a macroscopic matter wave. Experiments at the onset of this exciting regime were carried out in the group of Carl Wieman, where the collapse and explosion of a Bose-Einstein condensate with tuned interactions has been observed [1, 2] and in the group of Mark Kasevich, where number squeezing has been observed with a BEC in a one-dimensional optical lattice potential [3].

In this work I will present experiments in which we have been able to enter a new field of physics with ultracold quantum gases. By loading a Bose-Einstein condensate into a three-dimensional optical lattice potential, a novel quantum system is created that allows us to enter the regime of a strongly correlated boson system. In an optical lattice, neutral atoms are trapped in the intensity maxima or minima of a standing wave light field due to the optical dipole force. We have observed a zero temperature quantum phase transition from a superfluid to a Mott insulator and the collapse and revival of a macroscopic matter wave field. This new application of Bose-Einstein condensation offers the unique possibility to experimentally study fundamental questions of modern solid state physics, atomic physics, quantum optics, and quantum information.

Quantum phase transition from a superfluid to a Mott insulator

A Bose-Einstein condensate trapped in a three-dimensional optical lattice potential is a nearly perfect experimental realization of the Bose-Hubbard model, which describes bosonic particles with repulsive interactions hopping in a lattice potential [4]. This intriguing model shows a quantum phase transition between a superfluid and an insulating state, the so-called Mott insulator, as the ratio between the competing kinetic energy and interaction energy term in the Hamiltonian is varied. Such a quantum phase transition is driven by quantum fluctuations and therefore also occurs at absolute zero temperature, where all thermal fluctuations are frozen out.

The fact, that a Bose-Einstein condensate trapped in a lattice potential is described by a Bose-Hubbard model was first realized by Dieter Jaksch and coworkers [5] in the group of Peter Zoller. In contrast to all present realizations of this model, where the bosonic systems are either tightly bound composites of fermions that act like effective bosonic particles or correspond to bosonic excitations, the system of ultracold neutral atoms in an optical lattice potential has the big advantage of being highly controllable. Therefore Jaksch *et al.* have predicted that a quantum phase transition from a superfluid to a Mott insulator should be observable in such a system.

Recently we have been able to observe such a transition with a Bose-Einstein condensate of ^{87}Rb atoms, loaded into an optical lattice potential. When the lattice potential is smoothly ramped-up and superimposed to the condensate, the condensate splits up in more than 100.000 lattice sites, and the bosonic atoms can only move from one lattice site to the next by tunnel coupling. In the regime where the atom-atom interaction on a lattice site is small compared to the tunnel coupling, the ground state of the system is a superfluid state where each atom is delocalized over the entire lattice. The atoms exhibit long-range phase coherence and can be described by a macroscopic wave function with a well defined macroscopic phase on each lattice site. The atom number on a lattice site fluctuates, therefore in a measurement one would find a random atom number on each site. In the opposite limit, where the atom-atom interaction on a lattice site is much larger than the tunnel coupling, the system can lower its energy when each lattice site is filled with the same number of atoms. In this Mott insulating state each atom is localized to a lattice site and a gap in the excitation spectrum opens up. The macroscopic phase and the long range phase coherence vanish and the atoms can no longer be described by a macroscopic wave function.

In the experiment we can tune the ratio between the atom-atom interaction on a lattice site and the tunnel coupling over several orders of magnitude by changing the depth of the optical lattice potential. We have been able to demonstrate the reversible change between the superfluid and the Mott insulator ground state when this ratio has been varied beyond a critical value. In addition, the gap in the excitation spectrum has been detected.

The realization of the Bose Hubbard model with an ultracold gas of atoms trapped in an optical lattice potential opens new perspectives for studying fundamental solid state physics. Besides this the Mott insulator state is an intriguing starting point for experiments aiming for the coherent formation of molecules [6] or for the creation of large scale entanglement between atoms [7].

Collapse and Revival of a macroscopic matter wave field

A Bose-Einstein condensate represents the most "classical" form of a matter wave, just as an optical laser emits the most classical form of an electromagnetic wave. Beneath this giant matter wave, however, the discrete atoms represent a crucial granularity, i.e. a quantization of this matter wave field, which has been inaccessible to experiments with Bose-Einstein condensates up to now. Nevertheless, it has been recognized that such a quantization should lead to pronounced consequences for the wave nature of matter. The coherent collisions between the atoms lead to a periodic series of collapses and revivals of the matter wave field of a Bose-Einstein condensate. During the collapse, the coherent collisional dynamics even lead to the formation of Schrödinger cat states.

In the experiment, the collapse and revival of the coherent matter wave field of a Bose-Einstein condensate has been directly observed. The experiment demonstrates that collisions between a given number of atoms lead to a coherent collisional phase in the corresponding many particle state, which induces the periodic collapse and revival of the macroscopic matter wave field. Using a three-dimensional lattice potential has allowed us to bring the timescale for this fundamental process into an experimentally accessible regime. The observed coherent collisional phase is the cornerstone of novel quantum computation schemes with neutral atoms. [7].

As an application, the collapse and revival of the macroscopic matter wave field has been used to measure the sub-Poissonian atom number statistics of ultracold atoms stored in optical lattice potentials. A pronounced number squeezing has been observed even before the system is brought into the Mott insulator regime. The measured number squeezing is consistent with a theoretical Gutzwiller calculation.

Overview

- The second chapter is an overview about the theory of a weakly interacting Bose gas, the experimental apparatus and the experimental methods.
- The third chapter deals with superfluid quantum gases in optical lattice potentials. The theory of optical dipole potentials, the band structure of a lattice, and the discrete Gross Pitaevskii equation is discussed. The experimental part describes the generation of optical lattice potentials and the preparation and detection of ultracold atoms in such potentials and various experiments.
- In the fourth chapter, the quantum phase transition from a superfluid to a Mott insulator is presented. The Bose Hubbard Model is explained and experiments demonstrating the reversible quantum phase transition and the gap in the excitation spectrum are discussed.
- The fifth chapter reports on the observation of the collapse and revival of a macroscopic matter wave field. Theory and experimental results are discussed, and it is demonstrated how the collapse and revival can be used for measuring the sub-Poissonian atom number statistic in an optical lattice potential.

Publications of the PhD work

- *Collapse and Revival of the Macroscopic Wave Function of a Bose-Einstein Condensate.*
  Greiner, M., O. Mandel, T.W. Hänsch und I. Bloch,
  Nature, **419**(6901): p. 51, 2002.
- *Mott-Isolator-Zustand - Perfekte Ordnung am Nullpunkt.*
  Greiner, M., T.W. Hänsch und I. Bloch,
  Physik in unserer Zeit, **33**(2): p. 51, 2002.
- *Quantum phase transition from a superfluid to a Mott insulator in gas of ultracold atoms.*
  Greiner, M., O. Mandel, T. Esslinger, T.W. Hänsch und I. Bloch,
  Nature, **415**(6867): p. 39, 2002.
- *Bose-Einstein condensates in 1D-and 2D optical lattices.*
  Greiner, M., I. Bloch, O. Mandel, T.W. Hänsch und T. Esslinger,
  Applied Physics B-Lasers & Optics, **73**(8): p. 769, 2001.
- *Exploring phase coherence in a 2D lattice of Bose-Einstein condensates.*
  Greiner, M., I. Bloch, O. Mandel, T.W. Hänsch und T. Esslinger,
  Physical Review Letters, **87**(16): p. 160405/1, 2001.
- *Optics with an atom laser beam.*
  Bloch, I., M. Köhl, M. Greiner, T.W. Hänsch und T. Esslinger,
  Physical Review Letters, **87**(3): p. 030401/1, 2001.
- *Sympathetic cooling of ^{85}Rb and ^{87}Rb.*
  Bloch, I., M. Greiner, O. Mandel, T.W. Hänsch und T. Esslinger,
  Physical Review A, **64**(2): p. 021402/1, 2001.
- *Magnetic transport of trapped cold atoms over a large distance.*
  Greiner, M., I. Bloch, T.W. Hänsch und T. Esslinger,
  Physical Review A, **63**(3): p. 031401/1, 2001.

2 Bose-Einstein condensation in a weakly interacting gas of atoms

Bose-Einstein condensates (BEC) in dilute gases provide unique opportunities for exploring quantum phenomena on a macroscopic scale. They have first been realized 1995 in a remarkable series of experiments with rubidium [8] and sodium [9] vapors. In these experiments a dilute cloud of atoms is cooled to ultra low temperatures in the nano-kelvin regime. At a critical phase space density the quantum mechanical wave packets describing the individual bosonic atoms start to overlap and a Bose-Einstein condensate is formed. In such a condensate a macroscopic number of bosonic atoms collectively occupies the lowest energy state. In our experiments we prepare a nearly pure condensate of up to 10^6 atoms as a starting point for experiments with ultracold atoms in a three-dimensional periodic lattice potential.

In the first part of this chapter an introduction to the theoretical description of a Bose-Einstein condensate is given. In the second part our experimental setup for creating Bose-Einstein condensates is described.

2.1 Theory of a Bose-Einstein condensates

Bose-Einstein condensation (BEC) in a gas of particles obeying Bose statistics was predicted by Einstein in 1924 [10], based on ideas of Bose addressing the statistics of photons [11]. The original prediction was for a noninteracting gas, however, after the observation of superfluidity in ^{4}He Fritz London suggested that BEC was responsible for the superfluid properties despite the strong interactions in this system [12, 13]. Theoretically these strongly interacting systems are very difficult to describe. In contrast BECs in weakly interacting gases are by far better understood and can be excellently described in the framework of the Gross-Pitaevskii equation and Bogoliubov theory[1].

2.1.1 Noninteracting Bose gas

At zero temperature $T = 0$ a noninteracting Bose Gas is fully Bose condensed and all N particles are described by identical single particle wave functions. The many body wave function is therefore given by the product over these identical single particle wave functions $\phi(\mathbf{r})$:

$$\Psi_N(\mathbf{r}_1, \mathbf{r}_2, ..., \mathbf{r}_N) = \prod_{i=1}^{N} \phi(\mathbf{r}_i) \tag{2.1}$$

---

[1] There are several reviews of the theory of Bose-Einstein condensation in dilute gases, e.g. by Parkins and Walls [14], Dalfovo *et al.* [15], Leggett [16] and Pethick and Smith [17].

Such a Bose-Einstein condensate can be described by a macroscopic wave function or order parameter $\psi(\mathbf{r})$ [18]

$$\psi(\mathbf{r}) = \sqrt{N}\phi(\mathbf{r}), \tag{2.2}$$

which is, apart from the normalization, simply the Schrödinger wave function of the single particle state $\phi(\mathbf{r})$ into which the condensation occurs. The particle density is given by $n(\mathbf{r}) = |\psi(r)|^2$.

For a noninteracting Bose gas and an inhomogeneous system, this single particle state is simply the single particle ground state of the confining potential. In a harmonic trap, for example, the ground state wave function is a Gaussian wave function, and for a periodic potential the ground state single particle wave function is a Bloch wave function with a quasi momentum $q = 0$ (see chapter 3).

In the framework of "spontaneously broken gauge symmetry" [19, 20, 21, 16], where the many particle state is assumed to be a superposition of states with different particle numbers N and a well defined macroscopic phase, the order parameter can be defined as the expectation value of the single particle destruction operator $\hat{\psi}(\mathbf{r})$

$$\psi(\mathbf{r}) = \langle\hat{\psi}(\mathbf{r})\rangle, \tag{2.3}$$

This approach is very useful for describing Bose-Einstein condensates and for calculations. In our case it is particularly useful for understanding the collapse and revival of the macroscopic matter wave field (chapter 5). It should be mentioned that $\langle\hat{\psi}(\mathbf{r})\rangle = 0$ for a state with a fixed number of particles.

2.1.2 Interaction in a cold dilute gas

The atom-atom interaction in a cold dilute gas of bosonic atoms is dominated by elastic binary collisions and can be treated in the framework of scattering theory. The true interatomic scattering potential $V_{at}(r)$, where r is the spacing between the particles, is complicated and can only be calculated for Hydrogen in an ab initio calculation. For $r > 5$Å it can be approximated by a van der Waals interaction potential $\propto -C_6/r^6$ [22, 23, 24].

For cold gases the actual inter-particle potential plays a minor role. The only relevant scattering process is s-wave scattering, since the thermal de Broglie wavelength is much larger than the effective extension of the interaction potential. Therefore the interatomic potential can be replaced by an effective contact interaction

$$V_{at}(\mathbf{r}) = \frac{4\pi\hbar^2 a_s}{m}\cdot\delta(\mathbf{r}) = g\cdot\delta(\mathbf{r}), \tag{2.4}$$

where $\mathbf{r}$ is the relative coordinate between two atoms, m is the mass of the atoms, a_s is the s-wave scattering length and $g = 4\pi\hbar^2 a_s/m$ is the coupling constant. Therefore the interaction is fully determined by a single scattering length a_s. Julienne *et al.* [25] have determined the ^{87}Rb scattering length for both the $|F=1, m_F=-1\rangle$ and $|F=2, m_F=2\rangle$ state based on a series of experiments as $a_s = 103 \pm 5\,a_0 = 5.45 \pm 0.26$ nm, where $a_0 = 0.05292$ nm is the Bohr radius.

2.1.3 Weakly interacting Bose gas

Let us consider a gas of ultracold bosons with underlying binary collisions as described above. In second quantization, the many body Hamiltonian describing N interacting bosons confined by an external potential V_{ext} is given by

$$\begin{aligned}\hat{H} \;=\; & \int d\mathbf{r}\,\hat{\psi}^\dagger(\mathbf{r})\left(-\frac{\hbar^2}{2m}\nabla^2 + V_{ext}(\mathbf{r})\right)\hat{\psi}(\mathbf{r}) + \\ & \frac{1}{2}\int d\mathbf{r}\,d\mathbf{r}'\,\hat{\psi}^\dagger(\mathbf{r})\hat{\psi}^\dagger(\mathbf{r}')\,V_{at}(\mathbf{r}-\mathbf{r}')\,\hat{\psi}(\mathbf{r}')\hat{\psi}(\mathbf{r}),\end{aligned} \tag{2.5}$$

where $\hat{\psi}(\mathbf{r})$ and $\hat{\psi}^\dagger(\mathbf{r})$ are the boson field operators that annihilate and create a particle at the position $\mathbf{r}$, respectively. With equation 2.4 the second term becomes

$$4\pi\hbar^2 a_s/m\cdot\int d\mathbf{r}\,\hat{\psi}^\dagger(\mathbf{r})\hat{\psi}^\dagger(\mathbf{r})\,\hat{\psi}(\mathbf{r})\hat{\psi}(\mathbf{r}). \tag{2.6}$$

For a dilute gas, the system can be described by a mean field description. The diluteness of the gas is characterized by the ratio of the scattering length a_s and the inter particle spacing. This ratio can be expressed as a gas parameter $n\,a_s^3$, where n is the density, and is typically less then 10^{-3}. The basic idea of the mean field description, which was first developed by Bogoliubov in 1947 [26], is to separate out the condensate contribution to the bosonic field operator. If the gas is dilute enough, the Bose-Einstein condensate is basically described by a macroscopic wave function like in equation 2.2. Therefore, assuming spontaneously broken gauge symmetry, the bosonic field operator $\hat{\psi}(\mathbf{r}, t)$ can be replaced by its expectation value $\psi(\mathbf{r}, t) = \langle\hat{\psi}(\mathbf{r}, t)\rangle$, which is a complex function, and a fluctuating field operator $\delta\hat{\psi}(\mathbf{r}, t)$:

$$\hat{\psi}(\mathbf{r}, t) = \psi(\mathbf{r}, t) + \delta\hat{\psi}(\mathbf{r}, t) \tag{2.7}$$

When the fluctuations are neglected, this ansatz leads to the well known Gross-Pitaevskii equation [27, 28]

$$i\hbar\frac{\partial}{\partial t}\psi(\mathbf{r}, t) = \left(-\frac{\hbar^2\nabla^2}{2m} + V_{ext}(\mathbf{r}) + g\,|\psi(\mathbf{r}, t)|^2\right)\psi(\mathbf{r}, t), \tag{2.8}$$

which has the form of a non-linear Schrödinger equation. The effective repulsive atom-atom interaction is described as a mean field potential proportional to the atom density $n(\mathbf{r}) = |\psi(\mathbf{r})|^2$. In this weakly interacting regime, the many-particle wave function is still the product of identical single particle wave functions as for the ideal Bose gas in equation 2.1. Contrary to the noninteracting case the weakly interacting gas does not condense into the ground state of the single particle problem but instead into a state which is determined through the Gross Pitaevskii equation 2.8. The Gross Pitaevskii equation proved to be very successful for both the qualitative and quantitative description of condensate properties like interference between condensates [29], collective modes [15] or vortices [30].

When the condensate is solely described by a macroscopic wave function, however, all interaction induced correlations are neglected. In the weakly interacting regime $n\,a_s^3 \ll 1$ a better description beyond this mean field description can be found by including the fluctuations $\delta\hat{\psi}(\mathbf{r},t)$ of the Bogoliubov description. The fluctuations lead to a depletion of the condensate mode since excited states different than the condensate mode get populated. This depletion is of order $(n\,a_s^3)^{1/2}$ and is typically small in the experiments, about 1%.

The Bogoliubov theory may be formulated in a way, such that the many body ground state is approximated by an optimized product of identical, symmetric two particle functions $\varphi(\mathbf{r}_i,\mathbf{r}_j,t)$ [16]. In this particle number conserving approach[2] of the Bogoliubov theory it becomes evident that two particle correlations are incorporated in the way that configurations in which particles i and j are close together are suppressed.

2.1.4 Paths towards strongly correlated Bose systems

The description of the condensate as a weakly interacting gas is only valid in the weak coupling regime, when the interaction energy ϵ_{int} is small compared to the kinetic energy ϵ_{kin} per particle. The ratio between those energies is given by [31]

$$\frac{\epsilon_{int}}{\epsilon_{kin}} = \frac{gn}{\hbar^2 n^{2/3}/m} \approx 4\pi\,n^{1/3}a_s, \tag{2.9}$$

where n is the particle density. In Bose-Einstein condensates, the interparticle spacing $n^{-1/3}$ is usually much larger than the scattering length a_s. Therefore the ratio between the interaction and kinetic energy is very low, typically on the order of 0.02, and the condensate can be well described by a macroscopic wave function with only small quantum depletion.

In order to reach the strong coupling regime, where the condensate represents a strongly correlated Bose system, the interaction energy per particle has at least to be on the same order or larger than the kinetic energy. An obvious way to achieve this is to either raise the density or raise the scattering length as can be seen from equation 2.9. It is indeed possible to tune the scattering length to large values by using a Feshbach resonance. This has recently been realized for example in ^{85}Rb, where the scattering length has been tuned over several orders of magnitude and a collapse and explosion of the condensate has been observed [1, 2]. The problem of this approach, however, is that the life time of the condensate strongly decreases due to three-body losses. The rate for this losses is given by [32]

$$\dot{n}/n \propto \frac{\hbar}{m}\left(na_s^2\right)^2 \tag{2.10}$$

and is therefore strongly increased when the density or the scattering length becomes large.

An entirely different approach for reaching the strongly correlated regime is discussed in this work. By loading a Bose-Einstein condensate into a three-dimensional optical lattice potential, the condensate is split up in more than 100.000 lattice sites with a mean occupation of 1-2 atoms per site. The atoms can only move through the lattice by tunnelling from one site to the next. Therefore, the tunnelling energy now plays the role of the kinetic energy and the atoms get a large effective mass [33]. When the lattice potential depth is increased, the effective mass gets exponentially larger and the kinetic energy is dramatically decreased. Therefore, the ratio between the interaction and kinetic energy can become large without increasing the density or scattering length [31]. When the interaction energy becomes important, the system can no longer be described as a weakly interacting gas and the strongly correlated regime is entered. For a certain value of this ratio, a quantum phase transition from a superfluid to a Mott insulator occurs [4, 5].

---

[2] In this approach of the Bogoliubov theory no spontaneously broken gauge symmetry has to be assumed.

2.2 Experimental setup for a ^{87}Rb Bose-Einstein condensate

Experiments with Bose-Einstein condensates in three-dimensional optical lattice potentials require an exceptional optical access to the Bose-Einstein condensate. Laser light has to be precisely focused onto the condensate from six orthogonal directions in order to create a three-dimensional periodic dipole force potential. Previous apparatus did not provide such a good optical access. Therefore we designed and built a new kind of BEC apparatus. The basic idea is that the region of the magneto optical trap (MOT) is separated from the region where the Bose-Einstein condensate is created. The atoms are transferred between those places by moving a magnetic trapping potential in an L-shape over nearly half a meter (figure 2.1). Since there is no magneto optical trap at the final trapping site, an exceptional optical access to the BEC from six orthogonal directions is present. The apparatus is described in detail in my diploma thesis [34]. In this chapter I will give a short overview about the experimental methods we use.

2.2.1 Magneto optical trap

In a vapor cell magneto optical trap (MOT) atoms are captured from the background gas and cooled to the micro Kelvin regime [35, 36, 37, 38]. The basic idea of a MOT is to use dissipative light forces which introduce an effective friction force to slow down and cool an atomic gas. At the same time an inhomogeneous magnetic field is applied which introduces a spatial dependence of the light force leading to a confinement of the atom cloud. The schematic setup for a MOT is shown in figure 2.2. Six red detuned laser beams with circular polarization are directed onto the trap center. The magnetic field is created by an anti Helmholtz coil pair.

In the experiment we have realized a MOT which uses laser beams with a large beam diameter of 40 mm and thereby enables us to capture a large number of atoms from the background gas [39]. For the MOT beams we use light which is 18 MHz $\approx 3\Gamma_{D2}$ red detuned with respect to the $|F=2\rangle \rightarrow |F'=3\rangle$ transition, where Γ_{D2} is the line width of the $D2$ transition. In addition we apply a repump laser on the $|F=1\rangle \rightarrow |F'=2\rangle$ transition. This laser returns the atoms that are off resonantly excited to other states and fall into the $F=1$ ground state, back to the cycling transition. About $3 \cdot 10^9$ atoms are captured within 8 s in the MOT.

2.2.2 Magnetic trap setup

Generating magnetic trapping potentials

Neutral atoms can be captured in a magnetic trapping potential due to the interaction of their magnetic moment with an inhomogeneous magnetic field [40, 41, 42]. This method allows an efficient isolation of the atoms from the external environment. In contrast to a MOT, a magnetic trap forms a conservative trapping potential. Limitations of the density and temperature due to the light field and spontaneous processes in a MOT can be circumvented.

When an atom is placed in an inhomogeneous magnetic field $\mathrm{B}(r)$ the particle is subjected to an external force directed towards the magnetic field minimum or maximum depending on

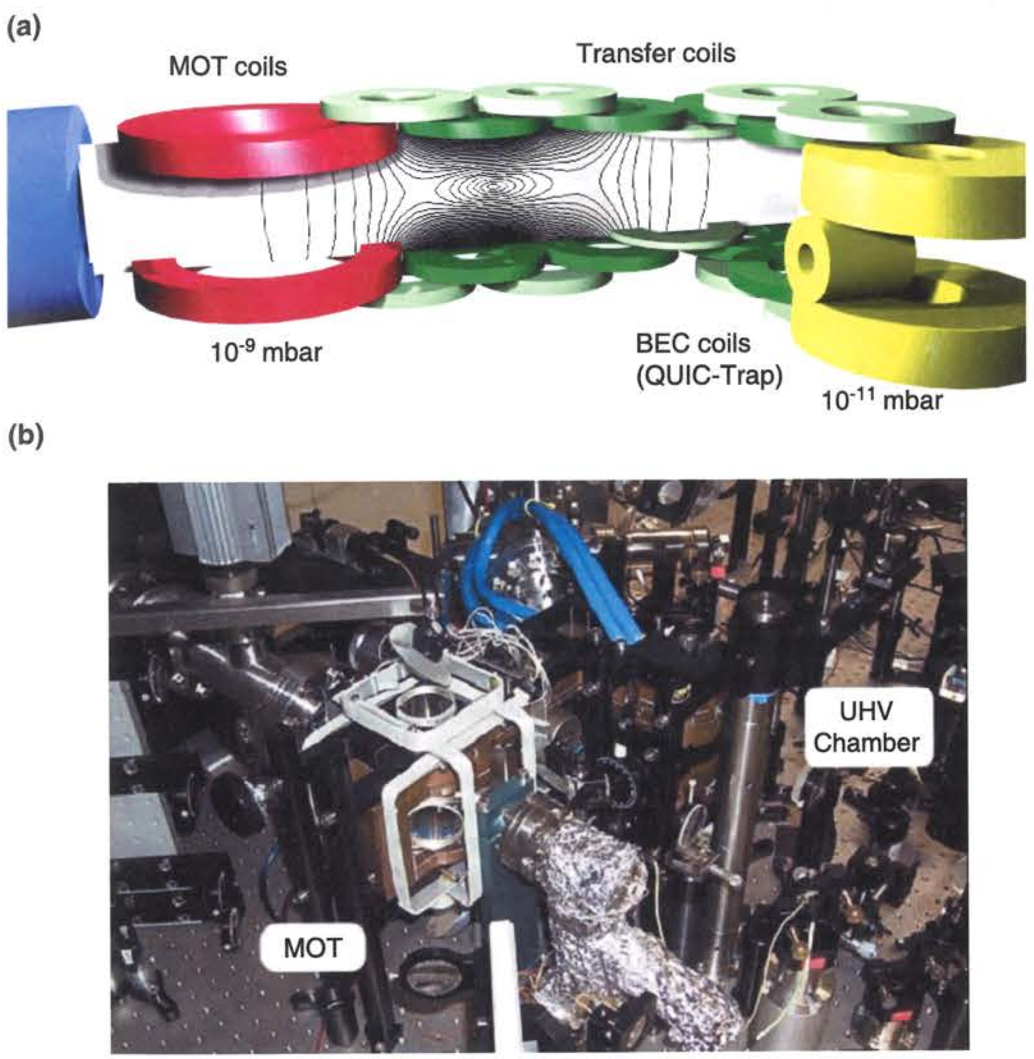

Figure 2.1: (a) Schematic setup of the apparatus. Ultracold atoms are transferred with a chain of quadrupole coil pairs into an ultra-high vacuum (UHV) chamber, in which the Bose-Einstein condensate is created. By separating the region of the MOT from the spatial region where the BEC is created, we have been able to achieve an excellent optical access to the BEC from all six spatial directions. (b) Photo of the apparatus. On the left side the optics for the MOT can be seen. The optics on the right side and in the background is for generating the optical lattice potential.

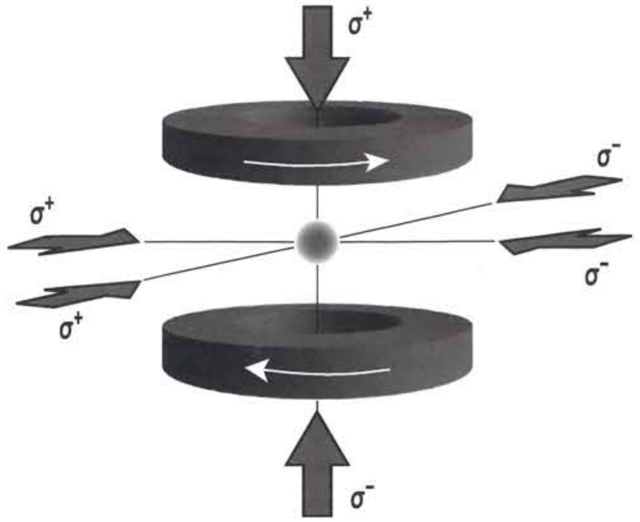

Figure 2.2: Geometry of a Magneto optical trap (MOT). The quadrupole field for the MOT is generated by an anti Helmholtz coil pair. Laser beams with circular polarized light from six directions are overlapped to the trap center.

the orientation of the magnetic moment. When an atom moves in such a field, it maintains the relative orientation of the magnetic moment if the change of the direction of the magnetic field is small compared to the Lamor frequency $\omega_L = \mu B/\hbar$. An atom with a magnetic quantum number m_F and a Landé g-Factor g_F in the hyperfine state F is therefore subjected to a potential formed by the Zeeman energy shift

$$V_{mag}(\mathbf{r}) = -g_F\, m_F\, \mu_B\, B(\mathbf{r}), \tag{2.11}$$

where μ_B is the Bohr magneton.

The simplest magnetic trap is created by an anti Helmholtz coil pair. In the center between two coils that carry opposite currents the magnetic field cancels and is equal to zero. From this point, the absolute value of the magnetic field increases linearly in each direction as $B(\mathbf{r}) \propto \sqrt{4x^2+y^2+z^2}$. Atoms in a low field seeking state are therefore captured in the trap center. In our experiment we use the low field seeking ground state $|F=2, m_F=2\rangle$.

Initial quadrupole trap

After a cloud of atoms is captured and cooled in the MOT, the light for the MOT is switched off and the atoms are transferred into a quadrupole magnetic trap. This quadrupole trap is formed by the same magnet coils which are used for the MOT (left coil pair on figure 2.1a). Therefore the center of the magnetic trapping potential is automatically aligned with the center of the MOT if all external fields are compensated. The magnetic field of this trap can be rapidly ramped up in about $500\,\mu$s by discharging an electrolytic capacitor over the magnet coils using an additional resistor which limits the peak current.

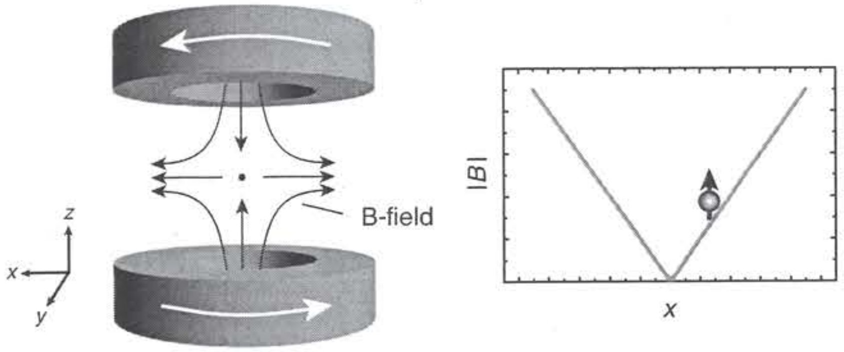

Figure 2.3: Quadrupole coil pair for generating a magnetic quadrupole trap. Two coils carry opposite currents and form a magnetic field which vanishes in the trap center and increases linearly in each direction.

Magnetic transport into the UHV chamber

The atoms are transported to the final trapping site by shifting the quadrupole trapping potential in a L-shaped path. This is achieved without moving mechanical parts but rather by regulating the currents in a chain of quadrupole coil pairs (see figure 2.1a). Using three pairs of quadrupole coils at the same time enables us to smoothly move the trapping potential without deforming the trap geometry (figure 2.4). This method significantly reduces heating of the atoms during the transport [43]. The atoms are heated by about 10% during the complete transport. We observe no losses due to shifting of the trapping potential. The efficiency of the transport is only limited by losses due to collisions with the background gas before the atoms enter the UHV chamber.

Ioffe-Pritchard trap

When the atoms are further cooled towards a BEC, they can not be trapped in a quadrupole magnetic trap anymore. This is due to the vanishing magnetic field in the center of a quadrupole trap. When atoms come close to the trap center, the orientation of the magnetic moment can not follow the direction of the magnetic field adiabatically and the atoms undergo Majorana spin flips [44]. This loss and heating mechanism is negligible at the initial temperature after the Molasses, but it becomes dominant when the atoms are further cooled [45, 9]. To circumvent this problem, we use a Ioffe-Pritchard type trap [46, 47], which creates a harmonic magnetic confinement with a finite magnetic offset field B_0 in the trap center. The magnetic trapping potential is formed by two large quadrupole coils and a small QUIC coil in between [48]. By slowly increasing the current in the QUIC coil, the Quadrupole trap is continuously converted into a Ioffe-Pritchard type trap.

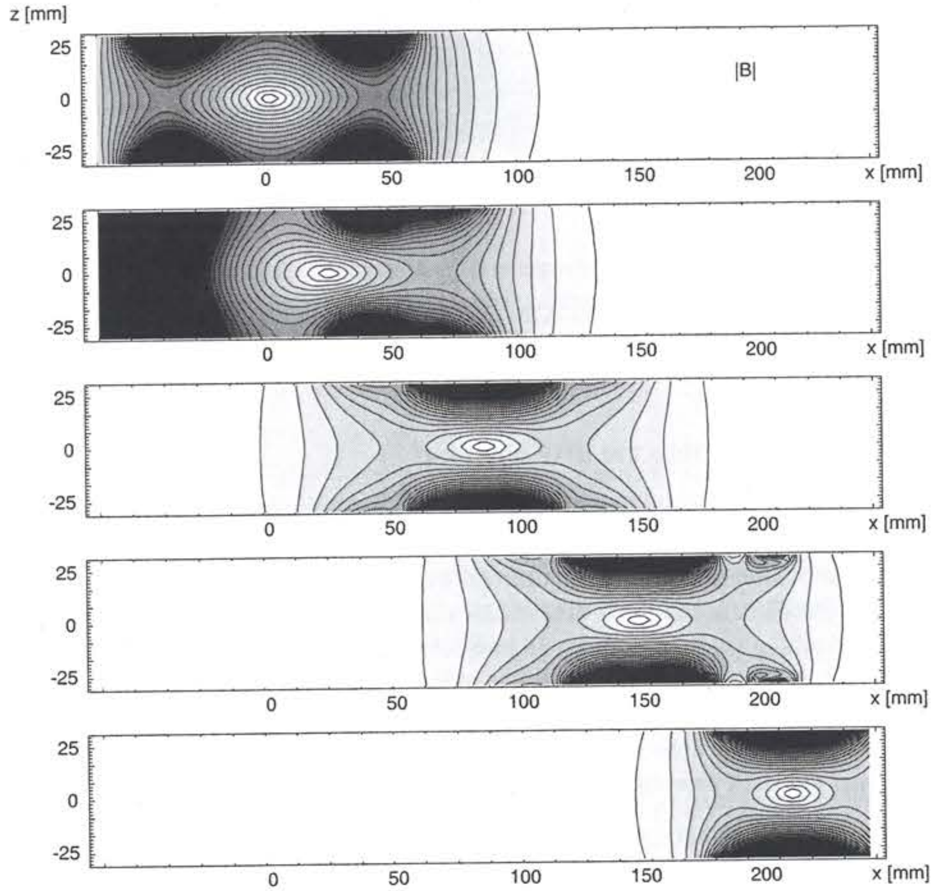

Figure 2.4: Magnetic transport: The graphs show iso-potential lines of the magnetic trapping potential for different stages of the transport. The potential is smoothly moved and a modulation of the trap geometry can be circumvented by using three coils at the same time.

For an offset field $B_0 = 1$ Gauss the trap is cigar shaped with typical radial trapping frequencies of 220 Hz and axial trapping frequencies of 24 Hz for the $|F=2, m_F=2\rangle$ state. We have installed an additional Helmholtz coil pair in order to increase the offset field to up to 200 Gauss. For $B_0 = 150$ Gauss the trap is nearly spherical with trapping frequencies of 24 Hz.

Magnet coils and power supplies

As magnet coils we use pancake shaped coils made from rectangular magnet wire. The coils are water cooled from the outside. As a power source we use four HP switching power supplies with a maximum output voltage of 13 V and a maximum current of 150 A. The current is controlled by the timing system and can follow arbitrary waveforms with a time constant of $\approx$30 ms. Each power supply can be switched to drive different magnet coils during the transport sequence.

2.2.3 Vacuum chamber

The vacuum system consists of two vacuum chambers. The first chamber is for the vapor cell MOT and has a heated Rubidium reservoir. The relatively high Rubidium pressure of about $2 \cdot 10^{-9}$ mbar enables us to rapidly capture a large number of atoms in the MOT. The trap life time in this chamber is limited by losses due to collisions with the background gas and is on the order of several seconds. The second chamber is the UHV chamber, where the BEC is created. The background pressure is on the order of 10^{-11} mbar leading to a measured trap life time of 90 s. In order to maintain the pressure difference both chambers are connected through a differential pumping tube with a length of 7 cm and a diameter of 8 mm. The chambers are pumped with ion pumps (Star cell, Varian) and a titanium sublimation pump in the UHV chamber. The BEC is created inside a rectangular glass cell with good optical quality and broadband anti reflex coating. This glass cell is sealed with an aluminium Helicoflex gasket.

2.2.4 Laser system

The laser frequencies we need for creating and imaging the BEC are centered on the Rubidium $D2$ line with a wavelength of 780 nm. For this wavelength single mode diode lasers with large output powers are available. We use several of these lasers and reduce their bandwidth to about 1 MHz by operating them as grating stabilized external cavity lasers [49]. The lasers are stabilized with various locking techniques. The repump laser on the $|F=1\rangle \rightarrow |F'=2\rangle$ transition and the pump laser on the $|F=2\rangle \rightarrow |F'=2\rangle$ transition are locked to the Rubidium spectrum by using a doppler free spectroscopy. The lock signal is generated by a heterodyne lock-in technique in the radio frequency domain [50, 51]. The main cooling laser on the $|F=2\rangle \rightarrow |F'=3\rangle$ transition is locked relative to the pump laser. Both lasers are superimposed on a fast photo diode that detects the beat frequency. The cooling laser is then stabilized to a constant beat frequency [52]. The frequency of this laser can be precisely tuned over several hundred MHz during the experiment. For the MOT this laser is amplified by injecting a tapered amplifier semiconductor laser to reach about 300 mW laser power [53]. After an optical fiber 110 mW are available for the MOT beams. The laser can be rapidly detuned during the optical molasses and is also used on resonance without amplification for absorption imaging of the BEC.

2.2.5 Time of flight absorption imaging

The spatial density distribution of an atom cloud can be measured by absorption imaging. When an atom cloud is illuminated by resonant laser light the atoms absorb light and cast a shadow on the light beam. This shadow can be measured by imaging the cloud with a charge coupled device (CCD) camera.

A light beam with the spatial Intensity $I_0(x,y)$ that propagates in the z direction through a cloud of atoms is attenuated according to the optical density $D(x,y)$:

$$I(x,y) = I_0(x,y) \cdot e^{-D(x,y)}. \tag{2.12}$$

The optical density $D(x,y)$ depends on the column density $\tilde{n}(x,y)$, which is the spatial density $n(x,y,z)$ integrated along the z direction

$$\begin{aligned} D(x,y) &= D_0(x,y) \cdot \frac{1}{1 + \frac{I}{I_{sat}} + \frac{4\Delta^2}{\Gamma^2}}, && (2.13) \\ \text{with} \quad D_0(x,y) &= 2\sigma_0 \cdot \int n(x,y,z)\, dz = 2\sigma_0 \cdot \tilde{n}(x,y), && (2.14) \end{aligned}$$

where $\sigma_0 = \lambda^2/2\pi$ is the polarization averaged resonant scattering cross section of the atoms, Δ the detuning of the light, I_{sat} the saturation intensity and Γ the natural line width of the transition. In the measurements two images are taken: one image with atoms and one without corresponding to $I(x,y)$ and $I_0(x,y)$ respectively. Therefore the column density $\tilde{n}(x,y)$ can be directly determined using the above equations. This imaging technique is destructive since it relies on incoherent scattering of photons and therefore leads to a strong heating of the atomic ensemble.

Bose condensed atomic clouds can usually only be imaged after free ballistic expansion, since the optical density is very high[3]. When all trapping potentials are switched off, the cloud expands according to the momentum distribution of the condensate. For a normal condensate the momentum distribution is strongly affected by the interaction energy, giving rise to a post release momentum kick. In the lattice experiments, this effect is often negligible and the time of flight image reveals the original momentum distribution of the atomic ensemble.

In the experiment we use resonant light on the $|F=2\rangle \rightarrow |F'=3\rangle$ transition for absorption imaging. After time of flight periods of typically 10-20 ms the light is applied for $\approx 80\,\mu s$.

---

[3] The optical density of a BEC can not be reduced by choosing a large detuning since in this case the refractive index of the cloud gets large and leads to lens like effects. However, with phase contrast imaging techniques the cloud can be imaged without expansion and non destructively [54, 55, 56].

The shadow image is recorded on a slow-scan CCD camera[4] using an achromatic imaging lens.

2.2.6 Experimental sequence

The following experimental steps are used to obtain a ^{87}Rb Bose-Einstein condensate in the $|F=2, m_F=2\rangle$ state:

- MOT: Within 4-8 s up to $3 \cdot 10^9$ atoms are captured in a vapor cell magneto optical trap. For the last 80 ms the detuning is increased to 22 MHz in order to increase the confinement in a compressed MOT.
- Molasses: At the end of the MOT phase we further cool the atoms in an optical molasses [57]. The magnetic field is switched off and the detuning is increased to 80 MHz within 14 ms. We apply the molasses for about 20 ms. After this time the temperature has dropped to $\approx 50\mu K$.
- Optical pumping: After the molasses phase we optically pump the atoms into the $|F=2, m_F=2\rangle$ state, which is a low field seeking state and can be trapped magnetically. This pump process is done by rapidly switching on an offset field of about 1 G and simultaneously applying σ^+ polarized light on the $|F=2\rangle \rightarrow |F'=2\rangle$ and $|F=1\rangle \rightarrow |F'=2\rangle$ transition for about 500 μs. The atoms scatter only a few photons and end up in the $|F=2, m_F=2\rangle$ state, which is a dark state for these transitions.
- Quadrupole magnetic trap: In order to transfer the atoms into the magnetic trap we rapidly switch on the Quadrupole magnetic magnetic field within $\approx 500\,\mu s$ to a field gradient is 70 G/cm in the vertical direction. For this gradient the size of the atom cloud is well matched to the trap geometry. After that we increase the trap confinement adiabatically to a magnetic field gradient of 150 G/cm within 200 ms.
- Magnetic transport: In a first step, we move the atoms as fast as possible from the vapor cell through the differential pumping tube into the good vacuum of the UHV chamber by shifting the magnetic trapping potential. The transport takes two seconds including a smooth acceleration and deceleration phase in order to avoid heating. Then we transport the atoms within two seconds in an orthogonal direction into the UHV glass cell, where we have an exceptional optical access to the BEC.
- QUIC trap: At the final trapping site the quadrupole trap is smoothly converted into a Ioffe Pritchard within 500 ms. The final trapping frequencies are 24 Hz in the axial (horizontal) direction and 220 Hz in the radial direction with an offset field of 1 G.
- Evaporative cooling: As a final cooling step we evaporatively cool the atoms by lowering the effective potential depth. This is done by radio-frequency (RF) induced transitions between the Zeeman levels into untrapped states. Wa apply a RF sweep for about 20 s and finally get a nearly pure condensate of about $5 \cdot 10^5$ atoms.

---

[4] AP7p from Apogee and cameras from FLI and Sony

- Changing the confinement: The offset field of the Ioffe trap can be changed after creating the Bose-Einstein condensate to values up to 200 G, resulting in a decreased radial confinement of the condensate. For 150 G the trap is spherical with trapping frequencies of 24 Hz. The offset field is typically changed within 500 ms.

After the Bose-Einstein condensate is created we can transfer it into various periodic dipole potentials, which are formed by interfering far red detuned laser beams as described in the next chapter. Finally the spatial distribution of the atom cloud after ballistic expansion can be measured by time of flight absorption imaging.

3 Superfluid Bose-Einstein condensates in optical lattice potentials

Ultracold atoms in a periodic arrangement of microscopic trapping potentials form an intriguing physical system which is closely related to systems in condensed matter physics. In this chapter I report on experiments where a Bose-Einstein condensate is adiabatically transferred in two and three-dimensional optical lattice potentials. In the first part of this chapter, I discuss the theory of optical lattices and describe the experimental realization. The second part of this chapter describes experiments with Bose-Einstein condensates stored in lattice potentials, where the condensate is still in the weakly interacting regime.

Periodical optical lattice potentials have been used in various experiments with cold atoms, for example in the context of atom diffraction [58, 59] with applications for atom optics and atom interferometry (for a review see [60]). Atoms have been confined in one direction in an optical standing wave [61, 62]. The first experiment where atoms have been cooled to the micro-kelvin regime in a multi dimensional optical lattice potential was carried out by A. Hemmerich and T. W. Hänsch [63, 64, 65], followed by Grynberg *et al.* [66](review [67]). The group of C. Salomon has managed to cool a gas to a momentum spread of $\delta p = \hbar k/4$ in one direction by using one-dimensional Raman laser cooling [68] and switching on a periodic lattice potential adiabatically. With this small momentum spread the momentum distribution is not spread out over the whole Brillouin zone anymore and each atom is delocalized over several lattice sites. Therefore it was possible to observe Bloch oscillations. Wannier Stark ladders have been observed in the group of M. Raizen [69]. In the group of T.W. Hänsch, Bragg spectroscopy has been performed on atoms in a three-dimensional lattice and superlattices have been studied [70, 71]. In addition, far off-resonant one-dimensional lattices have been realized using a CO_2 laser [72]. It has been shown that in such a system individual lattice sites can be addressed and controlled [73].

There have been various attempts to cool atoms directly in a three-dimensional optical lattice, some of them have been mentioned above. Raman cooling has been successfully used for cooling atoms in these potentials, and recently atoms have been cooled partially to the ground state with filling factors on the order of one [74, 75, 76]. The successful Bose-Einstein condensation of neutral atoms by evaporation cooling techniques, however, paved the way for a totally different approach. In a Bose Einstein condensate extremely low temperatures can be achieved. When a condensate is adiabatically transferred into an optical lattice potential, the new ground state of the periodic lattice potential is populated without further cooling. Tunnelling processes, Josephson dynamics, superfluidity and Bloch oscillations have been studied in one-dimensional lattice potentials [77, 78, 33, 79] as well as number squeezing [3]. Short optical standing wave pulses are also used for Raman spectroscopy [80, 81].

3.1 Theory of optical lattices

In order to have a large tunnel coupling between neighboring potentials it is highly desirable to keep the spacing between individual lattice sites as small as possible. This can be achieved by using the standing wave interference pattern of two counter propagating laser beams, where the lattice spacing equals half of the laser wavelength. In such an arrangement the atoms can be trapped in the intensity maxima or minima of the light field due to the optical dipole force [82, 83].

In this chapter we first introduce optical dipole potentials and lattice potentials in one, two and three dimensions. Then we discuss the form of the ground state of a Bose-Einstein condensate in such a lattice potential. This approach is valid when the interaction energy between the atoms is still much smaller than the tunnelling energy. The situation when this is not the case will be discussed in chapter 4.

3.1.1 Optical dipole potentials

Neutral atoms interact with a light field in both a dissipative and a conservative way. The dissipative component of the interaction arises due to the absorption of photons followed by subsequent spontaneous emission. It results in a dissipative force on the atoms caused by the momentum transfer of the absorbed and spontaneously emitted photons. This light force is widely used for laser cooling and magneto optical traps.

In contrast to this, the conservative component of the atom - light interaction arises due to the interaction of the light field with the light induced dipole moment of the atom. This interaction causes a shift in the potential energy, called the ac-Stark shift. For large detunings of the light versus the atomic resonances, spontaneous emission processes can be neglected and the energy shift can be used to create a conservative trapping potential for neutral atoms. By shining a spatially modulated light field onto a cloud of atoms an energy landscape can be formed, where the local potential energy is proportional to the local light intensity [84, 85].

Oscillator model

When an atom is placed into a laser light field, the electric field $\mathbf{E}$, oscillating with the complex amplitude E at a frequency $\omega = 2\pi\nu$, induces an oscillating atomic dipole moment $\mathbf{d}$. The dipole moment oscillates at the same frequency with the complex amplitude d given by [86]

$$d = \alpha(\omega) E. \tag{3.1}$$

Here $\alpha(\omega)$ is the complex polarizability which depends on the laser frequency ω. The resulting dipole potential is determined by time averaging over $\mathbf{d} \cdot \mathbf{E}$

$$V_{dip} = -\frac{1}{2}\langle \mathbf{dE} \rangle = -\frac{1}{2\epsilon_0 c}\mathrm{Re}(\alpha) I \tag{3.2}$$

with the laser field intensity

$$I = 1/2\epsilon_0 c |E|^2. \tag{3.3}$$

The potential energy of the atom in the light field is thus proportional to the laser intensity and the real part of the polarizability. Spontaneous scattering on the other hand is proportional to the imaginary part of the polarizability. The scattering rate is given by

$$\Gamma_{sc} = -\frac{\langle \dot{\mathbf{d}}\mathbf{E} \rangle}{\hbar\omega} = -\frac{1}{\hbar\epsilon_0 c}\mathrm{Im}(\alpha) I. \tag{3.4}$$

The wavelength dependent polarizability can be calculated with Lorentz's model of a classical damped oscillator:

$$\alpha(\omega) = 6\pi\epsilon_0 c^3 \frac{\Gamma/\omega_0^2}{\omega_0^2 - \omega^2 - i(\omega^3/\omega_0^2)\Gamma}. \tag{3.5}$$

Here ω_0 is the resonance frequency of the oscillator model and Γ is the on resonance damping rate. A more appropriate approach to calculate the atomic polarizability is given by a semiclassical model. In this model, the atom is treated as a two-level quantum system interacting with a classical field. For a large enough detuning saturation effects can be neglected ($\Gamma_{sc} \ll \Gamma$, this is usually the case for dipole traps) and the calculation yields the same result as equation (3.5). The damping Γ is then determined by the dipole matrix element between ground state $|g\rangle$ and excited state $|g\rangle$ in the two-level atom

$$\Gamma = \frac{\omega_0^3}{3\pi\epsilon_0 \hbar c^3} |\langle e|\mu|g\rangle|^2. \tag{3.6}$$

with $\mu = -e\mathbf{r}$ representing the dipole operator. The above expressions enable us to determine the strength of the dipole potential and the residual scattering rate as

$$V_{dip}(\mathbf{r}) = \frac{3\pi c^2}{2\omega_0^3}\left(\frac{\gamma}{\omega_0 - \omega} + \frac{\gamma}{\omega_0 + \omega}\right) I(\mathbf{r}) \quad \approx \frac{3\pi c^2}{2\omega_0^3}\frac{\Gamma}{\Delta} I(\mathbf{r}) \tag{3.7}$$

$$\Gamma_{sc}(\mathbf{r}) = \frac{3\pi c^2}{2\hbar\omega_0^3}\left(\frac{\omega}{\omega_0}\right)^3 \left(\frac{\gamma}{\omega_0 - \omega} + \frac{\gamma}{\omega_0 + \omega}\right) I(\mathbf{r}) \quad \approx \frac{3\pi c^2}{2\hbar\omega_0^3}\left(\frac{\Gamma}{\Delta}\right)^2 I(\mathbf{r}) \tag{3.8}$$

where $\Delta = \omega - \omega_0$ is the detuning of the light field relative to the atomic resonance. On the right hand side the rotating wave approximation has been employed. It is valid for small detunings $|\Delta| \ll \omega_0$ and is commonly used. However, for a detuning of 10% it already yields an error of 5% in the potential strength and 20% in the scattering rate.

The optical dipole potential in eq. 3.7 is proportional to the intensity of the light field and the sign depends on the laser detuning. For blue detuning ($\Delta > 0$), the sign is positive resulting in a repulsive potential. A red detuned light field ($\Delta < 0$) creates an attractive potential with a negative sign.

The proper detuning for an optical dipole potential depends on the available laser power and the maximum inelastic scattering rate which can be tolerated. On one hand, with small detunings it is possible to create larger trap depths for a given laser intensity, since the dipole potential scales as I/Δ. On the other hand the inelastic scattering rate scales quadratically with the detuning as I/Δ^2. The scattering rate as a function of the detuning and total trap depth is given by

$$\hbar\Gamma_{sc} = \frac{\Gamma}{\Delta} V_{dip}. \tag{3.9}$$

Therefore, the laser detuning for a dipole trap should be chosen as large as possible, within the available laser power, in order to minimize inelastic scattering processes and create a conservative potential.

Dressed state picture

An alternative description of dipole potentials is given by the dressed state picture [87], where the atom is considered together with a quantized light field. Lets consider a light field with n photons and an atom in the ground state $|g\rangle$. The unperturbed energy of this system is $\epsilon_g = n \cdot \hbar\omega$ since the atom in the ground state has a zero internal energy. If, on the other hand, the atom has absorbed one photon, the total unperturbed energy of the atom in the excited state and the light field with $n-1$ photons is $\epsilon_e = \hbar\omega_0 + (n-1)\cdot\hbar\omega = -\hbar\Delta + n\hbar\omega$.

The effect of the interaction can be determined with second order perturbation theory. For non degenerate states, an interaction described by the Hamiltonian H_{int} shifts the energy of the ith state by

$$\Delta E_i = \sum_{j\neq i} \frac{|\langle j|H_{int}|i\rangle|^2}{\epsilon_i - \epsilon_j}, \tag{3.10}$$

where ϵ_i is the unperturbed energy of the ith state. The Hamiltonian of the atom - light interaction can be written as $H_{int} = -\hat{\mu}\mathbf{E}$ with $\hat{\mu} = -e\mathbf{r}$ representing the electric dipole operator. For a two level atom this simplifies to $H_{int} = -\mu E$. The energy in the denominator simply becomes $\epsilon_g - \epsilon_e = \hbar\Delta$. Therefore the energy shift due to the atom - light interaction reads

$$\Delta E_{g/e} = \pm\frac{|\langle e|\mu|g\rangle|^2}{\Delta}|E|^2 = \pm\frac{3\pi c^2}{2\omega_0^3}\frac{\Gamma}{\Delta} I \tag{3.11}$$

with the plus and minus sign for the ground and excited state respectively. On the right hand side we have used equation 3.3 and 3.6. This energy shift is also called light shift or ac-stark shift. Since the atom is practically always in the ground state, the energy of the atom is changed according to the light shift in the ground state which results in the effective dipole potential $V_{dip} = \Delta E_g$. This is the same result as achieved with the semiclassical approach including the rotating wave approximation (eq. 3.7).

Multi-level atoms

For a multi level atom in a specific ground state $|g_i\rangle$ transitions to all excited states $|e_j\rangle$ have to be taken into account when calculating equation 3.10. The dipole matrix element for these transitions is given by

$$\mu_{ij} = \langle e_i|\mu|g_j\rangle = c_{ij}\|\mu\|, \tag{3.12}$$

where $\|\mu\|$ is the reduced matrix element and c_{ij} denotes the specific line strength. The resulting dipole potential is given by the sum over all excited states $|e_j\rangle$ and can be written as

$$V_{dip}^{(i)} = \frac{3\pi c^2\Gamma}{2\omega_0^3} I \cdot \sum_j \frac{c_{ij}^2}{\Delta_{ij}} \tag{3.13}$$

with the spontaneous decay rate Γ according to equation 3.6 and the specific detunings Δ_{ij}.

The ^{87}Rb isotope, which is used in the experiment, is an alkali atom with a nuclear spin $I = 3/2$. The fine structure splitting due to spin-orbit coupling leads to the D-line doublet $^2S_{1/2} \rightarrow {}^2P_{1/2}, {}^2P_{3/2}$ with transition frequencies of 795 nm and 780 nm respectively. Coupling to the nuclear spin then leads to a hyperfine splitting of the ground state of about 6.8 GHz and a splitting of the excited states on the order of hundred MHz. For a laser detuning which is large compared to the excited state hyperfine splitting the hyperfine structure is not resolved and the following equation can be derived [82]:

$$V_{dip}(\mathbf{r}) = \frac{\pi c^2\Gamma}{2\omega_0^3}\left(\frac{2 + Pg_F m_F}{\Delta_{2,F}} + \frac{1 - Pg_F m_F}{\Delta_{1,F}}\right) I(\mathbf{r}) \tag{3.14}$$

In this equation g_F is the Landé factor, m_F the magnetic quantum number and $P = 0, \pm1$ for linear and $\sigma^\pm$ polarized light respectively. $\Delta_{2,F}$ and $\Delta_{1,F}$ are the detunings relative to the D_2 and D_1 line.

If the laser detuning is also large compared to the fine structure splitting and the polarization of the laser is linear, the dipole potential is simply given by the two level result (equation 3.7 or 3.10) with a detuning relative to the center of the D_2 and D_1 line. It is convenient to introduce the saturation intensity $I_{sat} = \hbar\Gamma\omega_0^3/12\pi c^2$ which then yields

$$V_{dip}(\mathbf{r}) = \frac{\hbar\Gamma^2}{8\Delta}\frac{I(\mathbf{r})}{I_{sat}} \tag{3.15}$$

for this equation.

Red detuned focus trap

The conservative potential described above can be used to trap cold atoms. A far red detuned laser creates an attractive potential for the atoms. Thus a confinement in three dimensions can be realized with a tight Gaussian laser focus. The intensity profile of a Gaussian laser beam is given by

$$I(r, z) = \frac{2P}{\pi w^2(z)} e^{-2\frac{r^2}{w^2(z)}} \tag{3.16}$$

where $w(z) = w_0(1 + (z/z_R)^2)^{1/2}$ is the $1/e^2$ radius depending on the z coordinate, $z_R = \pi w^2/\lambda$ is the Rayleigh length and P is the total power of the laser light. The peak intensity

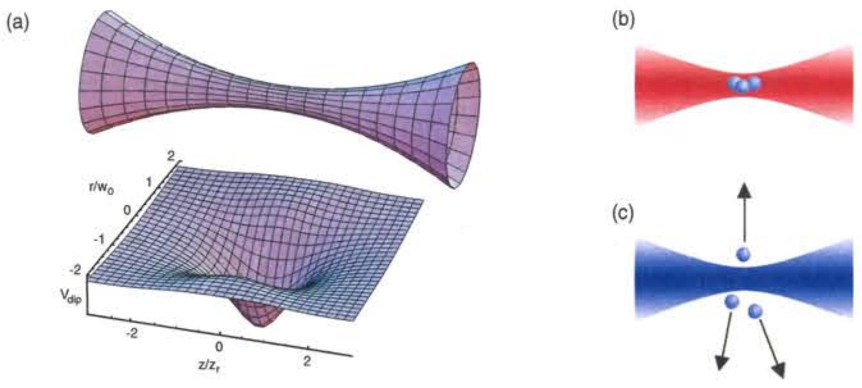

Figure 3.1: a) Schematical drawing of a Gaussian laser focus, plotted together with a cross section of the corresponding trapping profile for a red detuned focus trap. The trap creates strong radial and weak axial confinement (aspect ratio of potential profile not to scale). b) In a red detuned dipole trap the atoms are captured in the intensity maximum. c) Repulsion of atoms from a blue detuned dipole light field.

is given by $I_0 = 2P/\pi w_0^2$. A Gaussian beam with these parameters forms a cylindrically symmetric dipole trap. In the center of the trap the trapping potential can be approximated by

$$V(r,z) \simeq -V_0 \left[1 - 2\left(\frac{r}{w_0}\right)^2 - \left(\frac{z}{z_R}\right)^2\right], \tag{3.17}$$

resulting in trapping frequencies of $\omega_r = (4V_0/mw_0^2)^{1/2}$ and $\omega_z = (2V_0/mz_R^2)^{1/2}$. In Figure 3.1 a Gaussian laser focus is plotted together with the corresponding cross section of the trapping potential (ratio of axial and radial confinement not to scale). In the following discussion of periodic lattice potentials the radial confinement is important whereas the axial confinement is negligible compared to other sources of confinement.

3.1.2 Periodic lattice potentials

A periodic lattice potential with tightly confining potential wells can be created by realizing a dipole trap with superimposed counter propagating laser beams. These beams interfere and the interference pattern results in a periodic potential landscape.

1D lattice potential

The simplest possible lattice is a 1D lattice. It can be created e.g. by retroreflecting a Gaussian laser beam, such that a standing wave interference pattern is formed (fig. 3.2. This results in a periodic trapping potential given by:

$$V(r,z) = -V_{lat} \cdot e^{-2r^2/w_0^2} \cdot \sin^2(kz) \simeq -V_{lat} \cdot \left(1 - 2\frac{r^2}{w_0^2}\right) \cdot \sin^2(kz), \tag{3.18}$$

where w_0 denotes the beam waist, $k = 2\pi/\lambda$ is the absolute value of the wave vector of the laser light and V_{lat} is the potential depth of the optical lattice. Note that this depth is four times larger than the depth of the dipole trap without retro-reflection, due to the constructive interference between the two counterpropagating laser beams.

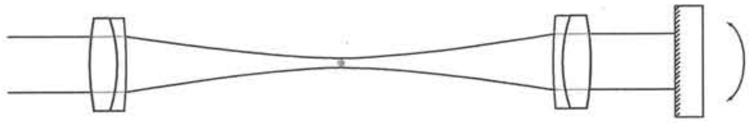

Figure 3.2: A standing wave laser field is formed by retroreflecting a Gaussian laser beam.

It is convenient to specify the lattice depth in units of recoil energies $E_r = \hbar^2 k^2/2m$ where m is the mass of a single atom. For a far detuned optical lattice potential, where the detuning is large compared to the excited state fine-structure, the lattice potential depth can be evaluated through:

$$\frac{V_{lat}}{E_r} = \frac{2m}{\hbar^2 k^2} \cdot \frac{3\pi c^2}{2\omega_0^3} \cdot \frac{\Gamma}{\Delta} \cdot \frac{2P}{\pi w_0^2}. \tag{3.19}$$

Here, Δ is the detuning relative to the center of the D1 and D2 line.

2D lattice potential

Periodic potentials in higher dimensions can be created by superimposing standing waves from different directions. To form a two-dimensional lattice potential two standing waves can be superimposed orthogonal to each other (Figure 3.3). At the center of the trap the potential has the form

$$V(y,z) = -V_{lat} \left\{\cos^2(ky) + \cos^2(kz) + 2\,\mathbf{e}_1 \cdot \mathbf{e}_2 \,\cos\phi\, \cos(ky)\cos(kz)\right\}. \tag{3.20}$$

Here k is the magnitude of the wave vector of the lattice light, $\mathbf{e}_1$ and $\mathbf{e}_2$ are polarization vectors of the standing waves and ϕ is a time phase between them. If the polarizations of the two standing waves are not perfectly orthogonal, they interfere with each other and the potential is changed depending on the time phase. This leads to a variation of the potential depth of neighboring lattice sites in a chequerboard like pattern (Figure 3.4). The resulting lattice potential is a square lattice with a "two atomic" basis. The time phase can be stabilized interferometrically (see chapter 3.2). However, a residual fluctuation of the time phase leads to a fluctuating potential depth of neighboring lattice sites. This can lead to decoherence and heating effects for certain configurations (see chapter 3.3.4).

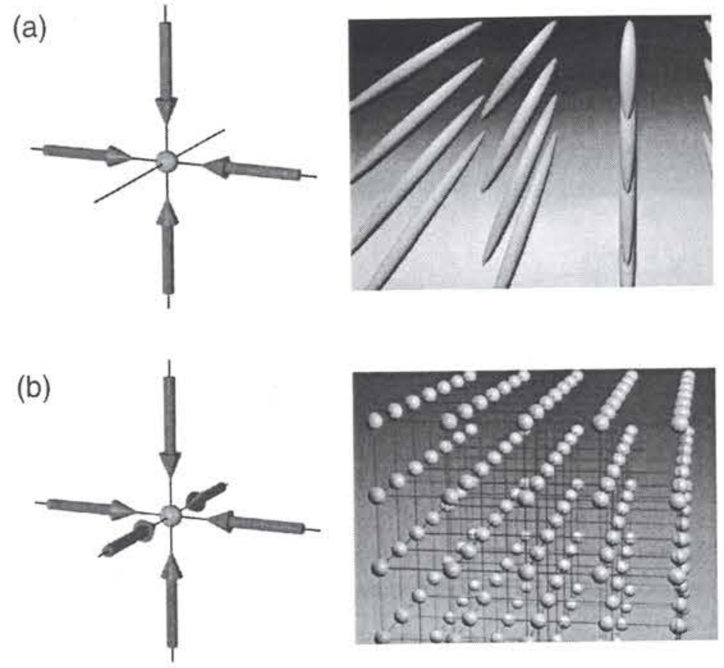

Figure 3.3: Schematical drawing of multidimensional optical lattice potentials, formed by superimposing counterpropagating, far red detuned laser beams superimposing. a) Two standing waves orthogonal to each other form an array of tightly confining potential tubes. b) A 3D lattice potential can be created by superimposing three standing waves.

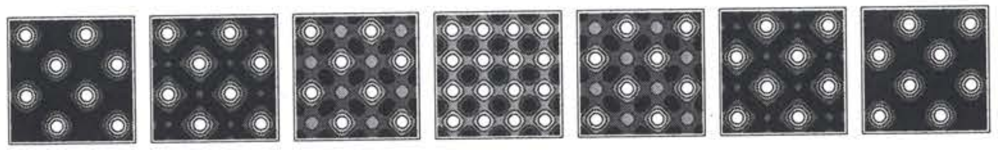

Figure 3.4: Chequerboard like lattice structure for a 2D lattice with parallel polarization and different time phases of $\phi = 0°$, $30°$, $60°$, $90°$, $120°$, $150°$ and $180°$ respectively.

A simple square lattice with a one atomic basis can be created by choosing orthogonal polarizations between the standing waves. In this case, the interference term in equation 3.20 vanishes and the resulting potential is simply the sum of the two superimposed 1D lattice potentials (like in figure 3.4, central plot, where the interference term also vanishes for a time phase of $\phi = 90°$). If the polarizations are not perfectly linear and orthogonal, a residual interference term might occur. This interference term can be suppressed by choosing different laser frequencies for both standing waves. For large frequency differences the time phase is rotating rapidly and the residual interference cancels out due to a time averaging of the effective potentials.

3D lattice potential

In our experiment we create a simple cubic lattice by superimposing three standing waves orthogonal to each other. The polarization between the three standing waves is mutually orthogonal, and we use different frequencies for the laser fields in order to time average any residual interferences between different standing waves. The beam pairs forming the standing wave in x, y and z direction have a Gaussian shape with $1/e^2$ radii w_x,w_y and w_z. The trapping potential for a red detuned lattice can then be written as

$$V(\mathrm{x}) = -V_x \cdot e^{-2\frac{y^2+z^2}{w_x^2}} \cdot \sin^2(kx) - V_y \cdot e^{-2\frac{x^2+z^2}{w_y^2}} \cdot \sin^2(ky) - V_z \cdot e^{-2\frac{x^2+y^2}{w_z^2}} \cdot \sin^2(kz). \quad (3.21)$$

Here V_x, V_y and V_z are the potential depths of the three superimposed 1D standing waves. In the center of the trap, for distances much smaller than the beam waist, the trapping potential can be approximated as the sum of a homogenous periodic lattice potential and an additional external harmonic confinement:

$$V(\mathrm{x}) \simeq V_x \cdot \sin^2(kx) + V_y \cdot \sin^2(ky) + V_z \cdot \sin^2(kz) + \frac{m}{2}\left(\omega_x^2 x^2 + \omega_y^2 y^2 + \omega_z^2 z^2\right), \quad (3.22)$$

where $\omega_{x,y,z}^2$ are the squares of the effective trapping frequencies of the external harmonic confinement. They are given by:

$$\omega_x^2 = \frac{4}{m}\left(\frac{V_y}{w_y^2} + \frac{V_z}{w_z^2}\right) = \frac{2\hbar^2 k^2}{m^2}\left(\frac{V_y/E_r}{w_y^2} + \frac{V_z/E_r}{w_z^2}\right); \qquad \omega_{y,z}^2 = (\text{cycl. perm.}). \quad (3.23)$$

In the experiment an additional confinement can be achieved by leaving on the magnetic trapping potential. In this case the squares of the trapping frequencies of the magnetic trap can simply be added to the confinement above.

For sufficiently deep optical lattices, the confinement of an individual lattice site can be approximated by a harmonic potential. For a given lattice depth V_{lat} in the x,y or z direction, the corresponding trapping frequencies can then be related to the lattice potential depth V_{lat} through:

$$\omega_{lat}^2 = V_{lat}\,\frac{2k^2}{m} \;=\; \frac{V_{lat}}{E_r}\,\frac{\hbar^2 k^4}{m^2}. \tag{3.24}$$

This equation is valid for the trap center. Away from the center the lattice depth is reduced due to the Gaussian beam shape, as can be seen from the exact equation 3.21. Along the $x-$axis for example, the trapping frequency on a lattice site falls off like

$$\omega_{lat\,x}(\mathbf{x}) = \omega_{lat\,x}(0)\cdot\exp\left(-\frac{y^2+z^2}{w_x^2}\right) \simeq \omega_{lat\,x}(0)\cdot\left(1-\frac{y^2+z^2}{w_x^2}\right) \tag{3.25}$$

This reduction is negligible for our typical experimental parameters and corresponds roughly to a 3% decrease of the external trapping frequency over the cloud of atoms. However, the change of the trapping frequency results in a change in the ground state energy $V_{GS} = \hbar/2(\omega_x+\omega_y+\omega_z)$ which in second order tends to decrease the external confinement due to the beam shape in equation 3.23. For an isotropic situation with $V_{x,y,z} = V_{lat}$, $w_{x,y,z} = w_0$ and $r^2 = x^2+y^2+z^2$ the effective potential of the external confinement can be calculated as

$$V_{ext}(r) = E_r\left(2\frac{V_{lat}}{E_r} - \sqrt{\frac{V_{lat}}{E_r}}\right)\frac{2r^2}{w_0^2}. \tag{3.26}$$

This results in an external confinement $\omega_{ext} = \omega_{x,y,z}$

$$\omega_{ext}^2 = \frac{4\,E_r}{m w_0}^2\cdot\left(2\frac{V_{lat}}{E_r} - \sqrt{\frac{V_{lat}}{E_r}}\right). \tag{3.27}$$

In contrast to equation 3.23 this value is corrected for the spatial change in the ground state energy.

3.1.3 Bloch Bands

Characteristic for the movement of a particle in a periodic potential is the emergence of a band structure. In this section the wave function of a single particle in a periodic lattice potential is calculated and the band structure is investigated.

A particle in a periodic potential $V(x)$ is described by the Schrödinger equation

$$H\phi_q^{(n)}(x) = E_q^{(n)}\phi_q^{(n)}(x) \qquad \text{with} \qquad H = \frac{1}{2m}\hat{p}^2 + V(x). \tag{3.28}$$

Solutions of this equation are called Bloch wave functions (see e.g. [88]) and can be written as a product of a plane wave $\exp(iqx/\hbar)$ and a function $u_q^{(n)}(x)$ with the same periodicity as the periodic potential:

$$\phi_q^{(n)}(x) = e^{iqx/\hbar}\cdot u_q^{(n)}(x). \tag{3.29}$$

Inserting this ansatz into eq. 3.28 leads to a Schrödinger equation for $u_q^{(n)}(x)$:

$$H_B\,u_q^{(n)}(x) = E_q^{(n)}u_q^{(n)}(x) \qquad \text{with} \qquad H_B = \frac{1}{2m}(\hat{p}+q)^2 + V(x) \tag{3.30}$$

Since both the potential $V_{lat}(x)$ and the functions $u_q^{(n)}(x)$ are periodic with the same periodicity, they can be written as a discrete Fourier sum:

$$V(x) = \sum_r V_r e^{i2rkx} \qquad \text{and} \qquad u_q^{(n)}(x) = \sum_l c_l^{(n,q)} e^{i2lkx}, \tag{3.31}$$

with l and r integers. With these sums the potential energy term of equation 3.30 becomes

$$V(x)u_q^{(n)}(x) = \sum_l\sum_r V_r e^{i2(r+l)kx} c_l^{(n,q)} \tag{3.32}$$

and the kinetic term becomes

$$\frac{(\hat{p}+q)^2}{2m}u_q^{(n)}(x) = \sum_l \frac{(2\hbar k l+q)^2}{2m} c_l^{(n,q)} e^{i2lkx}. \tag{3.33}$$

In the experiment, a sinusoidal lattice potential is created, such that:

$$V(x) = -V_{lat}\cos^2(kx) = -\frac{1}{4}V_{lat}\left(e^{2ikx} + e^{-2ikx} + 2\right) \tag{3.34}$$

Thus only two terms of the Fourier sum in equation 3.31 are nonzero: V_{-1}=V_1=$-1/4V_{lat}$ and V_0 can be set to zero. Using these results we can write the Schrödinger equation of 3.30 in matrix form as:

$$\sum_l H_{l,l'}\cdot c_l^{(n,q)} = E_q^{(n)} c_l^{(n,q)} \qquad \text{with} \qquad H_{l,l'} = \begin{cases} (2l+q/\hbar k)^2 E_r & \text{if } l = l' \\ -1/4\cdot V_0 & \text{if } |l-l'| = 1 \\ 0 & \text{else} \end{cases} \tag{3.35}$$

Here q is the quasi momentum, within the first Brillouin zone ranging from $q = -\hbar k$ to $\hbar k$. For a certain quasi momentum q the eigenvalues $E_q^{(n)}$ of H represent the eigenenergies in the n^{th} energy band. The corresponding eigenvector $c^{(n,q)}$ defines the appropriate Bloch wave function through equations 3.31 and 3.29. These eigenstates and eigenvectors can be simply calculated if the Hamiltonian is truncated for large positive and negative l. The corresponding coefficients $c^{(n,q)}$ become very small for large enough l, e.g. a restriction to $-5 \geq l \geq 5$ is a good choice if only the lowest energy bands are considered.

Figure 3.5 shows the band structure for a a one-dimensional sinusoidal lattice for different potential depths. For a vanishing lattice depth, there are no band gaps and the "bands" equal the free particle energy-momentum parabola reduced to the first Brillouin zone. When the lattice depth is increased, the band gaps become larger and the width of the energy bands becomes exponentially smaller.

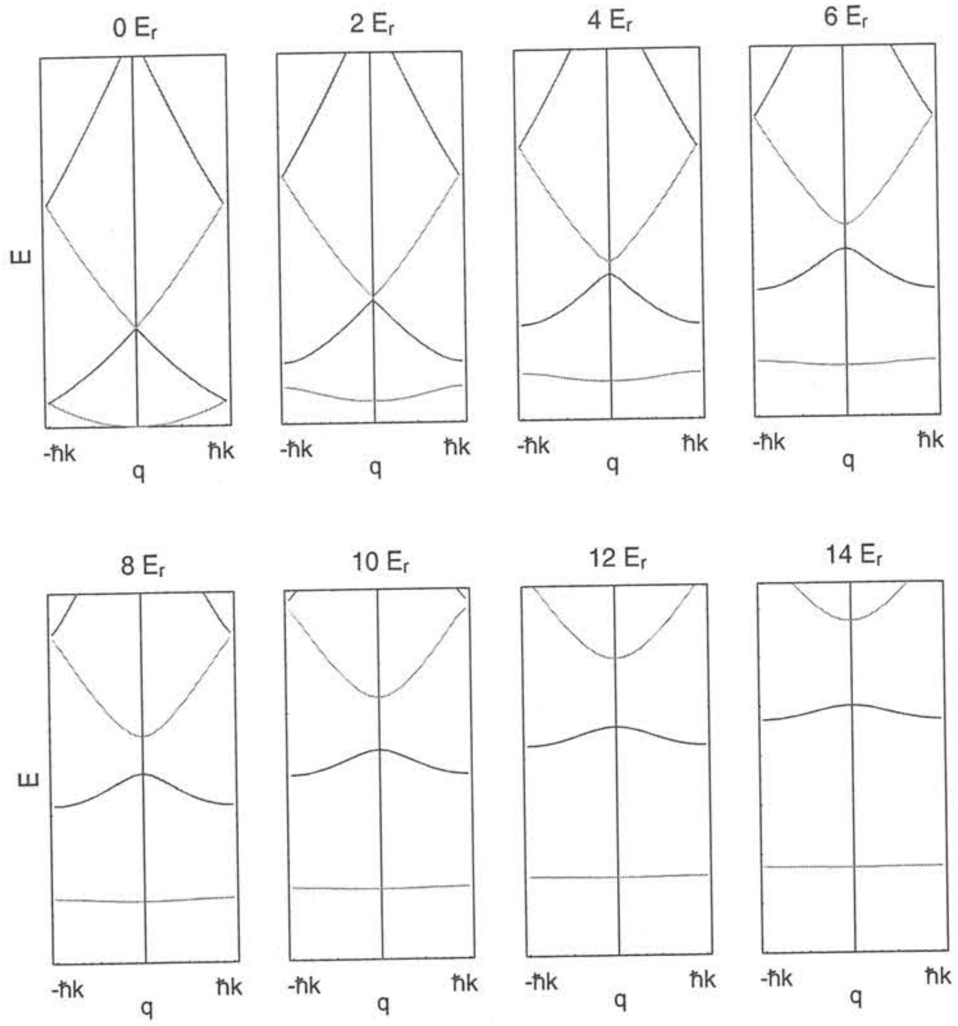

Figure 3.5: Band structure of an optical lattice: Energy of the Bloch state versus quasi momentum q in the first Brillouin zone, plotted for different lattice depths between 0 and 14 E_r. For deep lattices the lowest band becomes flat and the width of the first band gap corresponds to the level spacing $\hbar\omega$ on each lattice site.

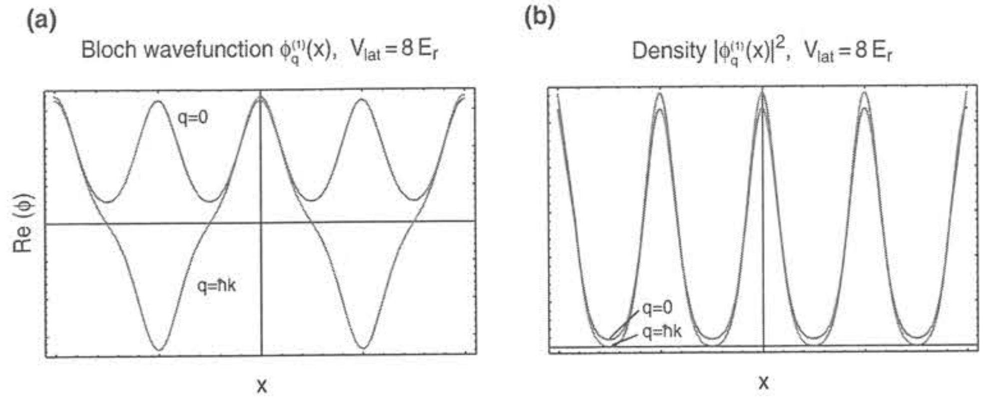

Figure 3.6: Real part (a) and probability density (b) of the Bloch wave functions $\phi_q^{(1)}(x)$ in the lowest band, corresponding to a quasi momentum of $q = 0$ and $q = \hbar k$. The lattice potential is a 1D sinusoidal potential with a lattice depth of 8 E_r.

Two and three-dimensional sinusoidal simple cubic lattices are in our case fully separable. Therefore the wave functions can be calculated separately for each axis and the total energy is given by the sum of the eigenenergies of all axes.

In figure 3.6a the real part of a Bloch wave function for an 8 E_r deep lattice is plotted. The symmetric function is the Bloch function $\phi_{q=0}^{(n=1)}(x)$ in the lowest band with a quasi momentum $q = 0$, and the anti symmetric one is the Bloch function with $q = \hbar k$ at the border of the Brillouin zone. Figure 3.6b shows the corresponding probability densities of the same wave functions.

The tunnelling matrix element J which describes the tunnel coupling between neighboring lattice sites is directly related to the width of the lowest energy band [89] through:

$$J = (\max(E_q^{(0)}) - \min(E_q^{(0)}))/4. \tag{3.36}$$

3.1.4 Wannier functions

Bloch states are completely delocalized energy eigenstates of the Schrödinger equation for a given quasi momentum q and energy band n. In contrast to this, Wannier functions constitute an orthogonal and normalized set of wave functions that are maximally localized to individual lattice sites. The Wannier function for a localized particle in the n^{th} energy band of the optical lattice potential is given by [90]

$$w_n(x-x_i) = \mathcal{N}^{-1/2}\sum_q e^{-iqx_i/\hbar}\phi_q^{(n)}(x). \tag{3.37}$$

Here x_i is the position of the i^{th} lattice site and $\mathcal{N}$ is a normalization constant.

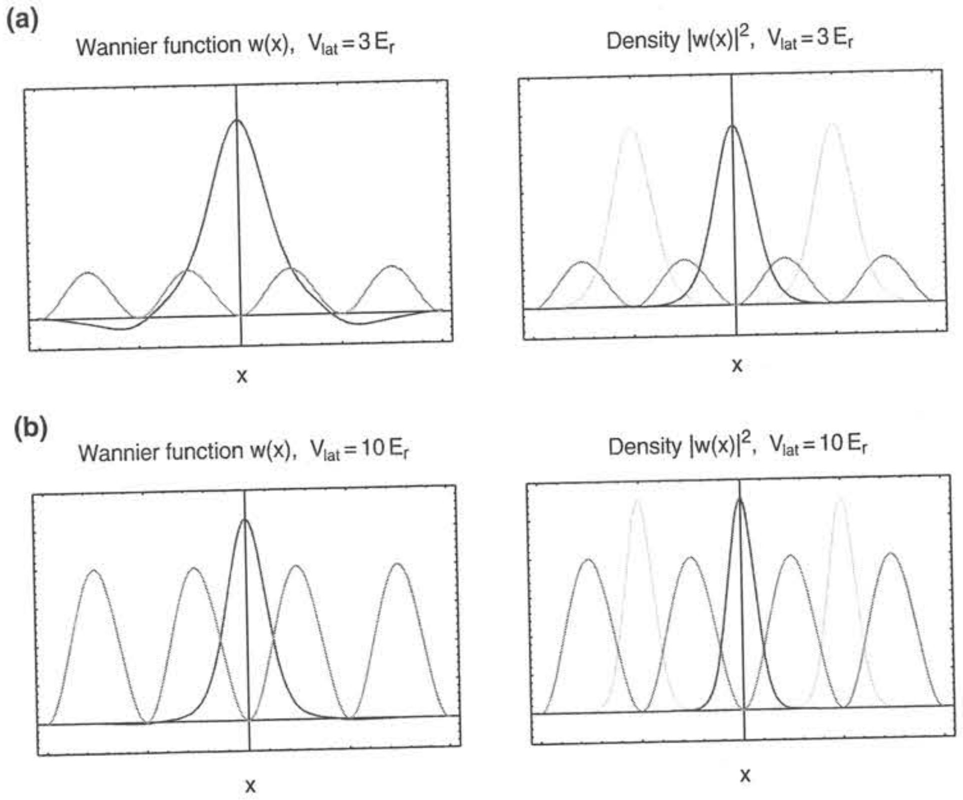

Figure 3.7: Wannier function and probability density for 3 E_r (a) and 10 E_r (b) deep lattices, plotted together with a schematic lattice potential. Wannier functions constitute an orthogonal set of maximally localized wave functions. For 3 E_r sidelobes are visible, for 10 E_r the sidelobes become very small corresponding to a decreased tunnelling probability.

If a particle is in a mode corresponding to this Wannier wave function, it is well localized to the i^{th} lattice site. Figure 3.7 shows the Wannier function and the density square of this function for a 3 E_r and 10 E_r deep lattice. Two side lobes of the Wannier function are visible which can be attributed to a non vanishing probability to find the atom in the neighboring lattice site due to tunnelling. The tunnelling matrix element J, which describes the tunnelling between neighboring lattice sites, can be calculated through equation 3.36, or alternatively by considering two Wannier functions of neighboring lattice sites i and j:

$$J = \int w_n(x-x_i)\left(-\frac{\hbar^2}{2m}\frac{\partial^2}{\partial x^2} + V(x)\right) w_n(x-x_j)\mathrm{d}x \tag{3.38}$$

For deep lattices the localized Wannier wave function can be approximated by a Gaussian ground state wave function. However, due to the much weaker side lobes of a Gaussian, the tunnel matrix element J is then underestimated by almost an order of magnitude.

The Wannier description becomes particulary important when the interaction between particles is taken into account. Local interactions of particles on a lattice site can best be described in a localized Wannier basis.

3.1.5 Ground state wave function of a BEC in an optical lattice

Discretization

In the weakly interacting regime, when the tunnel coupling between neighboring lattice sites is large compared to the interaction energy between two atoms, a Bose-Einstein condensate trapped in a periodic lattice potential can be described by a macroscopic wave function, which in turn can be determined through the Gross-Pitaevskii equation. If the chemical potential is small compared to the trap depth, a tight binding picture can be used to describe the system. In this regime the extension of the ground state wave function is much smaller than the lattice spacing, and the condensate effectively consists of tiny BECs with phases that are coupled due to tunnelling between the lattice sites. Such an arrangement behaves similarly to a Josephson junction [77, 33].

In the tight binding picture the atoms on a lattice site j can be described by a localized macroscopic wave function $\varphi_j(x)$. If the chemical potential on a lattice site is much smaller than the vibrational level spacing, the ground state wave function can be well approximated by the noninteracting ground state wave function of the lowest vibrational level. To a first approximation this is the Gaussian ground state wave function of a harmonic oscillator.

If the chemical potential is slightly larger, the broadening of the ground state wave function due to the repulsive interaction between the atoms has to be taken into account. In this case a better approximation for the ground state wave function can be found by determining an effective width of the wave function using a variational ansatz.

For a three-dimensional simple cubic lattice with a chemical potential much smaller than the level spacing in each direction the localized wave function can be described as the product of three Wannier functions $w(x)$ of the lowest Bloch band for each direction:

$$\varphi_j(\mathbf{x}) = w_x(x-x_i)\cdot w_y(y-y_i)\cdot w_z(z-z_i), \tag{3.39}$$

where x_i, y_i and z_i denote the position of the ith lattice site.

The situation is different for a one or two-dimensional optical lattice, where the confinement is usually very weak in two or one direction respectively. Along the axes of weak confinement the ground state wave function Θ will generally be broadened due to the repulsive interactions between the atoms. The resulting wave function can then be written as:

$$\begin{array}{ll} \text{1D lattice:} & \varphi_j(\mathbf{x}) = w_x(x-x_i)\cdot\Theta^{(y)}(y-y_i)\cdot\Theta^{(z)}(z-z_i) \\ \text{2D lattice:} & \varphi_j(\mathbf{x}) = w_x(x-x_i)\cdot w_y(y-y_i)\cdot\Theta^{(z)}(z-z_i) \end{array} \tag{3.40}$$

Using these localized wave functions we can define a macroscopic wave function which describes the total system. This wave function is the sum of localized wave functions at each lattice site j

$$\Psi(\mathbf{x}) = \sum_j \psi_j\cdot\varphi_j(\mathbf{x}); \qquad \psi_j = \sqrt{\overline{n}_j}\cdot e^{i\phi_j} \tag{3.41}$$

each having a well defined phase ϕ_j and an amplitude $\sqrt{\overline{n}_j}$, where $\overline{n}_j$ corresponds to the average atom number on the j^{th} lattice site. The total atom number is given by $\sum_j|\psi_j|^2 = \sum_j\overline{n}_j = N$. For this array of weakly coupled condensates, each described by ψ_j, the Hamiltonian is

$$\mathcal{H} = -J\sum_{<i,j>}\psi_i^*\psi_j + \sum_j\epsilon_j|\psi_j|^2 + \sum_j\frac{1}{2}U|\psi_j|^4, \tag{3.42}$$

where the first summation is carried out over neighboring lattice sites only. This term characterizes the Josephson energy of the system. The second term describes the inhomogeneity of the trapping potential, where ϵ_j is the energy offset of the j^{th} lattice site, given by $\epsilon_j = m/2\cdot\omega_{ext}^2 r_j^2$. The third term describes the on-site interaction energy, where U is the on-site interaction matrix element defined by

$$U = \frac{4\pi\hbar^2 a}{m}\int \mathrm{d}^3\mathbf{x}\,|\varphi_j(\mathbf{x})|^4, \tag{3.43}$$

with a being the scattering length of the atoms.

The dynamics of this Josephson junction array can be described by a discrete nonlinear Schrödinger equation (DNLSE), also called discrete Gross-Pitaevskii equation [33].

Ground state

In the inhomogeneous system it is important to find the new ground state of the combined lattice and external confining potential. For a purely periodic potential the energy is minimized if the phases of the wave functions on different lattice sites are equal, since then the Josephson energy is minimal. In the Bloch picture this corresponds to the Bloch state with zero quasi momentum (q=0).

But how will the atoms distribute over the lattice in the inhomogeneous system? In order to be in a stationary state, the phases of the wave functions on different lattice sites have to evolve with the same rate over time. This requires that their local chemical potentials are equal. In a Thomas Fermi approximation we can neglect the contribution of the kinetic energy term (which is the Josephson term in equation 3.42), so that the total energy on a single lattice site is given by

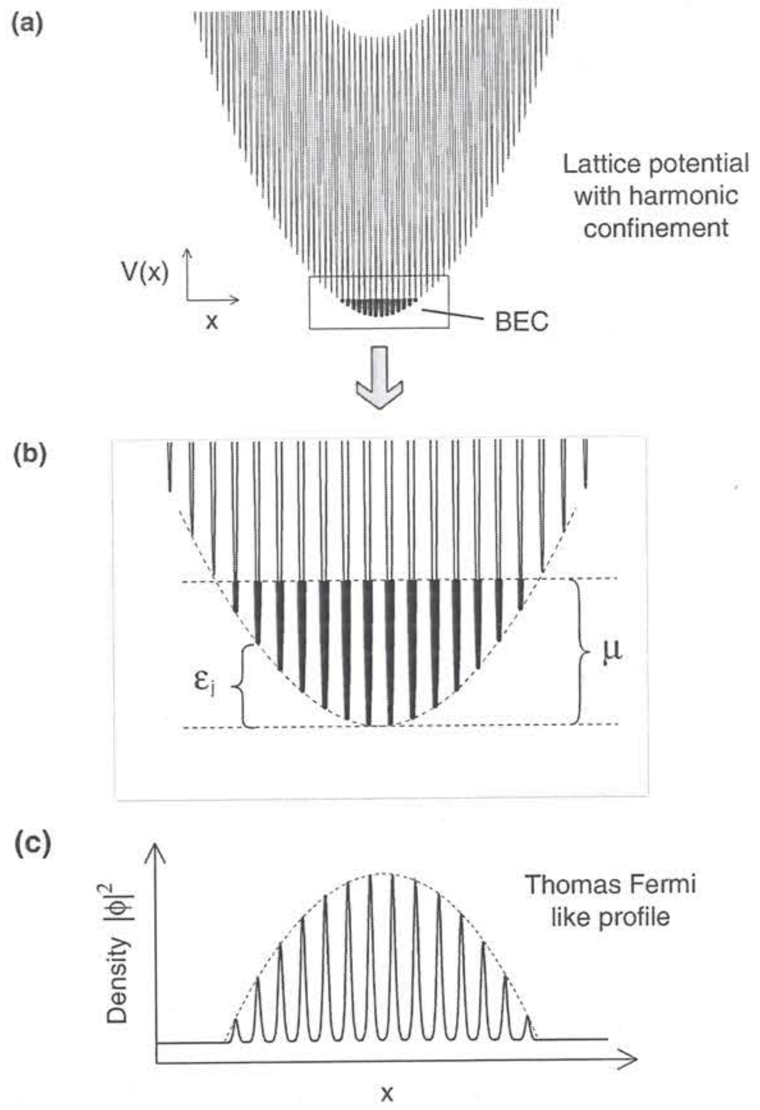

Figure 3.8: (a) The atoms are trapped in a periodic lattice potential with an additional external confinement due to the Gaussian laser beam profile and the magnetic trapping potential. (b) In the ground state the BEC is distributed over the lattice in a way that the chemical potential μ is constant over the lattice. The local chemical potential on a lattice site can be approximated as the sum of the energy offset ϵ_i and the interaction energy per atom, which is proportional to the density. Therefore the BEC is distributed over the lattice with a density profile of a Thomas Fermi parabola (c).

$$E_j \simeq \epsilon_j |\psi_j|^2 + \frac{U}{2} |\psi_j|^4 = \epsilon_j \overline{n}_j + \frac{U}{2} \overline{n}_j^2. \tag{3.44}$$

The local chemical potential can then be calculated as

$$\mu_j = \frac{\partial E_j}{\partial n_j} = \epsilon_j + U \cdot \overline{n}_j = \text{const.} \tag{3.45}$$

We ignore the discreteness of the lattice for the following calculation. This is justifiable if the lattice spacing is much larger than the extension of the atom cloud in the lattice. Furthermore we assume a spherical symmetric situation. Thus the density becomes continues $\overline{n}_i \rightarrow n(r)$ and the external confinement is given by $\epsilon_i \rightarrow \epsilon(r) = m/2\, \omega_{ext}^2 r^2$. Note that the density is normalized to the volume of one lattice site, thus $n(r)$ is the atom number per lattice site in the distance r from the trap center. The total atom number is then given by

$$N = \int n(\mathbf{x}) \frac{1}{a_{lat}^3} \mathrm{d}^3\mathbf{x} = \frac{4\pi}{a_{lat}^3} \int_0^\infty r^2 n(r)\, \mathrm{d}r \tag{3.46}$$

where a_{lat} is the lattice spacing. The condition for a constant chemical potential in equation 3.45 directly leads to a density distribution over the lattice, which is the usual Thomas Fermi parabola:

$$n(r) = \frac{1}{U} \left(\mu - \frac{1}{2} m\, \omega_{ext}^2\, r^2 \right) \tag{3.47}$$

The corresponding Thomas Fermi radius and the chemical potential depending on atom number and trap parameters are given by

$$r_{TF} = \sqrt{\frac{2\mu}{m\omega_{ext}^2}} \quad \text{and} \quad \mu = \left(\frac{15}{16} \frac{(\lambda/2)^3\, m^{3/2}\, N\, U\, \omega_{ext}^3}{\sqrt{2}\pi} \right)^{\frac{2}{5}}. \tag{3.48}$$

3.2 Creating multidimensional optical lattice potentials

The optical lattice potential is formed by superimposing several far red detuned standing waves at a wavelength around 850 nm. In this chapter the experimental setup for the lattice potential is described.

3.2.1 Laser beam setup

Our new Bose-Einstein condensate setup is designed in order to have free optical access to the Bose-Einstein condensate on three orthogonal axes. No magneto-optical trap is needed in the BEC chamber. Therefore, no optics for a MOT is blocking the optical access and we can shine in laser beams for the optical lattice from six orthogonal directions.

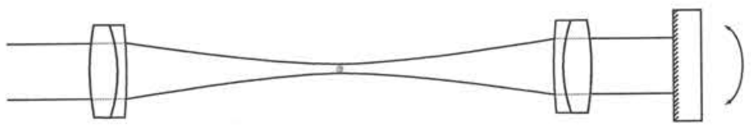

Figure 3.9: The standing wave laser field is formed by a retroreflected Gaussian laser focus.

Various types of periodic lattice potentials can be created by overlapping standing light waves with the atomic sample as discussed in chapter 3.1.2. The standing waves are formed by interfering counterpropagating beams with linear polarization. Figure 3.9 shows the setup we use. On the left side, a collimated Gaussian laser beam enters and is focused on the atomic sample with an achromatic lens. After the sample, the beam is recollimated again and is exactly retroreflected by an adjustable mirror. The retroreflected beam follows the inverse path and therefore forms a nearly perfect standing wave.

For a 2D and 3D lattice, we overlap two and three standing waves respectively. The beams are orthogonal to each other, thus forming a simple cubic lattice. For the 2D lattice we use light with the same frequency on each axis. By changing the polarization and the time phase of the two standing waves, we are able to control the interference term in equation 3.20. The time phase has to be stabilized interferometrically. It is measured by analyzing the polarization of the retroreflected beams after they are recombined on the beam splitter. The optical path length of one of the arms is adjusted by a piezo mounted mirror and a servo loop. By controlling the time phase, different lattice structures with a two atomic basis can be realized. However, the servo loop has a control accuracy of about 5%, and fluctuations of the time phase can lead to heating of the ultracold atoms. Therefore better results with little heating effects are achieved when the interference term is either minimized by using orthogonal polarizations and a timphase of 90° or it is maximized by choosing parallel polarizations and a time phase of 0°. In both cases fluctuations of the time phase have only little effect on the resulting trapping potential.

As a simple and effective alternative to the stabilization of the time phase we use standing waves with mutually orthogonal polarization and different frequencies on each axis. Due to the different frequencies any residual interference between beams travelling in orthogonal directions is time averaged to zero and therefore not seen by the atoms. The frequencies of the beams are shifted by acousto optical modulators with a relative frequency difference of about 30 MHz. This frequency is much larger than the trapping frequencies inside the lattice of about 30 kHz, therefore the time averaging is perfect in practice. This method is used for all experiments involving three-dimensional lattices.

The beam shape causes an additional confinement for a red detuned lattice (see Chapter 3.1.2), which adds to the confinement due to the magnetic trap. This confinement is harmonic in the trap center. In the experiments with 1D and 2D optical lattices [91] the beam waist w_0 ($1/e^2$ radius of the intensity) is approximately 75 μm. For the Mott insulator experiment [92] the beam waist is enlarged to 125 μm.

The alignment of the laser beams is a critical task. A precise overlap between the center of the Gaussian beams and the BEC is crucial for occupying the ground state in the lattice potential. A misalignment leads to potential gradients which can cause excitations of the BEC. The alignment is done in three steps: First, the position of the BEC is measured on a camera. Then the lattice beam is adjusted by imaging it onto the same camera. Finally the retroreflected beam is adjusted by assuring a perfect overlap of the returning beam after it leaves the first lens again. The alignment of the lattice beams can be checked by observing the displacement of the Bose-Einstein condensate after the lattice is adiabatically ramped up. By this method we estimate the precision of the alignment procedure to be about 10-20 μm.

All beams are spatially filtered and guided to the experiment using single mode, polarization maintaining fibers. Therefore the beam profile of the lattice beams is Gaussian to a good approximation. The laser intensity after each fiber is measured with a fast photodiode. Before each fiber an acousto-optical modulator controls the light intensity and shifts the laser frequency between 70 MHz and 120 MHz in order to create the different frequencies for each axis. The intensity is controlled by a fast servo loop with a response time of about 50 μs. This ensures that the lattice depth can be changed reproducibly or can be kept constant even if the laser intensity or the fiber transmittance fluctuates.

3.2.2 Laser system

For the experiments with 1D and 2D lattices we have used a diode laser operating at a wavelength of $\lambda = 852$ nm. To create a stable standing wave the coherence length should be much larger than the length difference in the optical path between the forward and backward travelling beam ($\simeq 0.5$ m). Thus we narrow the line width of the laser by seeding it with a grating stabilized diode laser. The injection locked laser has a line width of a few MHz, resulting in a coherence length of about 100 m. The diode laser (manufacturer: SDL) has an maximum output power of 150 mW. After all optical components the total power for the optical lattice is about 40 mW.

For the Mott insulator experiments with a three-dimensional optical lattice the beam waist has to be larger, thus more power is needed. One axis is operated by the injection seeded diode laser described above. For the other two axis we use an injection seeded tapered amplifier laser (TA laser chip manufactured by Toptica), seeded by the same laser. The tapered amplifier laser is operated at an output power of about 350 mW. After spatial filtering

and the transmission through all optical components about 2 × 50 mW is available for the lattice.

Recently we have changed to a Ti:Saphire laser (Coherent), which is pumped with a 10 W frequency doubled diode pumped solid state laser (Verdi V10, Coherent). At a wavelength of 835 nm the laser delivers about 700 mW output power in a single mode. With the current resonator mirrors, the laser can be tuned between 760 nm and 840 nm. After an optical fiber the power of the lattice laser beams in each of the three axis can reach 100 mW.

3.3 BEC in an optical lattice potential

3.3.1 Adiabatic loading of a BEC into a lattice potential

The Bose-Einstein condensate, which is initially trapped in a magnetic trapping potential, is adiabatically loaded into the optical lattice by slowly ramping up the optical lattice potential. If the lattice is ramped up slow enough, the wave function of the condensate remains in the many body ground state of the system. Two timescales of adiabaticity are relevant:

- **Adiabaticity with respect to the band population:** If the lattice potential is changed too fast, higher energy bands get populated. The time scale for adiabaticity is determined by the level spacing. The adiabaticity criterion for the transfer from the lowest into the nth energy band of a non interacting gas is given by [68]:

  $$|\langle n,q|d/dt|0,q\rangle| \ll |E_n^{(q)} - E_0^{(q)}|/\hbar, \tag{3.49}$$

  where $|n,q\rangle$ is the Bloch state with the quasi momentum q in the nth energy band. For $q \sim 0$, away from the border of the Brillouin zone, the right side of the equation remains finite ($|E_n^{(q)} - E_0^{(q)}| \sim 4\,E_r$) even for low potential depths $V_0 \leq 1\,E_r$. The condition eq. 3.49 then reads [68]:

  $$\frac{d}{dt}V_0/E_r \ll 32\sqrt{2}E_r/\hbar \sim 9 \cdot 10^5\,s^{-1} \tag{3.50}$$

  For larger potential depths the level spacing increases and adiabaticity is more easily fulfilled.

- **Adiabaticity with respect to the extension of the cloud over the lattice in the inhomogeneous system** [93]: For each lattice depth and for each strength of the external confinement, the many body ground state has a certain density profile (chapter 3.1.5). If parameters are changed, the atoms have to redistribute over the lattice in order to maintain a constant chemical potential. Thus this change has to be slow enough to be adiabatic.

  This time scale of adiabaticity is usually orders of magnitude slower than the time scale discussed above. For a three-dimensional red detuned lattice, however, the situation is very favorable: The chemical potential is given by (see also equation 3.45) $\mu = \epsilon_j + U \cdot \overline{n}_j$, where ϵ_j is the energy offset due to the external confinement on the j^{th} lattice site, U is the onsite interaction matrix element and $\overline{n}_j$ denotes the expectation value of the atom number on a site. For red detuning the energy offsetϵ_j, which causes the external confinement, increases linearly with the lattice depth since the atoms are captured in the intensity maxima. However, due to a reduced ground state extension on each site, U also changes approximately linearly for a 3D lattice. Therefore the increase of the external confinement is nearly perfectly compensated by the increase of the onsite interaction due to the tighter confinement on each lattice site. This means that the atoms hardly have to redistribute at all, and the chemical potential remains flat over the lattice when the lattice depth is changed. Note that the situation is different for a blue detuned lattice, where the atoms are captured in the intensity minima. There the change of the external confinement is small and has the wrong sign.

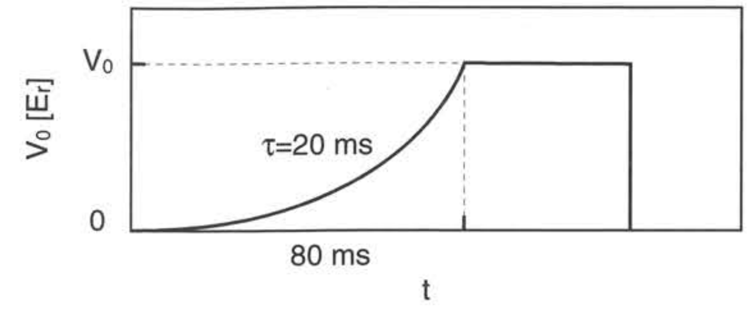

Figure 3.10: Slope for adiabatically transferring the BEC into the optical lattice potential. The potential depth is plotted versus time. The potential is exponentially ramped up to the final lattice depth in 80 ms with a time constant of 20 ms.

When we load the atoms into the lattice, we start with a nearly pure condensate in the magnetic trap. For the 1D and 2D experiments we start with a cigar shaped trap with radial trapping frequencies of 220 Hz and axial trapping frequencies of 24 Hz. For the Mott insulator experiments in a 3D lattice we start form an isotropic trapping potential by raising the bias field of the Ioffe trap. This is done after condensation by ramping up a homogenous offset field in about 500 ms. The resulting trapping frequencies are 24 Hz in each direction for the (F=2,m$_F$=2) state. When we load the atoms into the periodic lattice potential we leave the magnetic trapping potential on. The main reason for this is to compensate for the gravitational field, which would otherwise result in a strong potential gradient across the cloud. Therefore we change the external confinement which is the sum of the magnetic and optic confinement smoothly.

The periodic potential is usually ramped up with an exponential slope in about 80 ms (Figure 3.9). We were able to check that the process is adiabatic and that the many body ground state is occupied. The first criterion for adiabaticity can be checked by measuring the population of the energy bands (see chapter 3.3.6) showing that there is no occupation of higher energy bands. The second criterion is checked by probing the phases on the lattice sites after a certain hold time. Only if the chemical potential is flat, all phases remain constant and locked, and no excitations are visible.

3.3.2 Revealing the momentum distribution

How can we measure the macroscopic wave function of the BEC in the lattice? The lattice spacing is just $\lambda/2 = 425$ nm, therefore the optical resolution of the imaging system is not sufficient to resolve individual lattice sites. However, the momentum distribution can be measured by a time of flight measurement. For a coherent BEC in a lattice this momentum distribution carries in fact much more information than the spatial distribution of the atoms in the lattice.

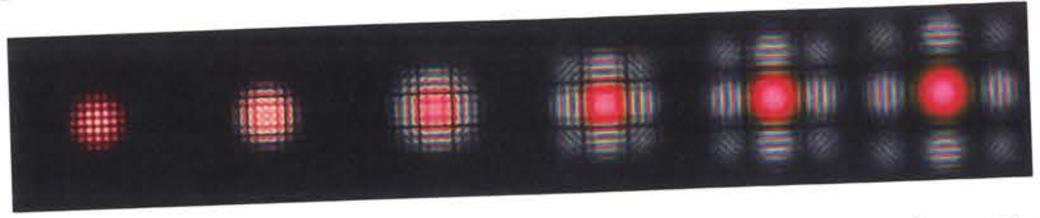

Figure 3.11: Simulation of the time of flight expansion for different evolution times. After switching off the lattice potential, a matter wave is emitted from each lattice site (left). As time evolves, the phase coherent matter waves overlap and form a multiple matter wave interference pattern. For long evolution times this pattern shows the momentum distribution with discrete momentum peaks arranged in a periodic pattern (right). This pattern corresponds to the reciprocal lattice and the Fourier transform of the wave function in the lattice. In the plot the phase of the matter wave is color coded, visualizing phase gradients as stripes.

The momentum distribution can be determined by a time of flight measurement. When all trapping potentials are switched off, the wave packets confined at each lattice site expand, start to overlap, and interfere with each other. Thus a coherent matter wave is emitted from each lattice site, resulting in a multiple matter wave interference pattern. Figure 3.11 shows a numerical simulation of the expansion and in figure 3.12 those patterns are shown for Bose-Einstein condensates released from 100.000 lattice sites of a 3D lattice. Narrow momentum peaks are visible, arranged in a periodic structure. These peaks are due to the periodicity of the lattice and require a constant macroscopic phase across the lattice sites. Figure 3.13 shows time of flight images of a three-dimensional optical lattice, taken from different directions.

Neglecting interaction effects during the expansion, the momentum distribution represents the Fourier transformation of the original macroscopic wave function in the lattice. The Fourier transform of the simple cubic lattice gives a simple cubic reciprocal lattice. Therefore the momentum peaks are also arranged in a simple cubic structure. When no phase fluctuations and interaction effects are present, the width of the momentum peaks is given by the Fourier transform of the envelope of the BEC in the lattice. On the other hand the envelope of the momentum distribution is the Fourier transform of the ground state extension of the wave function on each lattice site. Assuming Gaussian wave functions on each lattice site, the envelope is also Gaussian. The width of the envelope is then reciprocal to the width of the ground state extension.

Figure 3.14 shows the strength of the momentum peaks with $2\hbar k$ relative to the zero momentum peak, plotted for different potential depths. This number is given by the width of the envelope of the peaks and is therefore determined by the ground state extension of the wave function on a lattice site. The data are compared to an ab initio calculation. In this numerical calculation the ground state extension was assumed to be Gaussian and was

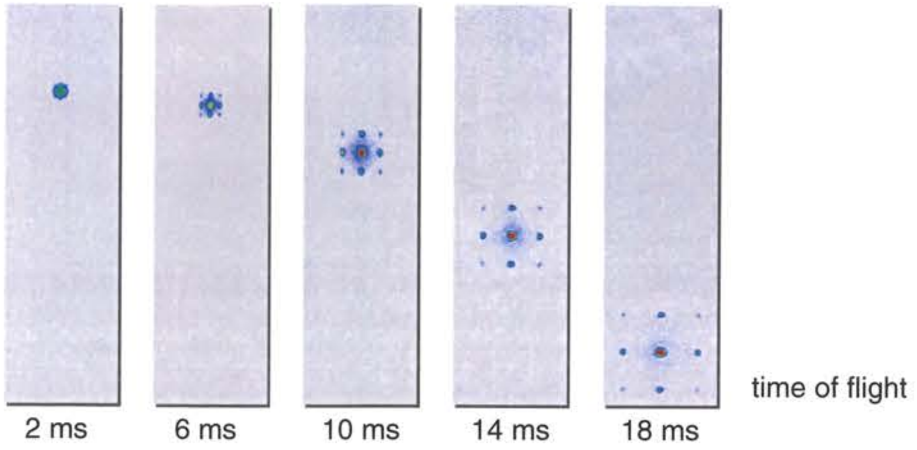

Figure 3.12: Time of flight absorption images of multiple matter wave interference pattern for different expansion times. Coherent BECs from 100 000 lattice sites expand, overlap and interfere with each other. Narrow momentum peaks are observed, demonstrating the long range phase coherence across the lattice

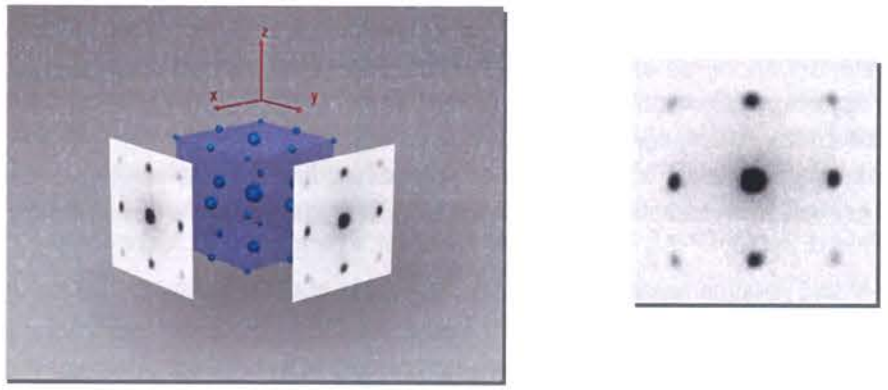

Figure 3.13: Schematical picture of the three-dimensional momentum distribution corresponding to a 3D lattice, together with measured time of flight images. These images show the projection in the direction of one lattice axis. Therefore different momentum peaks in this direction overlap and are not distinguishable. However, images taken from different sides show that the momentum distribution has a three-dimensional structure.

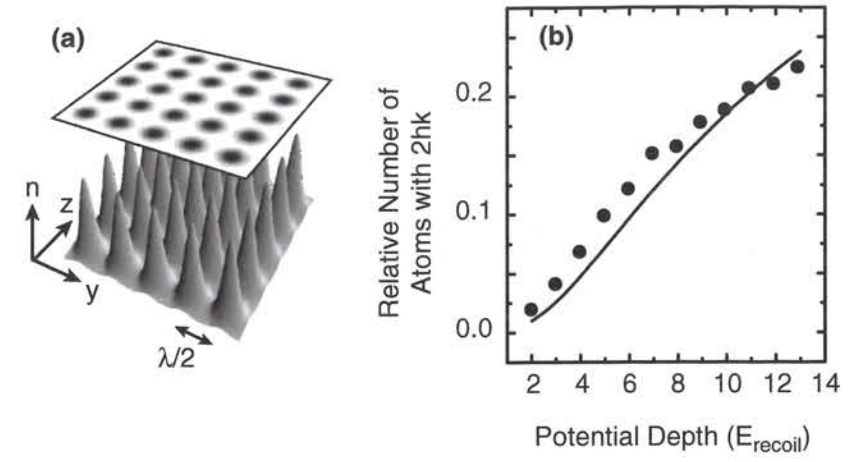

Figure 3.14: (a) Calculated density distribution of the atoms for a lattice potential depth of $12\,E_r$. (b) Fraction of atoms with momentum $p = \pm 2\,\hbar k$ relative to the number of atoms with $p = 0\,\hbar k$, extracted from time of flight images. The solid line is a theoretical calculation with no adjustable parameters.

determined using a variational ansatz, therefore also accounting for interaction effects (see also chapter 3.1.5).

In the experiment the width of the interference peaks is slightly broadened by the repulsive interaction during the expansion process. However, the width of the peaks can still be very small and can give a lower bound for the coherence length of the condensate in the lattice.

More generally, the momentum distribution can be expressed in terms of the one-particle density matrix $\rho_1(\vec{R}) = \langle \hat{a}^\dagger_{\vec{R}}\, \hat{a}_0 \rangle$, where $\hat{a}^\dagger_i$ creates in a particle in the ith lattice site (See also chapter 4) and $\vec{R}$ is the separation, an integer multiple of the primitive lattice vectors. It is then given by [94, 31]

$$n(\vec{k}) = n|w(\vec{k})|^2 \sum_{\vec{R}} e^{i\vec{k}\cdot\vec{R}} \rho_1(\vec{R}), \tag{3.51}$$

where $w(\vec{k})$ is the Fourier transform of the wannier function, describing the wave packet on each lattice site.

3.3.3 *s*-wave scattering

Besides the discrete momentum peaks, s-wave scattering spheres are visible in the time of flight images under certain circumstances (see figure 3.15) [95, 96]. They occur due to elastic scattering between atoms in different momentum components, which separate after the trapping potential is switched off. The atoms are scattered out of the condensate mode, since the relative velocity of the scattering particles is larger than a critical velocity, which is related to the Landau critical velocity and is of the order of the speed of sound.

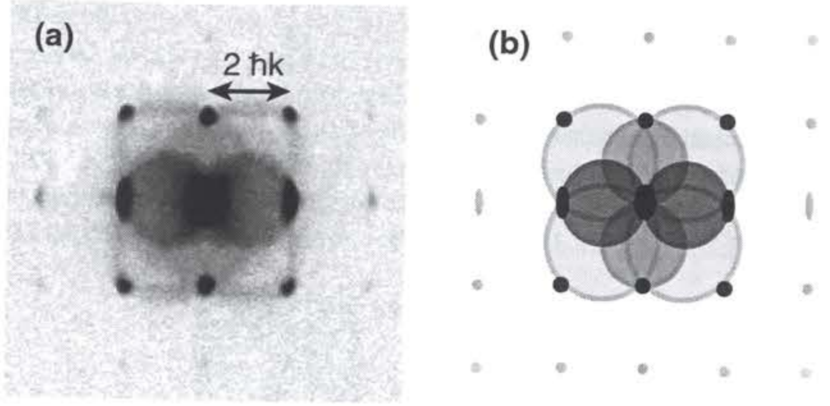

Figure 3.15: s-wave scattering spheres. (a) Average over 5 time of flight absorption images of released BECs that were stored in a 2D lattice. A tight cigar shaped external confinement leads to high densities and therefore enhances scattering processes. The lattice depth was $12\,E_r$ and the expansion time 12 ms. (b) Schematic image showing the expected discrete momentum states and s-wave scattering spheres.

In momentum space the target states for the scattering process are located on a spherical shell around the center of mass momentum due to energy and momentum conservation in the elastic scattering process. These target states are evenly distributed over the shell due to the spherical symmetry in the s-wave scattering process. Therefore the scattered atoms are visible as a circular halo in time of flight images, which represents the line-of-sight integrated spherical shell in momentum space.

In the experiment these shells become visible if the density of atoms in the lattice is large. This is especially the case for the situation where the optical lattice was superimposed on a cigar shaped magnetic trap [91]. For this situation strong scattering spheres can be observed in the horizontal direction since the large extension of the condensate in this direction leads to long interaction times and a large scattering probability. Scattering spheres in the vertical direction are weaker due to a shorter interaction time, but they are still visible. Even scattering spheres of the diagonal momentum peaks with a momentum of $\sqrt{2} \cdot 2\,\hbar k$ are nicely visible.

For 2D and 3D lattices with a weak magnetic confinement and moderate atom numbers, scattering spheres are hardly visible at all due to a much lower density. However, also in that regime residual scattering spheres can have an effect on quantitative measurements of the visibility of interference peaks. They appear as a non interfering background, apparently reducing the visibility of the interference pattern.

3.3.4 Geometrical structure factor

By choosing different polarizations and time phases for a two-dimensional lattice, the structure of the periodic trapping potential can be varied (see equation 3.20 and chapter 3.2). The lattice structure corresponds to a square lattice with a two-atomic basis (NaCl-structure in 2D) and a primitive lattice vector of the length $\sqrt{2} \cdot \lambda/2$, diagonal to the lattice beams. Changing the time phase leads to a change between the depth of adjacent lattice sites corresponding to the two-atomic basis. If the difference of the potential depth is much larger than the chemical potential, only the deeper lattice sites are populated with atoms. This is particularly the case if the polarizations are parallel and the time phase is set to 0°. For this situation the interference term in equation 3.20 is maximized and every second lattice site vanishes (see figure 3.16c). Figure 3.16d shows the corresponding time of flight image.

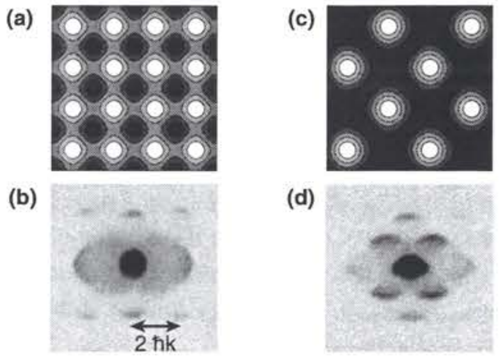

Figure 3.16: Time of flight images revealing the momentum distribution for different lattice configurations. For an optical lattice with orthogonal polarization vectors $\mathbf{e}_1 \cdot \mathbf{e}_2 = 0$ (a) the first diagonal momentum orders with $|p| = \sqrt{2}\hbar k$ are suppressed (b) due to their vanishing geometrical structure factor. In contrast, if $\mathbf{e}_1 \cdot \mathbf{e}_2 = 1$ and the time phase $\phi = 0$ as in (c), the resulting geometrical structure factor does not vanish for these momentum components and they are strongly visible (d)

When the polarization between the standing waves is orthogonal, the interference term in equation 3.20 vanishes and every lattice site has the same potential depth (figure 3.16a). For this situation we find a complete suppression of the first order diagonal momentum component with $|p| = \sqrt{2}\hbar k$ (figure 3.16b). This is caused by a destructive interference between matter waves emitted from neighboring diagonal lattice planes and results in a vanishing geometrical structure factor for the diagonal momentum components.

In the latter case, where the interference term vanishes, the depth of the potential wells corresponding to the two-atomic basis are identical. Therefore the resulting lattice is identical to a square lattice with a one atomic basis and a primitive lattice vector of the length $\lambda/2$ parallel to the lattice beams. All the following experiments are carried out in this regime. The polarizations between the standing waves are chosen mutually orthogonal, and residual interferences are time averaged by using different laser frequencies on each axis. Note that only for this lattice configuration the lattice potential is separable in all dimensions.

3.3.5 Observing Bloch oscillations

When a Bose-Einstein condensate is adiabatically loaded into an optical lattice, the Bloch state with a crystal momentum $q = 0$ is macroscopically occupied. Therefore the macroscopic phase is identical on each lattice site. The atoms are distributed over the lattice in a way that the chemical potential is constant across the lattice. Therefore the phases in all lattice sites obey the same time evolution and remain constant.

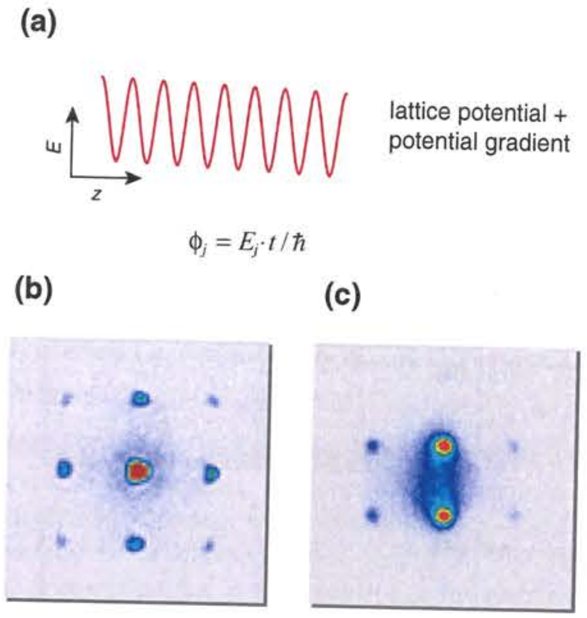

Figure 3.17: Applying a potential gradient and thereby tilting the lattice (a) leads to Bloch oscillations in the lowest band. Experimentally measured momentum distributions for a 3D lattice with $\Delta\phi = 0$ (b) and $\Delta\phi = \pi$ (c), corresponding to a quasi momentum of $q = 0$ and $q = \hbar k$ respectively.

By exposing the atoms to a potential gradient it is possible to imprint arbitrary phase gradients onto the condensate in the lattice. The phase on each lattice site evolves as $\phi_i = E_i \cdot t/\hbar$ according to the local potential energy. When a linear potential gradient is applied (Figure 3.17a), the phase difference between neighboring lattice sites $\Delta\phi = \phi(x_{i+1}) - \phi(x_i)$ evolves as

$$\Delta\phi = -\frac{V' \frac{\lambda}{2} t}{\hbar}. \tag{3.52}$$

Here, V' is the strength of the potential gradient $V(x) = V' \cdot x$.

In a band structure picture this phase evolution corresponds to Bloch oscillations in the lowest Bloch band. Thereby a Bloch state with an arbitrary quasi momentum $q = V't$ can be populated by applying the potential gradient for an appropriate time t.

In the experiment the potential gradient is created by shifting the harmonic magnetic trap. A displacement of the harmonic trap by the distance x_{shift} results in a potential which is the sum of the original trapping potential $V(x)$, a linear gradient $V' \cdot x$ and an offset c:

$$V_{\text{shift}}(x) = \frac{m}{2}\omega_{mag}^2(x - x_{\text{shift}})^2 = \frac{m}{2}\omega_{mag}^2\, x^2 - m\,\omega_{mag}^2\, x_{\text{shift}} \cdot x + c = V_0(x) + V' \cdot x + c. \tag{3.53}$$

The harmonic magnetic trap can be displaced by applying magnetic offset fields. These fields are created by driving current pulses through small coils which are mounted close to the glass cell. The coils have about 10 windings of a 1.5 mm wire and a diameter of about 16 mm. Two coils are mounted in different directions. The inductance is very low, enabling the creation of short pulses without ringing. The pulse current is stabilized by a servo loop. By applying appropriate pulse currents of up to 400 A the magnetic trap can be shifted by different amounts. This results in variable potential gradients. The dependence of the potential gradients on the applied currents was calculated numerically and cross checked via the Bloch oscillation period.

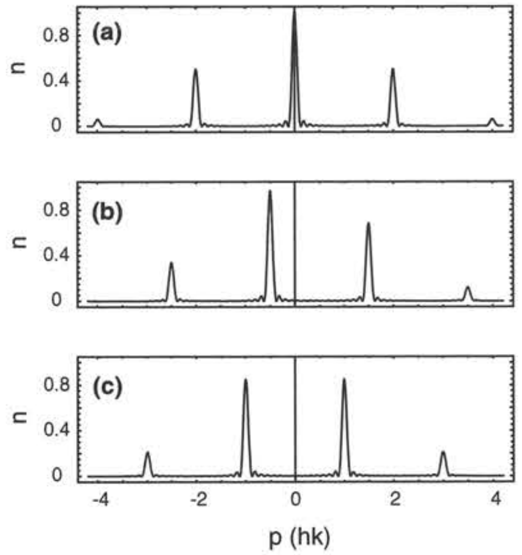

Figure 3.18: Theoretical momentum distribution for a BEC in a one-dimensional periodic potential. The graphs show different momentum states with with phase differences of (a) $\phi = 0$, (b) $\phi = \pi/2$ and (c) $\phi = \pi$ between neighboring lattice sites.

Figure 3.18 shows a calculation of the momentum distribution for different Bloch states in a 1D lattice. In figure 3.17 b and c, time of flight images are shown revealing the momentum distribution of Bloch states in a 3D lattice with a crystal momentum of $q = 0$ ($\Delta\phi = 0$) and $q = \hbar k$ ($\Delta\phi = \pi$) respectively.

Only for short times the time evolution of the BEC in the tilted lattice follows simple Bloch oscillations. If the potential gradient is applied for a longer period, a dephasing of the lattice sites and other excitations can be observed. The dephasing arises due to the nonlinearity of the BEC. Different sources for the loss of long range phase coherence have been reported:

- **Dynamical instability:** A condensate with repulsive interactions in a lattice is not stable for each Bloch state. For Bloch states close to the border of the Brillouin zone arbitrarily small excitations get amplified and the condensate will break apart due to dynamical instability effects [97, 98, 99, 78]. This can be qualitatively understood through the effective mass m_{eff} of the particles. The effective mass depends on the curvature of the energy band as $1/m_{eff} = d^2E(q)/dq^2$. It becomes negative for quasi momenta q close to the border of the Brillouin zone, between $q \approx \hbar k$ and $q = 2\hbar k$. Therefore the sign of the interaction parameter changes, resulting in effectively attractive interactions between the atoms. Such a condensate with attractive interactions is not stable.

- **Landau instability:** A dissipative behavior which is not governed by the Gross-Pitaevskii equation can occur if the fluid velocities are larger than the local speed of sound [78, 97]. When Landau instability occurs, the system can lower its energy by emitting phonons.

- **Solitons, vortices:** The above damping mechanisms assume a pure one-dimensional system. However, in experiments with one and two-dimensional lattices there are usually more degrees of freedom in the direction perpendicular to the lattice axis. Therefore, especially for an inhomogeneous system, the one-dimensional description is not sufficient since excitations in these degrees of freedom occur. These excitations can lead to a chaotic behavior and even lead to the formation of solitons and vortices [100].

3.3.6 Measurement of the band population

The population of the Brillouin zones can be directly measured by adiabatically ramping down the lattice potential and measuring the free space momentum distribution [101, 91]. Since the $n$nt Brillouin zone corresponds to the nth Energy band, the population of the states in each energy band and for each crystal momentum q can be probed independently.

Mapping crystal momentum to free particle momentum

In the normal time of flight expansion images the lattice potential is rapidly switched off and the image corresponds to the Fourier transform of the wave function, showing the momentum distribution of the atoms confined in the lattice. The lattice potential can instead also be ramped down adiabatically. If the ramp down time is slow compared to vibrational frequencies in the lattice, but fast enough such that the population of the energy bands is not changed

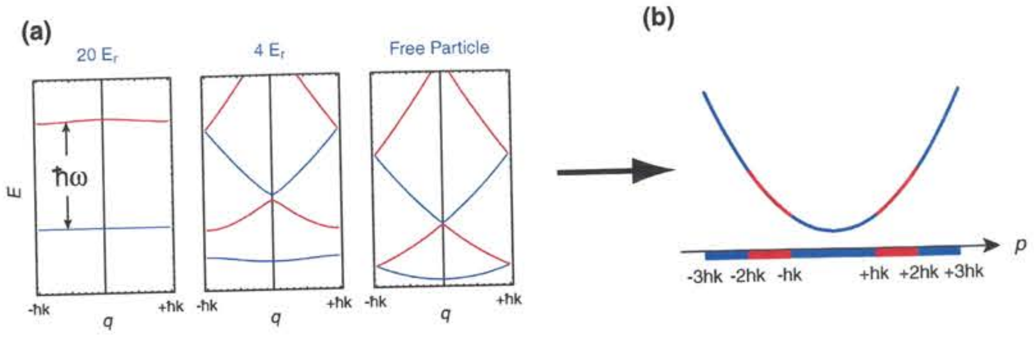

Figure 3.19: (a) Bloch bands for different potential depths. By adiabatically decreasing the lattice depth the band population is conserved and the crystal momentum q is mapped to the free particle momentum p (b). The nth band is therefore mapped to the nth momentum interval of the free particle momentum.

during the ramp, the crystal momentum is conserved and a state with crystal momentum q is finally mapped to a state with free particle momentum $p = q$ as the lattice is turned off. Figure 3.19 shows the situation for a 1D lattice. The nth energy band is mapped onto the nth momentum interval of the free particle which corresponds to the nth Brillouin zone of the lattice.

For higher dimensions the Brillouin zones are more complicated. Figure 3.20a shows the reciprocal lattice and Brillouin zones for a two-dimensional square lattice. However, the principle is the same and the nth energy band is mapped onto the nth Brillouin zone.

Imaging the Brillouin zones

In Figure 3.20b an experimental measurement of the band population of a dephased 2D lattice is shown. First, the magnetic confinement is switched off and the atoms are exposed to the linear gravitational potential. As described in chapter 3.3.5 the gradient leads to Bloch oscillations, and various instability effects lead to a dephasing of the condensate in the lattice and therefore to a loss of long range phase coherence. By this we prepare a homogenously populated first Brillouin zone. After 2 ms, the BEC is dephased and the lattice is ramped down in 2 ms starting from a potential depth of 12 E_r. We image the cloud after a ballistic expansion of 12 ms. The time of flight image in figure 3.20b exhibits a square like momentum distribution with a width of $2\hbar k$, coinciding with the first Brillouin zone. The distribution of the population of momenta in the first Brillouin zone is flat, and no population in higher Brillouin zones can be detected. This proves that the atoms occupy the lowest energy band homogenously and that no higher bands are populated.

For a three-dimensional simple cubic lattice, the shape of the first Brillouin zone is a cube. Therefore a dephased condensate in a cubic lattice creates a cubic cloud of gas after ballistic expansion. This can be seen in figure 3.20c, where a schematic image of the cubic cloud is shown together with real experimental time of flight images taken from two orthogonal

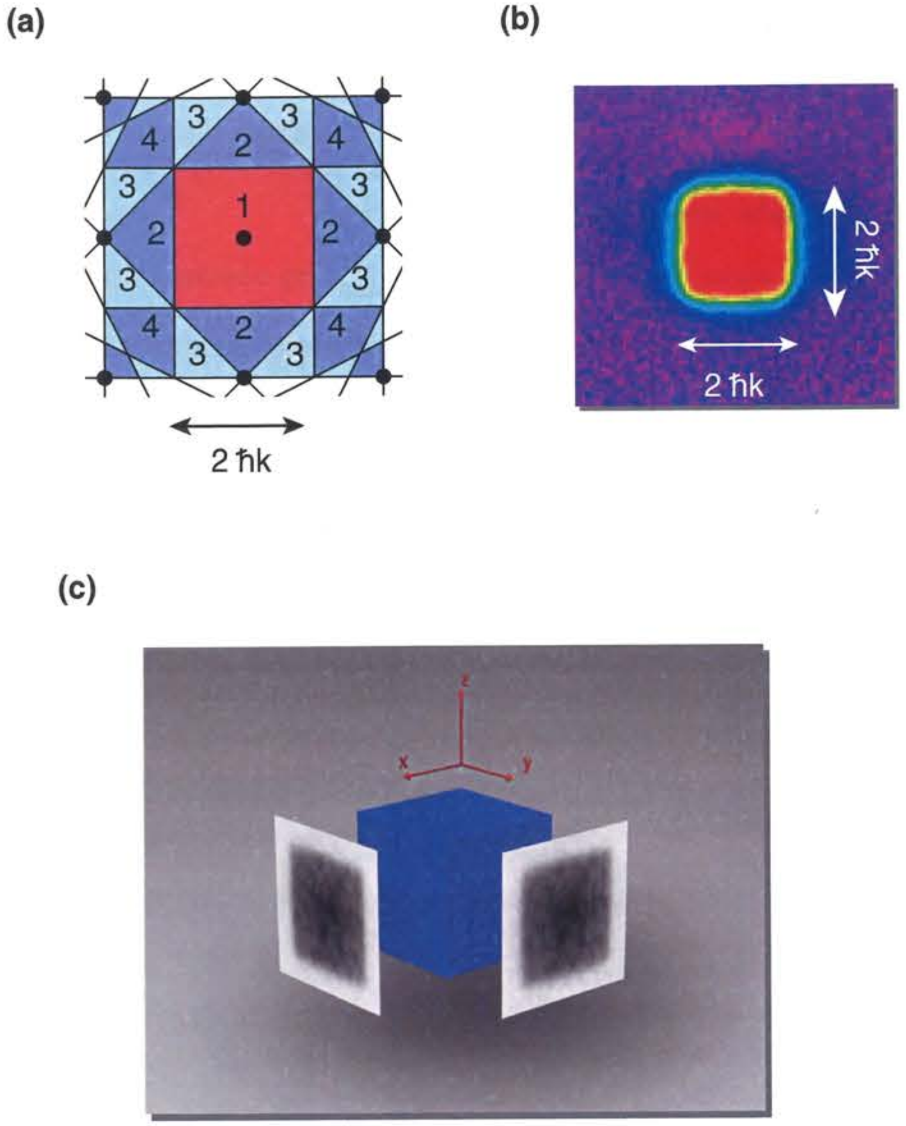

Figure 3.20: (a) Reciprocal lattice and Brillouin zones for a two-dimensional lattice. (b) Image of the experimentally measured band population of a dephased BEC in a 12 E_r deep lattice. The first Brillouin zone and therefore the lowest energy band is homogenously populated with no visible population in higher energy bands. (c) The shape of the first Brillouin zone of a 3D lattice is a cube, which is drawn schematically. The inset shows the measured cube-like momentum distribution for a dephased BEC in a 3D lattice.

directions.

The measurement of the band population demonstrates that it is possible to homogenously populate the lowest energy band while having no population in higher bands. In a tight binding picture this corresponds to a situation where in each lattice site only the vibrational ground state is occupied by the condensate, but the phase correlation between the sites is lost.

Populating higher energy bands

We can populate higher energy bands in the lattice by using stimulated Raman transitions, where states in different energy bands are connected by a stimulated two-photon process [80, 81]. In order to drive the transition we apply two Raman beams to the atoms in the lattice (Figure 3.21b). The frequency difference $\delta\omega_r = \delta E/\hbar$ between the beams corresponds to the energy difference δE between the Bloch states. The Raman beams are detuned by Δ_r with respect to an atomic transition. By changing the angle between the two beams the momentum transfer δq of the Raman beams can be arbitrarily chosen between $0\hbar k_r$ and $2\hbar k_r$, where k_r denotes the norm of the k-vector of the Raman beams. Therefore Bloch states in all bands and with arbitrary quasi momenta can be populated.

In a tight binding picture the Raman beams induce transitions between vibrational levels of each potential well (see 3.21a) and the change of the quasimomentum δq corresponds to the simultaneous change of the relative macroscopic phase between lattice sites.

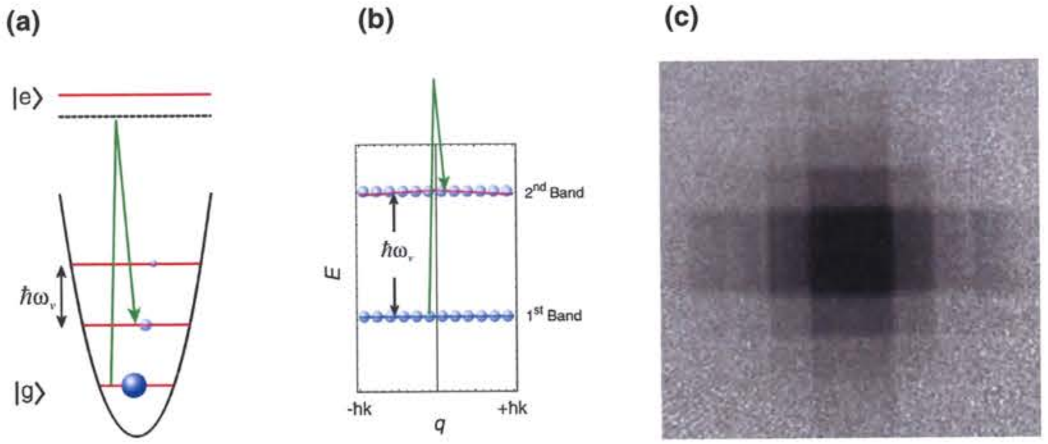

Figure 3.21: Population of higher energy bands. (a) Higher vibrational levels on each lattice site can be populated by stimulated Raman transitions. (b) In a Bloch picture this corresponds to Raman transitions between different energy bands. (c) Measured band population of a dephased BEC in a 2D lattice, where higher energy bands have been populated by stimulated Raman transitions. Therefore population of the corresponding higher Brillouin zones is visible.

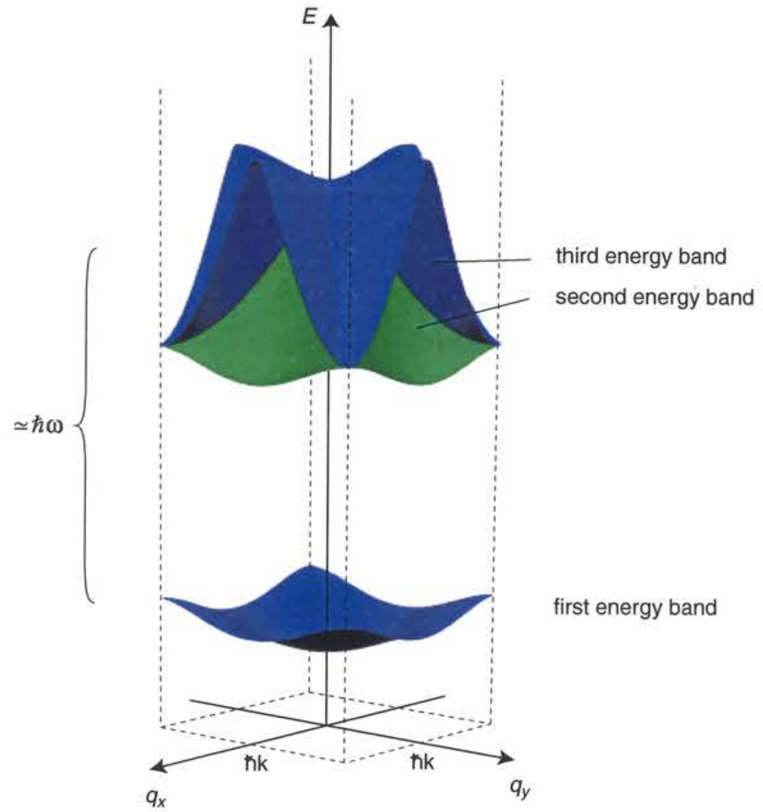

Figure 3.22: Band structure of a two-dimensional lattice with a lattice depth of $5\,E_r$. The distance between the first and second band corresponds to the level spacing $\hbar\omega$ of the potential wells. The second and third band overlap with each other.

In the experiment we first prepare a dephased BEC in the lattice, where the lowest energy band is populated homogenously. Then we shine in two Raman beams from two orthogonal directions, parallel to the primitive lattice vectors. The momentum transfer of this setup is $\sqrt{2}\hbar k_r$ in the diagonal direction. However, since we start with a homogenously populated lowest band, this band is entirely mapped onto a higher band which also gets populated homogenously . By choosing a proper detuning we can address the final energy band.

Figure 3.21c shows a ballistic expansion image of a dephased BEC in a 12 E_r deep 2D lattice, where higher energy bands are populated by stimulated Raman transitions and the quasi momentum was mapped to the free particle momentum by adiabatically decreasing the potential depth. Different Brillouin zones are visible. A comparison with the Brillouin scheme in Figure 3.20a shows that the second and third energy band can not be distinguished in the measurement. This is because both zones correspond to overlapping and nearly degenerate energy bands (figure 3.22), which reflect the two-fold degeneracy of the two-dimensional harmonic oscillator levels on each potential well. Therefore both bands are equally populated by the Raman transition and the triangular shape of the corresponding Brillouin zones is not visible.

---

4 Quantum phase transition from a superfluid to a Mott insulator

4.1 Bose-Hubbard Model of interacting bosons in a lattice

4.1.1 Bose-Hubbard Hamiltonian

In our experimental parameter regime the bosonic atoms with repulsive interactions in a periodic lattice potential are perfectly described by a Bose-Hubbard model [4], as realized by Jaksch *et al.* [5] . This model is a well known model in solid state physics. It is the simplest nontrivial model describing a bosonic many body system on a lattice which can not be mapped onto a single particle problem. Nevertheless it contains intriguing effects like a quantum phase transition from a superfluid state to a Mott insulating state.

Our starting point of the discussion is the Hamiltonian for interacting bosonic particles in an trapping potential $V(\mathbf{x})$ (see also chapter 2.1.3)

$$\begin{aligned} \hat{H} &= \int d^3x\, \hat{\psi}^\dagger(\mathbf{x}) \left(-\frac{\hbar^2}{2m}\nabla^2 + V(\mathbf{x}) \right) \hat{\psi}(\mathbf{x}) + \\ & \frac{1}{2}\frac{4\pi a_s \hbar^2}{m} \int d^3x\, \hat{\psi}^\dagger(\mathbf{x})\hat{\psi}^\dagger(\mathbf{x})\hat{\psi}(\mathbf{x})\hat{\psi}(\mathbf{x}), \end{aligned} \tag{4.1}$$

where $\hat{\psi}(\mathbf{x})$ is a boson field operator. In our system the trapping potential $V(\mathbf{x})$ is the sum of the periodic lattice potential, $V_{lat}(\mathbf{x})$ and an external confinement $V_{ext}(\mathbf{x})$ (see equation 3.22). In the interaction term a_s denotes the scattering length and m is the mass of an atom.

For a periodic potential and local atom-atom interactions it is favorable to work in the Wannier basis of wave functions localized to lattice sites (chapter 3.1.4 and equation 3.37). If the energies involved in the dynamic of the system are small compared to excitation energies to the second band, only Wannier functions of the lowest band have to be considered. Therefore we can expand the field operators $\hat{\psi}(\mathbf{x})$ in the basis of Wannier functions $w(\mathbf{x}-\mathbf{x}_i)$ of the lowest band

$$\hat{\psi}(\mathbf{x}) = \sum_i \hat{a}_i w(\mathbf{x}-\mathbf{x}_i). \tag{4.2}$$

Here $\hat{a}_i$ denotes the operator for annihilating a particle in the mode of the Wannier function $w(\mathbf{x}-\mathbf{x}_i)$, localized to the ith lattice site. Therefore $\hat{a}_i$ and the corresponding creation operator $\hat{a}_i^\dagger$ describe the annihilation and creation of a boson on the ith lattice site respectively. These operators obey the canonical commutation relations $[\hat{a}_i, \hat{a}_j^\dagger] = \delta_{ij}$.

Using this expansion and considering only tunnelling between neighboring lattice sites and on-site interaction Hamiltonian 4.1 reduces to the Bose-Hubbard Hamiltonian

$$\hat{H} = -J \sum_{<i,j>} \hat{a}_i^\dagger \hat{a}_j + \sum_i (\epsilon_i - \mu)\, \hat{n}_i + \sum_i \frac{1}{2} U\, \hat{n}_i(\hat{n}_i - 1). \tag{4.3}$$

Here $\hat{n}_i = \hat{a}_i^\dagger \hat{a}_i$ counts the number of bosons on the ith lattice site and the first summation is carried out over neighboring lattice sites. The Hamiltonian consist of three terms:

- The first term in the Bose-Hubbard Hamiltonian is the hopping term and describes the tunnelling of bosons between neighboring potential wells. The strength of the tunnel coupling is characterized by the tunnel matrix element $J = -\int d^3x w(\mathbf{x} - \mathbf{x}_i)(-\hbar^2\nabla^2/2m + V_{lat}(\mathbf{x}))w(\mathbf{x} - \mathbf{x}_j)$ (see also eq. 3.38). This term of the Hamiltonian tends to delocalize each atom over the lattice.
- The second term describes an external confinement which gives rise to an energy offset $\epsilon_i = V_{ext}(\mathbf{x}_i)$ on the ith lattice. For a homogenous system ϵ_i is zero. This term also introduces the chemical potential μ. It acts as a Lagrangian multiplier to fix the mean number of particles when a grand canonical ensemble is considered.
- The interaction of n atoms, each interacting with $n - 1$ other atoms on the same lattice site, is described by the third term of the Bose-Hubbard Hamiltonian. Here U quantifies the repulsion between two atoms on a single lattice site and is given by $U = (4\pi\hbar^2 a_s/m) \int |w(\mathbf{x})|^4 d^3x$. Due to the short range of the interactions compared to the lattice spacing, the interaction energy is well described by this term, which characterizes a purely on-site interaction. The interaction term tends to localize atoms to lattice sites.

For a given optical lattice potential U and J are readily evaluated numerically (see preceding chapter). When the potential depth of the optical lattice is increased, the tunnelling barrier between neighboring lattice sites is raised and therefore the tunnelling matrix element J decreases exponentially. The on-site interaction U on the oher hand is slightly increased in a deeper lattice due to a tighter confinement of the wave function on a lattice site. Therefore the ratio U/J can be continuously adjusted over a wide range by changing the strength of the lattice potential.

Note that the Hamiltonian of eq. 3.42, derived from a Gross Pitaevskii equation, is the limiting form of the more general Bose-Hubbard Hamiltonian eq. 4.3, when one can describe the many-body state through a macroscopic wave function.

4.1.2 Superfluid and Mott insulating ground state

The Bose-Hubbard Hamiltonian of equation 4.3 has two distinct ground states depending on the strength of the interactions U relative to the tunnel-coupling J. In order to gain insight into the two limiting ground-states, let us first consider the case of a double well system with only two interacting neutral atoms.

Double well case

In the double well system the two lowest lying states for non-interacting particles are the symmetric $|\varphi_S\rangle = 1/\sqrt{2}(|\varphi_L\rangle + |\varphi_R\rangle)$ and the anti-symmetric $|\varphi_A\rangle = 1/\sqrt{2}(|\varphi_L\rangle - |\varphi_R\rangle)$ states, where $|\varphi_L\rangle$ and $|\varphi_R\rangle$ are the ground states of the left and right hand side of the double well potential. The energy difference between $|\varphi_S\rangle$ and $|\varphi_A\rangle$ will be denoted by $2 \cdot J$, which characterizes the tunnel coupling between the two wells and depends strongly on the barrier height between the two potentials.

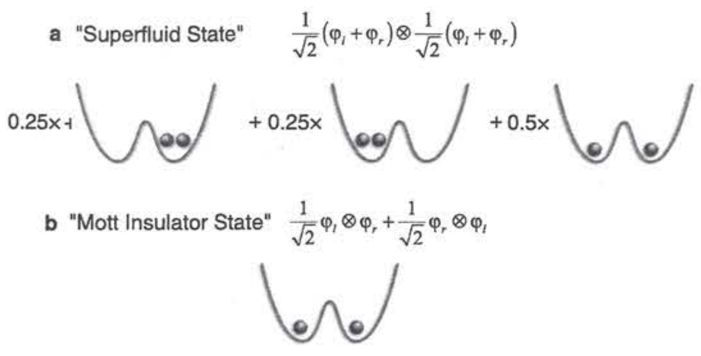

Figure 4.1: Ground state of two interacting particles in a double well. For interaction energies U smaller than the tunnel coupling J the ground state of the two-body system is realized by the "superfluid" state **a**. If on the other hand U is much larger than J, then the ground state of the two-body system is the Mott insulating state **b**.

In case of no interactions, the ground state of the two-body system is realized when each atom is in the symmetric ground state of the double well system (see Fig. 4.1a). For this situation the system is in a superposition of the state with both atoms in the left well, the state with both atoms in the right well and the state with one atom in the left and one in the right well. Such a situation yields an average occupation of one atom per site, however, the single site many body state is then actually in a superposition of zero, one and two atoms. Let us now consider the effects due to a repulsive interaction between the atoms. If both atoms are again in the symmetric ground state of the double well, the total energy of such a state will increase due to the repulsive interactions between the atoms. This higher energy cost is a direct consequence of having contributions where both atoms occupy the same site of the double well. This leads to an interaction energy of $1/2U$ for this state.

If this energy cost is much greater than the splitting $2 \cdot J$ between the symmetric and antisymmetric ground states of the noninteracting system, the system can minimize its energy when each atom is in a superposition of the symmetric and antisymmetric ground state of the double well $1/\sqrt{2}(|\varphi_S\rangle \pm |\varphi_A\rangle)$. The resulting many body state can then be written as $|\Psi\rangle = 1/\sqrt{2}(|\varphi_L\rangle \otimes |\varphi_R\rangle + |\varphi_R\rangle \otimes |\varphi_L\rangle)$. Here exactly one atom occupies the left and right site of the double well. Now the interaction energy vanishes because both atoms never occupy the same lattice site. The system will choose this new "Mott insulating" ground state when the energy costs of populating the antisymmetric state of the double well system are outweighed by the energy reduction in the interaction energy. It is important to note that precisely the atom number fluctuations due to the delocalized single particle wave functions make the "superfluid" state unfavorable for large U.

Such a change can be induced by adiabatically increasing the barrier height in the double well system, such that J decreases exponentially and the energy cost for populating the antisymmetric state becomes smaller and smaller. Eventually it will then be favorable for the system to change from the "superfluid" ground state, where both atoms are delocalized over the two wells, to the "Mott insulating" state, where each atom is localized to a single potential well.

Superfluid ground state

The above ideas can be readily extended to the multiple well case of the periodic potential of an optical lattice. If the tunnelling matrix element J is much larger than the onsite interaction U, the tunnelling term in the Bose Hubbard Hamiltonian is dominant. In the ground state each atom is then delocalized over the entire lattice and the many-body ground state can be described as a product state of identical Bloch waves. For N bosons on a lattice with M lattice sites it reads:

$$|\Psi_{SF}\rangle_{U/J\approx 0} \propto \left(\sum_{i=1}^{M} \hat{a}_i^\dagger\right)^N |0\rangle. \tag{4.4}$$

The system can be described by a macroscopic wave function since the many-body state is a product over identical single particle states. Therefore a macroscopic phase is well defined on each lattice site and the system is superfluid. When the system is in the ground state this macroscopic phase is constant across the lattice, giving rise to the narrow peaks in the multiple matter wave interference pattern discussed in the previous chapter. On the other hand the atom number per site is uncertain, and therefore one would find a random atom number in a measurement.

The matter wave field on the ith lattice site is characterized by the non-vanishing expectation value of the field operator $\psi_i = \langle\phi_i|\hat{a}_i|\phi_i\rangle$. Neglecting the onsite interaction U, the single site many-body wave function $|\phi_i\rangle$ is equivalent to a coherent state in second quantization, which is an eigenstate of $\hat{a}_i$. Therefore the many-body state on a lattice site is a superposition of different atom number states, following a Poissonian atom number distribution (figure 4.2) with a variance given by the average number of atoms on this lattice site $\mathrm{Var}(n_i) = \langle\hat{n}_i\rangle$. For a finite U the interaction will lead to number squeezing, resulting in a sub Poissonian number statistics (Chapter 5.3.1).

When one can describe the many-body state through a macroscopic wave function, the expectation value of the kinetic energy term $\langle -J \cdot \hat{a}_i^\dagger \hat{a}_j\rangle$ in the Bose Hubbard Hamiltonian becomes $-J\,\psi_i^*\psi_j$. The real part of this term is equal to $-J\,\cos(\varphi_j - \varphi_i)\cdot\sqrt{\bar{n}_i\bar{n}_j}$ (where $\varphi_j - \varphi_i$ is the phase difference of the macroscopic phase between neighboring lattice sites and $\bar{n}_i$ is the mean atom number on the ith lattice site) and can therefore be associated with the Josephson tunnelling energy. Thus a state with a well defined phase is able to lower the total energy by J per Josephson junction and atom. The expectation value of the interaction energy $U\cdot\hat{n}_i(\hat{n}_i-1)/2$ on the other hand becomes $U\cdot\bar{n}_i^2/2$. Therefore the Hamiltonian of eq. 3.42, originally derived from a Gross Pitaevskii equation, is the limiting form of the more general Bose-Hubbard Hamiltonian eq. 4.3 for a macroscopic wave function.

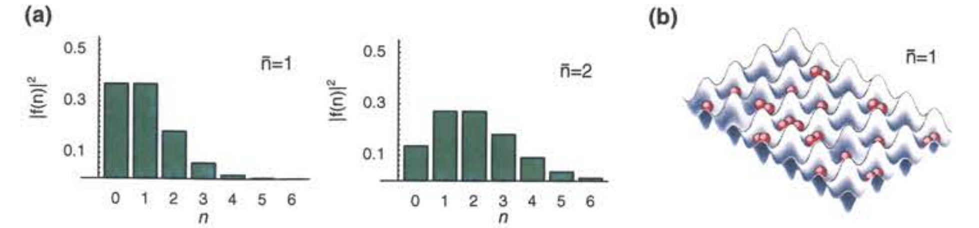

Figure 4.2: (a) Poissonian atom number statistics on a lattice site for $\bar{n}=1$ and $\bar{n}=2$ in the superfluid ground state at $U/J=0$,. The state on a lattice site is a coherent state with a superposition of different atom numbers and a well defined macroscopic phase. (b) In a measurement a random atom number would be found in each potential well.

Mott insulator ground state

If, on the other hand, interactions dominate the behavior of the Hamiltonian, such that $U/J \gg 1$, then fluctuations in the atom number on a single lattice site become energetically costly and the ground state of the system instead consists of localized atomic wave functions that minimize the interaction energy. The many-body ground state is then a product of local Fock states in the atom number for each lattice site. In this so called "atomic limit" the ground state of the many-body system for a homogenous system and a commensurate filling of n atoms per lattice site is given by:

$$|\Psi_{MI}(n)\rangle_{J\approx 0} \propto \prod_{i=1}^{M} (\hat{a}_i^\dagger)^n |0\rangle. \tag{4.5}$$

Now each atom is localized to a lattice site and the atom number on a lattice site is exactly determined (figure 4.3). On the other hand, the phase of the coherent matter wave field on a lattice site has obtained a maximum uncertainty. This is characterized by a vanishing of the matter wave field on the ith lattice site $\psi_i = \langle\phi_i|\hat{a}_i|\phi_i\rangle = 0$.

It is interesting to compare the expectation value of the interaction energy per lattice site for coherent and Fock states. For a coherent state in the superfluid regime it yields $U\cdot\bar{n}_i^2/2$, whereas for a Fock state in the Mott insulator regime with n_i atoms per lattice site the interaction energy becomes $U\cdot n_i(n_i-1)/2$. Therefore in this regime the system can lower

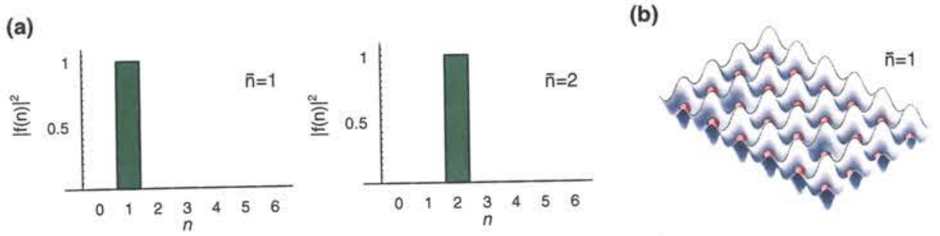

Figure 4.3: (a) Atom number statistics for the Mott insulator state for $\bar{n}=1$ and $\bar{n}=2$, with Fock states in the atom number on each site. This is the many body ground state in the limit $U \gg J$ and for a commensurate filling of the lattice. The macroscopic phase of the matter wave field has vanished, however, it is replaced by atom number correlations. (b) An atom number measurement now yields a well defined atom number on each site.

its total energy by $U/2$ per atom if Fock states in the atom number are formed instead of coherent states.

In the Mott insulator state the interactions between the atoms dominate the behavior of the system. No macroscopic phase coherence is prevalent in the system, but perfect correlations in the atom number exist between lattice sites. The many body state is not amenable anymore to a description as a macroscopic matter wave, nor can the system be treated by the theories for a weakly interacting Bose gas of Gross, Pitaevskii and Bogoliubov.

4.1.3 Quantum phase transition

When the strength of the interaction term relative to the tunnelling term in the Bose-Hubbard Hamiltonian is changed, the system reaches a quantum critical point in the ratio of U/J, for which the system will undergo a quantum phase transition from the superfluid ground state to the Mott insulator ground state. This continuous quantum phase transition is driven by quantum fluctuations [102]. Therefore such a quantum phase transition can also occur at zero Temperature $T = 0$, when all thermal fluctuations are frozen out.

The quantum phase transition from the superfluid to the Mott insulator state occurs at a quantum critical point of about $(U/J)_c = z \cdot 5.8$, where z is the number of nearest neighbors [4, 103, 104, 105] For large occupations $\bar{n} \gg 1$ the critical value is $(U/J)_c = z \cdot 4\bar{n}$, where $\bar{n}$ is the mean atom number. This value is evaluated by using a mean field approach and agrees reasonably with more rigorous calculations for the three dimensional case [106]. In one dimension there are deviations from the mean field approximation. The corresponding value is $(U/J)_c = 3.84$ for unity occupation and $(U/J)_c = 2.2\bar{n}$ for $\bar{n} \gg 1$ [107, 108]. An exact solution of the Bose-Hubbard model is not available except for the limes of infinite dimensions, where the Gutzwiller approximation becomes exact.

4.1.4 Bose Hubbard phase diagram

By considering a grand canonical ensemble a phase diagram of the Bose system with superfluid and Mott insulator phases can be achieved. The superfluid state is characterized by a finite long range phase coherence with a finite expectation value for the field operator $\langle \hat{a}_i \rangle \neq 0$ while for the Mott insulator the expectation value vanishes $\langle \hat{a}_i \rangle = 0$ and the gas is incompressible. A qualitative phase diagram was already derived in [4]. Figure 4.4 shows a phase diagram for a two-dimensional square lattice and a homogenous system, calculated with an analytic strong coupling series by N. Elstner and H. Monien [106]. The phase diagram shows the boundary between the Mott insulating and the superfluid phase as a function of the chemical potential μ and the tunnel coupling J, both in units of the onsite interaction U. The two lobes represent a parameter range for which the ground state is a Mott insulator with an atom number of one and two particles per lattice site, respectively.

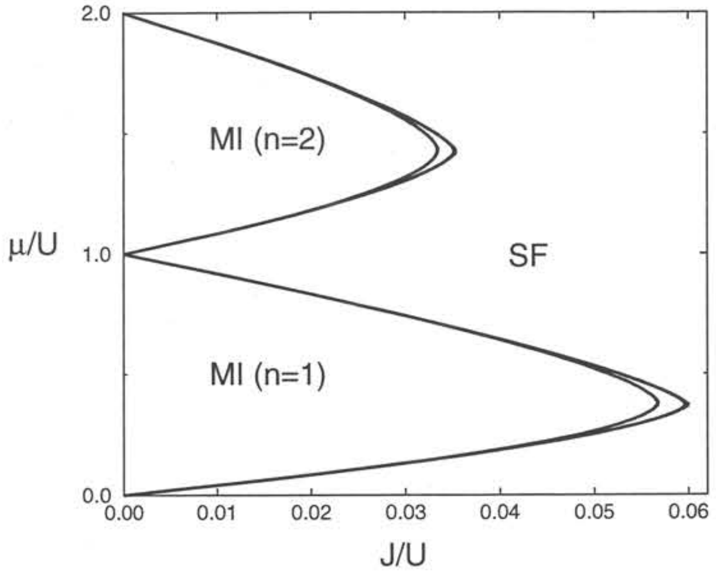

Figure 4.4: Superfluid - Mott insulator phase diagram, obtained in [106], for a two-dimensional square lattice with $z = 4$ next neighbors. This figure is published with the kind permission of H. Monien.

In this diagram the quantum critical point $(J/U)_c$ for a transition to a Mott insulator state with n atoms is given by the ratio of (J/U) at the right border of the corresponding lobe. For a larger chemical potential further lobes representing Mott insulator states with higher atom numbers can be found. For larger n the critical point scales approximately as $(J/U)_c \sim 1/n$.

In the Mott insulator phase an energy gap ΔE opens up in the excitation spectrum. This gap corresponds to particle-hole excitations (chapter 4.1.7) and its size is equal to the difference in μ between the top and bottom phase boundary at given U/J. Scaling theory [4] predicts that close to the critical point $(J/U)_c$ the gap vanishes as

$$\Delta E \sim ((J/U)_c - (J/U))^{z\nu}, \tag{4.6}$$

where $z\nu$ is the dynamical critical exponent less than unity. A mean field model with infinite range hopping yields $z\nu = 1/2$. Therefore the gap vanishes like the square root of $(J/U)_c - (J/U)$ and the phase boundary is parabolic. More rigorous calculations yield slightly larger values, resulting in a pointed tip of the Mott lobe , which can be seen in figure 4.4).

4.1.5 Gutzwiller approximation

In the Gutzwiller approximation [109, 103], the many-particle physics is treated with a mean field approach. The many body state is assumed to be a product state of localized states $|\Phi_i\rangle$ at each lattice site

$$|\Psi_{MF}\rangle = \prod_M |\Phi_i\rangle, \tag{4.7}$$

where the localized state is the superposition of different Fock states $|n\rangle$ with n particles on the ith lattice site

$$|\Phi_i\rangle = \sum_{n=0}^{\infty} f_n^{(i)} |n\rangle. \tag{4.8}$$

The $f_n^{(i)}$ are complex coefficients giving the amplitude for finding a certain atom number n on a lattice site. Both, the Mott insulator and the superfluid ground state can be expressed through the Gutzwiller ansatz in second quantization. For a certain ratio J/U and a fixed chemical potential or alternatively a fixed mean atom number, the coefficients $f_n^{(i)}$ can be found by minimizing the energy $\langle \Psi_{MF}|H_{BH}|\Psi_{MF}\rangle$. In chapter 5.3.1 this calculation is explicitly carried out in order to determine the sub Poissonian number statistics of a superfluid state for a finite U/J, which shows a pronounced number squeezing even before the Mott insulator regime is reached.

The factorized form of the many body state (equation 4.7) allows a very intuitive understanding of the physics in terms of coherent states, fock states and number squeezing, and it is well suited for calculations. However, it should be pointed out, that the Gutzwiller approach is not an exact description of the problem. This approach fails to account for the nontrivial correlations between different sites present at any finite J [31, 94, 110]. In the Gutzwiller ansatz it is assumed that phase correlations are constant across the lattice and do not depend on the distance. The local number fluctuations on a lattice site therefore completely vanish when the phase transition is crossed and when there is no long range phase coherence anymore. In an exact theory, however, short range phase correlations remain even when the long range phase coherence has vanished. Therefore the local number fluctuations do not fully vanish when the Mott-insulator phase entered. Instead the local on-site number distribution changes smoothly and fluctuations remain finite close to the transition point.

4.1.6 Ground state of an inhomogeneous system

Up to now a homogenous system with $\epsilon_i = 0$ was considered. However, in this case a pure Mott insulator state can only be achieved for a commensurate filling with an integer number of atoms per lattice site. If this condition is not fulfilled, the non-commensurate fraction of the atoms will basically form a superfluid phase on top of the commensurate filling of the Mott insulator state.

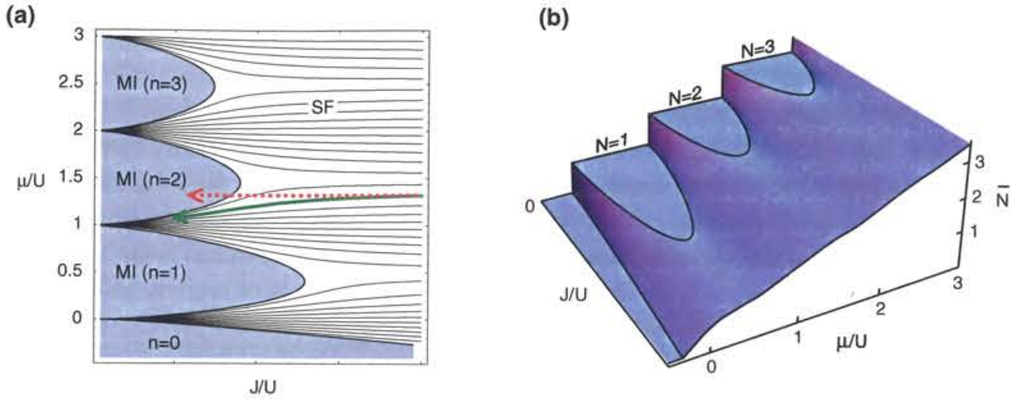

Figure 4.5: Schematic contour plot (a) and 3D plot (b) of the average atom number $\bar{n}$ per lattice site for a given chemical potential μ and ratio of J/U. (a) When the ratio of J/U is changed for a fixed $\bar{n}$ the system will follow the iso-$\bar{n}$ line denoted by the solid arrow. Therefore a superfluid phase will always persist for a non-commensurate filling. If, on the other hand, the chemical potential μ is fixed instead of $\bar{n}$, the system can cross the phase transition to a Mott insulator phase (dashed arrow). This is the case for an inhomogeneous system, where an approximately constant local chemical can be defined. The atoms on the other hand can redistribute over the lattice and thereby change the local density.

In Figure 4.5 the average atom number per lattice site is plotted schematically versus the chemical potential μ and the ratio of J/U, both as a contour plot and a 3D plot. Note that this graph is schematical and does not show a real calculation of the Bose Hubbard model. If the ratio of J/U is changed for a fixed mean atom number, the system will follow the isolines of fig 4.5a (solid arrow) and the chemical potential will change accordingly. This again shows that for a fixed and non commensurate density a pure Mott insulator state will never be reached in a homogenous system.

The situation is fundamentally different for a inhomogeneous system with a fixed total atom number and an external confinement like it is realized in the experiment. In this case the density of atoms in the lattice is not fixed since the atoms can redistribute over the lattice and change the local filling factor.

The Bose Hubbard Hamiltonian has a local character since only neighboring lattice sites are coupled. Therefore it is possible to define an effective local chemical potential

$$\mu_i = \mu - \epsilon_i \tag{4.9}$$

for the ith lattice site. If the change in the atom number between neighboring lattice sites is small, the system will locally behave like a homogenous system. However, now the (local) chemical potential in a certain area of the lattice is fixed instead of the density. Therefore when the ratio of J/U is changed the system can locally cross the boundary between the superfluid and the Mott insulator state (dashed arrow in 4.5a) instead of following the isoline of density (solid arrow), even for a situation where the local density was not commensurate in the beginning.

For such an inhomogeneous system the qualitative profile can be readily extracted from the phase diagram. In the trap center the energy offset ϵ_i is zero and the local chemical potential μ_i is equal to the total chemical potential μ. Going to the border of the atom cloud the local chemical potential will continuously decrease. This radial gradient in the local chemical potential leads to a shell structure with shells of Mott insulator regions and superfluid regions in between (see Fig. 4.6).

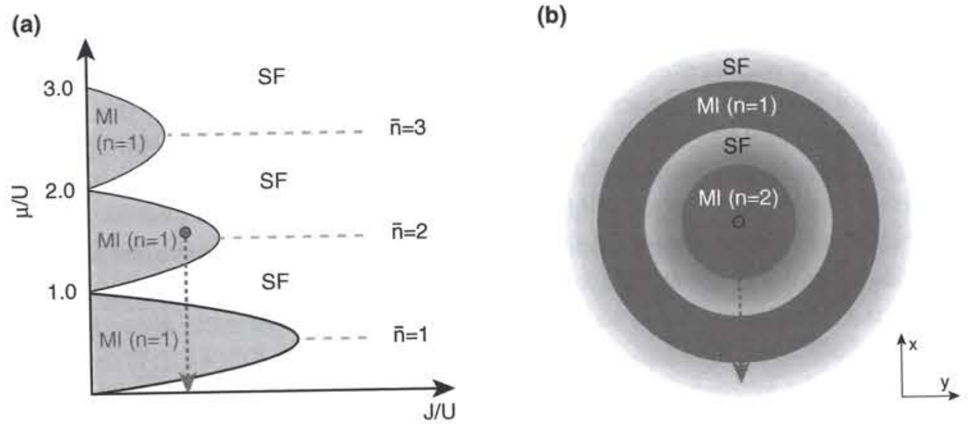

Figure 4.6: The profile of the many body ground state in an inhomogeneous lattice with an external confinement can qualitatively be extracted from a phase diagram (a). The arrow denotes the profile from the trap center where μ is maximal to the border of the atom cloud where $\mu = 0$. She shell structure of superfluid and Mott insulating shells in (b) can be readily extracted from the phase diagram (a).

Based on a Gutzwiller calculation a more quantitative study of the inhomogeneous system can be carried out. Jaksch et al. have calculated the density profile and the number fluctuations for a one and two-dimensional inhomogeneous system [5]. The two-dimensional calculation was done with a mean field approach whereas for the one-dimensional configuration the Bose Hubbard Hamiltonian was directly diagonalized. Figure 4.7 shows the density and the superfluid density for the two-dimensional case. The resulting shell structure of Mott insulating and superfluid regions can be easily identified.

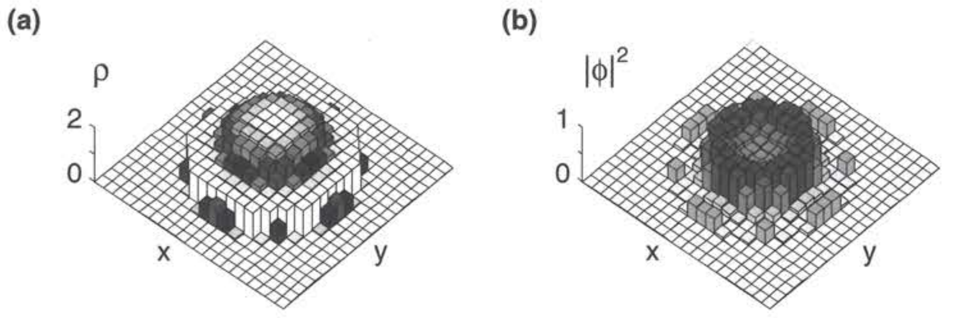

Figure 4.7: Density $\rho(x, y)$ (a) and superfluid density $|\phi(x, y)|^2$ (b) of a two-dimensional lattice with an external confinement and a ratio of $U/J = 35$ slightly across the phase transition [5]. A shell structure starts to form: Mott insulator shells with $n = 1$ and $n = 2$ are visible, characterized by a constant density and a vanishing superfluid density. In between those shells and at the border superfluid shells can be identified. This figure is published with the kind permission of D. Jaksch.

Niemeyer and Monien have performed a similar mean field calculation on a larger 2D lattice [111]. The results for different ratios of U/J are shown in figure 4.8. The “wedding cake” structure can be nicely identified. For increasing U/J the intermediate superfluid shells get more and more suppressed leading to sharper steps in the density. This is in good agreement with the qualitative picture obtained by studying the phase diagram.

Kashurnikov et al. have studied a system on a smaller lattice with a Quantum Monte Carlo continuous time worm algorithm instead of a mean field approach [94]. Their calculation show a similar behavior.

It is interesting to note that in a inhomogeneous system even though there are Mott insulating regions, the whole system should be able to adiabatically follow a change in the external confinement if the variation is done slow enough. This is because atoms can move superfluid on top of the commensurate Mott insulator regions and therefore move from one superfluid shell to another in order to maintain a constant chemical potential. A Mott insulating region should also be able to melt or grow if the chemical potential is changed on its border by changing the external confinement. Combining these two processes it should be possible for the Mott insulating regions to move through the lattice if the change is done very slowly.

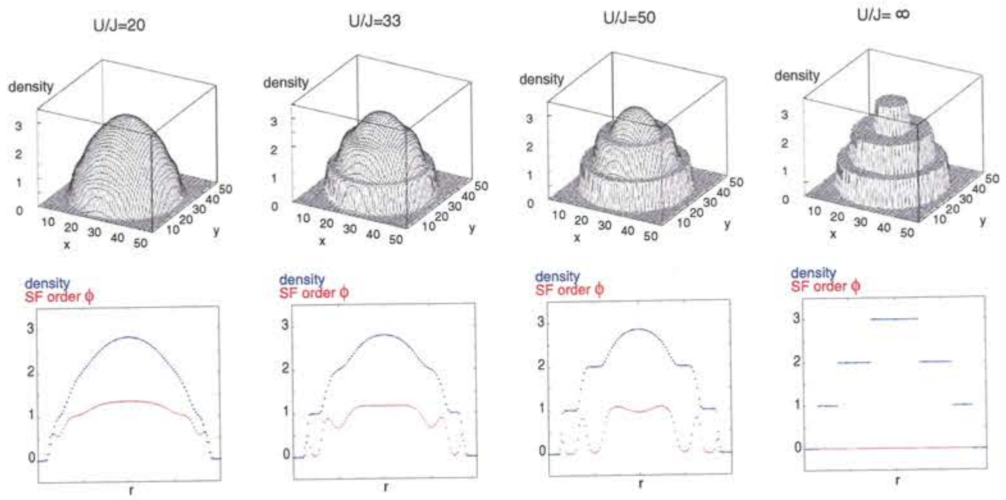

Figure 4.8: Density (upper row) and a profile of the Density and the superfluid order parameter ϕ (lower row) for a 2D lattice and different ratios of U/J, calculated by M. Niemeyer and H. Monien [111] and published with kind permission. The appearance of a "wedding cake" like shell structure and a suppression of the superfluid component can be nicely observed.

4.1.7 Excitation spectrum

An essential feature of a quantum phase transition is the change of the excitation spectrum when the critical point is crossed. For the superfluid phase the excitation spectrum is gapless. Arbitrarily small excitations, corresponding to finite phase differences between adjacent lattice sites, can be excited. When, on the other hand, the critical point is crossed and the Mott insulator regime is entered, a gap in the excitation spectrum opens up. This gap is responsible for the insulating properties.

Excitations in the Mott insulator regime correspond to charge excitations changing the atom number on a lattice site. Adding an extra atom to the ith lattice site results in a particle excitation

$$|\Psi_{MI}(n); i\rangle_{part} = \frac{1}{\sqrt{n+1}}\, \hat{a}_i^\dagger\, |\Psi_{MI}(n)\rangle, \tag{4.10}$$

whereas the reduction of the atom number by one produces a hole excitation

$$|\Psi_{MI}(n); i\rangle_{hole} = \frac{1}{\sqrt{n}}\, \hat{a}_i\, |\Psi_{MI}(n)\rangle. \tag{4.11}$$

The Energy of these particle and hole excitations for a fixed μ and (J/U) can be extracted from the phase diagram 4.4. The sum of the energy for a particle and a hole excitation is equal to the distance in μ direction with (J/U) fixed, from the upper or lower phase boundary respectively. For $U \gg J$ the energy of those excitations becomes

$$E^{(n)}_{part} = \frac{1}{2}U\,(n+1)n - \frac{1}{2}U\,n(n-1) - \mu = Un - \mu \tag{4.12}$$

$$E^{(n)}_{hole} = \frac{1}{2}U\,(n-1)(n-2) - \frac{1}{2}U\,n(n-1) - \mu = U(n-1) - \mu \tag{4.13}$$

If the total number of particles is conserved, the relevant excitation processes are the creation of particle-hole pairs. These pairs are the smallest possible excitations in the Mott insulator. They carry the energy ΔE

$$\Delta E = E^{(n)}_{part} - E^{(n)}_{hole} = U \tag{4.14}$$

which is equal to the onsite interaction U for $U \gg J$. Therefore the gap is as large as this energy. Close to the critical point the gap opens up with the critical exponent $z\nu$ (see equation 4.6).

In the Mott insulator state at $T = 0$ the movement of the atoms is blocked due to the gap in the excitation spectrum. For finite temperature, however, thermal particle or hole excitations can be created. For small nonzero temperature at constant μ, the thermally activated mobility or conductivity of the Mott state is proportional to $\exp(-\tilde{E}_g/k_B T)$, where $\tilde{E}_g$ is the smaller of the particle and hole excitation energies [4]. At fixed integer density $\tilde{E}_g$ is equal to half of the gap energy $\Delta E/2$.

4.2 Experimental observation of the quantum phase transition

Starting from a superfluid state we were able to reversibly change to a Mott insulator state by slowly increasing the lattice potential depth. In this section the creation and detection of the Mott insulator state is described.

4.2.1 BEC in a 3D lattice - a nearly ideal realization of the Bose-Hubbard Hamiltonian

The Bose-Hubbard Hamiltonian, described in chapter 4.1, is an important model in solid state physics. However, well accessible experimental systems which are governed by this Hamiltonian have been rare up to now. Systems which can be approximated by the Bose Hubbard model include granular superconductors [112, 113] and one and two-dimensional Josephson junction arrays [114, 115, 116, 117, 118].

Ultracold atoms, on the other hand, which are stored in a three-dimensional optical lattice like it is described in chapter 3, are a nearly ideal realization of the Bose-Hubbard model. Several properties of such a system are very favorable for studying this intriguing model:

- Due to the short range of the interaction between the atoms compared to the lattice spacing, the interaction energy is well described by a purely onsite interaction. The residual offsite interaction between atoms on neighboring lattice sites due to a finite overlap of their localized Wannier wave functions is about two orders of magnitude smaller then the onsite interaction (see figure 4.10) [89]. Therefore the Bose Hubbard Hamiltonian with purely onsite interaction is an excellent approximation.

- Neglecting higher order tunnelling processes to the second and third neighbor in the Bose Hubbard Hamiltonian is also a very good approximation. These processes are suppressed by about two orders of magnitude for lattice potential depths of $V_0 \gg 5\,E_r$ (see figure 4.10) [89].

- The restriction to the lowest band is well justified since higher energy bands are hardly populated. In the measurement of the band population in section 3.3.6 no occupation in higher energy bands was detected. These bands are well decoupled for a 3D lattice since the vibrational level spacing of the order of 30 kHz is about one order of magnitude larger than the energies relevant for the dynamics.

- The temperature of a Bose-Einstein condensate in an optical lattice is extremely low, leading to a long range phase coherence demonstrated in the time of flight images. In the absence of the lattice potential the temperature range is of the order of several hundred nano Kelvin. When the lattice potential is slowly ramped up the temperature is further decreased by adiabatic cooling. The system is well decoupled from the environment since the optical lattice potential can be precisely controlled and forms a conservative potential. The spontaneous scattering rate of photons from the lattice laser light is of the order of several seconds since the lattice is far detuned. Due to a red detuning the rate for light induced inelastic collisions is low when no photo association line is hit [119].

- A unique feature of the system is the possibility to dynamically change various parameters like the ratio of U/J over a wide range. This even provides the possibility to study the dynamics of the quantum phase transition. Other parameters like an external potential or in future experiments the scattering length can also be dynamically changed.

- Different parameters in the system can be probed. The multiple matter wave interference pattern in a time of flight image gives a direct measure of long range phase coherence in the system. In chapter 5.3.1 the number squeezing in the superfluid regime is measured.

These points show that ultracold atoms in a three-dimensional optical lattice are an intriguing tool for studying the Bose Hubbard model and its dynamics.

4.2.2 Experimental parameters

The experimental setup for studying the quantum phase transition from a superfluid to a Mott insulator is identical to the setup described in chapter 3. The experiments in that chapter correspond to the superfluid regime described above. By changing the potential depth of the optical lattice potential, the ratio of U/J can be changed in a continuous manner over several orders of magnitude. Thereby the system can be brought into the Mott insulator regime, where the interactions between the atoms dominate their behavior.

The experiments are done with ^{87}Rb atoms in the $|F=2, m_F=2\rangle$ state. Initially a nearly pure condensate of about $2 \cdot 10^5$ atoms is formed in a cigar shape Ioffe type trap with radial trapping frequencies of 240 Hz and axial trapping frequencies of 24 Hz. The confinement is then reduced in 500 ms by ramping up an offset field of 150 Gauss. This results in a spherical confinement of the atoms with trapping frequencies of 24 Hz in each direction. The Thomas Fermi radius of the condensate in the final magnetic trap is 26 μm.

After the condensate is prepared in the spherical magnetic trap, a three-dimensional optical simple cubic lattice is superimposed as described in chapter 3. The lattice depth is exponentially ramped up in 80 ms with a time scale of 20 ms. The laser light forming the lattice is red detuned at a wavelength of 852 nm. The beam waist of the standing waves of 125 μm creates an additional external confinement. It is chosen in a way that the Thomas Fermi radius remains approximately constant when the lattice depth is changed. Therefore the atoms have to redistribute over the lattice only slightly in order to maintain a constant chemical potential. Finally 150.000 lattice sites are occupied, which corresponds to an occupation of about 65 lattice sites in a single direction. The mean atom number in the trap center is about 2.5 atoms per site.

4.2.3 Entering the Mott insulator regime

The Mott insulator regime is entered when the lattice potential is smoothly ramped up to a large potential depth. As a first experiment we measured the long range phase coherence for different potential depths.

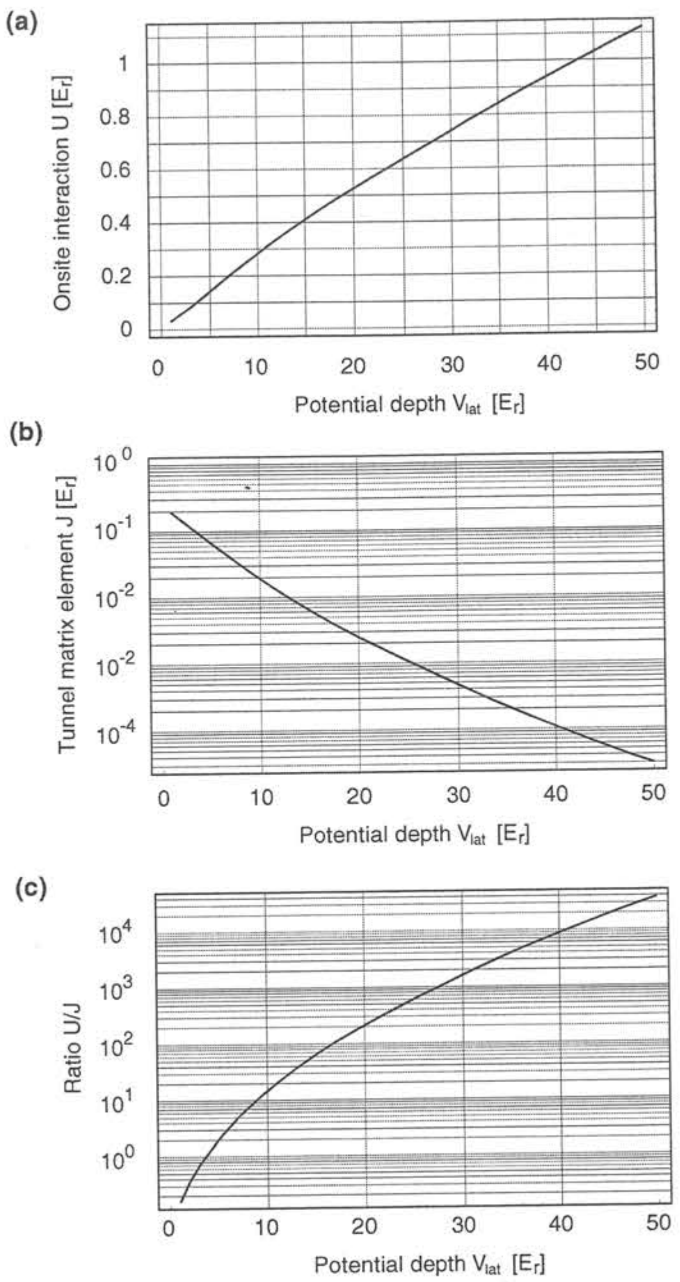

Figure 4.9: Onsite interaction U (a), tunnelling matrix element J (b) and ratio U/J (c) plotted versus the depth of the lattice potential V_{lat}. The ratio U/J can be varied over several orders of magnitude by changing the potential depth. The values are determined through a band structure calculation and by calculating the Wannier functions (chapter 3.1.4).

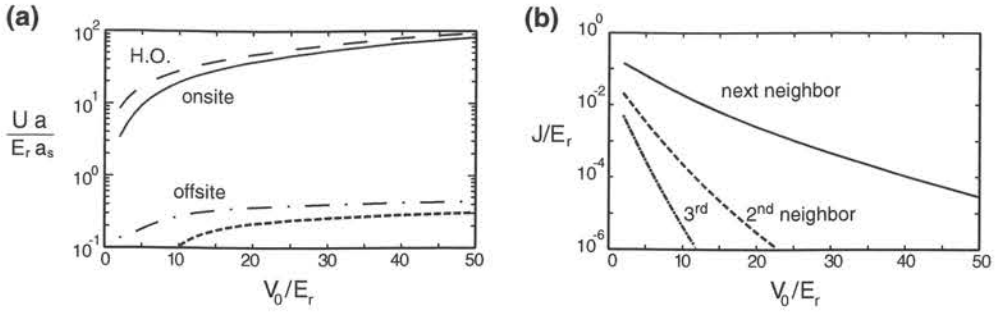

Figure 4.10: (a) Comparison of the onsite interaction (solid curve) with the offsite interaction (dash dotted curve). The offsite interaction is suppressed by about two orders of magnitude. The dashed curve labelled H.O. shows the onsite interaction when the Wannier functions are approximated by a ground state wave function of a harmonic oscillator. (b) Comparison of nearest neighbor hopping to 2nd (dashed curve) and 3rd (dash dotted curve) neighbor hopping. The calculations are performed for a three-dimensional lattice by D. Jaksch [89] and published with kind permission.

The long range phase coherence of the condensate in the optical lattice can be directly tested by observing the multiple matter wave interference pattern. It is formed after ballistic expansion when all trapping potentials are switched off (section 3.3.2). As we increase the lattice potential depth, the interference pattern is markedly changed. Figure 4.11 shows such time of flight images for different potential depths. For lattice depths up to about 10 E_r nearly perfect phase coherence can be observed, characterized by narrow interference maxima. As the lattice potential is raised, the higher order interference maxima initially increase because of a tighter localization of the atomic wave functions at a single lattice site. At a potential depth of around 13 E_r the interference peaks no longer increase in strength. Instead an incoherent background comes up and gains more and more strength as the potential depth is further increased. At a lattice depth of about 22 E_r no interference peaks are visible any more. It is interesting to note that the width of the interference peaks does not significantly broaden when the incoherent background gains more and more strength, indicating that the residual coherence is still predominantly long range in nature. Besides that a cross like structure is slightly visible before all structure vanishes (see fig. 4.11). We interpret this as a residual short range phase coherence between adjacent lattice sites.

This behavior can be explained for an inhomogeneous system if one assumes the formation of a shell structure of superfluid and Mott insulating regions after the quantum critical point is crossed. For a Mott insulator one would expect no interference pattern because of a vanishing expectation value of the field operator $\langle \hat{a}_i \rangle = 0$. This explains the loss of phase coherence deep in the Mott regime. The successive appearance of the non interfering background can be attributed to two effects. First, the superfluid shells continuously decrease for increasing ratios of U/J and the Mott insulating fraction grows. Second, number squeezing can lead to a reduction of the visibility of the interference pattern even slightly before the critical point is

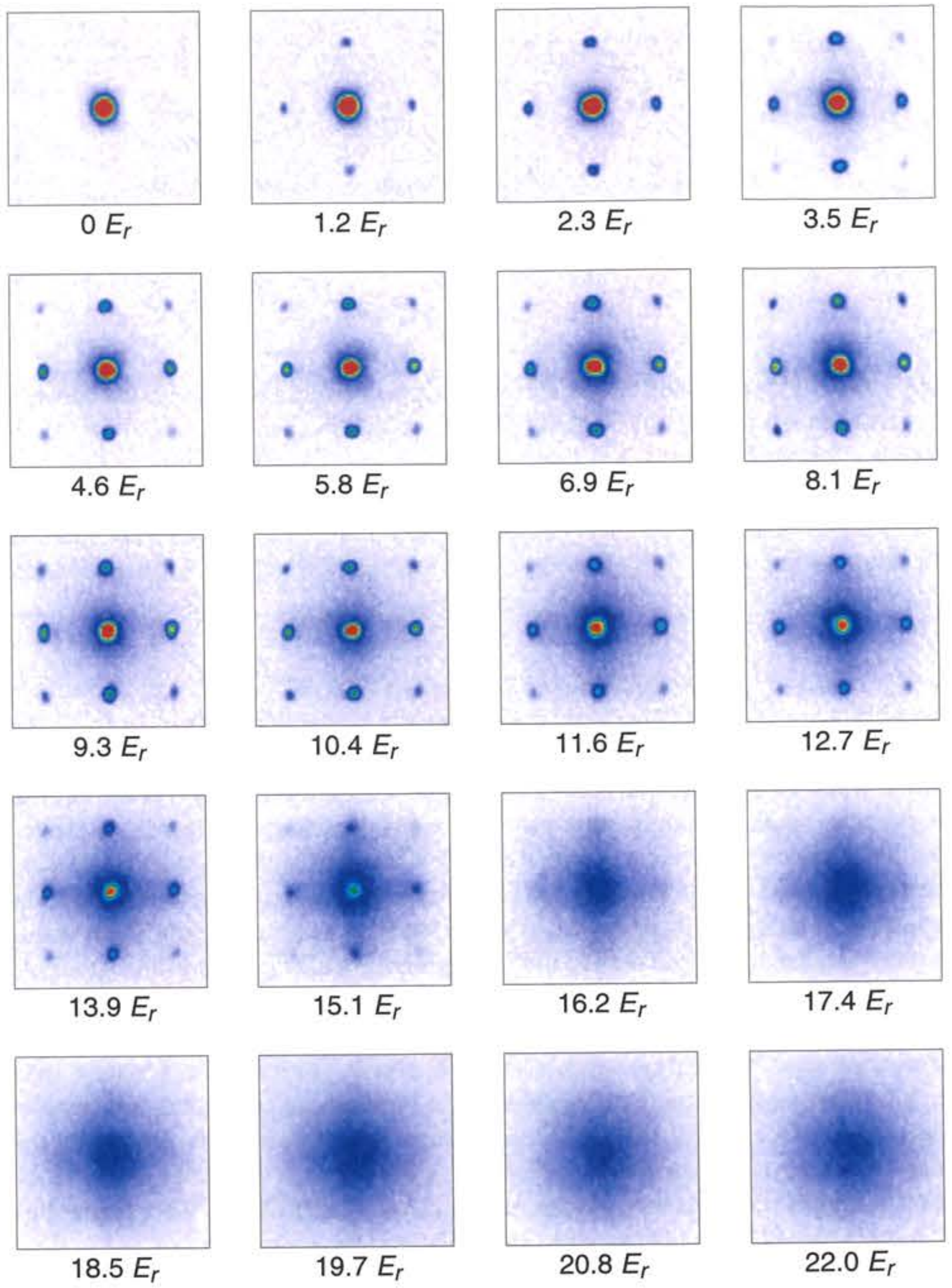

Figure 4.11: Absorption images of multiple matter wave interference pattern for different potential depths, after a time of flight period of 15 ms. In the superfluid regime for potential depths up to about 12 E_r narrow interference maxima are visible, demonstrating long range phase coherence across the lattice. For a potential depth of 22 E_r deep in the Mott insulator regime the interference pattern has totaly vanished.

crossed and in the superfluid shells (see sec. 5.3.1). Recent numerical calculations show, that in the Mott insulator state finite phase correlations between neighboring lattice sites persist for ratios of U/J, where long range phase correlations have already vanished [94, 110]. This is consistent with the observation of cross like structures before all interference structures vanish.

4.2.4 Restoring phase coherence

In order to test the reversibility of the quantum phase transition we measured how fast the long range phase coherence can be restored when the system is brought back into the superfluid regime. The measurement demonstrates that the phase coherence is restored amazingly fast when the optical lattice potential is lowered again to a value where the ground state of the many body system is superfluid.

For this experiment we first prepare a sample in the Mott insulator state by exponentially ramping up the lattice potential to a lattice depth of 22 E_r. The ramp time is 80 ms with a time constant of 20 ms (see fig. 4.13). After a hold time of 20 ms the lattice potential is reduced again to a potential depth of 9 E_r, where the ground state of the many body system is superfluid. This is done with a linear ramp for different ramp down times t. Immediately after the potential depth is reduced all trapping potentials are switched off and Absorption images are taken after free expansion of the condensate (fig. 4.13 b-d). From these images the width of the central momentum peak is fitted as a measure for long range phase coherence. In Figure 4.13 a the filled circles show the width of the central momentum peak starting from a Mott insulator state for different ramp down times t. After only 4 ms of ramp down time, the interference pattern is fully visible again and for a ramp down time of 14 ms the interference peaks have narrowed to their steady-state value, proving that phase coherence has been restored over the entire lattice.

An amazing result is that this time necessary for the transition from the Mott insulator state to a superfluid state is on the order of the tunnelling time $\tau_{\text{tunnel}} = \hbar/J$ between two neighboring lattice sites, which is about 2 ms for a 9 E_r deep lattice. At first sight it seems to be paradox that an atom, which is localized to a lattice site in the Mott insulator state, gets delocalized over the entire lattice in the superfluid state in a time which is not much larger than the tunnelling time to the next lattice site. However, the atoms are indistinguishable and therefore arguing that a specific atom is first localized and then delocalized doesn't make too much sense. Instead, in second quantization, it seems to be enough that the number statistics gets readjusted to a superfluid state, and this can in principle be the case after only one or two tunnelling times. Anyway, the outcome of the experiment suggests that the time which is necessary for the transition from a Mott insulator state to a superfluid state is short and the dynamics is fast. On the theoretical side dynamical calculations of the Bose Hubbard Hamiltonian across the quantum critical point are difficult.

For comparison we carried out the same experiment starting with a dephased sample, for which the interference pattern also vanishes, instead of a Mott insulator state. The state with random phases on each lattice site, which corresponds to a statistical mixture of all Bloch states of the lowest band, was created by applying a magnetic field gradient over a time of 10 ms during the ramp-up period. Nonlinear effects then lead to a dephasing. By adiabati-

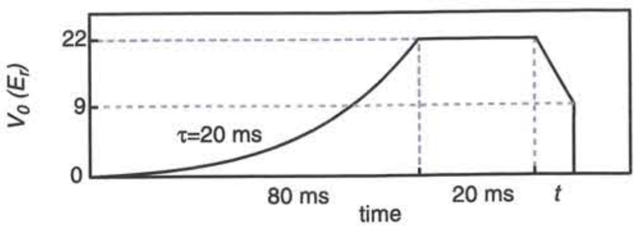

Figure 4.12: Experimental sequence for measuring the restoration of coherence when the system is brought from a Mott insulator state back to a superfluid state. First, the lattice is slowly ramped up to a potential depth of 22 $E_r$in 80 ms. After a hold time of 20 ms the potential depth is decreased in a time t to 9 $E_r$with a linear ramp.

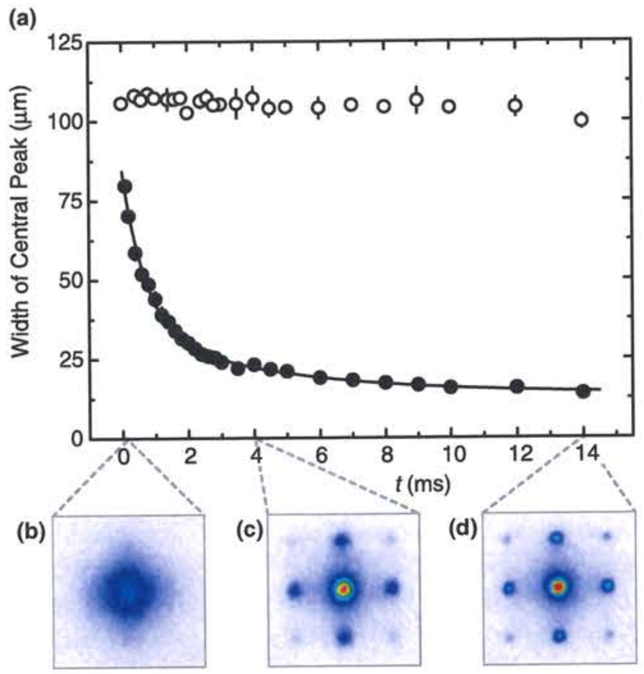

Figure 4.13: Restoring coherence after ramping the lattice potential back into the superfluid regime. The width of the central interference peak is plotted for different ramp down times t. In case of a Mott insulator state (filled circles) coherence is rapidly restored already after about 4 ms. The solid line is a double exponential fit with $\tau_1 = 0.94(7)$ ms and $\tau_2 = 10(5)$ ms. For a phase incoherent state (open circles), using the same experimental sequence, no interference pattern reappears again, even for ramping down times of up to 400 ms. Below, absorption images of the restored interference pattern coming from a Mott insulator phase after ramp down times t of 0.1 ms (b), 4 ms (c) and 14 ms (d) are shown.

cally ramping down the lattice potential we were able to measure the band population (see section 3.3.6) and ensured that the first energy band was homogenously populated. Otherwise the same experimental sequence was used. The open circles in figure 4.13 a show the result of the measurement. No phase coherence is restored after 14 ms. Even for evolution times t of up to 400 ms we didn't observe a reappearance of the interference pattern. This measurement demonstrates that the observed loss of coherence with increasing potential depth is not simply due to a dephasing of the condensate wave function.

4.2.5 Probing the gap in the excitation spectrum

In the Mott insulator state we found the system to be amazingly robust against perturbations. Even when potential gradients are applied or the system is shaken by modulating the external potential the phase coherence can be well reestablished when the lattice depth is decreased to a value, where the system is superfluid. This illustrates that only a low number of excitations is created in the Mott insulator regime. The reason for this robustness is the gap in the excitation spectrum that opens up after the critical point is crossed and which gives rise to the insulating behavior (chapter 4.1.7).

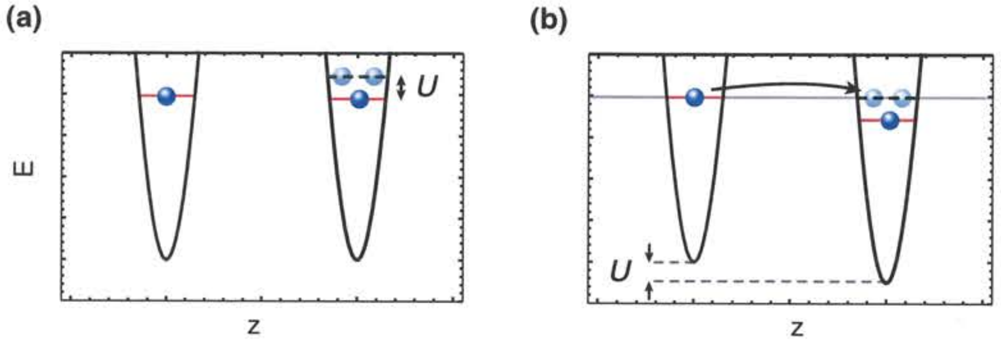

Figure 4.14: The Mott insulator state is characterized by a gap in the excitation spectrum. (a) The smallest excitation for a Mott insulator state with $n = 1$ atom per lattice site consists of removing an atom from a lattice site and adding it to a neighboring lattice sites. This process costs the onsite interaction energy U. (b) If a potential gradient is applied, the movement of the atoms is blocked until the energy difference between neighboring lattice sites equals the onsite interaction U. In this case, however, the atoms are allowed to tunnel again and particle-hole excitations are created.

In order to illustrate the insulator property in a simplified picture, lets assume a Mott insulator state in the regime $U \gg J$ with an occupancy of one atom per lattice site (fig. 4.14 a). If an atom hops to a neighboring lattice site, the site will be occupied by two atoms. These atoms repel each other and therefore the energy is raised by the onsite interaction energy U above the state with only one atom per lattice site. For this process, which corresponds to a particle hole excitation (eq. 4.14), a finite energy U is required. It is only available in virtual processes. Therefore in this Mott *insulator* state movement of atoms over the lattice is blocked and each atom is pinned to a lattice site due to the interaction. This reasoning is also valid for a Mott insulator state with a higher number of atoms per lattice site.

If a potential gradient is applied, the lattice gets tilted and the energy levels of neighboring lattice sites are shifted with respect to each other. For small potential gradients, the atoms are still pinned to their lattice sites and the system does not react to the gradient. It is interesting to compare this insulating behavior with the superfluid case: In the superfluid regime the atoms get accelerated and are able to move through the lattice even for an arbitrarily small gradient.

However, if the potential gradient is increased and the energy difference between neighboring lattice sites approaches the onsite interaction energy U, the energy level for two atoms in the lower well is shifted to the same energy as the level of one atom in the upper well (see fig. 4.14 b). For this situation the atom can tunnel to the next lattice site again and thereby create a particle hole excitation. The energy U for this excitation is provided by the potential gradient.

In order to probe the excitation spectrum for various potential depths we applied potential gradients to the sample and measured the response of the system. Figure 4.15 a shows the experimental sequence we used.

First the atoms are prepared in the ground state of the lattice by exponentially ramping up the lattice potential to a certain depth $V_{lat} = V_{max}$ in 80 ms, with a time constant of 20 ms. After that the potential depth V_{lat} is kept constant for 20 ms. Within this period, a potential gradient with a energy difference ΔE between neighboring lattice sites is applied for a time τ_{perturb}. It is created by shifting the harmonic magnetic trapping potential (see section 3.3.5) and points into the vertical direction. Finally the lattice potential is lowered again within 3 ms to a potential depth of $V_{lat} = 9\,E_r$ for which the system is superfluid again.

If excitations have been created during the application of the potential gradient at the potential depth $V_{lat} = V_{max}$ we will not be able to return to a perfectly coherent superfluid state by subsequently lowering the potential to a depth of $V_{lat} = 9\,E_r$. Instead, excitations created in the Mott insulator state will lead to excitations in the lowest energy band of the superfluid state after the phase coherence is restored. These excitations are fluctuations of the macroscopic phase between lattice sites. The strength of these statistical phase fluctuations can be measured as the width of the interference peaks in the multiple matter wave interference pattern, which can be achieved by a time of flight imaging.

Figure 4.15 b shows a typical time of flight image after the sequence described above is applied. In addition a potential gradient is applied for 300 μs just before the lattice potential is switched off. Thereby the Bloch state $q = 0$ is shifted to the boundary of the Brillouin zone $q = \hbar k$ with a phase difference of π between neighboring lattice sites in the vertical direction. This procedure is used in order to create two central interference maxima which are less affected by the mean field repulsion during the initial stage of the expansion period. From these time of flight images the widths of the two central peaks are determined by a 2D fit.

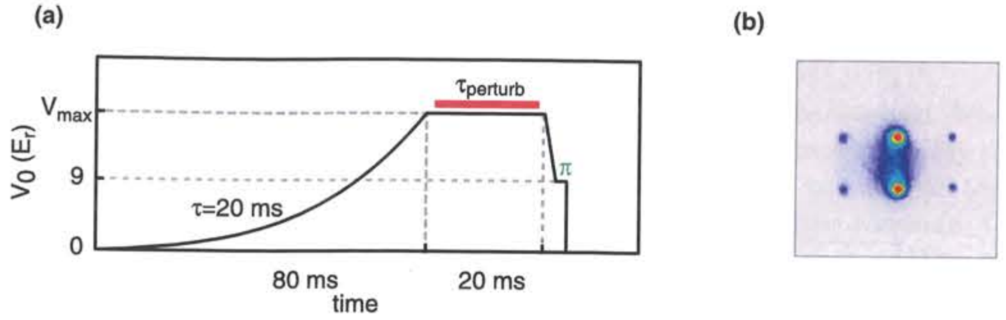

Figure 4.15: Experimental sequence for probing the excitation probability versus an applied vertical potential gradient. (a) First, the optical lattice potential is slowly increased to a potential depth $V_0 = V_{max}$. The atoms are held in the potential for 20 ms. Within this time, a potential gradient is applied for a time τ_{perturb}. Then, the lattice potential is lowered again within 3 ms to a value of $V_0 = 9\,E_r$, where the ground state is superfluid. We apply a second potential gradient for 300 μs with a fixed strength in order to populate the Bloch state with quasi momentum $q = \hbar k$ in the vertical direction. We measure the excitations created by the potential gradient by measuring the width of the interference peaks after the coherence is restored (b).

By this procedure a perturbation probability can be measured as the width of the interference peaks after restoring the macroscopic phase coherence. In Figure 4.16 the width of the interference peaks is plotted versus the applied potential gradient for different potential depths V_{max}. The perturbation times τ_{perturb} are prolonged for deeper lattice potentials in order to account for the increasing tunnelling times. For a completely superfluid sample at a lattice depth of $10\,E_r$ the system is easily perturbed already for small potential gradients. For larger gradients the sample is completely dephased and the measured width of the interference peaks saturates. When the potential depth is increased to $13\,E_r$, which is close to the expected transition point, two broad resonances start to appear in the graph of the excitation probability. And for a $20\,E_r$ deep lattice potential, deep in the Mott insulator regime, the situation has dramatically changed. Two narrow resonances are visible on top of an otherwise flat perturbation probability. The first large resonance occurs at an potential gradient with $\Delta E = U$. It can be directly attributed to the creation of particle hole pairs. This behavior directly demonstrates that an excitation gap has opened up. For small potential gradients, the system is not perturbed at all. Only when the potential gradient approaches the onsite interaction energy U the system is resonantly perturbed.

The second, weaker resonance occurs at exactly twice the energy difference of the first stronger resonance. Different processes could be responsible for a resonance at $\Delta E = 2U$. For a Mott insulator phase with more than one atoms per lattice site, two atoms could tunnel simultaneously and thereby create a double charged particle hole excitation. Alternatively two particle hole pairs could be created simultaneously as a second order process, with only one in the direction of the applied potential gradient. A third possibility would be a tunnelling

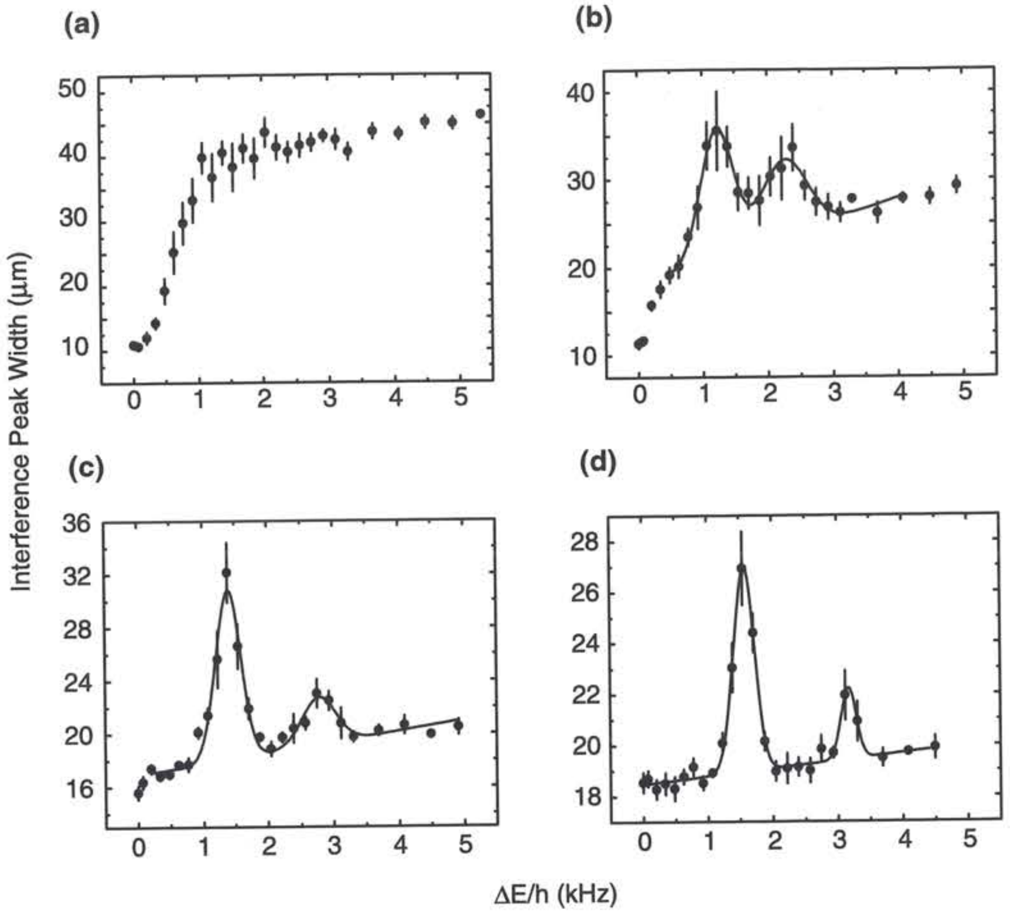

Figure 4.16: Width of the interference peaks after restoring coherence as a measure for the perturbation probability, plotted versus the energy difference between neighboring lattice sites ΔE. The gradient is applied for a time τ_{perturb}. (a) $V_{max} = 10\,E_r$, $\tau_{\text{perturb}} = 2\,\text{ms}$; (b) $V_{max} = 13\,E_r$, $\tau_{\text{perturb}} = 6\,\text{ms}$; (c) $V_{max} = 16\,E_r$, $\tau_{\text{perturb}} = 10\,\text{ms}$; (d) $V_{max} = 20\,E_r$, $\tau_{\text{perturb}} = 20\,\text{ms}$. The perturbation times have been prolonged for deeper lattice potentials in order to compensate for increasing tunnelling times. The solid line is a fit to the data based an two Gaussians on top of a linear background

process occurring between lattice sites with $n=1$ atom next to lattice sites with $n=2$ atoms. This process might occur close to the boarder between Mott insulating shells with $n=1$ and $n=2$ atoms or as a second order process after particle hole pairs are already created.

For potential depths between $10\,E_r$ and $20\,E_r$ a gradual crossover can be observed. When the lattice potential is increased, the linear background in the perturbation probability decreases. We attribute the linear background to the superfluid shells in between the Mott insulator regions. It decreases as the superfluid shells shrink for larger lattice potentials. On the other hand the resonances get more pronounced as the Mott insulating regions grow, and deep in the Mott regime the resonances seem to be more narrow. However, the absolute values for the strength of the linear background and the hight of the resonance peaks should be taken with care due to the qualitative nature of the measured perturbation probability.

The position of the first resonance can be seen to shift with increasing lattice potential. This happens because the onsite interaction U increases due to a tighter localization of the wave function on a lattice site. Figure 4.17 shows the position of the first resonance versus the lattice potential depth V_{max}. A comparison with an ab initio calculation of U, based on a Wannier functions from a band structure calculation (chapter 3.1.4), shows a good agreement within the experimental uncertainties. This demonstrates that the resonance indeed occurs for a potential gradient with $\Delta E = U$.

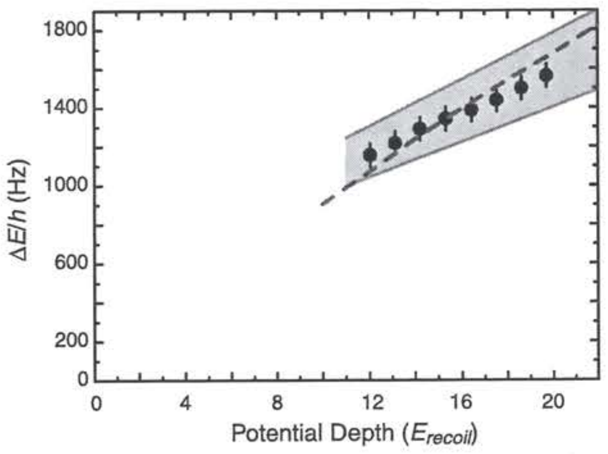

Figure 4.17: Potential gradient for which the Mott insulator phase can be resonantly perturbed, plotted versus the lattice potential depth V_{max}. The filled circles show experimental data points, together with error bars denoting a statistical error. The shaded gray area denotes the possible uncertainties of the experimental values due to systematic uncertainties in the calibration of the lattice potential depth and the applied gradient. The dashed line is the theoretical prediction for the onsite interaction matrix element U.

4.2.6 Determination of the transition point

The theoretical prediction for the transition point from the superfluid phase to the Mott insulator phase is $U/J = z \cdot 5.8$ for single occupancy in a lattice with z next neighbors [4, 103, 104, 105]. It is interesting to compare this prediction with the experimental signatures described above.

For an inhomogeneous system like in the experiment the transition from a superfluid to a Mott insulator is not expected to occur suddenly. Instead, after the transition point is crossed, first a thin Mott insulating shell with $n = 1$ should form, which will grow when the lattice is raised further (see section 4.1.6). After the transition point for $n = 2$ is crossed, a second Mott insulating shell with $n = 2$ should form and successively grow. No observable is expected to change abruptly.

This is consistent with the experimental observation. At a lattice depth of $V_{lat} = 12(1) - 13(1)\,E_r$ the multiple matter wave interference pattern starts to vanish. At about the same potential depth the resonances in the excitation spectrum start to appear, indicating the occurrence of a Mott insulator state. We therefore expect the experimental transition point to lie above $V_{lat} = 10(1)\,E_r$, where no resonances are visible and below $V_{lat} = 13(1)\,E_r$. For a potential depth of 13 E_r, we calculate a ratio of $U/J \approx 36$. This is in good agreement with the theoretical prediction.

Recently it was proposed to detect the transition point by observing sidelobes in the interference pattern, which form as a result of the formation of a Mott insulating shell [94]. However, these sidelobes are very small for the present experimental system and therefore difficult to detect.

5 Collapse and revival of a macroscopic matter wave field

The most fascinating feature of a Bose Einstein condensate is that a macroscopic number of bosonic atoms is described by a single giant matter wave. This macroscopic matter wave field is, in many respects, analogous to a coherent light field emitted by an optical laser. However, the matter wave field is quantized and the individual atoms represent a crucial granularity. This quantization was not accessible to experiments up to now. However, it has been realized that this quantization together with the interaction between particles can lead to pronounced effects which go far beyond the usual mean field descriptions of a Bose-Einstein condensate [120, 121, 122, 123, 124, 125, 126].

In this chapter I report on the direct observation of the collapse and revival of a macroscopic matter wave field of a Bose-Einstein condensate [127]. This dynamical behavior is a direct consequence of the quantization of the matter wave field and the interaction between the atoms. Furthermore, this measurement shows that cold collisions between individual ultracold atoms are fully coherent, which is important for novel quantum computation schemes based on cold collisions [7, 128, 129, 130]. In the last part of this chapter I demonstrate how the collapse and revival can be used as a tool for measuring the variance in the number statistics of a matter wave field.

5.1 Theory of the collapse and revival

Lets assume a Bose-Einstein condensate, or alternatively a superfluid or a superconductor, that is rapidly split into two parts, such that initially a well defined relative macroscopic phase is established. The macroscopic phase implies that each part can be described by a state which is close to a coherent state with Poissonian atom number statistics. However, if interactions between the particles are taken into account, the coherent state is no longer an eigenstate of both parts. The initially coherent state evolves in time, and an interesting question arises: how does the macroscopic phase evolve and what happens to the macroscopic matter wave field? The intriguing time evolution which occurs for such a coherent state subjected to interaction between the particles is discussed in the following sections.

5.1.1 Cold collisions

Ultracold bosonic atoms interact with each other through binary s-wave collisions. Inelastic three body collisions can be neglected for our experimental parameters as well as higher partial wave scattering processes. The interactions between the atoms can be quantified by the s-wave scattering length a. For ^{87}Rb the scattering length is positive and the atoms will therefore repel each other.

When two such atoms are placed into the ground state of a confining potential, the atoms collide with each other (figure 5.1). The cold collisions lead to an increase of the total energy by the interaction energy U. This energy is given by $U = 4\pi\hbar^2 a/m \int d^3\mathbf{x}\, |w(\mathbf{x})|^4$, where $w(\mathbf{x})$ is the ground state wave function and m the mass of the particles. This relation is valid when the level spacing ω is much larger than the total interaction energy.

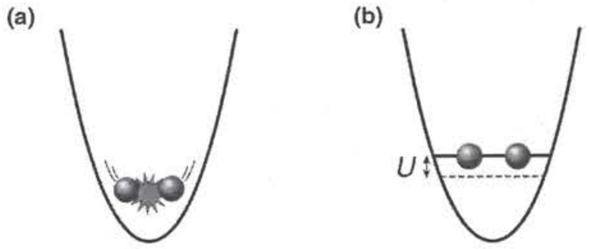

Figure 5.1: (a) two interacting atoms in the ground state of a confining potential. (b) Cold collisions are coherent and cause no dissipation. They just increase the total energy by the interaction energy U.

For a larger number of atoms, where each of the n atoms interact with the $n-1$ other atoms, the interaction energy is given by $E_{int} = U\, n(n-1)/2$. Here U does not depend on the atom number for $E_{int} \ll \hbar\omega$. The Hamiltonian governing the system after subtracting the ground state energy reads

$$\hat{H} = \frac{1}{2} U\, \hat{n}(\hat{n}-1), \tag{5.1}$$

where $\hat{n}$ counts the number of atoms in the confining potential. This Hamiltonian is equal to the Bose-Hubbard Hamiltonian 4.3 when the lattice sites are fully separated (J = 0) and only a single site is considered.

It is interesting to note that the cold collisions do not cause dissipation. Instead they are coherent, since the initial and final state of the scattering process is well defined. The only effect is the increase of the total energy by the interaction energy. However, the interaction energy corresponds to a strong nonlinearity which can have pronounced effects on the many particle physics.

5.1.2 Coherent states

Lets assume that a coherent or Glauber state (see e.g. [131]) in second quantization is prepared in the ground state of a confining potential. A sample which is described by such a state has a well defined macroscopic phase. In general such a well defined phase can be created artificially using a quantum measurement process [124, 132, 133] and comparing it to a phase standard [134].

A coherent state $|\alpha\rangle$ is the eigenstate of the annihilation operator $\hat{a}$

$$\hat{a}|\alpha\rangle = \alpha|\alpha\rangle. \tag{5.2}$$

The field operators $\hat{a}$ and $\hat{a}^\dagger$ are, respectively, the annihilation and creation operators for atoms occupying the condensate mode in the ground state of the confining potential, and the atom number operator is equal to $\hat{n} = \hat{a}^\dagger\hat{a}$

The eigenvalue α corresponding to the coherent state $|\alpha\rangle$ is a complex vector and describes a classical field $\psi = \alpha$. The argument denotes the macroscopic phase φ of the field, and the length corresponds to the field amplitude, i.e. the square root of the mean atom number $\bar{n} = \langle\hat{n}\rangle = \langle\hat{a}^\dagger\hat{a}\rangle$:

$$\alpha = \sqrt{\bar{n}} \cdot e^{i\varphi}. \tag{5.3}$$

In the basis of Fock states $|n\rangle$ a coherent state is a superposition of states with different atom numbers:

$$|\alpha\rangle = e^{-|\alpha|^2/2} \sum_n \frac{\alpha^n}{\sqrt{n!}} |n\rangle \tag{5.4}$$

Therefore the atom number remains uncertain and follows a Poissonian distribution with a variance given by $\mathrm{Var}(n) = \langle\hat{n}\rangle$.

5.1.3 Dynamical evolution of a coherent state with interactions

The dynamics of the state in the confining potential is solely determined by the interaction between the atoms and is therefore governed by the Hamiltonian in equation 5.1. The eigenstates of this Hamiltonian are number states $\hat{H}|n\rangle = E_n|n\rangle$, with eigenenergies

$$E_n = \frac{1}{2} U\, n(n-1). \tag{5.5}$$

The eigenenergies are quadratic in the atom number and therefore introduce a nonlinearity. Each number state acquires a collisional phase shift and evolves in time like

$$|n\rangle(t) = |n\rangle\, e^{iE_n t/\hbar} = |n\rangle\, e^{iU\, n(n-1)\, t/2\hbar}. \tag{5.6}$$

A coherent state, on the other hand, is no eigenstate of the Hamiltonian in equation 5.1. It is a superposition of several number states, and each of them evolves differently in time according to its eigenenergy.

If the eigenenergy depends only linearly on the atom number ($E_n \propto n$), a coherent state $|\alpha\rangle$ remains a coherent state for all times though it is no eigenstate of the Hamiltonian. It evolves to a different coherent state $|\alpha(t)\rangle$ with a time dependent macroscopic phase $\alpha(t)$. Therefore, only the macroscopic phase is changed.

The situation, however, is fundamentally different if the eigenenergy depends on the atom number in a nonlinear way like in equation 5.6. With this quadratic dependence, the time evolution of the initially coherent state is given by

$$|\Phi(t)\rangle = e^{-|\alpha|^2/2} \sum_n \frac{\alpha^n}{\sqrt{n!}} \cdot e^{iU\, n(n-1)\, t/2\hbar}\, |n\rangle. \tag{5.7}$$

Each number state acquires a nonlinear collisional phase shift, and the number states dephase with respect to each other. Therefore the coherent state does not remain a coherent state for all times.

Collapse

When the many particle state evolves away from a coherent state, the property of having a macroscopic phase vanishes. This property can be quantified by the expectation value of the field operator $\langle\hat{a}\rangle$. It denotes to which extent the many particle state can be described by a classical field ψ, which is equal to the expectation value of the field operator. It can be calculated from equation 5.7 and reads [120, 123]

$$\begin{aligned}\psi(t) = \langle\Phi(t)|\hat{a}|\Phi(t)\rangle &= \sqrt{\bar{n}}\sum_n \frac{\bar{n}^n e^{-\bar{n}}}{n!}\cdot e^{i(E_n-E_{n+1})t/\hbar} \\ &= \sqrt{\bar{n}}\cdot\exp\left(\bar{n}(e^{-iUt/\hbar}-1)\right) \qquad (5.8)\end{aligned}$$

For short times this can be approximated as

$$\psi(t) \simeq \sqrt{\bar{n}}\, e^{-i\bar{n}Ut/\hbar}\cdot e^{-\bar{n}U^2t^2/2\hbar^2}. \qquad (5.9)$$

Therefore the macroscopic matter wave field ψ collapses with a characteristic collapse time $t_c=\hbar/\sqrt{\bar{n}}U$.

Revival

At the revival time $t_{rev} = h/U$ each number state has acquired a collisional phase shift which is an integer multiple of 2π: The state with one atom has not evolved, the state with two atoms has obtained a shift by 2π, the state with three atoms $3\cdot 2\pi$ and so forth. Therefore the phase of each number state has evolved to the initial phase modulo 2π and the many body state is identical to the initial coherent state $|\Phi(t=\hbar/U)\rangle = |\Phi(t=0)\rangle$. The macroscopic phase is then reestablished and the macroscopic matter wave field ψ has revived at this time.

The dynamical evolution is periodic with a period equal to the revival time t_{rev}. Two subsequent collapses and revivals are shown in figure 5.2, where the expectation value of the field operator, which is evaluated through equation 5.8, is plotted versus time for different atom numbers.

5.1.4 Visualization of the time evolution

The periodic time evolution described above can be visualized by plotting the Q-function, which is used in quantum optics [135, 136]. The Q-function

$$Q(\beta,t) = \frac{|\langle\beta|\Phi(t)\rangle|^2}{\pi} \qquad (5.10)$$

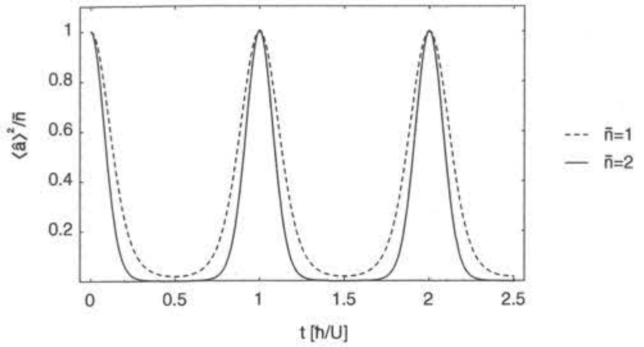

Figure 5.2: Periodic collapse and revival of the macroscopic matter wave field. The expectation value of the field operator is plotted as $|\langle\hat{a}\rangle|^2/\bar{n}$ versus time for $\bar{n}=1$ and $\bar{n}=2$ respectively. First, the matter wave field collapses on a characteristic time scale given by $t_c = \hbar/\sqrt{\bar{n}}U$. However, at integer multiples of the revival time $t_{rev} = h/U$, the initial quantum state is restored and the matter wave field revives.

denotes the overlap between an arbitrary coherent state $|\beta\rangle$ and the dynamically evolving state $|\Phi(t)\rangle$. It quantifies the probability to find the system in a state with a certain macroscopic phase $\varphi = \arg(\beta)$ and a certain average atom number $\bar{n} = |\beta|^2$.

In Figure 5.3 the Q-Function is plotted for different evolution times t. For $t = 0$ the many body state $|\phi\rangle$ is equivalent to a coherent state $|\alpha\rangle$. Therefore, the state has maximum overlap with the state $|\beta\rangle = |\alpha\rangle$ (fig. 5.3a). However, the overlap with coherent states $|\beta\rangle$ which have similar phases and atom numbers does not vanish, since coherent states are only quasi-orthogonal.

As time evolves, the macroscopic phase gets initially more and more uncertain (fig. 5.3b). For a time $h/2U$, however, the state is an exact superposition of two coherent states $|\alpha_1\rangle$ and $|\alpha_2\rangle$, with $\alpha_{1,2} = \pm i\alpha$, corresponding to the macroscopic phases of $\pm\pi/2$ respectively. This state is a Schrödinger cat state, since it is a superposition of two macroscopic quantum states. In a measurement one would find either one or the other phase. Both phases are 180° out of phase and occur with the same probability. Therefore, the expectation value of $\langle\hat{a}\rangle$ vanishes and the macroscopic matter wave field has collapsed. At a time h/U the original coherent state is restored again and the matter wave field has revived.

5.2 Experimental realization

The quantum dynamics that has been described above can in principle be observed whenever a Bose-Einstein condensate is prepared in a state with a well defined macroscopic phase. Experimentally this can be achieved by splitting a condensate in two or more parts with a well defined relative phase, or by other quantum measurement processes [124, 132, 133]. In our experiment we split a condensate in many parts with a well defined relative phase by using a three-dimensional optical lattice potential. Therefore we can assign a macroscopic phase to each of those parts.

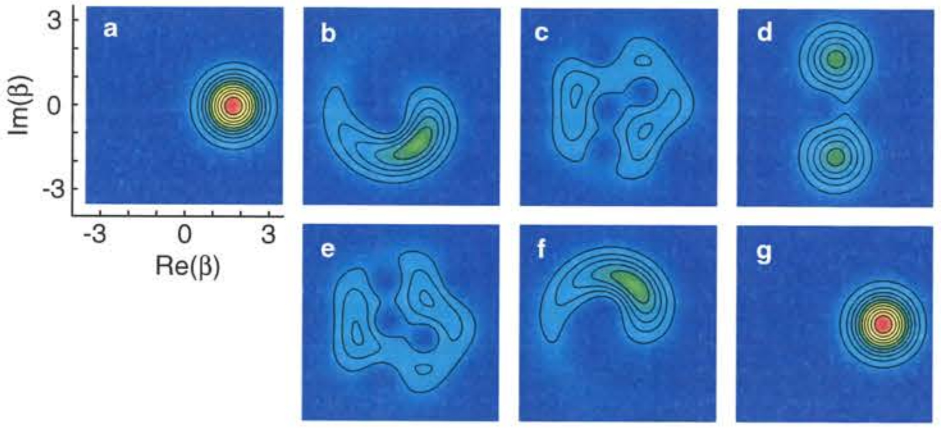

Figure 5.3: Quantum dynamics of a coherent state owing to cold collisions. The contour plots (a)-(g) show the overlap $|\langle\beta|\Phi(t)\rangle|^2$ of an arbitrary coherent state $|\beta\rangle$ with the dynamically evolving state $|\Phi(t)\rangle$ for different times t. (a) $t=0$; (b) $t=0.1\,h/U$; (c) $t=0.4\,h/U$; (d) $t=0.5\,h/U$; (e) $t=0.6\,h/U$; (f) $t=0.9\,h/U$; (g) $t=h/U$; The plotted overlap quantifies the probability to measure a certain macroscopic phase $\varphi = \arg(\beta)$ and a certain average atom number $\bar{n} = |\beta|^2$. First, the macroscopic phase gets more and more uncertain (a-c). At $t = t_{rev}/2$ (d) the state has evolved to a Schrödinger cat state of two coherent states, which are 180° out of phase. The macroscopic field has collapsed. At $t=t_{rev}$, however, the coherent state is restored and the macroscopic field has fully revived

It should be pointed out that the collapse and revival of a macroscopic field has also been theoretically predicted to occur for a coherent light field propagating in a nonlinear medium [135, 137, 136]. However, it has never been observed experimentally because the available nonlinearities have been much too small.

Usually a Bose Einstein condensate with a large atom number is trapped in a shallow potential. For such a system various difficulties arise, which have prevented an observation of such effects so far. The onsite interaction U for example is typically less than a Hertz. Therefore it would take more than a second before a revival could be observed. It would be hard to prevent a trivial dephasing due to technical fluctuations on this time scale. Moreover, in this regime the total interaction energy is much larger than the level spacing of the confining potential. The macroscopic matter wave is therefore described by a Thomas Fermi wave function instead of the ground state wave function $w(x)$ of the confining potential. The onsite interaction U then depends on the atom number n, and equation 5.8 is not valid any more. Under certain circumstances, however, a revival should still be observable [123].

The system of a Bose Einstein condensate in a three-dimensional optical lattice is much more favorable for studying dynamics of the many body quantum state. In order to create a coherent state in the ground state of a confining potential, we split a Bose-Einstein condensate into more than 100.000 potential wells by rapidly raising the potential depth of the optical lattice potential. In the deep lattice, the individual potential wells are isolated from each other, and coherent states with an initially well defined macroscopic phase are projected into each potential well. Such a system with microscopic potential wells has several advantages:

- The onsite interaction energy U is about four orders of magnitude larger ($\approx 1.5\,\mathrm{kHz}$) than for a normal BEC in a magnetic trapping potential. Thereby the revival time h/U is brought into an experimentally accessible range.

- The interaction energy is much smaller than the level spacing, therefore U is independent on the atom number and equation 5.8 remains valid.

- The atom number inside each well $\bar{n} \approx 1 - 2$ is small. Therefore the collapse time is not much shorter than the revival time, which is experimentally favorable for the detection of the revival.

After coherent states are prepared inside each of the isolated potential wells, the atom-atom interaction affects the quantum dynamics discussed in the previous chapter. The time evolution of the matter wave field can be measured by probing the multiple matter wave interference pattern.

5.2.1 Creating an array of coherent states

In the experiment we create coherent states of the matter wave field by loading a Bose-Einstein condensate into a three-dimensional optical lattice potential. This system is described by the Bose-Hubbard Hamiltonian (see chapter 4). For a shallow lattice potential, where the tunnel coupling between neighboring lattice sites J is much larger than the onsite repulsive interaction energy U, the system is superfluid and all atoms can be described by a macroscopic matter wave (chapter 4.1.2). Each atom is then delocalized over the entire lattice and, for a homogenous system where N atoms are distributed over M lattice sites, the many particle state can be written as the product state of identical single particle Bloch states with zero quasi momentum

$$|\Psi\rangle_{U/J\approx 0} \propto \left(\sum_{i=1}^{M} \hat{a}_i^{\dagger}\right)^{N} |0\rangle. \tag{5.11}$$

For a grand canonical ensemble this state can be written in second quantization as a product over single site many body states $|\Phi_i\rangle$ such that

$$|\Psi\rangle_{U/J\approx 0} \approx \prod_{i=1}^{M} |\Phi_i\rangle \tag{5.12}$$

Here, a spontaneously broken gauge symmetry is assumed. For large N and M the single site many body state $|\Phi_i\rangle$ is almost identical to a coherent state $|\alpha_i\rangle$ with a well defined macroscopic phase and Poissonian atom number distribution. Furthermore, all the matter waves in different potential wells are phase coherent, with constant relative macroscopic phases between lattice sites. For a finite ratio of U/J, the atom number distribution on each site becomes sub Poissonian [3] owing to the repulsive interactions between the atoms, even before entering the Mott insulator state. This situation of number squeezed coherent states is discussed in detail in the subsequent chapter 5.3.

After creating coherent states $|\Phi_i\rangle = |\alpha_i\rangle$ in each potential well, we increase the potential depth rapidly in order to isolate the potential wells from each other. In the deep lattice, tunnelling between potential wells is strongly suppressed. Therefore, each well is described by the single site Hamiltonian 5.1. The coherent states in the isolated potential wells independently undergo the dynamics described in the previous chapter.

In the experiment we use the same setup and similar experimental parameters as in the Mott insulator experiment. We start with a nearly pure condensate of about $1 \cdot 10^5$ ^{87}Rb atoms in the $|F = 2, m_F = 2\rangle$ state. The BEC is stored in a harmonic magnetic trapping potential with isotropic trapping frequencies of $\omega = 2\pi \cdot 24$ Hz. We transfer the magnetically trapped atoms into the optical lattice potential by slowly increasing the intensity of the laser beams forming the lattice within 80 ms. This is done in an exponential ramp with a time constant of 20 ms. In this first step we ramp the lattice to a potential depth V_A of up to 11 recoil energies E_r, where the system is still completely superfluid and the ground state can be described by states close to coherent states in each potential well. Due to the onsite interaction, however, these states get more and more number squeezed as the potential depth V_A approaches the critical value for the Mott insulator phase transition (see section 5.3).

In a second step we rapidly increase the lattice potential depth to a value V_B of up to 35 E_r, where the tunnelling between adjacent potential wells become negligible (Figure 5.4). Thereby we project the superfluid ground state with coherent states at each lattice site into

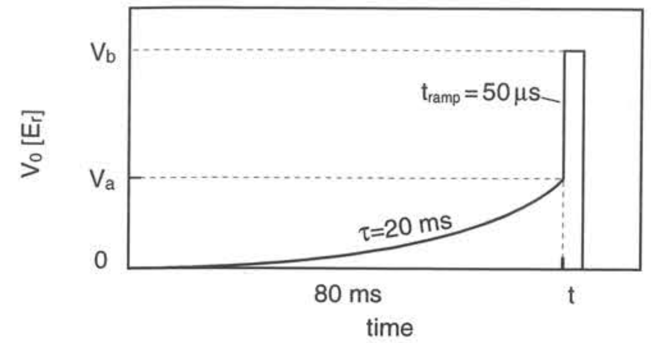

Figure 5.4: Potential depth of the optical lattice versus time. First, the potential is slowly ramped to a potential depth V_a, where the system is entirely superfluid. Then the potential depth is rapidly increased to V_b, where the potential wells are isolated from each other. By this procedure the superfluid state is projected into individual potential wells with coherent states in each well. The succeeding time evolution inside each well is well described by the Hamiltonian discussed in the previous chapter. Finally, after a variable hold time t, all trapping potentials are switched off and a multiple matter wave interference pattern is observed by time of flight absorption imaging.

isolated potential wells. The potential depth is increased from V_A to V_B in 50 μs. This timescale is chosen such that it is fast compared to the tunnelling time. Therefore the atom number statistics is preserved during the ramp. The ramp time is also fast compared to the collapse and revival time. On the other hand, the timescale is chosen slow enough to ensure that all atoms remain in the vibrational ground state of each well. We can check this condition by measuring the band population after ramping up the the lattice potential (chapter 3.3.6).

5.2.2 Time evolution of the multiple matter wave interference pattern

After preparing coherent states (which might be number squeezed) in isolated potential wells and isolating the potential wells from each other, we want to study the time evolution due to the interaction. Therefore we hold the atoms for different times t in the deep lattice. After this hold time, all trapping potentials are suddenly turned off and we observe the multiple matter wave interference pattern after a time of flight period of 16 ms. The interference pattern reveals the long range phase coherence and only forms when the many particle state can be described by a macroscopic matter wave field with a well defined macroscopic phase on each lattice site.

A sequence of such time of flight images for different hold times t can be seen in figure 5.5. On the first image, a clear interference pattern with a good visibility is observed directly after rapidly increasing the potential depth from $V_A = 8\,E_r$ to a $V_B = 22\,E_r$, where the ground state would be a Mott insulator state showing no interference pattern. The interference pattern on this image demonstrate that we really project the states, which are described by a coherent matter wave field, into the isolated potential wells with a constant macroscopic

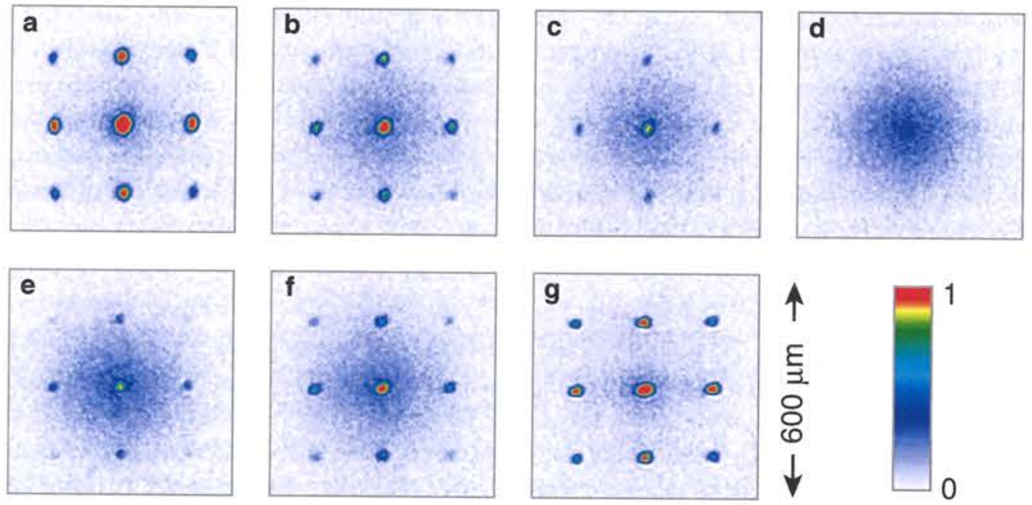

Figure 5.5: Dynamical evolution of the multiple matter wave interference pattern observed after rapidly increasing the tunnelling barrier. After a hold time t, all trapping potentials are shut off and absorption images are taken. The hold times are (a), 0 μs; (b), 100 μs;(c), 150 μs;(d), 250 μs;(e), 350 μs;(f), 400 μs;(g), 550 μs; The collapse and revival of the interference pattern is caused by a collapse and revival of the macroscopic matter wave field in each potential well.

phase across the lattice. On the next images, the interference dims out and a non coherent background gains more and more strength, until for a hold time of 250 μs the interference pattern has totaly collapsed. After longer hold times, the interference pattern reappears and has nearly perfectly revived after a hold time of 550 μs. The collapse and revival of the interference pattern is directly related to the collapses and revivals of the individual coherent matter wave fields in each potential well.

It is interesting to compare the outcome of a collapse and revival experiment in a double well system to the outcome in our multiple well system. In a double well system, an interference pattern with a perfect visibility would be observed in each single realization of the experiment for all times. However, when the matter wave fields have collapsed in both wells, the interference patterns would change randomly for each realization. At the time, where the Schrödinger cat state has formed, the pattern would alternate between two possible interference pattern corresponding to identical and opposite phases on both lattice sites. Averaging over many realizations would then yield the ensemble average value $\psi = 0$ that indicates the randomness of the interference pattern associated with the collapse of the matter wave fields. For the multiple well set up used in our experiment, however, the interference pattern in a single realization of the experiment can only be observed if the matter wave fields in each potential well have constant relative phase to each other, which requires that $\psi \neq 0$. The matter wave field ψ is therefore directly connected to the visibility of the multiple matter wave interference pattern in a single realization of the experiment.

The visibility of the interference pattern can be measured by comparing the number of atoms in the interference peaks N_{coh} to the total atom number N_{tot}. The numbers are extracted from the multiple matter wave interference pattern. First, a two-dimensional Gaussian function is fitted to the incoherent background, excluding 130 μm × 130 μm squares around the interference peaks. Then, the number of atoms in these squares is counted by a pixel sum, from which the number of atoms in the incoherent Gaussian background in these fields is subtracted to yield N_{coh}.

In order to compare the visibility of the interference pattern N_{coh}/N_{tot} with the matter wave field in each potential well $\psi_i(t) = \langle \Phi_i(t)|\hat{a}_i^\dagger|\Phi_i(t)\rangle$, we sum the coherent fraction in each well over all M lattice sites:

$$\frac{N_{coh}}{N_{tot}} = \frac{\sum_{i=1}^{M} |\psi_i(t)|^2}{N_{tot}} \tag{5.13}$$

The dynamical evolution of the matter wave field $\psi_i(t)$ depends on the mean atom number $\bar{n}$, the ratio of $(U/J)_A$ at the initial potential depth V_A, which can cause a number squeezing, and on the interaction strength U_B at the final potential depth V_B. For a inhomogeneous system like in our experiment, $\bar{n}$ varies over the sample, and equation 5.13 corresponds to an average over the temporal evolution of the matter wave field for different mean atom numbers $\bar{n}$. By introducing the classical probability distribution $W(\bar{n})$, which describes the probability of finding a lattice site with $\bar{n}$ atoms, the sum in eq. 5.13 can be converted to an integral. The visibility is then given by

$$\frac{N_{coh}}{N_{tot}} = \frac{\int W(\bar{n})\, |\psi_i(t, \bar{n}, (U/J)_A, U_B)|^2\, d\bar{n}}{N_{tot}} \tag{5.14}$$

In chapter 5.3, $\psi_i(t, \bar{n}, (U/J)_A, U_B)$ is calculated explicitly using a Gutzwiller ansatz.

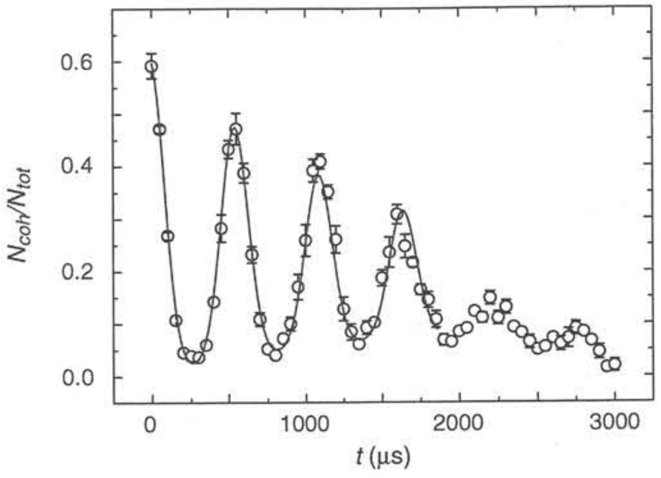

Figure 5.6: Visibility N_{coh}/N_{tot} of the multiple matter wave interference pattern versus time. This collapse and revival of the interference pattern is directly related to the collapses and revivals of the the individual coherent matter wave fields in each potential well.

Figure 5.6 shows the experimentally determined time evolution of the visibility N_{coh}/N_{tot} after rapidly increasing the potential depth from $V_A = 8\,E_r$ to a $V_B = 22\,E_r$. Up to five revivals are visible. The solid line is a fit of a model given by equation 5.8, where we assume that the dynamics of the inhomogeneous system described by equation 5.14 is similar to a homogenous system with a average atom number $\bar{n}$. The fit includes an exponential damping and a linear background.

The damping is mainly due to an inhomogeneous time evolution of the macroscopic phase across the lattice. By rapidly jumping to the potential depth V_B we abruptly change the external confinement of the atoms given by the Gaussian beam shape of the lattice beams (chapter 3.1.5). To first order, this inhomogeneous change of the potential energy is compensated by the change in the interaction matrix element U. However, we still obtain a parabolic profile of the chemical potential over the cloud of atoms in the optical lattice, which leads to a broadening of the interference peaks over time. This effect can be clearly identified in Figure 5.7, where the interference peaks show a ring structure already for the second revival. When the interference peaks become broader than the rectangular areas, in which the coherent atoms are counted, we cannot determine N_{coh} correctly anymore.

Besides this effect the slight variation of the potential depth over the lattice can lead to a difference in U, which we estimate to be smaller then $\sim 3\%$. This leads to an asynchronous

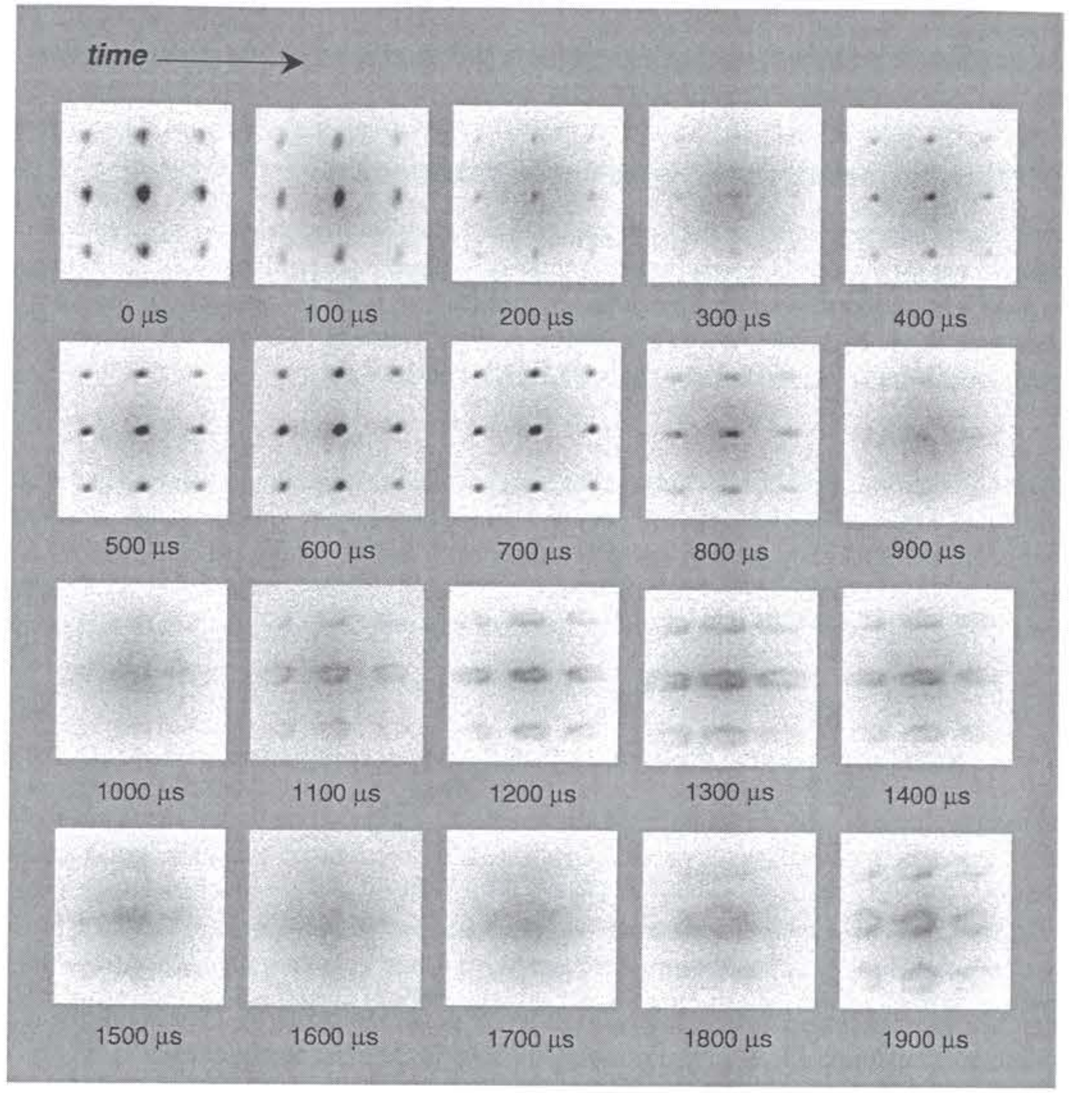

Figure 5.7: Multiple matter wave interference pattern after different evolution times. The interference peaks in the second and third revival show a ring like structure. This structure arises due to an inhomogeneous evolution of the macroscopic phase. After rapidly increasing the potential depth we obtain a parabolic profile of the chemical potential across the lattice, which leads to a broadening of the interference peaks in a ring shape. When the peaks become broader than the rectangular area in which they are counted, the visibility cannot be determined anymore. This is the main damping effect in the time evolution of the visibility (figure 5.6)

revival over the lattice, which also contributes to the damping of the visibility. The finite initial visibility of $\sim 60\%$ can be attributed to atoms in higher order momentum peaks ($\sim 10\%$ of the total atom number), s-wave scattering spheres (chapter 3.3.3), a quantum depletion of the condensate for the initial potential depth from $V_A = 8\, E_r$ and a finite condensate fraction due to the finite temperature of the system.

5.2.3 Precision measurement of the onsite interaction

Measuring the time evolution of the collapse and revival opens the intriguing possibility to precisely measure the onsite interaction energy U as a frequency. The revival of the matter wave field is expected to occur at times that are multiples of h/U, independent of the atom number statistics in each well. Therefore, besides a slight variation of U over the lattice, the interference pattern revives at the same time in each potential well.

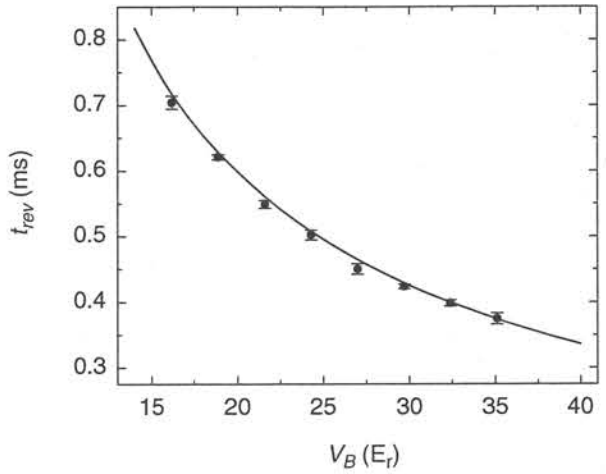

Figure 5.8: Revival time t_r after jumping to different potential depths V_B. The solid line is an ab initio calculation of h/U. By measuring the revival time the onsite interaction U can be measured as a frequency with high precision.

Figure 5.8 shows a plot of the revival time $t_{rev} = h/U$ versus the final potential depth V_B. As U depends on the potential depth, we observe an increased revival time for deeper lattice potentials. The solid line is an ab initio calculation of h/U with no adjustable parameters. It is based on a band structure calculation. The error bars show the statistical uncertainties. In addition to this the experimental data points have a systematic uncertainty of 15% in the values for the potential depth.

5.3 Number squeezing of a BEC in an optical lattice

Up to now, we assumed that the many-body state in each potential well can be described by a coherent state in second quantization with a Poissonian atom number statistics. However, at the initial potential depth V_a, where a superfluid state is prepared before jumping into the deep lattice, the finite onsite atom-atom interaction U causes an atom number squeezing of the coherent states [3]. This number squeezing results in a sub Poissonian atom number statistics.

The collapse and revival also happens for number squeezed coherent states. The revival time t_{rev} is identical, however, the collapse time t_c is changed since it depends on the variance of the atom number statistics σ_n^2, such that

$$t_c = \frac{t_{rev}}{2\pi\,\sigma_n}. \tag{5.15}$$

Therefore we can directly measure the variance of the number statistics at different potential depths V_a by measuring the corresponding collapse times. The measurement in chapter 5.3.2 shows that the atom number distribution becomes pronounced sub Poissonian even before number states are formed in the Mott insulator regime. The measurement is in good agreement with the following Gutzwiller calculation revealing the number statistics for small U/J.

5.3.1 Gutzwiller calculation of sub Poissonian atom number statistics

When the tunnelling matrix element J between neighboring lattice sites is much larger than the onsite repulsion between the atoms U, the atoms are in the superfluid ground state with long range phase coherence across the lattice. For a vanishing ratio of $U/J \simeq 0$ the many particle states on each lattice sites corresponds to coherent states in second quantization, with a Poissonian atom number statistics. For a finite ratio of U/J, however, the interaction between the atoms lead to number squeezed states with a sub Poissonian atom number statistics.

In a Gutzwiller calculation [109, 138, 103, 5] the many particle state $|\Psi\rangle$ can be approximated by a product state of many particle states $|\Phi_i\rangle$ which are localized to the ith lattice site

$$|\Psi\rangle \approx \prod_i |\Phi_i\rangle. \tag{5.16}$$

These localized states can be expressed as a superposition of different number states on a lattice site

$$|\Phi_i\rangle = \sum_{n=0}^{\infty} f_n^{(i)} |n\rangle, \tag{5.17}$$

where $f_n^{(i)}$ denotes the complex coefficients for the state with n atoms on the ith lattice site and is normalized such that $\sum_{n=0}^{\infty} |f_n^{(i)}|^2 = 1$. Therefore $|f_n^{(i)}|^2$ is the probability to find n atoms on the ith site.

The ground state for a system with given parameters can be found by varying the coefficients $f_n^{(i)}$ and minimizing the total energy. The atoms in the lattice are described by a Bose Hubbard Hamiltonian (see also Chapter 4.1), which consists of three parts: The kinetic energy term, the interaction energy term and a third term describing inhomogeneities and introducing a chemical potential μ

$$\begin{aligned} H_{BH} &= H_{kin} + H_{int} + H_\mu \\ &= -J \sum_{<i,j>} \hat{a}_i^\dagger \hat{a}_j + \sum_i \frac{1}{2} U\, \hat{n}_i(\hat{n}_i - 1) + \sum_i (\epsilon_i - \mu)\, \hat{n}_i. \end{aligned} \tag{5.18}$$

The summation in the first term is carried out over next neighbors. The expectation values for the kinetic energy term and the inhomogeneity / chemical potential term on the ith lattice site can be easily expressed by the coefficients $f_n^{(i)}$:

$$\langle \Phi_i | H_{int} | \Phi_i \rangle = \frac{U}{2} \langle \Phi_i | \hat{n}_i(\hat{n}_i - 1) | \Phi_i \rangle = \frac{U}{2} \sum_n |f_n^{(i)}|^2\, n(n-1) \tag{5.19}$$

$$\langle \Phi_i | H_\mu | \Phi_i \rangle = (\epsilon_i - \mu) \langle \Phi_i | \hat{n}_i | \Phi_i \rangle = (\epsilon_i - \mu) \sum_n |f_n^{(i)}|^2\, n \tag{5.20}$$

The expectation value of the kinetic energy term can be expressed by the expectation value of the field operator $\langle \hat{a}_i \rangle$ since the field operators of different lattice sites commute:

$$\langle \Psi | H_{kin} | \Psi \rangle = -J \sum_{<i,j>} \langle \Phi_i | \langle \Phi_j | \hat{a}_i^\dagger \hat{a}_j | \Phi_j \rangle | \Phi_i \rangle = -J \sum_{<i,j>} \langle \hat{a}_i \rangle^* \langle \hat{a}_j \rangle \tag{5.21}$$

It is interesting to note that for coherent states $|\Phi_i\rangle = |\alpha_i\rangle$ with $\hat{a}_i|\alpha_i\rangle = \alpha_i|\alpha_i\rangle$, where $\alpha_i = \sqrt{\bar{n}_i} \cdot \exp i\varphi_i$ and φ_i is the macroscopic phase on the ith site, the product of the expectation values of the field operators reduces to

$$Re(\langle \hat{a}_i \rangle^* \langle \hat{a}_j \rangle) = Re(\alpha_i^* \alpha_j) = \sqrt{\bar{n}_i \bar{n}_j} \cos(\varphi_j - \varphi_i), \tag{5.22}$$

which is analog to the phase term in the well known Josephson tunnelling energy between lattice sites. In the Gutzwiller calculation, on the other hand, the expectation values are expressed more generally by the coefficients $f_n^{(i)}$

$$\langle \hat{a}_i \rangle = \sum_{n,m} \langle \Phi_i | n \rangle \langle n | \hat{a}_i | m \rangle \langle m | \Phi_i \rangle = \sum_n f_n^{(i)*} f_{n+1}^{(i)} \sqrt{n+1} \tag{5.23}$$

$$\langle \hat{a}_i^\dagger \rangle = \sum_{n,m} \langle \Phi_i | n \rangle \langle n | \hat{a}_i^\dagger | m \rangle \langle m | \Phi_i \rangle = \sum_n f_{n+1}^{(i)*} f_n^{(i)} \sqrt{n+1} = \langle \hat{a}_i \rangle^* \tag{5.24}$$

We now want to find the ground state of a homogenous system for a given ratio U/J. We assume that this ground state is a product of identical states on each of the M lattice sites. Therefore we can set

$$|\Phi_i\rangle = |\Phi\rangle, \quad |\Psi\rangle = \prod_M |\Phi\rangle, \quad \langle \hat{a}_i \rangle = \langle \hat{a} \rangle \quad \text{and} \quad f_n^{(i)} = f_n. \tag{5.25}$$

The expectation value of the energy per lattice site is then given by

$$\langle H \rangle = \langle E_{kin} \rangle + \langle E_{int} \rangle + \langle E_\mu \rangle \qquad \text{with} \tag{5.26}$$

$$\langle E_{kin} \rangle = \frac{\langle \Psi | H_{kin} | \Psi \rangle}{M} = -Jz|\langle a \rangle|^2 = -Jz \Big| \sum_n f_n{}^* f_{n+1} \sqrt{n+1} \Big|^2 \tag{5.27}$$

$$\langle E_{int} \rangle = \langle \Phi | H_{int} | \Phi \rangle = \frac{U}{2} \sum_n |f_n|^2\, n(n-1) \tag{5.28}$$

$$\langle E_\mu \rangle = \langle \Phi | H_\mu | \Phi \rangle = \mu \langle n \rangle = \mu \sum_n |f_n|^2 n, \tag{5.29}$$

where z denotes the number of nearest neighbors ($z = 6$ for a simple cubic 3D lattice).

The ground state can be determined by finding a set of $\{f_n\}$ which minimizes $\langle H \rangle$. This can be either done for a given chemical potential μ, or for a given mean atom number $\langle n \rangle = \sum_n |f_n|^2 n$. The set of the coefficient $\{f_n\}$ can be truncated for atom numbers much larger than the mean atom number. We calculated these coefficients numerically for different ratios of U/J.

A more analytical study can be performed by introducing a squeezing parameter g [109], which becomes $g = 1$ for a coherent state and approaches zero as the state gets more and more squeezed and finally becomes a number state. The numerically determined coefficients $f_n^{(num)}$ are well approximated by the coefficients defined through

$$\tilde{f}_n = g^{\frac{n(n-1)}{2}} \frac{\lambda^{n/2}}{\sqrt{n}}. \tag{5.30}$$

These coefficients need to be normalized such that $f_n = \tilde{f}_n / \sum_n |\tilde{f}_n|^2$. The parameter $\lambda(g, \bar{n})$ depends on g and the mean atom number $\bar{n}$ and was determined numerically. The expectation value of the Hamiltonian can be expressed by $\langle H \rangle = \bar{H}(g, \bar{n})$ (or the chemical potential μ instead of $\bar{n}$). The value for $g = g(\bar{n}, U/J)$ (or $g = g(\mu, U/J)$, respectively) which minimizes $\langle H \rangle$ can then be found numerically.

An analytical result for the weakly interacting regime, where $U/J \ll (U/J)_c$, is given by [109]

$$g \approx \frac{1}{1 + \frac{U}{2zJ}}. \tag{5.31}$$

Here, z is the number of nearest neighbors.

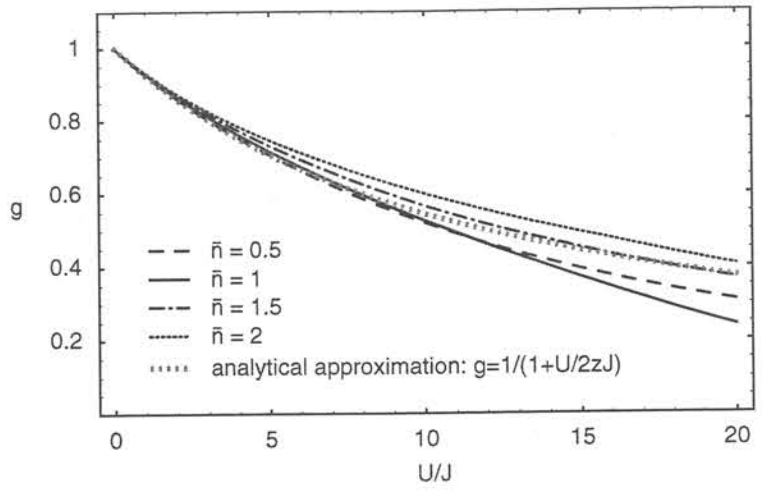

Figure 5.9: Squeezing parameter g, plotted versus the ratio between the onsite interaction and the tunnelling U/J for different mean atom numbers $\bar{n}$. The numerical calculation is compared to the analytical approximation given in [109]. For vanishing onsite interaction U the squeezing parameter is equal to $g = 1$, corresponding to coherent states with a Poissonian atom number statistics. For $1 > g > 0$ the number statistics gets sub Poissonian. The graph shows that a pronounced number squeezing is expected even before the phase transition to a Mott insulator is reached at about $U/J \simeq 35$,

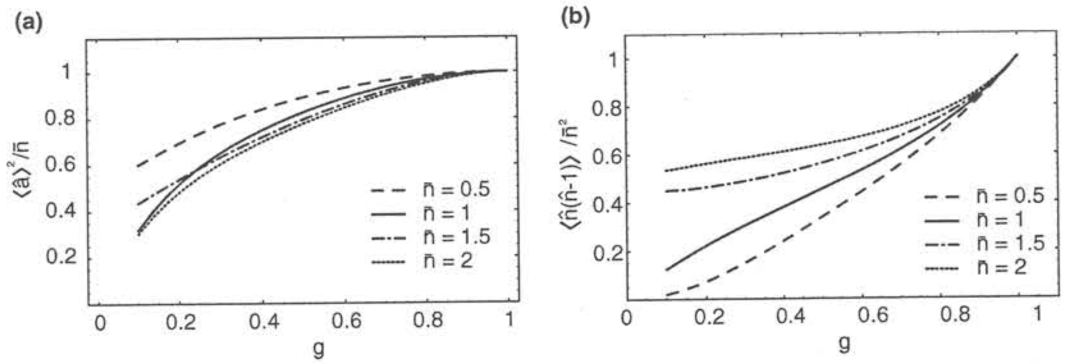

Figure 5.10: (a) Expectation value of the field operator, plotted as $|\langle\hat{a}\rangle|^2/\bar{n}$ versus g for different $\bar{n}$. The plotted value corresponds to the fraction of atoms which can be described by the macroscopic wave function and is therefore equal to the expected visibility of a multiple matter wave interference pattern. (b) Reduction of the strength of the onsite interaction, achieved by number squeezing. $\langle\hat{n}(\hat{n}-1)\rangle/\bar{n}^2$ is plotted versus g for different $\bar{n}$.

(a) poissonian number distribution for g = 1

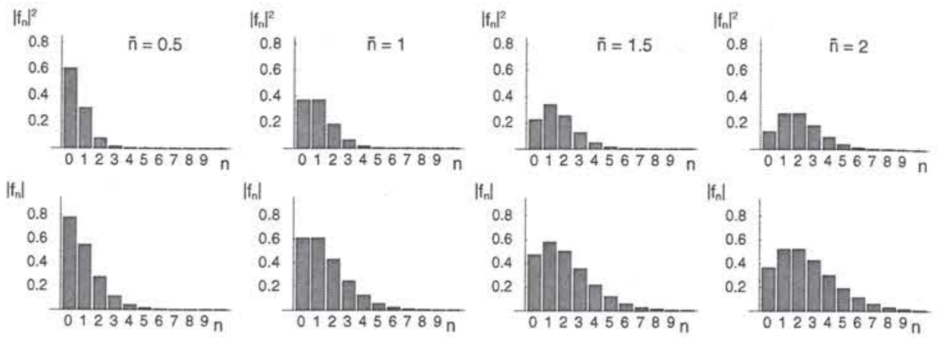

(b) sub poissonian number distribution for g = 0.6

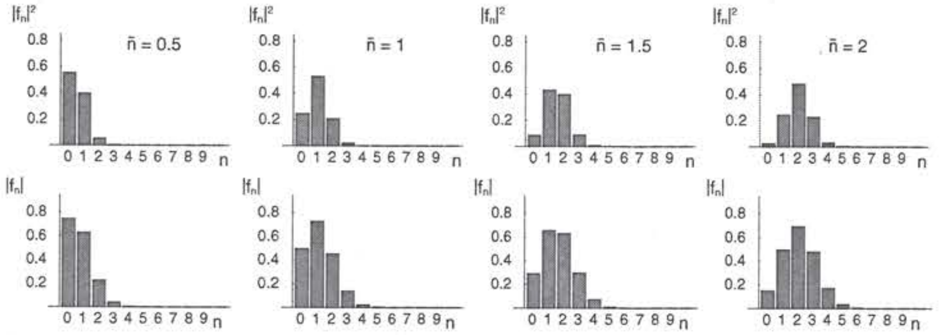

(c) sub poissonian number distribution for g = 0.2

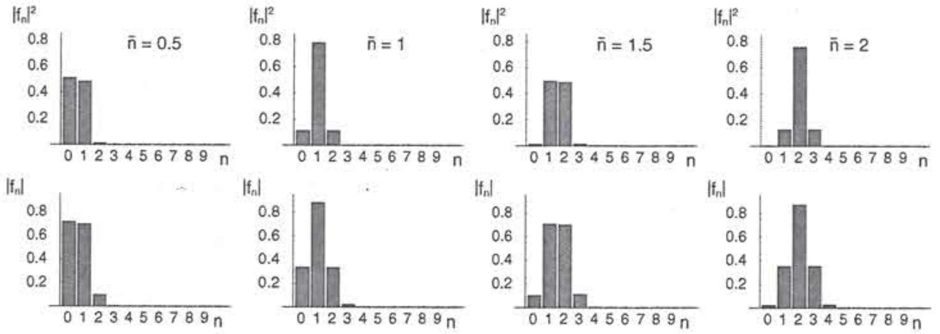

Figure 5.11: Atom number statistics for number squeezed states. The probability $|f_n|^2$ and amplitude $|f_n|$ to find n atoms on a site is plotted as a histogram for different mean atom numbers $\bar{n}$ and for squeezing parameters of (a) $g = 1$, (b) $g = 0.6$ and (c) $g = 0.2$ respectively.

The results of the numerical calculations are presented in figures 5.9-5.11. In figure 5.9, the squeezing parameter g is plotted versus U/J for different $\bar{n}$ and compared to the analytical solution equation . Figure 5.10a demonstrates the effect of the number squeezing on the expectation value of the field operator. The plotted ratio $|\langle\hat{a}\rangle|^2/\bar{n}$ corresponds to the reduction in the visibility of the interference pattern. In Figure 5.10b the reduction of the expectation value for the onsite interaction energy due to the squeezing is illustrated. It is characterized by $\langle\hat{n}(\hat{n}-1)\rangle/\bar{n}^2$, which is plotted versus g. Figure 5.11 shows the atom number statistics as a bar chart of the probabilities $|f_n|^2$ and the coefficients $|f_n|$ for different mean atom numbers and squeezing parameters g. It can be seen that the atom number statistics is markedly changed even before the Mott insulator regime is entered.

5.3.2 Measurement of sub Poissonian atom number statistics

In order to measure the atom number statistics in the superfluid regime we carry out the collapse and revival experiment for different initial potential depths V_a. After the potential wells are separated from each other, the number squeezed states undergo qualitatively the same dynamics as the coherent states with a collapse and revival of the macroscopic matter wave field. The revival time t_{rev} is identical. However, two parameters change:

- The collapse time depends on the the atom number statistics as $t_c = t_{rev}/(2\pi\,\sigma_n)$ and is therefore changed when number squeezing occurs.
- The initial expectation value of the field operator $|\psi(t)|^2 = |\langle\hat{a}\rangle|^2$ is smaller than $\bar{n}$ (see figure 5.10). Therefore, not all atoms are described by the macroscopic matter wave field. Instead the quantum depletion is finite. This results in a reduced visibility of the initial interference pattern equal to $|\langle\hat{a}\rangle|^2/\bar{n}$.

By measuring the collapse time t_c we are able to determine the number squeezing at the initial potential depth V_a.

Time evolution

After separating the potential wells, the atoms inside each well are described by the Hamiltonian in eq. 5.1 with the time evolution

$$|\Phi(t)\rangle = \sum_n f_n \cdot e^{i\,U\,n(n-1)\,t/2\hbar}\,|n\rangle. \tag{5.32}$$

The phase of each number state, which is the eigenstate of the Hamiltonian, evolves according to its eigenenergy.

In Figure 5.12, the collapse and revival of the matter wave field is plotted for different squeezing parameters g. The collapse time strongly depends on the squeezing strength. Figure 5.12 shows the Q-function (see chapter 5.1.4) for various g and t. These graphs demonstrate that initially, for $t=0$, the phase uncertainty increases with the squeezing. At $t = 0.5\,h/U$ the number squeezed states also form Schrödinger cat states.

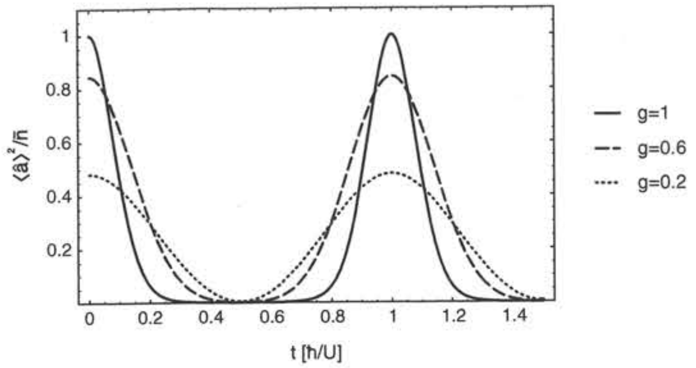

Figure 5.12: Collapse and revival of the macroscopic matter wave field for squeezed coherent states on each lattice site. The expectation value of the field operator is plotted as $|\langle\hat{a}\rangle|^2/\bar{n}$ versus time for squeezing parameters $g=1$, $g=0.6$ and $g=0.2$ and a mean atom number $\bar{n}=2$. The collapse time strongly depends on the squeezing parameter g.

Measurement

We measured the visibility of the multiple matter wave pattern versus time for potential depths V_a between $4\,E_r$ and $13\,E_r$ and $V_b = 20\,E_r$. In order to extract the collapse and revival time we fit the data with a model given by a periodic sum of Gaussian functions:

$$f_{fit} = \sum_n \exp\frac{-(t - n\,t_{rev})^2}{t_c^2} \tag{5.33}$$

Here t_c is measured as the $1/e$ half width of the Gaussian function, and t_{rev} corresponds to the spacing of the Gaussian function. In addition we allow an offset, scaling and decay. First, we determine the revival time by fitting the distance between the first two revivals. Then we determine the collapse time by fitting the data in the region between about $0.2\,t_r$ and $1.4\,t_r$.

Figure 5.14a shows the data of the first revival for an initial potential depth of $V_a = 4\,E_r$(filled circles) and $V_a = 11\,E_r$(open circles) respectively. The error bars denote statistical errors. The data of both curves is scaled to the same height, in order to compare the widths of the collapse times. The interference contrast of the curve $V_a = 11\,E_r$is 20% smaller than that for $V_a = 4\,E_r$. The solid and dashed lines are fits of the above model to the data.

This data clearly shows a significant increase in the collapse time when jumping from greater potential depths. For our setup, the average atom number per lattice site $\bar{n}$ is almost constant, since to first order it doesn't depend on the potential depth V_a. Therefore, the change of the collapse time is due to number squeezing. The data indicates, that the atom number statistics has indeed become sub Poissonian.

It is interesting to compare the measured collapse time to an ab initio calculation for differ-

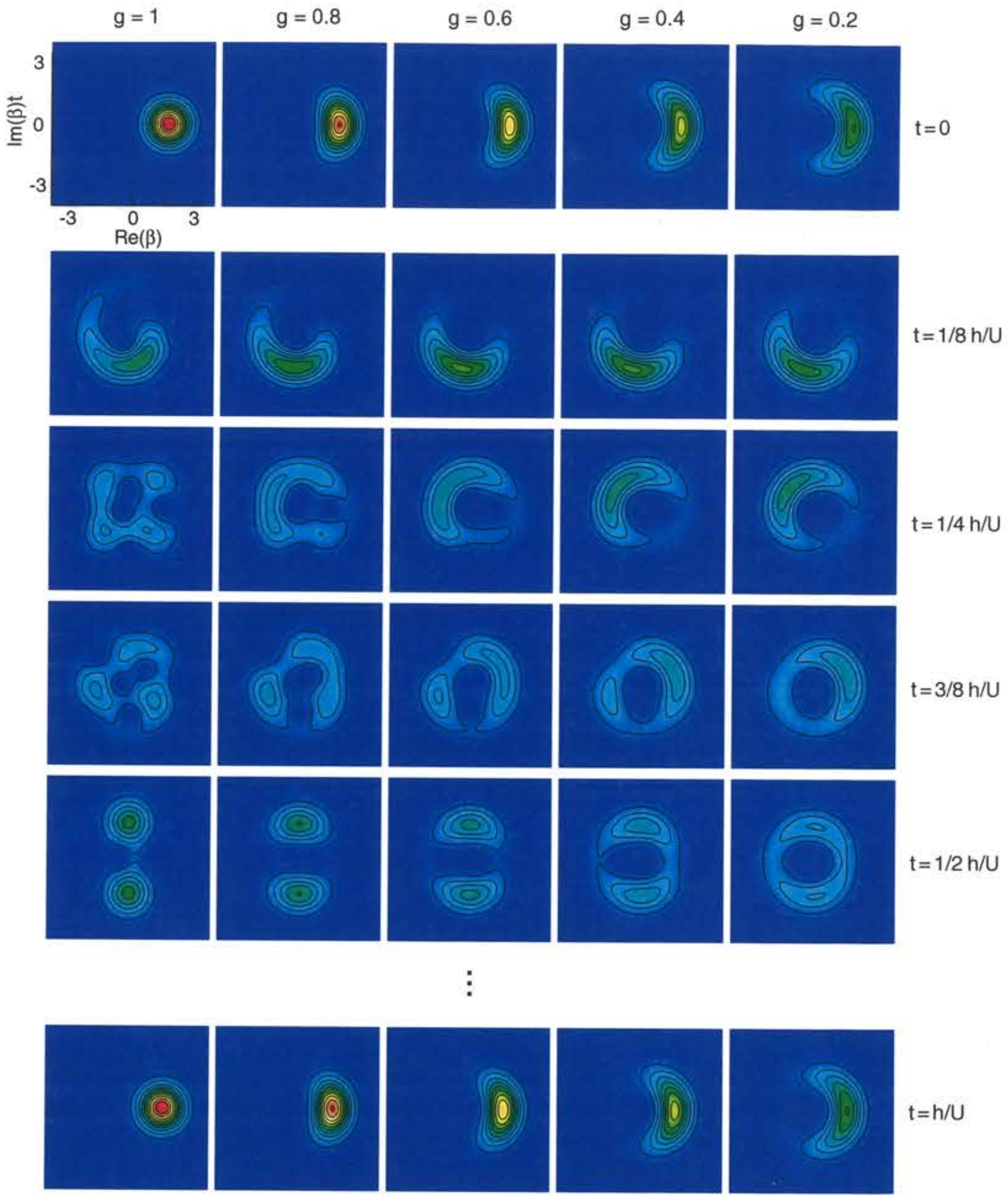

Figure 5.13: The graph shows the overlap between the dynamically evolving state $|\Phi(t)\rangle$ and an arbitrary coherent state$|\beta\rangle$ for various squeezing parameters g and times t, and a mean atom number of $\bar{n}=3$. For $t=0$ the phase uncertainty for the squeezed states is nicely visible. At $t=0.5\,h/U$ Schrödinger cat states are formed, even in the presence of number squeezing.

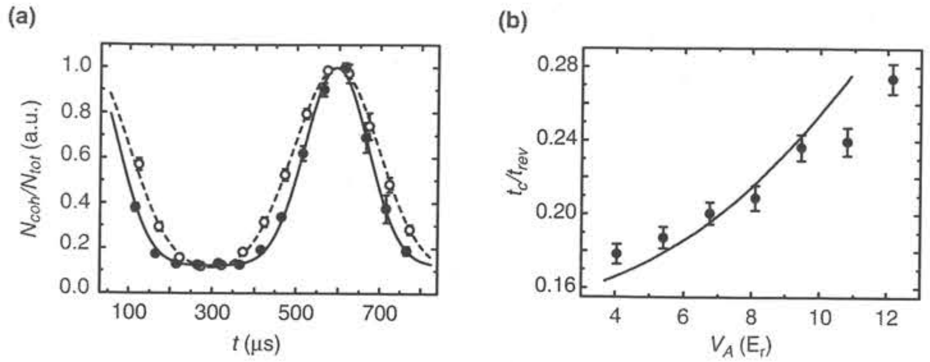

Figure 5.14: Increase of the collapse time for number squeezed states. (a) First revival for an initial potential depth of $V_a = 4\,E_r$(filled circles) and $V_a = 11\,E_r$(open circles). The interference contrast N_{coh}/N_{tot} is plotted versus time in arbitrary units. For the deeper initial potential depth the collapse time is significantly prolonged due to number squeezing for finite U/J. (b) Collapse time t_c relative to the revival time t_{rev}. The measured data is in reasonable agreement with a ab initio theoretical calculation, shown as a solid line.

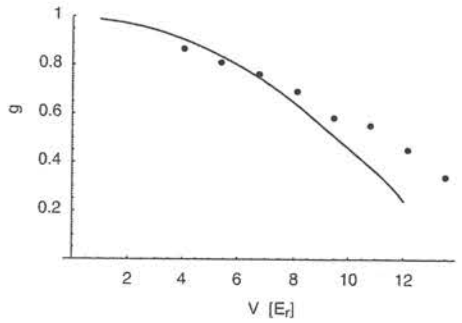

Figure 5.15: Fitted squeezing factor g together with an ab initio calculation of g. Taking experimental uncertainties into account, the data is in reasonable agreement with the theoretical prediction and demonstrates strong number squeezing of the superfluid state in the lattice.

ent potential depths V_a. In order to determine the expected collapse time, we first calculate the number squeezed states for various potential depths and mean atom numbers $\bar{n}$ through the Gutzwiller calculation described above. Then we determine the expected time evolution of the interference contrast for our inhomogeneous system through equation 5.14. We assume a Thomas Fermi profile (eq. 3.47) with a calculated maximum mean atom number in the trap center of $\bar{n} = 2$. Finally, we fit this calculated curve with the same model (equation 5.33) in order to determine an effective collapse time t_c. The curve is well matched by the fit with an RMS error in the order of one percent. Figure 5.14b shows a comparison of the calculated collapse time and the measured data. Considering the systematic experimental uncertainties in the determination of the potential depth V_a of $\approx 15\%$ and an uncertainty in the total atom number of $\approx 20\%$, we find a reasonable agreement between both the experimental data and the theoretical prediction. Close to the phase transition to the Mott insulator the measured number squeezing is slightly less than expected from the Gutzwiller calculation. This might be due to the fact that the Gutzwiller approach underestimates the number fluctuations close to the transition point due to residual short range correlations, which are not included in the mean field approach [31, 94, 110] (see also chapter 4.1.5).

By analyzing the data in a slightly different way we determine the squeezing factor g for different potential depths V_a in a more direct way. This is possible by calculating the expected collapse and revival of the interference contrast for the inhomogeneous system through equation 5.14 depending on g. For this calculation we assume that g is independent on $\bar{n}$, which is reasonable for $\bar{n}$ larger than about 0.5. Furthermore we assume a maximum mean atom number in the trap center which was determined as $\bar{n}_{max} = 2$ with an accuracy of about 20%. Figure 5.15 shows the fitted squeezing factors g for different potential depths together with ab initio calculation. The data and the theoretical prediction shows a reasonable agreement considering systematic uncertainties in the determination of the potential depth V_a of $\approx 15\%$.

6 Outlook

Bose-Einstein condensates trapped in three-dimensional optical lattice potentials allow to enter a new regime in the many body physics of ultracold atomic gases. The realization of a Mott insulator and the observation of a collapse and revival of the macroscopic matter wave field described in this work demonstrates some of the new possibilities offered by this novel quantum system. In the following I want to summarize various ideas for future experiments that address fundamental questions of modern solid state physics, atomic physics, quantum optics and quantum information.

Ultracold atoms in optical lattice potentials represent a rather perfect realization of the Bose-Hubbard model with a high degree of control. Parameters like the ratio between the onsite interaction and tunnel coupling or the filling factor can be widely adjusted, and observables like long range phase coherence or number statistics can be measured. Apart from measurements of ground state properties, this control also allows quantitative measurements of the dynamics in the system, which have not been possible with other realizations of the Bose-Hubbard model so far. For example, the dynamics and time scale of the quantum phase transition from a superfluid to a Mott insulator is still an open question. Gutzwiller calculations [6] and density-matrix renormalization group calculations [139] have recently been performed and suggest a surprisingly fast dynamics. The calculations are consistent with the present experimental observations discussed in this work. However, there remain a number of open question concerning the dynamical behavior and further experiments could deliver valuable insight in the dynamics. Another example is the response of the many body state when a large potential gradient is applied. This process has recently been investigated theoretically [140, 141]. The results allows a better understanding of the measured resonant perturbation probability, and based on the calculations refined measurement techniques have been proposed. For future experiments the parameter regime could be extended by tuning the scattering length through Feshbach resonances [1, 2, 142, 143]. Furthermore the application of random potentials could be introduced to realize a Bose glass phase [4, 108].

Hamiltonians other than the pure Bose-Hubbard hamiltonian could be realized and studied with an ultracold gas in three-dimensional optical lattice potentials. For example by using a multi component gas and interspecies Feshbach resonances, an intriguing system could be created. Furthermore it should be possible to extend the type of interactions to effective next neighbor interaction [144, 145], dipolar interactions [146], or spin interaction due to spin dependent tunnelling [147].

By loading ultracold fermionic atoms into a lattice potential, the original fermionic version of the Hubbard model could be realized experimentally [148]. The fermionic Hubbard Hamiltonian still contains many open questions on the theoretical side, and therefore it is especially attractive to study this Hamiltonian experimentally. In the attractive case it describes the BCS- to Bose-crossover for Cooper-pairing and in the repulsive case antiferromagnetic superconducting phases appear. The combination of fermionic and bosonic atoms in the same lattice potential would further extend the class of Hamiltonians which can be realized and investigated with ultracold atoms.

From the perspective of atomic and molecular physics a Mott-insulating state with precisely two atoms per site is an ideal starting point for the formation of molecular condensates [6]. Molecules could be created in a very controlled way on each lattice site by photo-association. Melting the resulting Mott insulator state of molecules would then form a molecular condensate.

In a two-dimensional optical lattice potential [91] an array of tightly confining potential tubes can be created. Inside these tubes a one-dimensional quantum gas can be studied. Striking effects in such a system are the occurrence of a Tonks gas of impenetrable bosons [149, 150, 151, 152] and the occurrence of a commensurate-incommensurate transition, where atoms are pinned to a Mott insulating state for an arbitrarily weak lattice potential [153, 31]. When the interaction energy dominates the kinetic energy, the bosonic atoms effectively behave as non-interacting fermions and a strongly correlated 1D quantum gas is created. By using a Feshbach resonance the Tonks gas should be observable in a two-dimensional lattice. The Tonks gas would require a very low number of atoms inside each 1D potential tube. However, the detection of the gas would benefit from the several thousand copies of similar 1D systems in the array of potential tubes.

The creation of vortices inside a lattice potential well could allow the study of the integer and fractional quantum hall effect in an ultracold gas. It has been recently shown that the Hamiltonian of bosons in a rotating trapping potential is formally identical to the Hamiltonian of electrons in the quantum Hall effect [154, 155, 156]. The possibility of having many copies of a system with a low atom number could enable the observation of a highly correlated quantum liquid described by Laughlin states [157].

A new class of experiments is made possible when spin-dependent optical lattice potentials are used. It has been suggested that by spin-dependently shifting the lattice potential, atoms on different lattice sites can be brought into contact [158, 7]. Very recently we have been able to realize such a coherent transport of neutral atoms in spin-dependent optical lattice potentials [159]. After first preparing localized atomic wave functions in an optical lattice through a Mott insulating phase, we bring each atom in a superposition of two internal spin states by applying a microwave field. The state selective optical potentials are used to split the wave function of a single atom and transport the corresponding wave packets in two opposite directions. We have been able to demonstrate coherence between the wave packets of an atom delocalized over up to 7 lattice sites. By state selectively moving atoms one could induce interactions between almost any two atoms on different lattice sites in a controlled way. In a preliminary experiment we have already observed the effects of a collisional phase shift induced by bringing together atoms from neighboring lattice sites. On this basis it should be possible to realize quantum gates between different atoms [158, 128, 130, 160] or to create highly entangled cluster states [7, 128, 129] that could form the basis of a one way quantum computer [130]. Furthermore, spin waves [144] and quantum random walks could be studied [161]. A major difficulty of a quantum gate and quantum computation schemes mentioned above is that they require the addressability of individual lattice sites for readout. However, even without addressability a quantum computer could be realized in the sense of a quantum simulator which could be used to simulate fundamental complex condensed matter

physics Hamiltonians [145].

7 Appendix

7.1 Level scheme for ^{87}Rb

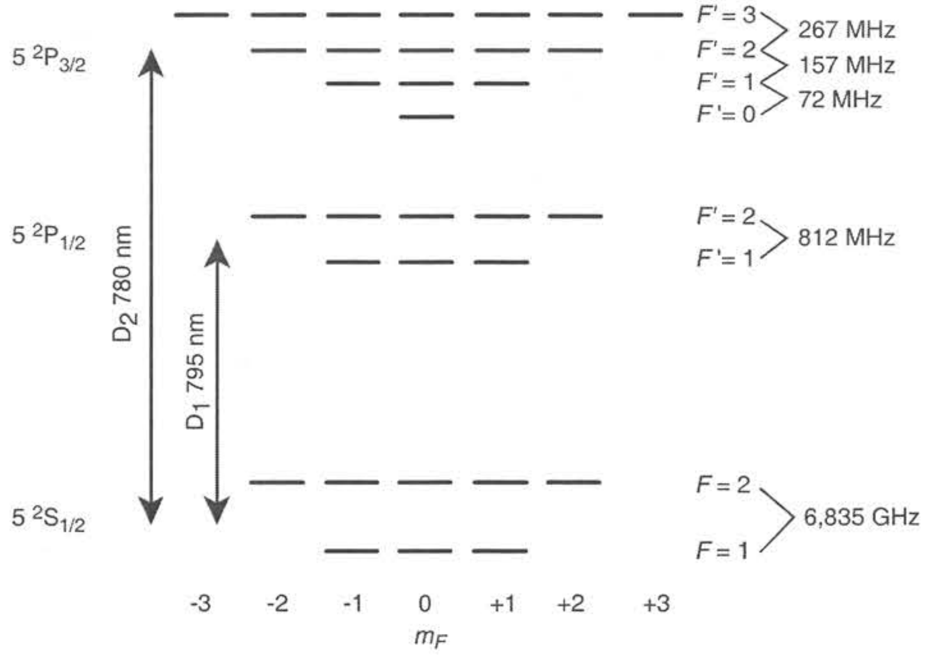

Figure 7.1: Level scheme of ^{87}Rb with nuclear spin $I = 3/2$.

7.2 Data on ^{87}Rb

Nuclear spin I	3/2
Mass	86,9902 u [162]
g-Faktor g_I	-0.0009951414
Vacuum wavelength D_1-transition λ_{D1}	794,979 nm [162]
Vacuum wavelength D_2-transition λ_{D2}	780,241 nm [162]
Line width D_1-transition Γ_{D1}	$2\pi \times 5,58$ MHz [162]
Line width D_2-transition Γ_{D2}	$2\pi \times 6,01$ MHz [162]
Life time $\|5^2P_{1/2}\rangle$	28,5 ns [162]
Life time $\|5^2P_{3/2}\rangle$	26,5 ns [162]
Saturation intensity	1,654 mW/cm^2 [162]
Ground state hyperfine splitting ν_{hfs}	6834682612.8 Hz [163]
Triplet scattering length a_T	$106 \pm 4\,a_0$ [164]
Singlet scattering length a_S	$90 \pm 1\,a_0$ [164]
$\|F=1, m_F=-1\rangle$scattering length a	$103 \pm 5\,a_0$ [25]
Three body loss rate K_3	$4,3 \times 10^{-29}$ cm^6/s [165]

Bibliography

[1] S.L. Cornish, N.R. Claussen, J.L. Roberts, E.A. Cornell, and C.E. Wieman. Stable ^{85}Rb Bose-Einstein condensates with widely tunable interactions. *Phys. Rev. Lett.*, 85(9):1795, August 2000.

[2] E. A. Donley, N. R. Claussen, S. L. Cornish, J. L. Roberts, E. A. Cornell, and C. E. Wieman. Dynamics of collapsing and exploding Bose-Einstein condensates. *Nature*, 412:295–299, 2001.

[3] C. Orzel, A. K. Tuchman, M. L. Fenselau, M. Yasuda, and M. A. Kasevich. Squeezed states in a Bose-Einstein condensate. *Science*, 291:2386–2389, 2001.

[4] M. P. A. Fisher, P. B. Weichman, G. Grinstein, and D. S. Fisher. Boson localization and the superfluid-insulator transition. *Phys. Rev. B*, 40:546–570, 1989.

[5] D. Jaksch, C. Bruder, J. I. Cirac, C. W. Gardiner, and P. Zoller. Cold bosonic atoms in optical lattices. *Phys. Rev. Lett.*, 81:3108–3111, 1998.

[6] D. Jaksch, V. Venturi, J. I. Cirac, C. J. Williams, and P. Zoller. Creation of a molecular condensate by dynamically melting a Mott insulator. *Phys. Rev. Lett.*, 89:040402, 2002.

[7] D. Jaksch, H. J. Briegel, J. I. Cirac, C. W. Gardiner, and P. Zoller. Entanglement of atoms via cold controlled collisions. *Phys. Rev. Lett.*, 82:1975–1978, 1999.

[8] M.H. Anderson, J.R. Ensher, M.R. Matthews, C.E. Wieman, and E.A. Cornell. Observation of Bose-Einstein condensation in a dilute atomic vapor. *Science*, 269(0):198, July 1995.

[9] K. B. Davis, M.-O. Mewes, M. A. Joffe, M. R. Andrews, and W. Ketterle. Evaporative cooling of sodium atoms. *Physical Review Letters*, 74:5202, 1995.

[10] A. Einstein. Quantentheorie des einatomigen idealen Gases. Zweite Abhandlung. *Sitzungber. Preuss. Akad. Wiss.*, 1925:3, January 1925.

[11] S. N. Bose. Plancks Gesetz und Lichtquantenhypothese. *Zeitschrift für Physik*, 26:178, 1924.

[12] F. London. On the Bose-Einstein condensation. *Phys. Rev.*, 54(0):947, December 1938.

[13] Fritz London. The λ-phenomenon of liquid helium and the Bose-Einstein degeneracy. *Nature*, 141(3571):643, April 1938.

[14] A.S. Parkins and D.F. Walls. The physics of trapped dilute-gas Bose-Einstein condensates. *Phys. Rep.*, 303(1):1, September 1998.

[15] F. Dalfovo, S. Giorgini, L. P. Pitaevskii, and S. Stringari. Theory of Bose-Einstein condensation in trapped gases. *Rev. Mod. Phys.*, 71(3):463, April 1999.

[16] A. J. Leggett. Bose-einstein condensation in the alkali gases: Some fundamental concepts. *Rev. Mod. Phys.*, 73:307, 2001.

[17] C. J. Pethick and H. Smith. *Bose-Einstein condensation in Dilute Gases*. Cambridge University Press, 2002.

[18] O. Penrose and L. Onsager. Bose-Einstein condensation and liquid helium. *Physical Review*, 104:576, 1956.

[19] P. W. Anderson. *Rev. Mod. Phys.*, 38:298, 1966.

[20] Anthony J. Leggett and Fernando Sols. On the concept of spontaneously broken gauge symmetry in condensed matter physics. *Found. Phys.*, 21(3):353, 1991.

[21] A.J. Leggett. Broken gauge symmetry in a Bose condensate. In A. Griffin, D.W. Snoke, and S. Stringari, editors, *Bose-Einstein Condensation*, page 452. Cambridge University Press, 1995.

[22] J. Weiner, V. S. Bagnato, S. Zilio, and P. S. Julienne. *Rev. Mod. Phys.*, 71:1, 1999.

[23] J. Dalibard. Collisional dynamics of ultra-cold atomic gases. In M. Inguscio, S. Stringari, and C.E. Wieman, editors, *Proceedings of the International School of Physics - Enrico Fermi*, page 321. IOS Press, 1999.

[24] D.J. Heinzen. Ultracold atomic interactions. In M. Inguscio, S. Stringari, and C.E. Wieman, editors, *Proceedings of the International School of Physics - Enrico Fermi*, page 351. IOS Press, 1999.

[25] P.S. Julienne, F.H. Mies, E. Tiesinga, and C.J. Williams. Collisional stability of double Bose condensates. *Phys. Rev. Lett.*, 78(10):1880, March 1997.

[26] N. Bogoliubov. On the theory of superfluidity. *J. Phys.*, 11(1):23, 1947.

[27] E. P. Gross. Structure of a quantized vortex in boson systems. *Nuovo Cimento*, 20:451, 1961.

[28] L.P. Pitaevskii. Vortex lines in an imperfect Bose gas. *Sov. Phys. JETP*, 13(2):451, August 1961.

[29] M.R. Andrews, C.G. Townsend, H.-J. Miesner, D.S. Durfee, D.M. Kurn, and W. Ketterle. Observation of interference between two Bose-Einstein condensates. *Science*, 275(0):637, January 1997.

[30] K.W. Madison, F. Chevy, W. Wohlleben, and J. Dalibard. Vortex formation in a stirred Bose-Einstein condensate. *Phys. Rev. Lett.*, 84(5):806, January 2000.

[31] W. Zwerger. Mmott-Hubbard transition of cold atoms in optical lattices. *cond-mat/0211314*, 2002.

[32] P.O. Fedichev, M.W. Reynolds, and G.V. Shlyapnikov. Three-body recombination of ultracold atoms to a weakly bound s level. *Phys. Rev. Lett.*, 77(14):2921, September 1996.

[33] F. S. Cataliotti, S. Burger, C. Fort, P. Maddaloni, F. Minardi, A. Trombettoni, A. Smerzi, and M. Inguscio. Josephson junction arrays with Bose-Einstein condensates. *Science*, 293:843–846, 2001.

[34] M. Greiner. Magnetischer Transfer von Atomen - ein Weg zur einfachen Bose-Einstein-kondensation. Master's thesis, LMU München, 1999.

[35] E. L. Raab, M. Prentiss, A. Cable, S. Chu, and D. E. Pritchard. Trapping of neutral-sodium atoms with radiation pressure. *Physical Review Letters*, 59:2631, 1987.

[36] C. S. Adams and E. Riis. Laser cooling and trapping of neutral atoms. *Progress in Quantum Electronics*, 21:1, 1997.

[37] W. D. Phillips. Laser cooling and trapping of neutral atoms. *Reviews of Modern Physics*, 70:721, 1998.

[38] H. J. Metcalf and P. van der Straten. *Laser Cooling and Trapping*. Graduate Texts in Contemporary Physics. Springer, 1999.

[39] K. E. Gibble, S. Kasapi, and S. Chu. Improved magneto-optic trapping in a vapor cell. *Optics Letters*, 17(7):526, April 1991.

[40] B. Martin. Universität bonn report no. bonn-ir-75-8, Universität Bonn, 1975.

[41] N. Niehues. Universität bonn report no. bonn-ir-76-35, Universität Bonn, 1976.

[42] A. L. Migdall, J. V. Prodan, W. D. Phillips, T. H. Bergeman, and H. J. Metcalf. First observation of magnetically trapped neutral atoms. *Physical Review Letters*, 54:2596, 1985.

[43] M. Greiner, I. Bloch, T. W. Hänsch, and T. Esslinger. Magnetic transport of trapped cold atoms over a large distance. *Phys. Rev. A*, 63:031401, 2001.

[44] E. Majorana. Atomi orientati in campo magnetico variabile. *Nuovo Cimento*, 9:43, 1933.

[45] W. Petrich, M. H. Anderson, J. R. Ensher, and E. A. Cornell. Stable, tightly confining magnetic trap for evaporative cooling of neutral atoms. *Physical Review Letters*, 74:3352, 1995.

[46] D. E. Pritchard. Cooling neutral atoms in a magnetic trap for precision spectroscopy. *Physical Review Letters*, 51:1336, 1983.

[47] T. Bergeman, G. Erez, and H. Metcalf. Magnetostatic trapping fields for neutral atoms. *Physical Review A*, 35:1535, 1987.

[48] T. Esslinger, I. Bloch, and T. W. Hänsch. Bose-Einstein condensation in a quadrupole-ioffe-configuration trap. *Physical Review A*, 58:R2664, 1998.

[49] L. Ricci, M. Weidemüller, T. Esslinger, A. Hemmerich, C. Zimmermann, V. Vuletic, W. König, and T. W. Hänsch. A compact grating-stabilized diode laser system for atomic physics. *Optics Communication*, 117:541, 1995.

[50] T. W. Hänsch, M. D. Levenson, and A. L. Schawlow. *Physical Review Letters*, 26:946, 1971.

[51] J.C. Camparo. *Contemp. Phys*, 26:443, 1985.

[52] U. Schünemann, H. Engler, R. Grimm, M. Weidemueller, and M. Zielonkowski. Simple scheme for tunable frequency offset locking of two lasers. *Review of Scientific Instruments*, 70:242, 1999.

[53] A. Zach. Diplomarbeit LMU München, 1998.

[54] E. Hecht and A. Zajac. *Optics*. Addison-Wesley, 1979.

[55] M. R. Andrews, M.-O. Mewes, N. J. van Druten, D. S. Durfee, D. M. Kurn, and W. Ketterle. Direct, nondestructive observation of a Bose-Einstein condensates. *Science*, 273:84, 1996.

[56] M. Greiner. Phasenkontrastabbildung eines rubidium bosekondensats. Praktikumsprotokoll FII Praktikum LMU München, 1998.

[57] J. Dalibard and C. Cohen-Tannoudji. Laser cooling below the Doppler limit by polarization gradients: simple theoretical-models. *J. Opt. Soc. Am. B*, 6(11):2023, November 1989.

[58] P. L. Gould, G. A. Ruff, and D. E. Pritchard. Diffraction of atoms by light: The near-resonant Kapitza-Dirac effect. *Phys. Rev. Lett.*, 56:827–830, 1986.

[59] P. J. Martin, B. G. Oldaker, A. H. Miklich, and D. E. Pritchard. Bragg scattering of atoms from a standing light wave. *Phys. Rev. Lett*, 60:515–518, 1988.

[60] C. S. Adams, M. Sigel, and J. Mlynek. Atom optics. *Phys. Rep.*, 240:143, 1994.

[61] P. Verkerk, B. Lounis, C. Salomon, C. Cohen-Tannoudji, J. Y. Courtois, and G. Grynberg. Dynamics and spatial order of cold cesium atoms in a periodic optical potential. *Phys. Rev. Lett*, 68:3861, 1992.

[62] O. S. Jessen, C. Gerz, P. D. Lett, W. D. Phillips, S. L. Rolston, R. J. C. Spreeuw, and C. I. Westbrook. Observation of quantized motion of rb atoms in an optical field. *Phys. Rev. Lett*, 69:49, 1992.

[63] A. Hemmerich and T. W. Hänsch. Two-dimesional atomic crystal bound by light. *Phys. Rev. Lett*, 70:410–413, 1993.

[64] A. Hemmerich, M. Weidemüller, T. Esslinger, C. Zimmermann, and T. W. Hänsch. Trapping atoms in a dark optical lattice. *Phys. Rev. Lett*, 75:37–40, 1995.

[65] M. Weidemüller, A. Hemmerich, A. Görlitz, T. Esslinger, and T. W. Hänsch. Bragg diffraction in an atomic lattice bound by light. *Phys. Rev. Lett.*, 75:4583, 1995.

[66] G. Grynberg, B. Lounis, P. Verkerk, J. Y. Courtois, and C. Salomon. Quantized motion of cold cesium atoms in two- and three-dimensional optical potentials. *Phys. Rev. Lett*, 70:2249–2252, 1993.

[67] M. Prentiss. Bound by light. *Science*, 260:1078, 1993.

[68] M. B. Dahan, E. Peik, J. Reichel, Y. Castin, and C. Salomon. Bloch oscillations of atoms in an optical potential. *Phys. Rev. Lett*, 76:4508, 1996.

[69] S. R. Wilkinson, C. F. Bharucha, K. W. Madison, Q. Niu, and M. G. Raizen. Observation of atomic wannier-stark ladders in an accelerating optical potential. *Phys. Rev. Lett*, 76:4512–4515, 1996.

[70] A. Görlitz, M. Weidemüller, T. W. Hänsch, and A. Hemmerich. Observing the position spread of atomic wave packets. *Phys. Rev. Lett*, 78:2096, 1997.

[71] A. Görlitz, T. Kinoshita, T. W. Hänsch, and A. Hemmerich. Realization of bichromatic optical superlattices. *Phys. Rev. A*, 64:011401, 2001.

[72] S. Friebel, C. D. Andrea, J. Walz, M. Weiz, and T. W. Hänsch. co_2-laser optical lattice with cold rubidium atoms. *Phys. Rev. A*, 57:R20, 1998.

[73] R. Scheunemann, F. S. Cataliotti, T. W. Hänsch, and M. Weitz. Resolving and addressing atoms in individual sites of a co_2-laser optical lattice. *Phys. Rev. A*, 62:051801, 2000.

[74] V. Vuletic, C. Chin, A. Kerman, and S. Chu. Degenerate raman sideband cooling of trapped cesium atoms at very high atomic densities. *Phys. Rev. Lett*, 81:5768–5771, 1998.

[75] M. T. DePue, C. McCormick, S. L. Winoto, S. Oliver, and D. S. Weiss. Unity occupation of sites in a 3d optical lattice. *Phys. Rev. Lett.*, 82:2262–2265, 1999.

[76] A. J. Kerman, V. Vuletic, C. Chin, and S. Chu. Beyond optical molasses: 3d Raman sideband cooling of atomic cesium to high phase-space density. *Phys. Rev. Lett*, 84:439–442, 2000.

[77] B.P. Anderson and M.A. Kasevich. Macroscopic quantum interference from atomic tunnel arrays. *Science*, 282:1686, November 1998.

[78] S. Burger, F.S. Cataliotti, C. Fort, F. Minardi, M. Inguscio, M.L. Chiofalo, and M.P. Tosi. Superfluid and dissipative dynamics of a Bose-Einstein condensate in a periodic optical potential. *Phys. Rev. Lett.*, 86(20):4447, May 2001.

[79] O. Morsch, J. H. Müller, M. Christiani, D. Ciampini, and E. Arimondo. Bloch oscillations and mean-field effects of bose-einstein condensates in 1d optical lattices. *Phys. Rev. Lett*, 87:140402, 2001.

[80] M. Kozuma, L. Deng, E.W. Hagley, J. Wen, R. Lutwak, K. Helmerson, S.L. Rolston, and W.D. Phillips. Coherent splitting of Bose-Einstein condensed atoms with optically induced Bragg diffraction. *Phys. Rev. Lett.*, 82(5):871, February 1999.

[81] J. Stenger, S. Inouye, A.P. Chikkatur, D.M. Stamper-Kurn, D.E. Pritchard, and W. Ketterle. Bragg spectroscopy of a Bose-Einstein condensate. *Phys. Rev. Lett.*, 82(23):4569, June 1999.

[82] R. Grimm, M. Weidemüller, and Yu. B. Ovchinnikov. Optical dipole traps for neutral atoms. *Adv. At. Mol. Opt. Phys.*, 42:95–170, 2000.

[83] P. S. Jessen and I. H. Deutsch. Optical lattices. *Advances in Atomic, Molecular and Optical Physics*, 37, 1996.

[84] J.E. Bjorkholm, R.E. Freeman, A. Ashkin, and D.B. Pearson. Observation of focusing on neutral atoms by the dipole forces of resonance-radiation pressure. *Phys. Rev. Lett.*, 41(20):1361, November 1978.

[85] Steven Chu, J.E. Bjorkholm, A. Ashkin, and A. Cable. Experimental observation of optically trapped atoms. *Phys. Rev. Lett.*, 57(3):314, July 1986.

[86] J. D. Jackson. *Classical electrodynamics*. Wiley, New York, 1962.

[87] Claude N. Cohen-Tannoudji. Manipulating atoms with photons. *Rev. Mod. Phys.*, 70(3):707, July 1998.

[88] N. W. Ashcroft and N. D. Mermin. *Solid state physics*. Saunders College Publishing, Fort Worth, TX,, 1976.

[89] D. Jaksch. *Bose-Einstein Condensation and Applications*. PhD thesis, Leopold-Franzens-Universität Innsbruck, Austria, 1999.

[90] C. Kittel. *Quantum Theory of Solids*. John Wiley and Sons, New York, 1963.

[91] M. Greiner, I. Bloch, O. Mandel, T. W. Hänsch, and T. Esslinger. Exploring phase coherence in a 2D lattice of Bose-Einstein condensates. *Phys. Rev. Lett.*, 87(16):160405, October 2001.

[92] M. Greiner, O. Mandel, T. Esslinger, T. W. Hänsch, and I. Bloch. Quantum phase transition from a superfluid to a Mott insulator in a gas of ultracold atoms. *Nature*, 415:39, January 2002.

[93] Y.B. Band, Boris Malomed, and Marek Trippenbach. Adiabaticity in nonlinear quantum dynamics: Bose-Einstein condensate in a time-varying box. *Phys. Rev. A*, 65:033607, February 2002.

[94] V. A. Kashurnikov, N. V. Prokof'ev, and B. V. Svistunov. Revealing the superfluid-Mott-insulator transition in an optical lattice. *Phys. Rev. A*, 66:031601, 2002.

[95] Y.B. Band, Marek Trippenbach, J.P. Burke, Jr., and P.S. Julienne. Elastic scattering loss of atoms from colliding Bose-Einstein condensate wave packets. *Phys. Rev. Lett.*, 84(24):5462, June 2000.

[96] A. P. Chikkatur, A. Görlitz, D. M. Stamper-Kurn, S. Inouye, S. Gupta, and W. Ketterle. Suppression and enhancement of impurity scattering in a bose-einstein condensate. *Phys. Rev. Lett.*, 85:483, 2000.

[97] Biao Wu and Qian Niu. Landau and dynamical instabilities of the superflow of Bose-Einstein condensates in optical lattices. *Phys. Rev. A*, 64:061603(R), November 2001.

[98] J. C. Bronski, L. D. Carr, B. Deconinck, J. N. Kutz, , and K. Promislow. Stability of repulsive Bose-Einstein condensates in a periodic potential. *Phys. Rev. E*, 63:036612, 2001.

[99] F. Kh. Abdullaev, A. Gammal, Lauro Tomio, and T. Frederico. Stability of trapped Bose-Einstein condensates. *Phys. Rev. A*, 63:043604, March 2001.

[100] R. G. Scott, A. M. Martin, T.M. Fromhold, S. Bujkiewicz, F.W. Sheard, and M. Leadbeater. Creation of solitons and vortices by bragg reflection of bose-einstein condensates in an optical lattice. *cond-mat/0206543*, 2002.

[101] A. Kastberg, W. D. Phillips, S. L. Rolston, R. J. C. Spreeuw, and P. S. Jessen. Adiabatic cooling of cesium to 700 nk in an optical lattice. *Phys. Rev. Lett.*, 74:1542–1545, 1995.

[102] S. Sachdev. *Quantum Phase Transitions*. Cambridge University Press, Cambridge, 2001.

[103] K. Sheshadri, H.R. Krishnamurthy, R. Pandit, and T. V. Ramakrishnan. Superfluid and insulating phases in an interacting-boson model: Mean-field theory and the rpa. *Europhys. Lett.*, 22:257–263, 1993.

[104] J. K. Freericks and H. Monien. Phase diagram of the Bose Hubbard model. *Europhys. Lett.*, 26:545–550, 1995.

[105] D. van Oosten, P. van der Straten, and H. T. C. Stoof. Quantum phases in an optical lattice. *Phys. Rev. A*, 63:053601, 2001.

[106] N. Elstner and H. Monien. Dynamics and thermodynamics of the Bose-Hubbard model. *Phys. Rev. B*, 59:12184–12187, 1999.

[107] T. D. Kühner and H. Monien. Phases of the one-dimensional bose-hubbard model. *Phys. Rev. B*, 58:R14741, 1998.

[108] S. Rapsch, U. Schollwöck, and W. Zwerger. Density matrix renormalization group for disordered bosons in one dimension. *Europhys. Lett.*, 46:559, 1999.

[109] D. S. Rokhsar and B. G. Kotliar. Gutzwiller projection for bosons. *Phys. Rev. B*, 44:10328–10332, 1991.

[110] R. Roth and K. Burnett. Superfluidity and interference pattern of ultracold bosons in optical lattices. *cond-mat/0209066*, 2002.

[111] M. Niemeyer and H. Monien. private communication, 2001.

[112] B. G. Orr, H. M. Jaeger, A. M. Goldman, and C. G. Kuper. Global phase coherence in two-dimensional granular superconductors. *Phys. Rev. Lett.*, 56:378–381, 1986.

[113] D. B. Haviland, Y. Liu, and A. M. Goldman. Onset of superconductivity in the two-dimensional granular superconductors. *Phys. Rev. Lett.*, 62:2180–2183, 1989.

[114] R. M. Bradley and S. Doniach. Quantum fluctuations in chains of Josephson junctions. *Phys. Rev. B*, 30:1138–1147, 1984.

[115] L. J. Geerligs, M. Peters, L. E. M. de Groot, A. Verbruggen, and J. E. Mooij. Charging effects and quantum coherence in regular Josephson junction arrays. *Phys. Rev. Lett*, 63:326–329, 1989.

[116] W. Zwerger. Global and local phase coherence in dissipative Josephson-junction arrays. *Europhys. Lett.*, 9:421–426, 1989.

[117] H. S. J. van der Zant, F. C. Fritschy, F. C. Elion, W. J. Elion, L. J. Geerligs, and J. E. Mooij. Field-induced superconductor-to-insulator transitions in Josephson-junction arrays. *Phys. Rev. Lett.*, 69:2971–2974, 1992.

[118] A. Oudenaarden and J. E. Mooij. One-dimensional Mott insulator formed by quantum vortices in Josephson junction arrays. *Phys. Rev. Lett.*, 76:4947–4950, 1996.

[119] Paul S. Julienne. Cold binary atomic collisions in a light field. *J. Res. Natl. Inst. Stand. Tech.*, 101(4):487, July 1996.

[120] E.M. Wright, D.F. Walls, and J.C. Garrison. Collapses and revivals of Bose-Einstein condensates formed in small atomic samples. *Phys. Rev. Lett.*, 77(11):2158, September 1996.

[121] E.M. Wright, T. Wong, M.J. Collett, S.M. Tan, and D.F. Walls. Collapses and revivals in the interference between two Bose-Einstein condensates formed in small atomic samples. *Phys. Rev. A*, 56(1):591, July 1997.

[122] M. Lewenstein and L. You. Quantum phase diffusion of a Bose-Einstein condensate. *Phys. Rev. Lett.*, 77(17):3489, October 1996.

[123] A. Imamoḡlu, M. Lewenstein, and L. You. Inhibition of coherence in trapped Bose-Einstein condensates. *Phys. Rev. Lett.*, 78(13):2511, March 1997.

[124] Y. Castin and J. Dalibard. Relative phase of two Bose-Einstein condensates. *Phys. Rev. A*, 55(6):4330, June 1997.

[125] J. A. Dunningham, M. J. Collet, and D. F. Walls. Quantum state of a trapped Bose-Einstein condensate. *Phys. Lett. A*, 245:49–54, 1998.

[126] W. Zhang and D. F. Walls. Bosonic-degeneracy-induced quantum correlation in a nonlinear atomic beam splitter. *Phys. Rev. A*, 52:4696–4703, 1995.

[127] M. Greiner, O. Mandel, Theodor W. Hänsch, and I. Bloch. Collapse and revival of the matter wave field of a Bose-Einstein condensate. *Nature*, 419:51–54, 2002.

[128] H. J. Briegel, T. Calarco, D. Jaksch, and P. Zoller J. I. Cirac. Quantum computing with neutral atoms. *J. Mod. Opt*, 47:415–451, 2000.

[129] H. J. Briegel and R. Raussendorf. Persistent entanglement in arrays of interacting particles. *Phys. Rev. Lett.*, 86:910–913, 2001.

[130] R. Raussendorf and H. J. Briegel. A one-way quantum computer. *Phys. Rev. Lett*, 86:5188–5191, 2001.

[131] D. F. Walls and G. J. Milburn. *Quantum Optics*. Springer, Berlin, 1994.

[132] J. Javanainen and S. M. Yoo. Quantum phase of a Bose-Einstein condensate with an arbitrary number of atoms. *Phys. Rev. Lett.*, 76(2):161, January 1996.

[133] J.I. Cirac, C.W. Gardiner, M. Naraschewski, and P. Zoller. Continuous observation of interference fringes from Bose condensates. *Phys. Rev. A*, 54(5):R3714, November 1996.

[134] J.A. Dunningham and K. Burnett. Phase standard for Bose-Einstein condensates. *Phys. Rev. Lett.*, 82(19):3729, May 1999.

[135] G. J. Milburn and C. A. Holmes. Dissipative quantum and classical liouville mechanics of the anharmonic oscillator. *Phys. Rev. Lett.*, 56:2237–2240, 1986.

[136] D. J. Daniel and G. J. Milburn. Destruction of quantum coherence in a nonlinear oscillator via attenuation and amplification. *Phys. Rev. A*, 39:4628–4640, 1989.

[137] B. Yurke and D. Stoler. Generating quantum mechanical superpositions of macroscopically distinguishable states via amplitude dispersion. *Phys. Rev. Lett.*, 57:13–16, 1986.

[138] W. Krauth, M. Caffarel, and J. P. Bouchaud. Gutzwiller wave function for a model of strongly interacting bosons. *Phys. Rev. B*, 45:3137–3140, 1992.

[139] Corinna Kollath. *private communication.*

[140] Subir Sachdev, K. Sengupta, and S. M. Girvin. Mott insulator in strong electric fields. *Phys. Rev. B.*, 66:075128, 2002.

[141] K. Braun-Munzinger, J. A. Dunningham, and K. Burnett. Excitations of bose condensates in optical lattices. *cond-mat/0211701.*

[142] J.L. Roberts, N.R. Claussen, S.L. Cornish, E.A. Donley, E.A. Cornell, and C.E. Wieman. Controlled collapse of a Bose-Einstein condensate. *Phys. Rev. Lett.*, 86(19):4211, May 2001.

[143] J.L. Roberts, James P. Burke, Jr., N.R. Claussen, S.L. Cornish, E.A. Donley, and C.E. Wieman. Improved characterization of elastic scattering near a Feshbach resonance in ^{85}Rb. *Phys. Rev. A*, 64:024702, July 2001.

[144] A. Sorensen and K. Molmer. Spin-spin interaction and spin squeezing in an optical lattice. *Phys. Rev. Lett.*, 83:2274, 1999.

[145] E. Jane, G. Vidal, W. Dür, P. Zoller, and J. I. Cirac. Simulation of quantum dynamics with quantum optical systems. *Quantum Information and Computation*, Vol. 3, No. 1:15–37, 2003.

[146] K. Goral, L. Santos, and M. Lewenstein. Quantum phases of dipolar bosons in optical lattices. *Phys. Rev. Lett.*, 88:170406, 2002.

[147] L. M. Duan, E. Demler, and M. D. Lukin. Controlling spin exchange interactions of ultracold atoms in optical lattices. *cond-mat/0210564.*

[148] W. Hofstetter, J. I. Cirac, P. Zoller, E. Demler, and M. D. Lukin. High-temperature superfluidity of fermianic atoms in optical lattices. *Phys. Rev. Lett.*, 89:220407, 2002.

[149] L. Tonks. The complete equation of state of one, two and three-dimensional gases of hard elastic spheres. *Phys. Rev.*, 50:955, 1936.

[150] M. Giradeau. Relationship between systems of impenetrable bosons and fermions in one dimension. *J. Math. Phys.*, 1:516, 1960.

[151] D. S. Petrov, G. V. Shlyapnikov, and J. T. M. Walraven. Regimes of quantum degeneracy in trapped 1d gases. *Phys. Rev. Lett*, 85:3745, 2000.

[152] V. Dunjko, M. Lorent, and M. Olshanii. Bosons in cigar-shaped traps: Thomas-fermi regime, tonks-girardeau regime, and in between. *Phys. Rev. Lett*, 86:5413, 2001.

[153] H. P. Büchler, G. Blatter, and W. Zwerger. *Commensurate-incommensurate transition of cold atoms in an optical lattice.* cond-mat/0208391, 2002.

[154] N. W. Wilkin and J. M. F. Gunn. Condensation of composite bosons in a rotating BEC. *Phys. Rev. Lett.*, 84(1):6, January 2000.

[155] B. Paredes, P.O. Fedichev, J.I. Cirac, and P. Zoller. 1/2-Anyons in small atomic Bose-Einstein condensates. *Phys. Rev. Lett.*, 87(1):010402, July 2001.

[156] B. Paredes, P. Zoller, and J. I. Cirac. Fermionizing a small gas of ultracold bosons. *Phys. Rev. A*, 66:033609, 2002.

[157] R. B. Laughlin. Anomalous quantum hall effect: An incompressible quantum fluid with fractionally charged excitations. *Phys. Rev. Lett*, 50:1395, 1983.

[158] G. K. Brennen, C. M. Caves, P. S. Jessen, and I. H. Deutsch. Quantum logic gates in optical lattices. *Phys. Rev. Lett.*, 82:1060, 1999.

[159] O. Mandel, M. Greiner, A. Widera, T. Rom, T. W. Hänsch, and I. Bloch. Coherent transport of neutral atoms in spin-dependent optical lattice potentials. *cond-mat/0301169.*

[160] G. K. Brennen and I. H. Deutsch. Quantum logic for trapped atoms via molecular hyperfine interactions. *Phys. Rev. A*, 65:022313, 2002.

[161] W. Dür, R. Raussendorf, V. M. Kendon, and H. J. Briegel. Quantum walks in optical lattices. *Phys. Rev. A*, 66:052319, 2002.

[162] A. A. Radzig and B. M. Smirnow. *Reference Data on Atoms, Molecules and Ions*, volume 31 of *Springer Series in Chemical Physics*. Springer, 1985.

[163] S. Bize, Y. Sortais, M. S. Santos, C. Mandache, A. Clairon, and C. Salomon. High-accuracy measurement of the ^{87}rb ground-state hyperfine splitting in an atomic fountain. *Europhysics Letters*, 45:558, 199.

[164] J. L. Roberts, N. R. Claussen, J. P. Jr. Burke, C. H. Green, E. A. Cornell, and C. E. Wieman. Resonant magnetic field control of elastic scattering in cold ^{85}rb. *Physical Review Letters*, 81:5109, 1998.

[165] E. A. Burt, R. W. Ghrist, C. J. Myatt, M. J. Holland, E. A. Cornell, and C. E. Wieman. Coherence, correlations and collisions: What one learns about bose-einstein condensates from their decay. *Physical Review Letters*, 79:337, 1997.

Danksagung

Mein herzlicher Dank gilt allen, die zum Gelingen dieser Arbeit beigetragen haben. Ganz besonders möchte ich mich bedanken bei

- Prof. T. W. Hänsch, der die Arbeit mit viel Interesse und Begeisterung unterstützt. Er gewährt viel Freiheit und ist oft mit einer pfiffigen Idee zur Stelle. Besonders fasziniert hat mich sein äußerst intuitives Verständnis der Physik;
- Immanuel Bloch für die phantastische Zusammenarbeit. Es macht riesig Spaß, mit ihm über Physik zu diskutieren, an neuen Ideen zu feilen und gemeinsam im Labor zu arbeiten. Von seiner Aktivität und Begeisterung habe ich mich gerne anstecken lassen. ... und wenn er mal nicht im Labor sein kann, sorgt sein Handy dafür, daß er stets auf dem laufenden ist ...
- Olaf Mandel, mit dem ich viele gemeinsame Stunden im Labor verbracht habe. Es macht mir viel Freude, mit ihm zusammenzuarbeiten und gemeinsam an Lösungen zu tüfteln. ...und ich bin mir sicher, daß der erste funktionsfähige Quantencomputer, den Olaf in ein paar Jahren gebaut haben wird, mit *Pinguin inside* funktionieren wird...
- Tim Rom, Alexander Altmeyer und Artur Widera, die seit etwa einem Jahr am Experiment arbeiten und ein tolles Team stellen. Es macht Spaß, mit Ihnen zu diskutieren und zu arbeiten, und ich bin mir sicher, daß sie noch viele tolle Experimente hervorbringen werden. Es war oft sehr lustig ... jedoch habe ich schon etwas Sorgen, mit welch Sprüchen sie mich so alles auf dem Doktorhut zitieren werden ...
- Tilman Esslinger, mit dem ich während meiner Diplomarbeit und dem Anfang der Doktorarbeit zusammengearbeitet habe sowie Michael Köhl. Bei allen Werkstudenten, vor allem bei Thorsten Best, der noch die letzten Magnetfeldfluktuationen gebändigt hat. Bei Wolfgang Eckardt, einem unheimlich netten Kollegen und lebensfrohen Mensch, der leider viel zu früh gestorben ist;
- allen Mitgliedern der Arbeitsgruppe Hänsch und Weinfurter, insbesondere auch bei Jakob Reichel, Peter Hommelhoff und Wolfgang Hänsel, mit denen ich viel diskutiert habe; Bei Christian Kurtsiefer, der mir viele Tips gegeben hat und bei Markus Weber, Jürgen Volz und Patrick Zarda, mit denen ich viele Diskussionen und viel Spaß hatte;
- Toni Scheich, der unglaublich professionelle Geräte für unser Experiment entwickelt hat, und bei Gabriele Gschwendtner, unserer lebhaften Sekretärin. Bei Stefan Manus, und allen Mitarbeitern der Werkstätten an der LMU und am MPQ, insbesondere Wolfgang Simon und Karl Linner;

- Ich möchte mich für viele spannende und anregende Diskussionen bedanken, zum Beispiel bei Peter Zoller, Ignacio Cirac, Wilhelm Zwerger, Dieter Jaksch, Hans Briegel, Robert Raussendorf, Keith Burnett, Yuri Kagan, Maciej Lewenstein, Hartmut Monien, Matthias Niemeyer, Henk Stoof, Peter van der Straten, Jan von Delft, Corinna Kollath, Jook Walraven und vielen, vielen anderen;
- meinem Lehrer Dr. P. A. Kreuels;
- Karen ;-)
- meinen Freunden, die mich willkommen heissen auch nachdem ich zwischendurch immer mal wieder ins Labor abgetaucht bin;
- und ganz lieb bei meinen Eltern Monika und Dieter und meiner Schwester Leonie.

VOLUME 87, NUMBER 16 PHYSICAL REVIEW LETTERS 15 OCTOBER 2001

Exploring Phase Coherence in a 2D Lattice of Bose-Einstein Condensates

Markus Greiner, Immanuel Bloch, Olaf Mandel, Theodor W. Hänsch,* and Tilman Esslinger
Sektion Physik, Ludwig-Maximilians-Universität, Schellingstrasse 4/III, D-80799 Munich, Germany
and Max-Planck-Institut für Quantenoptik, D-85748 Garching, Germany

(Received 4 May 2001; published 1 October 2001)

Bose-Einstein condensates of rubidium atoms are stored in a two-dimensional periodic dipole force potential, formed by a pair of standing wave laser fields. The resulting potential consists of a lattice of tightly confining tubes, each filled with a 1D quantum gas. Tunnel coupling between neighboring tubes is controlled by the intensity of the laser fields. By observing the interference pattern of atoms released from more than 3000 individual lattice tubes, the phase coherence of the coupled quantum gases is studied. The lifetime of the condensate in the lattice and the dependence of the interference pattern on the lattice configuration are investigated.

DOI: 10.1103/PhysRevLett.87.160405 PACS numbers: 03.75.Fi, 03.65.Nk, 05.30.Jp, 32.80.Pj

The physics of Bose-Einstein condensation is governed by a hierarchy of energy scales. The lowest energy is usually the atomic oscillation frequency in the trap which is much smaller than the chemical potential of the condensate. Here we report on experiments in which we enter a regime where this order is inverted. By overlapping two optical standing waves with the magnetically trapped condensate we create a two-dimensional periodic lattice of tightly confining potential tubes. In each of the several thousand tubes the chemical potential is far below the trapping frequencies in the radial direction. The radial motion of the atoms is therefore confined to zero point oscillations, and transverse excitations are completely frozen out. In the degenerate limit, these 1D quantum gases are expected to show a remarkable physics not encountered in 2D and 3D, for instance, a continuous crossover from bosonic to fermionic behavior as the density is lowered [1–5].

In our two-dimensional periodic array of quantum gases the tunnel coupling between neighboring lattice sites is controlled with a high degree of precision by changing the intensity of the optical lattice beams. A similar control over coupling between adjacent pancake-shaped condensates was achieved in recent experiment using a single standing wave laser field [6,7]. After suddenly releasing the atoms from the trapping potential we observe the multiple matter wave interference pattern of several thousand expanding quantum gases. This allows us to study the phase coherence between neighboring lattice sites, which is remarkably long lived. Even for long storage times, when the phase coherence between neighboring lattice sites is lost and no interference pattern can be observed anymore, the radial motion of the atoms remains confined to zero point oscillations.

Similar to our previous work [8], almost pure Bose-Einstein condensates with up to 5×10^5 ^{87}Rb atoms are created in the $|F = 2, m_F = 2\rangle$ state. The cigar-shaped condensates are confined in the harmonic trapping potential of a QUIC trap (a type of magnetic trap that incorporates the quadrupole and Ioffe configuration) [9] with an axial trapping frequency of 24 Hz and radial trapping frequencies of 220 Hz. The lattice potential is formed by overlapping two perpendicular optical standing waves with the Bose-Einstein condensate as shown in Fig. 1. All lattice beams are derived from the output of a laser diode operating at a wavelength of $\lambda = 852$ nm and have spot sizes w_0 ($1/e^2$ radius for the intensity) of approximately 75 μm at the position of the condensate. The resulting potential for the atoms is directly proportional to the intensity of the interfering laser beams [10], and for the case of linearly polarized light fields it can be expressed by

$$U(y,z) = U_0\{\cos^2(ky) + \cos^2(kz) + 2\mathbf{e}_1 \cdot \mathbf{e}_2 \cos\phi \cos(ky)\cos(kz)\}. \quad (1)$$

Here U_0 describes the potential maximum of a single standing wave, $k = 2\pi/\lambda$ is the magnitude of the wave vector of the lattice beams, and $\mathbf{e}_{1,2}$ are the polarization vectors of the horizontal and vertical standing wave laser fields, respectively. The potential depth U_0 is conveniently measured in units of the recoil energy $E_r = \hbar^2 k^2/2m$, with m being the mass of a single atom. The time-phase difference between the two standing waves is given by the

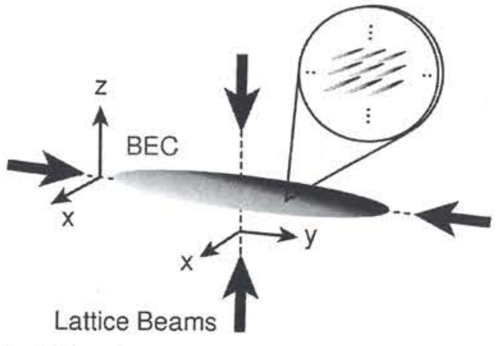

FIG. 1. Schematic setup of the experiment. A 2D lattice potential is formed by overlapping two optical standing waves along the horizontal axis (y axis) and the vertical axis (z axis) with a Bose-Einstein condensate in a magnetic trap. The condensate is then confined to an array of several thousand narrow potential tubes (see inset).

0031-9007/01/87(16)/160405(4)$15.00

variable ϕ [11]. In our setup this time phase is measured interferometrically and controlled with a piezomounted mirror and a servoloop. Furthermore, the intensity of the lattice beams is stabilized in order to ensure a constant potential depth during our measurements. The intensity pattern in the y-z plane extends along the x direction, such that the resulting potential can be viewed as a lattice of narrow tubes with a spacing of $\lambda/2$ between neighboring lattice sites. These tubes provide a tight harmonic confinement along the radial direction which leads to large trapping frequencies $\omega_r \approx \hbar k\sqrt{2U_0/m}$. In our setup potential depths of up to $12E_r$ are reached, resulting in a maximum radial trapping frequency of $\omega_r \approx 2\pi \times 18.5$ kHz. The confinement along the symmetry axis of a single tube is determined by the harmonic confinement of the magnetic trap and the confinement due to the Gaussian intensity profile of the lattice laser beams. The trapping frequency along the symmetry axis of a single lattice tube can be varied between $\omega_{\mathrm{ax}} \approx 2\pi \times 10$–$300$ Hz. The spontaneous scattering rate due to the lattice laser light is always less than $\Gamma_{\mathrm{sc}} = 0.06\ \mathrm{s}^{-1}$ and therefore negligible for our measurement times.

In order to transfer the atoms into the lattice potential, the laser power of the lattice beams is gradually increased in a linear ramp to its final strength within 40 ms. The atoms are then held for a variable amount of time in the combined potential of the interfering laser beams and the magnetic trap. The number of occupied lattice sites can be estimated by counting the number of lattice sites within the Thomas-Fermi extension of the magnetically trapped condensate. For the above parameters we find that up to 3000 lattice sites are populated, with an average population of $\bar{N}_i \approx 170$ atoms per lattice site.

When the atoms are released from the combined potential of the optical lattice and the magnetic trap, the condensate wave functions on different lattice sites expand and interfere with each other. This interference pattern is imaged after a fixed expansion time using absorption imaging, with the imaging axis oriented along the x axis and positioned parallel to the symmetry axis of the individual lattice tubes. The results are displayed in Fig. 2 for a 2D-lattice potential with a maximum potential depth of $12E_r$ and orthogonal polarization vectors $\mathbf{e}_1 \cdot \mathbf{e}_2 = 0$. In comparison, Fig. 3 shows the results for three different potential depths of the optical lattice and 1D vertical (z axis), 1D horizontal (y axis), and 2D vertical+horizontal lattice configurations (orthogonal polarization vectors $\mathbf{e}_1 \cdot \mathbf{e}_2 = 0$). Several important features can be seen on these images. First, discrete interference maxima are visible that are arranged in a regular structure. These interference maxima not only require a periodic density modulation of the atoms but also phase coherence of the condensate wave function throughout the lattice. They directly reveal the momentum distribution of the atoms in the lattice. Second, s-wave scattering spheres [12,13] become more visible as the higher order momentum components are more strongly populated with increasing potential depth. These scattering spheres occur due to collisions between atoms in the separating momentum components after the trapping potential is switched off. The collision probability between atoms in the horizontal momentum components $|p_y| = 2\hbar k$ and the $|p| = 0$ momentum component is high, due to the large extension of the condensate in the horizontal direction. This yields long interaction times and thus a high scattering probability. Along the vertical direction, the size of the condensate is almost an order of magnitude smaller and the interaction times are correspondingly shorter, resulting in a much lower scattering probability. Furthermore, s-wave scattering spheres can also be seen in the diagonal direction due to collisions between the diagonal momentum components and the central $p = 0\hbar k$ momentum component. For a maximum trapping depth of $12E_r$ all of these eight scattering spheres [see Fig. 2(b)] are clearly visible in Fig. 2(a). For the parameters used in our experiment the photon scattering rate is 2 orders of magnitude

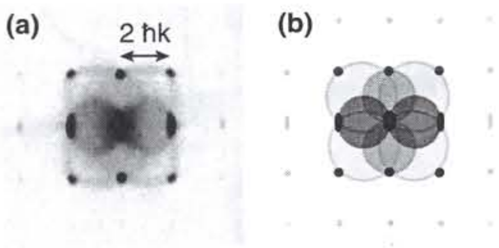

FIG. 2. (a) Average over 5 absorption images of released Bose-Einstein condensates that were stored in a 2D optical lattice potential. The maximum potential depth of the lattice was $12E_r$ and the ballistic expansion time was set to 12 ms. (b) Schematic image showing the expected discrete momentum states and the possible s-wave scattering spheres. Higher order momentum components (e.g., $4\hbar k$) are also visible in (a).

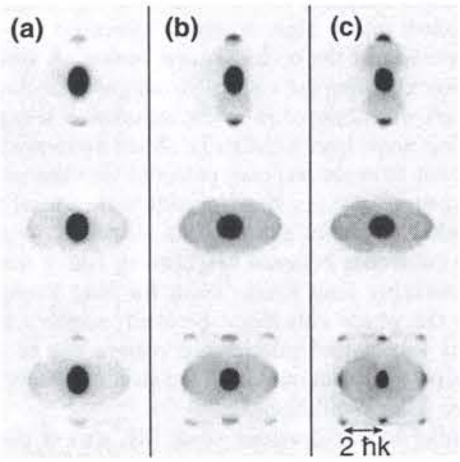

FIG. 3. Absorption images of Bose-Einstein condensates released from optical lattices of different geometry and intensity. Top row: One-dimensional lattice oriented vertically. Middle row: One-dimensional lattice oriented horizontally. Bottom row: Two-dimensional lattice oriented along the vertical and horizontal direction. The images were taken for peak optical lattice depths of (a) $4E_r$, (b) $8E_r$, and (c) 12 E_r.

below that in Ref. [14], so that superradiant effects should not occur. Because of the symmetry of our standing wave field we do not expect additional momentum components to be generated by four-wave mixing [15].

The wave function of the Bose-Einstein condensate in the optical lattice can be expressed as a sum of localized wave functions on each lattice site. Such a localized wave function is described by a Gaussian wave function for the ground state of the tightly confining radial axis of a single lattice tube, with radial widths as low as 90 nm. Along the weakly confining axis of a lattice tube, the repulsive interactions between the atoms result in a parabolic Thomas-Fermi profile with a maximum radial width of $\approx 5\,\mu$m. The maximum chemical potential per lattice tube of $\mu \approx h \times 6$ kHz is then much smaller than the radial energy level spacing, confining the radial atomic motion to zero point oscillations.

In addition to a strong dependence of the visibility of the higher order momentum components on the localization of the wave function, we find a suppression of momentum components due to structural properties of the optical lattice. For a lattice configuration with orthogonal polarization vectors between the two standing waves for which the last term in the sum of Eq. (1) vanishes [see Fig. 4(a)], the first order diagonal momentum components with $|p| = \sqrt{2}\,\hbar k$ are completely suppressed, as can be seen in Fig. 4(b). This is caused by a destructive interference between matter waves emitted from neighboring diagonal lattice planes and results in a vanishing geometrical structure factor of these momentum components [16]. If the lattice configuration is changed to parallel polarization vectors between the two standing waves, such that $\mathbf{e}_1 \cdot \mathbf{e}_2 = 1$, and the time phase is set to $\phi = 0$, the last term in Eq. (1) modifies the geometry of the lattice [see Fig. 4(c)]. For this lattice configuration the geometrical structure factor for the diagonal momentum components with $|p| = \sqrt{2}\,\hbar k$ does not vanish, and these components are clearly visible in the experiment [see Fig. 4(d)].

We determine the lifetime of the condensate in the optical lattice by measuring the number of condensed atoms after ramping down the lattice potential. The following experimental sequence is used. The lattice is ramped up to its final strength within 40 ms and then the atoms are held for a variable period of time in the lattice potential. Subsequently, the lattice potential is ramped down within 40 ms and the remaining number of condensed atoms is measured using absorption imaging after a ballistic expansion. The slow ramp speed ensures that the many-body wave function adjusts adiabatically to the changing optical potential. The results of these measurements are displayed in Fig. 5 for a lattice configuration with orthogonal polarization vectors $\mathbf{e}_1 \cdot \mathbf{e}_2 = 0$ [see Fig. 4(a)]. The reduction of the lifetime of the condensate due to the presence of the optical lattice is shown for three different potential depths. We believe that this reduced lifetime is caused by residual fluctuations of the lattice potential which lead to a dephasing of neighboring condensates with time. In a deep potential the dephasing occurs faster due to the reduced tunnel coupling. This may also be considered in a band structure picture, where the width of the energy bands decreases strongly with increasing potential depth, so that the system becomes more susceptible to perturbations. As a result, transitions within a single band may occur; i.e., the atoms remain within the ground state of a single lattice site, but no longer exhibit phase coherence to neighboring sites. The dephased Bose-Einstein condensates are not expected to recombine into a single condensate when the optical lattice potential is turned off adiabatically. We identify this as the major contribution to the observed decrease in condensate fraction with increasing storage time. We have also verified that the remaining condensate fraction and the interference pattern after a sudden switch-off vanish for the same parameters and holding times. Because of the background of atoms which undergo s-wave

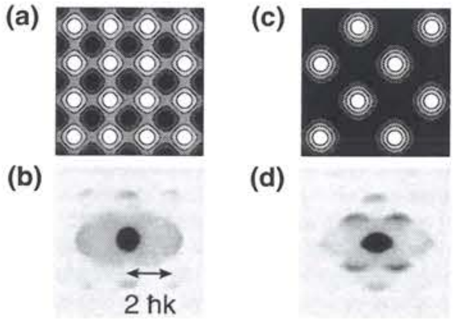

FIG. 4. Influence of the lattice configuration on the momentum distribution. For an optical lattice of (a) with orthogonal polarization vectors $\mathbf{e}_1 \cdot \mathbf{e}_2 = 0$ the first diagonal momentum orders with $|p| = \sqrt{2}\,\hbar k$ are suppressed (b) due to their vanishing geometrical structure factor. In contrast, if $\mathbf{e}_1 \cdot \mathbf{e}_2 = 1$ and $\phi = 0$ as in (c), the resulting geometrical structure factor does not vanish for these momentum components and they are strongly visible (d).

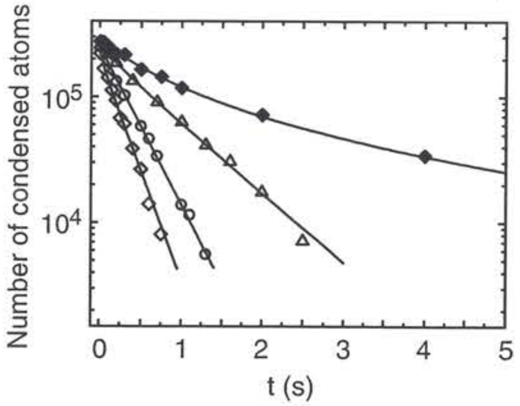

FIG. 5. Remaining number of condensed atoms after a variable hold time in the combined potential of the magnetic trap and the lattice potential (open data points) and in a pure magnetic trapping potential (solid diamonds). The maximum potential depth of the lattice was $4E_r$ (open triangles), $8E_r$ (open circles), and $12E_r$ (open diamonds), respectively.

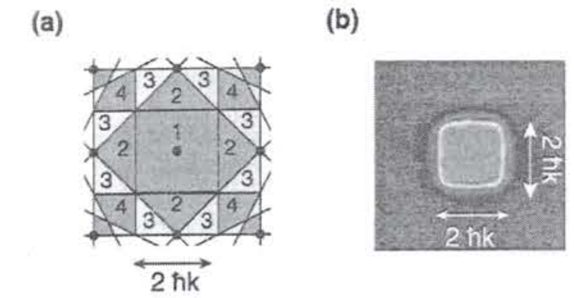

FIG. 6 (color). (a) Reciprocal lattice and Brillouin zones for the two-dimensional Bravais lattice of Fig. 4(a). (b) False color image of the experimentally measured band population of a dephased Bose-Einstein condensate in a $12E_r$ deep optical lattice where phase coherence between neighboring lattice sites has been lost.

scattering, the measurement of the interference pattern is less suitable to quantitatively analyze the coherent fraction of atoms in the lattice.

The dephasing of the condensate wave function in the optical lattice becomes clearly visible when we introduce an external perturbation by switching off the magnetic trapping field and thereby exposing the atoms to the linear gravitational potential. For a $12E_r$ deep optical lattice and 2 ms after switching off the magnetic field we can no longer observe an interference pattern in the density distribution of the released atoms. This indicates that phase coherence of the atoms across the lattice has been lost. To experimentally determine which energy bands are populated by the dephased Bose-Einstein condensate, we ramp down the optical potential in 2 ms, after the 2 ms hold time in the pure optical potential. This ramp speed ensures that we are adiabatic with respect to the atomic motion in a single lattice site and preserve the band population. The momentum distribution of the atomic cloud is obtained by imaging the atoms after 12 ms of ballistic expansion. Atoms originating from the lowest energy band are then expected to obtain momenta that lie within the first Brillouin zone of the lattice [17]. The Brillouin zones of a two-dimensional Bravais lattice are displayed in Fig. 6(a). The experimentally measured momentum distribution shown in Fig. 6(b) exhibits a pronounced squarelike momentum distribution of width $2\hbar k$ coinciding with the first Brillouin zone of the Bravais lattices. This proves that the atoms from the dephased condensate populate only the lowest energy band of the lattice and remain in the radial ground state of a single lattice tube even if the phase coherence between neighboring lattice sites has vanished.

Employing the same method we have measured the band population in the combined potential of the magnetic trap and the optical lattice. For a $12E_r$ deep lattice and after a storage time of 1 s we find that 60% of the initial number of atoms are still present and that all of these atoms remain confined to the first energy band. For the same parameters no significant condensate fraction was measured (see Fig. 5). So far, we cannot identify whether axial excitations are present in a single lattice tube.

In conclusion, we have created an experimental system which now enables us to study the physics of ultracold 1D quantum gases (see also [18]). A variety of fundamental questions of the physics in reduced dimensions can now be addressed in the experiment. The correlation properties of 1D quantum gases are intrinsically different from those encountered in 3D. It is expected that in a 1D gas the decrease of temperature leads to a continuous transformation of the correlation properties from the ideal gas case to the regime which is dominated by quantum statistics and interactions [4]. In the extreme limit of low atomic densities or large interactions even the character of the bosonic particles changes and the gas acquires Fermi properties [1–5].

By adding a further standing wave laser field we can extend the geometry of the lattice to three dimensions. This should pave the way towards the observation of a quantum phase transition in a dilute gas of atoms from a superfluid to a Mott insulator phase [19]. We believe that straightforward modification of our experiment should allow us to reach this regime.

We thank Wilhelm Zwerger and Martin Holthaus for stimulating discussions and Anton Scheich for experimental assistance during the construction of the experiment. We also acknowledge support by the Deutsche Forschungsgemeinschaft.

---

*Also at Department of Physics, University of Florence, Italy.

[1] M. Girardeau, J. Math. Phys. (N.Y.) **1**, 516 (1960).
[2] E. H. Lieb and W. Liniger, Phys. Rev. **130**, 1605 (1962); E. H. Lieb, Phys. Rev. **130**, 1616 (1963).
[3] M. Olshanii, Phys. Rev. Lett. **81**, 938 (1998).
[4] D. S. Petrov, G. V. Shlyapnikov, and J. T. M. Walraven, Phys. Rev. Lett. **85**, 3745 (2000).
[5] M. D. Girardeau, E. M. Wright, and J. M. Triscari, Phys. Rev. A **63**, 033601 (2001).
[6] B. P. Anderson and M. A. Kasevich, Science **281**, 1686 (1998).
[7] C. Orzel *et al.*, Science **291**, 2386 (2001).
[8] M. Greiner, I. Bloch, T. W. Hänsch, and T. Esslinger, Phys. Rev. A **63**, 031401 (2001).
[9] T. Esslinger, I. Bloch, and T. W. Hänsch, Phys. Rev. A **58**, 2664 (1998).
[10] R. Grimm, M. Weidemüller, and Y. B. Ovchinnikov, Adv. At. Mol. Opt. Phys. **42**, 95–170 (2000), and references therein.
[11] A. Hemmerich *et al.*, Europhys. Lett. **18**, 391 (1992).
[12] Y. B. Band *et al.*, Phys. Rev. Lett. **84**, 5462 (2000).
[13] A. P. Chikkatur *et al.*, Phys. Rev. Lett. **85**, 483 (2000).
[14] S. Inouye *et al.*, Science **285**, 571 (1999).
[15] L. Deng *et al.*, Nature (London) **398**, 218 (1999).
[16] See, for example, N. W. Ashcroft and N. D. Mermin, *Solid State Physics* (Saunders College Publishing, Fort Worth, TX, 1976).
[17] A. Kastberg *et al.*, Phys. Rev. Lett. **74**, 1542 (1995).
[18] A. Görlitz *et al.*, cond-mat/0104549.
[19] D. Jacksch *et al.*, Phys. Rev. Lett. **81**, 3108 (1998).

Quantum phase transition from a superfluid to a Mott insulator in a gas of ultracold atoms

Markus Greiner*, Olaf Mandel*, Tilman Esslinger†, Theodor W. Hänsch* & Immanuel Bloch*

* *Sektion Physik, Ludwig-Maximilians-Universität, Schellingstrasse 4/III, D-80799 Munich, Germany, and Max-Planck-Institut für Quantenoptik, D-85748 Garching, Germany*
† *Quantenelektronik, ETH Zürich, 8093 Zurich, Switzerland*

For a system at a temperature of absolute zero, all thermal fluctuations are frozen out, while quantum fluctuations prevail. These microscopic quantum fluctuations can induce a macroscopic phase transition in the ground state of a many-body system when the relative strength of two competing energy terms is varied across a critical value. Here we observe such a quantum phase transition in a Bose–Einstein condensate with repulsive interactions, held in a three-dimensional optical lattice potential. As the potential depth of the lattice is increased, a transition is observed from a superfluid to a Mott insulator phase. In the superfluid phase, each atom is spread out over the entire lattice, with long-range phase coherence. But in the insulating phase, exact numbers of atoms are localized at individual lattice sites, with no phase coherence across the lattice; this phase is characterized by a gap in the excitation spectrum. We can induce reversible changes between the two ground states of the system.

A physical system that crosses the boundary between two phases changes its properties in a fundamental way. It may, for example, melt or freeze. This macroscopic change is driven by microscopic fluctuations. When the temperature of the system approaches zero, all thermal fluctuations die out. This prohibits phase transitions in classical systems at zero temperature, as their opportunity to change has vanished. However, their quantum mechanical counterparts can show fundamentally different behaviour. In a quantum system, fluctuations are present even at zero temperature, due to Heisenberg's uncertainty relation. These quantum fluctuations may be strong enough to drive a transition from one phase to another, bringing about a macroscopic change.

A prominent example of such a quantum phase transition is the change from the superfluid phase to the Mott insulator phase in a system consisting of bosonic particles with repulsive interactions hopping through a lattice potential. This system was first studied theoretically in the context of superfluid-to-insulator transitions in liquid helium[1]. Recently, Jaksch *et al.*[2] have proposed that such a transition might be observable when an ultracold gas of atoms with repulsive interactions is trapped in a periodic potential. To illustrate this idea, we consider an atomic gas of bosons at low enough temperatures that a Bose–Einstein condensate is formed. The condensate is a superfluid, and is described by a wavefunction that exhibits long-range phase coherence[3]. An intriguing situation appears when the condensate is subjected to a lattice potential in which the bosons can move from one lattice site to the next only by tunnel coupling. If the lattice potential is turned on smoothly, the system remains in the superfluid phase as long as the atom–atom interactions are small compared to the tunnel coupling. In this regime a delocalized wavefunction minimizes the dominant kinetic energy, and therefore also minimizes the total energy of the many-body system. In the opposite limit, when the repulsive atom–atom interactions are large compared to the tunnel coupling, the total energy is minimized when each lattice site is filled with the same number of atoms. The reduction of fluctuations in the atom number on each site leads to increased fluctuations in the phase. Thus in the state with a fixed atom number per site phase coherence is lost. In addition, a gap in the excitation spectrum appears. The competition between two terms in the underlying hamiltonian (here between kinetic and interaction energy) is fundamental to quantum phase transitions[4] and inherently different from normal phase transitions, which are usually driven by the competition between inner energy and entropy.

The physics of the above-described system is captured by the Bose–Hubbard model[1], which describes an interacting boson gas in a lattice potential. The hamiltonian in second quantized form reads:

$$H = -J\sum_{\langle i,j\rangle}\hat{a}_i^\dagger\hat{a}_j + \sum_i \epsilon_i\hat{n}_i + \frac{1}{2}U\sum_i \hat{n}_i(\hat{n}_i - 1) \qquad (1)$$

Here $\hat{a}_i$ and $\hat{a}_i^\dagger$ correspond to the bosonic annihilation and creation operators of atoms on the ith lattice site, $\hat{n}_i = \hat{a}_i^\dagger\hat{a}_i$ is the atomic number operator counting the number of atoms on the ith lattice site, and ϵ_i denotes the energy offset of the ith lattice site due to an external harmonic confinement of the atoms[2]. The strength of the tunnelling term in the hamiltonian is characterized by the hopping matrix element between adjacent sites i,j $J = -\int d^3x\, w(\mathbf{x}-\mathbf{x}_i)(-\hbar^2\nabla^2/2m + V_{\mathrm{lat}}(\mathbf{x}))w(\mathbf{x}-\mathbf{x}_j)$, where $w(\mathbf{x}-\mathbf{x}_i)$ is a single particle Wannier function localized to the ith lattice site (as long as $n_i \approx O(1)$), $V_{\mathrm{lat}}(\mathbf{x})$ indicates the optical lattice potential and m is the mass of a single atom. The repulsion between two atoms on a single lattice site is quantified by the on-site interaction matrix element $U = (4\pi\hbar^2 a/m)\int|w(\mathbf{x})|^4 d^3x$, with a being the scattering length of an atom. In our case the interaction energy is very well described by the single parameter U, due to the short range of the interactions, which is much smaller than the lattice spacing.

In the limit where the tunnelling term dominates the hamiltonian, the ground-state energy is minimized if the single-particle wavefunctions of N atoms are spread out over the entire lattice with M lattice sites. The many-body ground state for a homogeneous system ($\epsilon_i = \text{const.}$) is then given by:

$$|\Psi_{\mathrm{SF}}\rangle_{U=0} \propto \left(\sum_{i=1}^{M}\hat{a}_i^\dagger\right)^N |0\rangle \qquad (2)$$

Here all atoms occupy the identical extended Bloch state. An important feature of this state is that the probability distribution for the local occupation n_i of atoms on a single lattice site is poissonian, that is, its variance is given by $\mathrm{Var}(n_i) = \langle \hat{n}_i \rangle$. Furthermore, this state is well described by a macroscopic wavefunction with long-range phase coherence throughout the lattice.

If interactions dominate the hamiltonian, the fluctuations in atom number of a Poisson distribution become energetically very costly and the ground state of the system will instead consist of localized atomic wavefunctions with a fixed number of atoms per site that minimize the interaction energy. The many-body ground state is then a product of local Fock states for each lattice site. In this limit, the ground state of the many-body system for a commensurate filling of n atoms per lattice site in the homogeneous case is given by:

$$|\Psi_{\mathrm{MI}}\rangle_{J=0} \propto \prod_{i=1}^{M} (\hat{a}_i^{\dagger})^n |0\rangle \qquad (3)$$

This Mott insulator state cannot be described by a macroscopic wavefunction like in a Bose condensed phase, and thus is not amenable to a treatment via the Gross-Pitaevskii equation or Bogoliubov's theory of weakly interacting bosons. In this state no phase coherence is prevalent in the system, but perfect correlations in the atom number exist between lattice sites.

As the strength of the interaction term relative to the tunnelling term in the Bose–Hubbard hamiltonian is changed, the system reaches a quantum critical point in the ratio of U/J, for which the system will undergo a quantum phase transition from the superfluid state to the Mott insulator state. In three dimensions, the phase transition for an average number of one atom per lattice site is expected to occur at $U/J = z \times 5.8$ (see refs 1, 5, 6, 7), with z being the number of next neighbours of a lattice site. The qualitative change in the ground-state configuration below and above the quantum critical point is also accompanied by a marked change in the excitation spectrum of the system. In the superfluid regime, the excitation spectrum is gapless whereas the Mott insulator phase exhibits a gap in the excitation spectrum[5–8]. An essential feature of a quantum phase transition is that this energy gap Δ opens up as the quantum critical point is crossed.

Studies of the Bose–Hubbard hamiltonian have so far included granular superconductors[9,10] and one- and two-dimensional Josephson junction arrays[11–16]. In the context of ultracold atoms, atom number squeezing has very recently been demonstrated with a Bose–Einstein condensate in a one-dimensional optical lattice[17]. The above experiments were mainly carried out in the limit of large boson occupancies n_i per lattice site, for which the problem can be well described by a chain of Josephson junctions.

In our present experiment we load ^{87}Rb atoms from a Bose–Einstein condensate into a three-dimensional optical lattice potential. This system is characterized by a low atom occupancy per lattice site of the order of $\langle n_i \rangle \approx 1 - 3$, and thus provides a unique testing ground for the Bose–Hubbard model. As we increase the lattice potential depth, the hopping matrix element J decreases exponentially but the on-site interaction matrix element U increases. We are thereby able to bring the system across the critical ratio in U/J, such that the transition to the Mott insulator state is induced.

Experimental technique

The experimental set-up and procedure to create ^{87}Rb Bose–Einstein condensates are similar to those in our previous experimental work[18,19]. In brief, spin-polarized samples of laser-cooled atoms in the ($F = 2$, $m_F = 2$) state are transferred into a cigar-shaped magnetic trapping potential with trapping frequencies of $\nu_{\mathrm{radial}} = 240$ Hz and $\nu_{\mathrm{axial}} = 24$ Hz. Here F denotes the total angular momentum and m_F the magnetic quantum number of the state. Forced radio-frequency evaporation is used to create Bose–Einstein condensates with up to 2×10^5 atoms and no discernible thermal component. The radial trapping frequencies are then relaxed over a period of 500 ms to $\nu_{\mathrm{rad}} = 24$ Hz such that a spherically symmetric Bose–Einstein condensate with a Thomas–Fermi diameter of 26 μm is present in the magnetic trapping potential.

In order to form the three-dimensional lattice potential, three optical standing waves are aligned orthogonal to each other, with their crossing point positioned at the centre of the Bose–Einstein condensate. Each standing wave laser field is created by focusing a laser beam to a waist of 125 μm at the position of the condensate. A second lens and a mirror are then used to reflect the laser beam back onto itself, creating the standing wave interference pattern. The lattice beams are derived from an injection seeded tapered amplifier and a laser diode operating at a wavelength of $\lambda = 852$ nm. All beams are spatially filtered and guided to the experiment using optical fibres. Acousto-optical modulators are used to control the intensity of the lattice beams and introduce a frequency difference of about 30 MHz between different standing wave laser fields. The polarization of a standing wave laser field is chosen to be linear and orthogonal polarized to all other standing waves. Due to the different frequencies in each standing wave, any residual interference between beams propagating along orthogonal directions is time-averaged to zero and therefore not seen by the atoms. The resulting three-dimensional optical potential (see ref. 20 and references therein) for the atoms is then proportional to the sum of the intensities of the three standing waves, which leads to a simple cubic type geometry of the lattice:

$$V(x, y, z) = V_0(\sin^2(kx) + \sin^2(ky) + \sin^2(kz)) \qquad (4)$$

Here $k = 2\pi/\lambda$ denotes the wavevector of the laser light and V_0 is the maximum potential depth of a single standing wave laser field. This depth V_0 is conveniently measured in units of the recoil energy $E_{\mathrm{r}} = \hbar^2 k^2/2m$. The confining potential for an atom on a single lattice site due to the optical lattice can be approximated by a harmonic potential with trapping frequencies ν_{r} on the order of $\nu_{\mathrm{r}} \approx (\hbar k^2/2\pi m)\sqrt{V_0/E_{\mathrm{r}}}$. In our set-up potential depths of up to 22 E_{r} can be reached, resulting in trapping frequencies of approximately $\nu_{\mathrm{r}} \approx 30$ kHz. The gaussian intensity profile of the laser beams at the position of the condensate creates an additional weak isotropic harmonic confinement over the lattice, with trapping frequencies of 65 Hz for a potential depth of 22 E_{r}.

The magnetically trapped condensate is transferred into the optical lattice potential by slowly increasing the intensity of the lattice laser beams to their final value over a period of 80 ms using an exponential ramp with a time constant of $\tau = 20$ ms. The slow ramp speed ensures that the condensate always remains in the many-body ground state of the combined magnetic and optical trapping potential. After raising the lattice potential the condensate has been distributed over more than 150,000 lattice sites (~65 lattice sites in a single direction) with an average atom number of up to 2.5 atoms per lattice site in the centre.

In order to test whether there is still phase coherence between different lattice sites after ramping up the lattice potential, we suddenly turn off the combined trapping potential. The atomic wavefunctions are then allowed to expand freely and interfere with each other. In the superfluid regime, where all atoms are delocalized over the entire lattice with equal relative phases between different lattice sites, we obtain a high-contrast three-dimensional interference pattern as expected for a periodic array of phase coherent matter wave sources (see Fig. 1). It is important to note that the sharp interference maxima directly reflect the high degree of phase coherence in the system for these experimental values.

Entering the Mott insulator phase

As we increase the lattice potential depth, the resulting interference pattern changes markedly (see Fig. 2). Initially the strength of higher-order interference maxima increases as we raise the potential height, due to the tighter localization of the atomic wavefunctions at a single lattice site. Quite unexpectedly, however, at a potential depth of around 13 E_{r} the interference maxima no longer increase in strength (see Fig. 2e): instead, an incoherent background of atoms gains more and more strength until at a potential depth of 22 E_{r} no interference pattern is visible at all. Phase coherence has obviously been completely lost at this lattice potential depth. A remarkable feature during the evolution from the coherent to the incoherent state is that when the interference pattern is still visible no broadening of the interference peaks can be detected until they completely vanish in the incoherent background. This behaviour can be explained on the basis of the superfluid–Mott insulator phase diagram. After the system has crossed the quantum critical point $U/J = z \times 5.8$, it will evolve in the inhomogeneous case into alternating regions of incoherent Mott insulator phases and coherent superfluid phases[2], where the superfluid fraction continuously decreases for increasing ratios U/J.

Restoring coherence

A notable property of the Mott insulator state is that phase coherence can be restored very rapidly when the optical potential is lowered again to a value where the ground state of the many-body system is completely superfluid. This is shown in Fig. 3. After only 4 ms of ramp-down time, the interference pattern is fully visible again, and after 14 ms of ramp-down time the interference peaks have narrowed to their steady-state value, proving that phase coherence has been restored over the entire lattice. The timescale for the restoration of coherence is comparable to the tunnelling time $\tau_{\mathrm{tunnel}} = \hbar/J$ between two neighbouring lattice sites in the system, which is of the order of 2 ms for a lattice with a potential depth of 9 E_{r}. A significant degree of phase coherence is thus already restored on the timescale of a tunnelling time.

It is interesting to compare the rapid restoration of coherence coming from a Mott insulator state to that of a phase incoherent state, where random phases are present between neighbouring lattice sites and for which the interference pattern also vanishes. This is shown in Fig. 3b, where such a phase incoherent state is created during the ramp-up time of the lattice potential (see Fig. 3 legend) and where an otherwise identical experimental sequence is used. Such phase incoherent states can be clearly identified by adiabatically mapping the population of the energy bands onto the Brillouin zones[19,21]. When we turn off the lattice potential adiabatically, we find that a statistical mixture of states has been created, which homogeneously populates the first Brillouin zone of

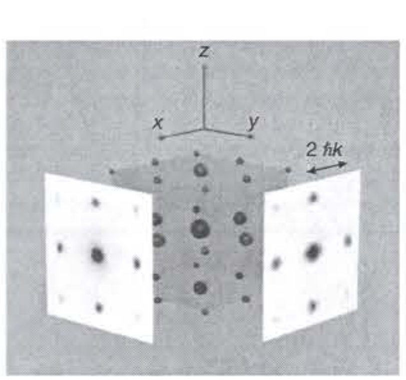

Figure 1 Schematic three-dimensional interference pattern with measured absorption images taken along two orthogonal directions. The absorption images were obtained after ballistic expansion from a lattice with a potential depth of $V_0 = 10E_{\mathrm{r}}$ and a time of flight of 15 ms.

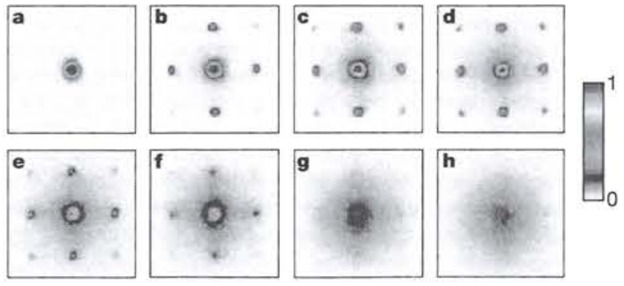

Figure 2 Absorption images of multiple matter wave interference patterns. These were obtained after suddenly releasing the atoms from an optical lattice potential with different potential depths V_0 after a time of flight of 15 ms. Values of V_0 were: **a**, 0 E_{r}; **b**, 3 E_{r}; **c**, 7 E_{r}; **d**, 10 E_{r}; **e**, 13 E_{r}; **f**, 14 E_{r}; **g**, 16 E_{r}; and **h**, 20 E_{r}.

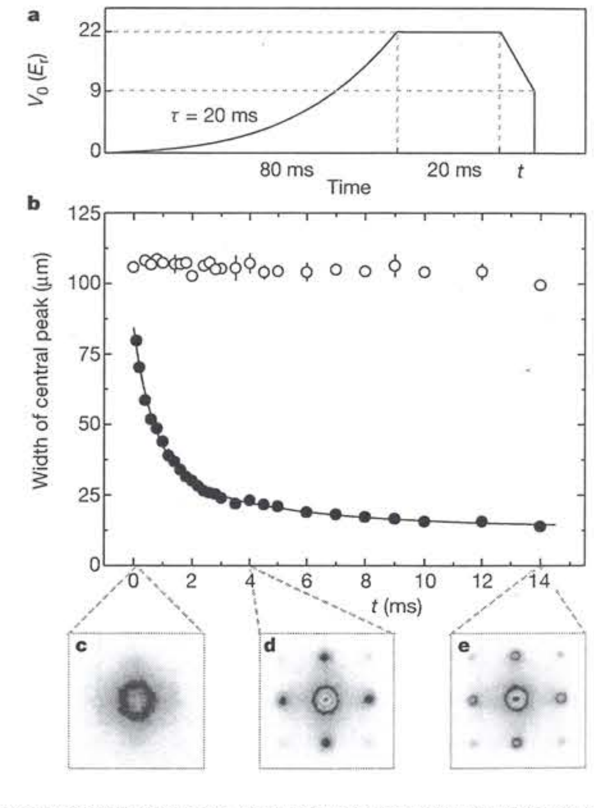

Figure 3 Restoring coherence. **a**, Experimental sequence used to measure the restoration of coherence after bringing the system into the Mott insulator phase at $V_0 = 22E_{\mathrm{r}}$ and lowering the potential afterwards to $V_0 = 9E_{\mathrm{r}}$, where the system is superfluid again. The atoms are first held at the maximum potential depth V_0 for 20 ms, and then the lattice potential is decreased to a potential depth of 9 E_{r} in a time t after which the interference pattern of the atoms is measured by suddenly releasing them from the trapping potential. **b**, Width of the central interference peak for different ramp-down times t, based on a lorentzian fit. In case of a Mott insulator state (filled circles) coherence is rapidly restored already after 4 ms. The solid line is a fit using a double exponential decay ($\tau_1 = 0.94(7)$ ms, $\tau_2 = 10(5)$ ms). For a phase incoherent state (open circles) using the same experimental sequence, no interference pattern reappears again, even for ramp-down times t of up to 400 ms. We find that phase incoherent states are formed by applying a magnetic field gradient over a time of 10 ms during the ramp-up period, when the system is still superfluid. This leads to a dephasing of the condensate wavefunction due to the nonlinear interactions in the system. **c–e**, Absorption images of the interference patterns coming from a Mott insulator phase after ramp-down times t of 0.1 ms (**c**), 4 ms (**d**), and 14 ms (**e**).

the three-dimensional lattice. This homogeneous population proves that all atoms are in the vibrational ground state of the lattice, but the relative phase between lattice sites is random. Figure 3b shows that no phase coherence is restored at all for such a system over a period of 14 ms. Even for evolution times t of up to 400 ms, no reappearance of an interference pattern could be detected. This demonstrates that the observed loss of coherence with increasing potential depth is not simply due to a dephasing of the condensate wavefunction.

Probing the excitation spectrum

In the Mott insulator state, the excitation spectrum is substantially modified compared to that of the superfluid state. The excitation spectrum has now acquired an energy gap Δ, which in the limit $J \ll U$ is equal to the on-site interaction matrix element $\Delta = U$ (see refs 5–8). This can be understood within a simplified picture in the following way. We consider a Mott insulator state with exactly $n = 1$ atom per lattice site. The lowest lying excitation for such a state is the creation of a particle–hole pair, where an atom is removed from a lattice site and added to a neighbouring lattice site (see Fig. 4a). Due to the on-site repulsion between two atoms, the energy of the state describing two atoms in a single lattice site is raised by an amount U in energy above the state with only a single atom in this lattice site. Therefore in order to create an excitation the finite amount of energy U is required. It can be shown that this is also true for number states with exactly n atoms per lattice site. Here the energy required to make a particle–hole excitation is also U. Hopping of particles throughout the lattice is therefore suppressed in the Mott insulator phase, as this energy is only available in virtual processes. If now the lattice potential is tilted by application of a potential gradient, tunnelling is allowed again if the energy difference between neighbouring lattice sites due to the potential gradient equals the on-site interaction energy U (see Fig. 4b). We thus expect a resonant excitation probability versus the applied energy difference between neighbouring lattice sites for a Mott insulator phase.

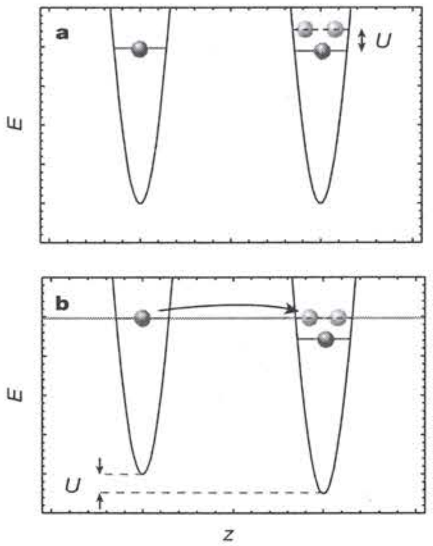

Figure 4 Excitation gap in the Mott insulator phase with exactly $n = 1$ atom per lattice site. **a**, The lowest lying excitations in the Mott insulator phase consist of removing an atom from a lattice site and adding it to neighbouring lattice sites. Owing to the on-site repulsion between the atoms, this requires a finite amount U in energy and hopping of the atoms is therefore suppressed. **b**, If a potential gradient is applied to the system along the z-direction, such that the energy difference between neighbouring lattice sites equals the on-site interaction energy U, atoms are allowed to tunnel again. Particle–hole excitations are then created in the Mott insulator phase.

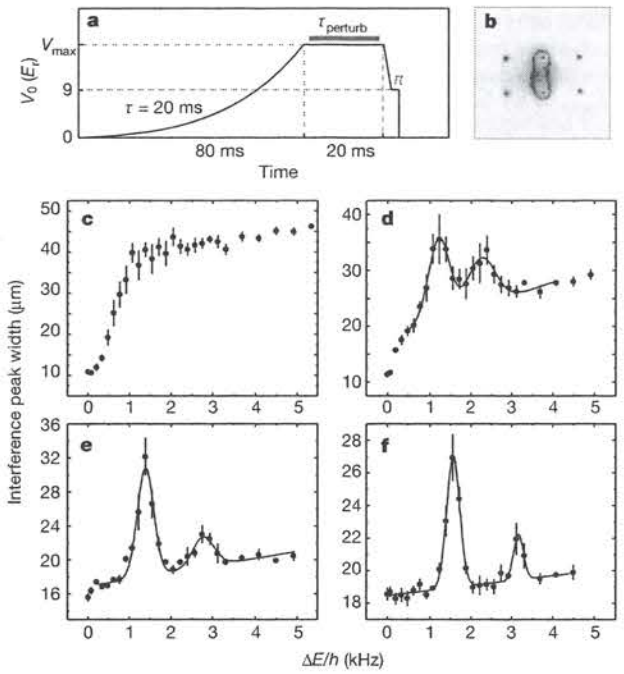

Figure 5 Probing the excitation probability versus an applied vertical potential gradient. **a**, Experimental sequence. The optical lattice potential is increased in 80 ms to a potential depth $V_0 = V_{\mathrm{max}}$. Then the atoms are held for a time of 20 ms at this potential depth, during which a potential gradient is applied for a time τ_{perturb}. The optical potential is then lowered again within 3 ms to a value of $V_0 = 9E_r$, for which the system is superfluid again. Finally, a potential gradient is applied for 300 μs with a fixed strength, such that the phases between neighbouring lattice sites in the vertical direction differ by π. The confining potential is then rapidly turned off and the resulting interference pattern is imaged after a time of flight of 15 ms (**b**). Excitations created by the potential gradient at a lattice depth of $V_0 = V_{\mathrm{max}}$ will lead to excitations in the superfluid state at $V_0 = 9E_r$. Here excitations correspond to phase fluctuations across the lattice, which will influence the width of the observed interference peaks. **c–f**, Width of interference peaks versus the energy difference between neighbouring lattice sites ΔE, due to the potential gradient applied for a time τ_{perturb}. **c**, $V_{\mathrm{max}} = 10E_r$, $\tau_{\mathrm{perturb}} = 2$ ms; **d**, $V_{\mathrm{max}} = 13E_r$, $\tau_{\mathrm{perturb}} = 6$ ms; **e**, $V_{\mathrm{max}} = 16E_r$, $\tau_{\mathrm{perturb}} = 10$ ms; and **f**, $V_{\mathrm{max}} = 20E_r$, $\tau_{\mathrm{perturb}} = 20$ ms. The perturbation times τ_{perturb} have been prolonged for deeper lattice potentials in order to account for the increasing tunnelling times. The solid lines are fits to the data based on two gaussians on top of a linear background.

We probe this excitation probability by using the experimental sequence shown in Fig. 5a. If excitations have been created during the application of the potential gradient at the potential depth $V_0 = V_{\mathrm{max}}$, we will not be able to return to a perfectly coherent superfluid state by subsequently lowering the potential to a depth of $V_0 = 9E_r$. Instead, excitations in the Mott insulator phase will lead to excitations in the lowest energy band in the superfluid case. These excitations are simply phase fluctuations between lattice sites, and cause a broadening of the interference maxima in the interference pattern (see Fig. 5b). Figure 5c–f shows the width of the interference peaks versus the applied gradient for four different potential depths V_{max}. For a completely superfluid system at 10 E_r, the system is easily perturbed already for small potential gradients and for stronger gradients a complete dephasing of the wavefunctions leads to a saturation in the width of the interference peaks. At a potential depth of about 13 E_r two broad resonances start to appear in the excitation spectrum, and for a potential depth of 20 E_r a dramatic change in the excitation spectrum has taken place. Two narrow resonances are now clearly visible on top of an otherwise completely flat excitation probability. The slightly higher offset of the excitation probability for a deep optical lattice (Fig. 5e, f) compared to the initial width of the interference peaks in Fig. 5c, is due to the fact that after 3 ms ramp down time from a deep optical lattice, the system is still in the dynamical process of restoring coherence coming from the Mott insulator phase. For longer hold times this offset approaches almost the same initial width as in Fig. 5c, showing that we are not able to excite the system at all except for the two resonance gradients. At these large potential depths, the narrow resonances show that the energy gap Δ of the system, which is measured here as the minimum energy difference between neighbouring lattice sites for which the system can be perturbed, is almost equal to the centre position of the resonance.

We have in fact found the Mott insulator state to be extremely robust to external perturbations, such as a modulation of the trapping potential or a modulation of the gradient potential, as long as the resonance gradients are avoided. The first resonance can be directly attributed to the creation of single particle–hole excitations in the Mott insulator state, and directly proves that we have indeed entered the Mott insulator regime. The second, weaker resonance occurs at exactly twice the energy difference of the first, stronger resonance. It can most probably be attributed to at least one of the following processes: (1) simultaneous tunnelling of two particles in a Mott insulator phase with $n > 1$ atoms, (2) second-order processes, in which two particle–hole pairs are created simultaneously, with only one in the direction of the applied gradient, and (3) tunnelling processes occurring between lattice sites with $n = 1$ atom next to lattice sites with $n = 2$ atoms. In comparison, a two-dimensional lattice at a maximum potential depth of $V_{\mathrm{max}} = 20E_r$, which we still expect to be in the superfluid regime, shows no resonances but a smooth excitation spectrum, similar to Fig. 5c.

The position of the resonances in the three-dimensional lattice can be seen to shift with increasing potential depth due to the tighter localization of the wave packets on a lattice site (see Fig. 6). We have compared the position of the first resonance versus the potential depth V_{max} to an *ab initio* calculation of U based on Wannier functions from a band structure calculation, and find good agreement within our experimental uncertainties (see Fig. 6).

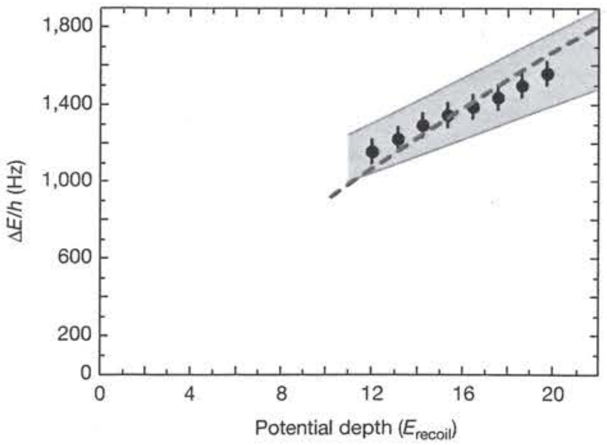

Figure 6 Energy difference between neighbouring lattice sites ΔE for which the Mott insulator phase can be resonantly perturbed versus the lattice potential depth V_{max}. Experimental data points are shown as filled circles, and the shaded grey area denotes the possible variation of experimental values due to systematic uncertainties in the calibration of the potential depth and the applied gradient. The dashed line is the theoretical prediction for the on-site interaction matrix element U, based on Wannier functions from a band structure calculation.

Transition point

Both the vanishing of the interference pattern and the appearance of resonances in the excitation spectrum begin to occur at potential depths of $V_0 = 12(1)–13(1)\,E_r$, indicating the transition to the Mott insulator phase. We therefore expect the experimental transition point to lie above $V_0 = 10(1)\,E_r$, where no resonances are visible, and below $V_0 = 13(1)\,E_r$. It is important to compare this parameter range to the theoretical prediction based on the expected critical value $U/J = z \times 5.8$. In our simple cubic lattice structure, six next neighbours surround a lattice site. J and U can be calculated numerically from a band structure calculation for our experimental parameters, from which we find that $U/J \approx 36$ for a potential depth of 13 E_r. The theoretical prediction for the transition point is therefore in good agreement with the experimental parameter range for the transition point.

Outlook

We have realized experimentally the quantum phase transition from a superfluid to a Mott insulator phase in an atomic gas trapped in an optical lattice. The experiment enters a new regime in the many-body physics of an atomic gas. This regime is dominated by atom–atom interactions and it is not accessible to theoretical treatments of weakly interacting gases, which have so far proved to be very successful in describing the physics of Bose–Einstein condensates[22]. The experimental realization of the Bose–Hubbard model with an atomic gas now allows the study of strongly correlated many-body quantum mechanics with unprecedented control of parameters. For example, besides controlling mainly the tunnelling matrix element, as done in this work, it should be possible in future experiments to control the atom–atom interactions via Feshbach resonances[23,24].

The atoms in the Mott insulator phase can be considered as a new state of matter in atomic gases with unique properties. Atom number fluctuations at each lattice site are suppressed, and a well-defined phase between different lattices sites no longer exists. These number states have been proposed for the realization of a Heisenberg-limited atom interferometer[25], which should be capable of achieving improved levels of precision. The Mott insulator phase also opens a new experimental avenue for recently proposed quantum gates with neutral atoms[26]. ☐

Received 26 October; accepted 29 November 2001.

---

1. Fisher, M. P. A., Weichman, P. B., Grinstein, G. & Fisher, D. S. Boson localization and the superfluid-insulator transition. *Phys. Rev. B* **40,** 546–570 (1989).
2. Jaksch, D., Bruder, C., Cirac, J. I., Gardiner, C. W. & Zoller, P. Cold bosonic atoms in optical lattices. *Phys. Rev. Lett.* **81,** 3108–3111 (1998).
3. Stringari, S. Bose-Einstein condensation and superfluidity in trapped atomic gases. *C.R. Acad. Sci.* **4,** 381–397 (2001).
4. Sachdev, S. *Quantum Phase Transitions* (Cambridge Univ. Press, Cambridge, 2001).
5. Sheshadri, K., Krishnamurthy, H. R., Pandit, R. & Ramakrishnan, T. V. Superfluid and insulating phases in an interacting-boson model: Mean-field theory and the RPA. *Europhys. Lett.* **22,** 257–263 (1993).
6. Freericks, J. K. & Monien, H. Phase diagram of the Bose Hubbard model. *Europhys. Lett.* **26,** 545–550 (1995).
7. van Oosten, D., van der Straten, P. & Stoof, H. T. C. Quantum phases in an optical lattice. *Phys. Rev. A* **63,** 053601-1–053601-12 (2001).
8. Elstner, N. & Monien, H. Dynamics and thermodynamics of the Bose-Hubbard model. *Phys. Rev. B* **59,** 12184–12187 (1999).
9. Orr, B. G., Jaeger, H. M., Goldman, A. M. & Kuper, C. G. Global phase coherence in two-dimensional granular superconductors. *Phys. Rev. Lett.* **56,** 378–381 (1986).
10. Haviland, D. B., Liu, Y. & Goldman, A. M. Onset of superconductivity in the two-dimensional limit. *Phys. Rev. Lett.* **62,** 2180–2183 (1989).
11. Bradley, R. M. & Doniach, S. Quantum fluctuations in chains of Josephson junctions. *Phys. Rev. B* **30,** 1138–1147 (1984).
12. Geerligs, L. J., Peters, M., de Groot, L. E. M., Verbruggen, A. & Mooij, J. E. Charging effects and quantum coherence in regular Josephson junction arrays. *Phys. Rev. Lett.* **63,** 326–329 (1989).
13. Zwerger, W. Global and local phase coherence in dissipative Josephson-junction arrays. *Europhys. Lett.* **9,** 421–426 (1989).

14. van der Zant, H. S. J., Fritschy, F. C., Elion, W. J., Geerligs, L. J. & Mooij, J. E. Field-induced superconductor-to-insulator transitions in Josephson-junction arrays. *Phys. Rev. Lett.* **69,** 2971–2974 (1992).
15. van Oudenaarden, A. & Mooij, J. E. One-dimensional Mott insulator formed by quantum vortices in Josephson junction arrays. *Phys. Rev. Lett.* **76,** 4947–4950 (1996).
16. Chow, E., Delsing, P. & Haviland, D. B. Length-scale dependence of the superconductor-to-insulator quantum phase transition in one dimension. *Phys. Rev. Lett.* **81,** 204–207 (1998).
17. Orzel, C., Tuchman, A. K., Fenselau, M. L., Yasuda, M. & Kasevich, M. A. Squeezed states in a Bose-Einstein condensate. *Science* **291,** 2386–2389 (2001).
18. Greiner, M., Bloch, I., Hänsch, T. W. & Esslinger, T. Magnetic transport of trapped cold atoms over a large distance. *Phys. Rev. A* **63,** 031401-1–031401-4 (2001).
19. Greiner, M., Bloch, I., Mandel, O., Hänsch, T. W. & Esslinger, T. Exploring phase coherence in a 2D lattice of Bose-Einstein condensates. *Phys. Rev. Lett.* **87,** 160405-1–160405-4 (2001).
20. Grimm, R., Weidemüller, M. & Ovchinnikov, Yu. B. Optical dipole traps for neutral atoms. *Adv. At. Mol. Opt. Phys.* **42,** 95–170 (2000).
21. Kastberg, A., Phillips, W. D., Rolston, S. L., Spreeuw, R. J. C. & Jessen, P. S. Adiabatic cooling of cesium to 700 nK in an optical lattice. *Phys. Rev. Lett.* **74,** 1542–1545 (1995).
22. Dalfovo, F. D., Giorgini, S., Pitaevskii, L. P. & Stringari, S. Theory of Bose-Einstein condensation in trapped gases. *Rev. Mod. Phys.* **71,** 463–512 (1999).
23. Inouye, S. *et al.* Observation of Feshbach resonances in a Bose–Einstein condensate. *Nature* **392,** 151–154 (1998).
24. Donley, E. A. *et al.* Dynamics of collapsing and exploding Bose–Einstein condensates. *Nature* **412,** 295–299 (2001).
25. Bouyer, P. & Kasevich, M. Heisenberg-limited spectroscopy with degenerate Bose-Einstein gases. *Phys. Rev. A* **56,** R1083–R1086 (1997).
26. Jaksch, D., Briegel, H.-J., Cirac, J. I., Gardiner, C. W. & Zoller, P. Entanglement of atoms via cold controlled collisions. *Phys. Rev. Lett.* **82,** 1975–1978 (1999).

Acknowledgements

We thank W. Zwerger, H. Monien, I. Cirac, K. Burnett and Yu. Kagan for discussions. This work was supported by the DFG, and by the EU under the QUEST programme.

Competing interests statement

The authors declare that they have no competing financial interests.

Correspondence and requests for materials should be addressed to I.B. (e-mail: imb@mpq.mpg.de).

---

family formation predict that the memory of spin of the original unshattered parent body is lost[3], and existing models of spin angular momentum suggest that collisional evolution randomizes asteroid spin vectors regardless of their initial orientations[2], although the absolute timescale is uncertain. Here, I briefly identify two possible general explanations for future study.

One possibility is that randomly oriented gravitational aggregates from the initial collision have further fragmented, creating smaller objects that have the same spin obliquities as the remnants from which they were formed. Secondary fragmentation of the largest remnant of the initial break-up has previously been proposed to explain the existence of several objects of comparable size among the largest Koronis family members[16], but if the spin clusters were formed in this way then the absence of obvious corresponding associations in proper orbital elements also needs to be explained. To test this hypothesis, further work is needed to better understand the behaviour and evolution of gravitational aggregates.

A second possible explanation for spin clusters is that some dynamical process is aligning the obliquities and matching the rotation rates. Thermal effects can change obliquities and spin rates of small irregular asteroids, but calculations for Ida suggest that asteroids of comparable size are unlikely to have been substantially affected[17]. If a secular effect has clustered the spin vectors, then the present understanding of the timescale over which thermal processes have affected the spin cluster objects may be incomplete, or some nonthermal process may be at work. Finding similar clustering of spins for 20–40-km asteroids outside the Koronis family would support the hypothesis of a secular effect. □

Received 24 May; accepted 18 July 2002; doi:10.1038/nature00993.

1. Chapman, C. R., Paolicchi, P., Zappalà, V., Binzel, R. P. & Bell, J. F. in *Asteroids II* (eds Binzel, R. P., Gehrels, T. & Matthews, M. S.) 386–415 (Univ. Arizona Press, Tucson, 1989).
2. Binzel, R. P. Collisional evolution in the Eos and Koronis asteroid families: Observational and numerical results. *Icarus* **73,** 303–313 (1988).
3. Michel, P., Benz, W., Tanga, P. & Richardson, D. C. Collisions and gravitational reaccumulation: Forming asteroid families and satellites. *Science* **294,** 1696–1700 (2001).
4. Zappalà, V., Bendjoya, Ph., Cellino, A., Farinella, P. & Froeschle, C. Asteroid families: Search of a 12,487-asteroid sample using two different clustering techniques. *Icarus* **116,** 291–314 (1995).
5. Binzel, R. P. A photoelectric survey of 130 asteroids. *Icarus* **72,** 135–208 (1987).
6. Slivan, S. M. *Spin-Axis Alignment of Koronis Family Asteroids* PhD thesis, Massachusetts Institute of Technology (1995).
7. Slivan, S. M. & Binzel, R. P. Forty-eight new rotation lightcurves of 12 Koronis family asteroids. *Icarus* **124,** 452–470 (1996).
8. Slivan, S. M. *et al.* Spin vectors in the Koronis family: Comprehensive results from two independent analyses of 213 rotation lightcurves. *Icarus* (submitted).
9. Drummond, J. D., Weidenschilling, S. J., Chapman, C. R. & Davis, D. R. Photometric geodesy of main-belt asteroids. II. Analysis of lightcurves for poles, periods, and shapes. *Icarus* **76,** 19–77 (1988).
10. Kaasalainen, M. & Torppa, J. Optimization methods for asteroid lightcurve inversion. I. Shape determination. *Icarus* **153,** 24–36 (2001).
11. Kaasalainen, M., Torppa, J. & Muinonen, K. Optimization methods for asteroid lightcurve inversion. II. The complete inverse problem. *Icarus* **153,** 37–51 (2001).
12. Binzel, R. P. *et al.* Asteroid 243 Ida: Ground-based photometry and a pre-Galileo physical model. *Icarus* **105,** 310–325 (1993).
13. Davies, M. E. *et al.* The north pole direction and the control network of the asteroid 243 Ida. *Bull. Am. Astron. Soc.* **26,** 1154–1155 (1994).
14. Miller, I. & Freund, J. E. *Probability and Statistics for Engineers* (Prentice-Hall, Englewood Cliffs, New Jersey, 1977).
15. Belton, M. J. S. *et al.* First images of asteroid 243 Ida. *Science* **265,** 1543–1547 (1994).
16. Marzari, F., Davis, D. & Vanzani, V. Collisional evolution of asteroid families. *Icarus* **113,** 168–187 (1995).
17. Rubincam, D. P. Radiative spin-up and spin-down of small asteroids. *Icarus* **148,** 2–11 (2000).
18. Bowell, E., *et al.* in *Asteroids II* (eds Binzel, R. P., Gehrels, T. & Matthews, M. S.) 524–556 (Univ. Arizona Press, Tucson, 1989).
19. Landolt, A. U. *UVBRI* photometric standard stars around the celestial equator. *Astron. J.* **88,** 439–460 (1983).

Acknowledgements

I thank R. Binzel for advice and encouragement, and M. Kaasalainen, L. Crespo da Silva, M. Lyndaker and M. Krčo for contributions at various stages of this work.

Competing interests statement

The authors declare that they have no competing financial interests.

Correspondence and requests for materials should be addressed to the author (e-mail: slivan@mit.edu).

Collapse and revival of the matter wave field of a Bose–Einstein condensate

Markus Greiner, Olaf Mandel, Theodor W. Hänsch & Immanuel Bloch

Sektion Physik, Ludwig-Maximilians-Universität, Schellingstrasse 4/III, D-80799 Munich, Germany, and Max-Planck-Institut für Quantenoptik, D-85748 Garching, Germany

A Bose–Einstein condensate represents the most 'classical' form of a matter wave, just as an optical laser emits the most classical form of an electromagnetic wave. Nevertheless, the matter wave field has a quantized structure owing to the granularity of the discrete underlying atoms. Although such a field is usually assumed to be intrinsically stable (apart from incoherent loss processes), this is no longer true when the condensate is in a coherent superposition of different atom number states[1–6]. For example, in a Bose–Einstein condensate confined by a three-dimensional optical lattice, each potential well can be prepared in a coherent superposition of different atom number states, with constant relative phases between neighbouring lattice sites. It is then natural to ask how the individual matter wave fields and their relative phases evolve. Here we use such a set-up to investigate these questions experimentally, observing that the matter wave field of the Bose–Einstein condensate undergoes a periodic series of collapses and revivals; this behaviour is directly demonstrated in the dynamical evolution of the multiple matter wave interference pattern. We attribute the oscillations to the quantized structure of the matter wave field and the collisions between individual atoms.

In order to determine the evolution with time of a many-atom state with repulsive interactions in a confining potential, we first assume that all atoms occupy only the ground state of the external potential. The hamiltonian governing the system after subtracting the ground-state energy of the external potential is then solely determined by the interaction energy between the atoms:

$$\hat{H} = \frac{1}{2} U \hat{n}(\hat{n} - 1) \qquad (1)$$

Here $\hat{n}$ counts the number of atoms in the confining potential, and U is the on-site interaction matrix element that characterizes the energy cost due to the repulsive interactions when a second atom is added to the potential well. It can be related to the s-wave scattering length a and the ground-state wavefunction $w(\mathbf{x})$ through $U = 4\pi\hbar^2 a/m \int |w(\mathbf{x})|^4 \, \mathrm{d}^3x$, as long as the vibrational level spacing of the external potential is large compared with the interaction energy. The eigenstates of the above hamiltonian are Fock states $|n\rangle$ in the atom number, with eigenenergies $E_n = Un(n-1)/2$. The evolution with time (t) of such an n-particle state is then simply given by $|n\rangle(t) = |n\rangle(0) \times \exp(-iE_n t/\hbar)$, where ħ is Planck's constant (h) divided by 2π.

We now consider a coherent state $|\alpha\rangle$ (see, for example, ref. 7) of the atomic matter field in a potential well. Such a coherent state with a complex amplitude α and an average number of atoms $\bar{n} = |\alpha|^2$ can be expressed as a superposition of different number states $|n\rangle$ such that $|\alpha\rangle = \exp(-|\alpha|^2/2)\sum_n \frac{\alpha^n}{\sqrt{n!}}|n\rangle$. Now the system is in a superposition of different eigenstates, which evolve in time according to their eigenenergies E_n. This allows us to calculate the evolution with time of an initially coherent state:

$$|\alpha\rangle(t) = \mathrm{e}^{-|\alpha|^2/2} \sum_n \frac{\alpha^n}{\sqrt{n!}} \mathrm{e}^{-i\frac{1}{2}Un(n-1)t/\hbar} |n\rangle \qquad (2)$$

Evaluating the atomic field operator $\hat{a}$ for such a state then yields the

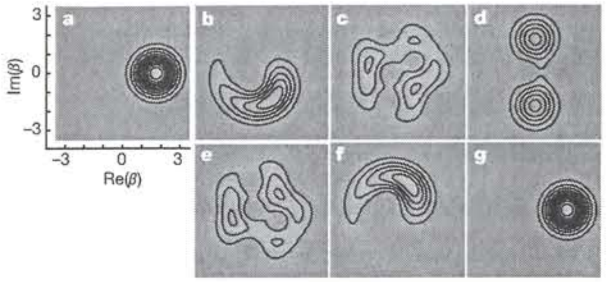

Figure 1 Quantum dynamics of a coherent state owing to cold collisions. The images **a**–**g** show the overlap $|\langle\beta|\alpha(t)\rangle|^2$ of an arbitrary coherent state $|\beta\rangle$ with complex amplitude β with the dynamically evolved quantum state $|\alpha\rangle(t)$ (see equation (2)) for an average number of $|\alpha|^2 = 3$ atoms at different times t. **a**, $t = 0\,h/U$; **b**, 0.1 h/U; **c**, 0.4 h/U; **d**, 0.5 h/U; **e**, 0.6 h/U; **f**, 0.9 h/U; and **g**, h/U. Initially, the phase of the macroscopic matter wave field becomes more and more uncertain as time evolves (**b**), but remarkably at $t_{\mathrm{rev}}/2$ (**d**), when the macroscopic field has collapsed such that $\psi \approx 0$, the system has evolved into an exact 'Schrödinger cat' state of two coherent states. These two states are 180° out of phase, and therefore lead to a vanishing macroscopic field ψ at these times. More generally, we can show that at certain rational fractions of the revival time t_{rev}, the system evolves into other exact superpositions of coherent states—for example, at $t_{\mathrm{rev}}/4$, four coherent states, or at $t_{\mathrm{rev}}/3$, three coherent states[2,4]. A full revival of the initial coherent state is then reached at $t = h/U$. In the graph, red denotes maximum overlap and blue vanishing overlap with 10 contour lines in between.

macroscopic matter wave field $\psi = \langle\alpha(t)|\hat{a}|\alpha(t)\rangle$, which has an intriguing dynamical evolution. At first, the different phase evolutions of the atom number states lead to a collapse of ψ. However, at integer multiples of the revival time $t_{\mathrm{rev}} = h/U$ all phase factors in the sum of equation (2) re-phase modulo 2π, leading to a perfect revival of the initial coherent state. The collapse time t_{c} depends on the variance σ_n^2 of the atom number distribution, such that $t_{\mathrm{c}} \approx t_{\mathrm{rev}}/\sigma_n$ (see refs 1–5). A more detailed picture of the dynamical evolution of ψ can be seen in Fig. 1, where the overlap of an arbitrary coherent state $|\beta\rangle$ with the state $|\alpha\rangle$ (t) is shown for different evolution times up to the first revival time of the many-body state[8,9].

In our experiment, we create coherent states of the matter wave field in a potential well, by loading a magnetically trapped Bose–Einstein condensate into a three-dimensional optical lattice potential. For low potential depths, where the tunnelling energy J is much larger than the on-site repulsive interaction energy U in a single well, each atom is spread out over all lattice sites. For the case of a homogeneous system with N atoms and M lattice sites, the many-body state can then be written in second quantization as a product of identical single-particle Bloch waves with zero quasi-momentum $|\Psi\rangle_{U/J=0} \propto \left(\sum_{i=1}^{M} \hat{a}_i^{\dagger}\right)^N |0\rangle$. It can be approximated by a product over single-site many-body states $|\phi_i\rangle$, such that $|\Psi\rangle_{U/J=0} \approx \prod_{i=1}^{M} |\phi_i\rangle$. In the limit of large N and M, the atom number distribution of $|\phi_i\rangle$ in each potential well is poissonian and almost identical to that of a coherent state. Furthermore, all the matter waves in different potential wells are phase coherent, with constant relative phases between lattice sites. As the lattice potential depth V_{A} is increased and J decreases, the atom number distribution in each potential well becomes markedly subpoissonian[10] owing to the repulsive interactions between the atoms, even before entering the Mott insulating state[11–13]. After preparing superposition states $|\phi_i\rangle$ in each potential well, we increase the lattice potential depth rapidly in order to create isolated potential wells. The hamiltonian of equation (1) then determines the dynamical evolution of each of these potential wells.

The experimental set-up used here to create Bose–Einstein condensates in the three-dimensional lattice potential (see Methods) is similar to that used in our previous work[11,14,15]. Briefly, we start with a quasi-pure Bose–Einstein condensate of up to 2×10^5 ^{87}Rb atoms in the $|F = 2, m_F = 2\rangle$ state in a harmonic magnetic trapping potential with isotropic trapping frequencies of $\omega = 2\pi \times 24\,$Hz. Here F and m_F denote the total angular momentum and the magnetic quantum number at the atom's hyperfine state. In order to transfer the magnetically trapped atoms into the optical lattice potential, we slowly increase the intensity of the lattice laser beams over a time of 80 ms so that a lattice potential depth V_{A} of up to 11 recoil energies E_{r} (see Methods) is reached[11]. This value of V_{A} is chosen so that the system is still completely in the superfluid regime[16]. We then rapidly increase the lattice potential depth to a value V_{B} of up to 35 E_{r} within a time of 50 μs so that the tunnel coupling between neighbouring potential wells becomes negligible. The timescale for the jump in the potential depth is chosen such that it is fast compared with the tunnelling time between neighbouring potential wells, but sufficiently slow to ensure that all atoms remain in the vibrational ground state of each well. In this way, we preserve the atom number distribution of the potential depth V_{A} at the potential depth V_{B}.

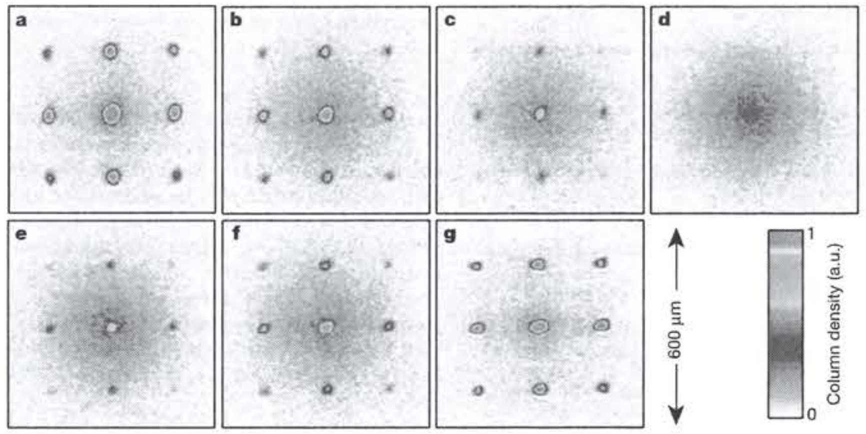

Figure 2 Dynamical evolution of the multiple matter wave interference pattern observed after jumping from a potential depth $V_{\mathrm{A}} = 8\,E_{\mathrm{r}}$ to a potential depth $V_{\mathrm{B}} = 22\,E_{\mathrm{r}}$ and a subsequent variable hold time t. After this hold time, all trapping potentials were shut off and absorption images were taken after a time-of-flight period of 16 ms. The hold times t were **a**, 0 μs; **b**, 100 μs; **c**, 150 μs; **d**, 250 μs; **e**, 350 μs; **f**, 400 μs; and **g**, 550 μs. At first, a distinct interference pattern is visible, showing that initially the system can be described by a macroscopic matter wave with phase coherence between individual potential wells. Then after a time of ∼250 μs the interference pattern is completely lost. The vanishing of the interference pattern is caused by a collapse of the macroscopic matter wave field in each lattice potential well. But after a total hold time of 550 μs (**g**) the interference pattern is almost perfectly restored, showing that the macroscopic matter wave field has revived. The atom number statistics in each well, however, remains constant throughout the dynamical evolution time. This is fundamentally different from the vanishing of the interference pattern with no further dynamical evolution, which is observed in the quantum phase transition to a Mott insulator, where Fock states are formed in each potential well. From the above images the number of coherent atoms N_{coh} is determined by first fitting a broad two-dimensional gaussian function to the incoherent background of atoms. The fitting region for the incoherent atoms excludes 130 μm × 130 μm squares around the interference peaks. Then the number of atoms in these squares is counted by a pixel-sum, from which the number of atoms in the incoherent gaussian background in these fields is subtracted to yield N_{coh}. a.u., arbitrary units.

We follow the dynamical evolution of the matter wave field after jumping to the potential depth V_{B} by holding the atoms in the optical lattice for different times t. After these hold times, we suddenly turn off the confining optical and magnetic trapping potentials and observe the resulting multiple matter wave interference pattern after a time-of-flight period of 16 ms. An example of such an evolution can be seen in Fig. 2, which shows the collapse and revival of the interference pattern over a time of 550 μs. This collapse and revival of the interference pattern is directly related to the collapses and revivals of the individual coherent matter wave fields in each potential well. It is important to note a crucial difference between the outcome of a collapse and revival experiment in a double-well system and our multiple-well system. In a double-well system, a perfect interference pattern would be observed in each single realization of the experiment for all times. However, when the matter wave fields have collapsed in both wells, this interference pattern would alternate randomly for each realization. Averaging over several single realizations would then yield the ensemble average value $\psi = 0$ that indicates the randomness of the interference pattern associated with the collapse of the matter wave fields. For the multiple-well set-up used here, however, the interference pattern in a single realization of the experiment can only be observed if the matter wave fields in each potential well have constant relative phase to each other, which requires that $\psi \neq 0$. The matter wave field ψ is therefore directly connected to the visibility of the multiple matter wave interference pattern in a single realization of the experiment.

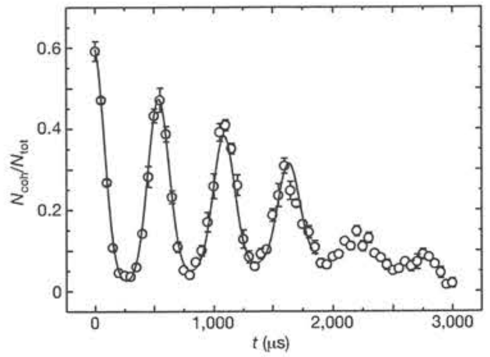

Figure 3 Number of coherent atoms relative to the total number of atoms monitored over time for the same experimental sequence as in Fig. 2. The solid line is a fit to the data assuming a sum of gaussians with constant widths and constant time separations, including an exponential damping and a linear background. The damping is mainly due to the following process: after jumping to a potential depth V_{B} and thereby abruptly changing the external confinement and the on-site matrix element U, we obtain a parabolic profile of the chemical potential over the cloud of atoms in the optical lattice, which leads to a broadening of the interference peaks over time. When the interference peaks become broader than the rectangular area in which they are counted, we cannot determine N_{coh} correctly any more, which explains the rather abrupt damping that can be seen—for example, between the third and fourth revival in the above figure. Furthermore, the difference in U of ∼3% over the cloud of atoms contributes to the damping of $N_{\mathrm{coh}}/N_{\mathrm{tot}}$ over time. The finite contrast in $N_{\mathrm{coh}}/N_{\mathrm{tot}}$ of initially 60% can be attributed to atoms in higher-order momentum peaks (∼10% of the total atom number), *s*-wave scattering spheres created during the expansion[14], a quantum depletion of the condensate for the initial potential depth of $V_{\mathrm{A}} = 8\,E_{\mathrm{r}}$, and a finite condensate fraction due to the finite temperature of the system.

In order to analyse quantitatively the temporal evolution of the interference pattern, we evaluate the number of atoms in the first and central order interference peaks N_{coh} versus the total number of atoms N_{tot} in the time-of-flight images. In the optical lattice, the matter wave field in each potential well $\psi_i(t) = \langle\phi_i(t)|\hat{a}_i|\phi_i(t)\rangle$ collapses and revives owing to the nonlinear dynamics discussed above. In order to relate the time evolution of the global fraction of coherent atoms $N_{\mathrm{coh}}/N_{\mathrm{tot}}$ to such a single-site time evolution $\psi_i(t)$ with $\bar{n}_i$ atoms on average on this lattice site, we sum the coherent fraction in each well over all M lattice sites: $N_{\mathrm{coh}}/N_{\mathrm{tot}} = 1/N_{\mathrm{tot}}\sum_{i=1}^{M} |\psi_i(t)|^2$. This sum can be converted into an integral using the classical probability distribution $W(\bar{n})$ which describes the probability of finding a lattice site with an average number of $\bar{n}$ atoms. If the single-site dynamics is given by $\psi(t, \bar{n}, (U/J)_{\mathrm{A}}, U_{\mathrm{B}})$, then the total number of coherent atoms can be determined by $N_{\mathrm{coh}} = \int W(\bar{n})|\psi(t, \bar{n}, (U/J)_{\mathrm{A}}, U_{\mathrm{B}})|^2\,\mathrm{d}\bar{n}$. Using the Bose–Hubbard model and assuming a homogenous system, we are able to numerically calculate the initial atom number statistics on a single lattice site for finite U/J up to $U/J \approx 20$ and small $\bar{n}$ using a Gutzwiller ansatz[13,17]. This allows us to predict the dynamical evolution of the matter wave field on a single lattice site $\psi(t, \bar{n}, (U/J)_{\mathrm{A}}, U_{\mathrm{B}})$. Figure 3 shows the experimentally determined evolution of $N_{\mathrm{coh}}/N_{\mathrm{tot}}$ over time after jumping to the potential depth V_{B}. Up to five revivals are visible, after which a damping of the signal prevents further detection of revivals.

The revival of the matter wave field in each potential well is expected to occur at times that are multiples of h/U, independent of the atom number statistics in each well. Therefore, in our inhomogeneous system, the macroscopic interference pattern should revive at the same times on all sites. As the on-site matrix element U increases for greater potential depths, we expect the revival time to decrease as V_{B} increases. This is shown in Fig. 4, where we have measured the revival period for different final potential depths V_{B}. We find excellent agreement between an *ab initio* calculation of h/U

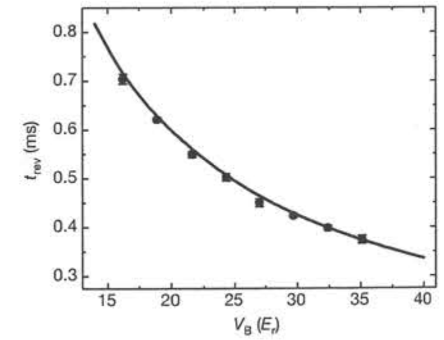

Figure 4 Revival period in the dynamical evolution of the interference pattern after jumping to different potential depths V_{B} from a potential depth of $V_{\mathrm{A}} = 5.5\,E_{\mathrm{r}}$. The solid line is an *ab initio* calculation of h/U with no adjustable parameters based on a band structure calculation. In addition to the statistical uncertainties shown in the revival times, the experimental data points have a systematic uncertainty of 15% in the values for the potential depth.

from a band structure calculation and our data points. The revivals also directly prove the quantization of the underlying Bose field, and provide experimental proof that collisions between atoms lead to a fully coherent collisional phase $Un(n-1)t/2\hbar$ of the $|n\rangle$-particle state over time, even on the level of individual pairs of atoms.

As we increase our initial lattice potential depth V_A, we expect the atom number distribution in each well to become markedly subpoissonian owing to the increasing importance of the interactions as U/J increases. This in turn should lead to an increase of the collapse time, which depends on the variance of the superimposed number states. We have verified this by measuring the collapse time for different values of V_A (Fig. 5a). We can clearly observe a significant increase in the collapse time, when jumping from greater potential depths. For example, when jumping from $V_A = 11\,E_r$, t_c/t_{rev} is more than 50% larger than when jumping from $V_A = 4\,E_r$. This indicates that the atom number distribution in each potential well has indeed become subpoissonian, because for our experimental parameters the average atom number per lattice site, $\bar{n}_i$ remains almost constant when V_A is increased. A comparison of the collapse time for different initial potential depths V_A to a theoretical prediction is shown in Fig. 5b.

The observed collapse and revival of the macroscopic matter wave field of a Bose–Einstein condensate directly demonstrate behaviour of ultracold matter beyond mean-field theories. Furthermore, the collapse times can serve as an independent, efficient probe of the atom number statistics in each potential well. It would be interesting to start from a Mott insulating state and use the coherent collisions between single atoms, which have been demonstrated here, to create a many-atom entangled state[18–20]. This highly entangled state could then serve as a promising starting point for quantum computing with neutral atoms[19,21]. □

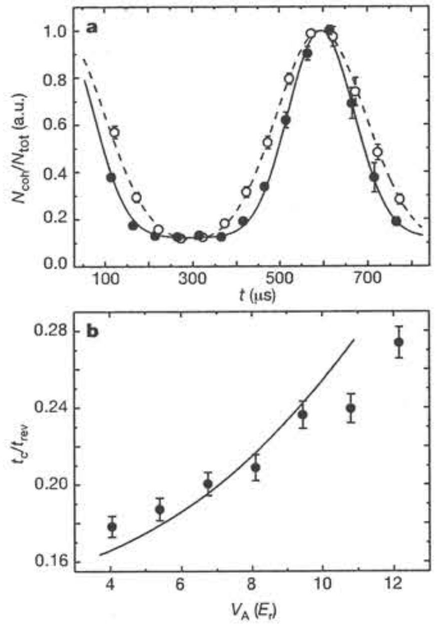

Figure 5 Influence of the atom number statistics on the collapse time. **a**, First revival observed in the ratio N_{coh}/N_{tot} after jumping from different initial potential depths $V_A = 4\,E_r$ (filled circles) and $V_A = 11\,E_r$ (open circles) to a potential depth of $V_B = 20\,E_r$. The data have been scaled to the same height in order to compare the widths of the collapse times, where the contrast of the curve at $V_A = 11\,E_r$ was 20% smaller than that for $V_A = 4\,E_r$. The solid and dashed line are fits to the data assuming a sum of two gaussians with constant widths t_c (measured as the 1/e half width of the gaussian), spaced by the corresponding revival time t_{rev} for the potential depth $V_B = 20\,E_r$. **b**, Collapse time t_c relative to the revival time t_{rev} after jumping from different potential depths V_A to a potential depth $V_B = 20\,E_r$. The solid line is an *ab initio* theoretical prediction based on the averaged time-evolution of the matter wave fields in each lattice potential well described in the text. Considering the systematic experimental uncertainties in the determination of the potential depths V_A of ~15% and an uncertainty in the total atom number of ~20%, we find a reasonable agreement between both the experimental data and the theoretical prediction. a.u., arbitrary units.

Methods

Optical lattices

A three-dimensional array of microscopic potential wells is created by overlapping three orthogonal optical standing waves at the position of the Bose–Einstein condensate. The atoms are then trapped in the intensity maxima of the standing-wave light field owing to the resulting dipole force. The laser beams for the periodic potential are operated at a wavelength of $\lambda = 838$ nm with beam waists of ~125 μm at the position of the Bose–Einstein condensate. This gaussian laser beam profile leads to an additional isotropic harmonic confinement of the atoms with trapping frequencies of 60 Hz for lattice potential depths of 20 E_r. Here E_r denotes the recoil energy $E_r = \hbar^2k^2/2m$, with $k = 2\pi/\lambda$ being the wavevector of the laser light and m the mass of a single atom. In this configuration, we populate almost 150,000 lattice sites with an average atom number per lattice site of up to 2.5 in the centre of the lattice. The lattice structure is of simple cubic type, with a lattice spacing of $\lambda/2$ and oscillation frequencies in each lattice potential well of ~30 kHz for a potential depth of 20 E_r.

Received 9 April; accepted 4 July 2002; doi:10.1038/nature00968.

---

1. Wright, E. M., Walls, D. F. & Garrison, J. C. Collapses and revivals of Bose-Einstein condensates formed in small atomic samples. *Phys. Rev. Lett.* **77,** 2158–2161 (1996).
2. Wright, E. M., Wong, T., Collett, M. J., Tan, S. M. & Walls, D. F. Collapses and revivals in the interference between two Bose-Einstein condensates formed in small atomic samples. *Phys. Rev. A* **56,** 591–602 (1997).
3. Imamoglu, A., Lewenstein, M. & You, L. Inhibition of coherence in trapped Bose-Einstein condensates. *Phys. Rev. Lett.* **78,** 2511–2514 (1997).
4. Castin, Y. & Dalibard, J. Relative phase of two Bose-Einstein condensates. *Phys. Rev. A* **55,** 4330–4337 (1997).
5. Dunningham, J. A., Collett, M. J. & Walls, D. F. Quantum state of a trapped Bose-Einstein condensate. *Phys. Lett. A* **245,** 49–54 (1998).
6. Zhang, W. & Walls, D. F. Bosonic-degeneracy-induced quantum correlation in a nonlinear atomic beam splitter. *Phys. Rev. A* **52,** 4696–4703 (1995).
7. Walls, D. F. & Milburn, G. J. *Quantum Optics* (Springer, Berlin, 1994).
8. Milburn, G. J. & Holmes, C. A. Dissipative quantum and classical Liouville mechanics of the anharmonic oscillator. *Phys. Rev. Lett.* **56,** 2237–2240 (1986).
9. Daniel, D. J. & Milburn, G. J. Destruction of quantum coherence in a nonlinear oscillator via attenuation and amplification. *Phys. Rev. A* **39,** 4628–4640 (1989).
10. Orzel, C., Tuchman, A. K., Fenselau, M. L., Yasuda, M. & Kasevich, M. A. Squeezed states in a Bose-Einstein condensate. *Science* **291,** 2386–2389 (2001).
11. Greiner, M., Mandel, O., Esslinger, T., Hänsch, T. W. & Bloch, I. Quantum phase transition from a superfluid to a Mott insulator in a gas of ultracold atoms. *Nature* **415,** 39–44 (2002).
12. Fisher, M. P. A., Weichman, P. B., Grinstein, G. & Fisher, D. S. Boson localization and the superfluid-insulator transition. *Phys. Rev. B* **40,** 546–570 (1989).
13. Jaksch, D., Bruder, C., Cirac, J. I., Gardiner, C. W. & Zoller, P. Cold bosonic atoms in optical lattices. *Phys. Rev. Lett.* **81,** 3108–3111 (1998).
14. Greiner, M., Bloch, I., Mandel, O., Hänsch, T. W. & Esslinger, T. Exploring phase coherence in a 2D lattice of Bose-Einstein condensates. *Phys. Rev. Lett.* **87,** 160405-1–160405-4 (2001).
15. Greiner, M., Bloch, I., Hänsch, T. W. & Esslinger, T. Magnetic transport of trapped cold atoms over a large distance. *Phys. Rev. A* **63,** 031401-1–031401-4 (2001).
16. Cataliotti, F. S. *et al.* Josephson junction arrays with Bose-Einstein condensates. *Science* **293,** 843–846 (2001).
17. Rokhsar, D. S. & Kotliar, B. G. Gutzwiller projection for bosons. *Phys. Rev. B* **44,** 10328–10332 (1991).
18. Jaksch, D., Briegel, H. J., Cirac, J. I., Gardiner, C. W. & Zoller, P. Entanglement of atoms via cold controlled collisions. *Phys. Rev. Lett.* **82,** 1975–1978 (1999).
19. Briegel, H. J., Calarco, T., Jaksch, D., Cirac, J. I. & Zoller, P. Quantum computing with neutral atoms. *J. Mod. Opt.* **47,** 415–451 (2000).
20. Briegel, H. J. & Raussendorf, R. Persistent entanglement in arrays of interacting particles. *Phys. Rev. Lett.* **86,** 910–913 (2001).
21. Raussendorf, R. & Briegel, H. J. A one-way quantum computer. *Phys. Rev. Lett.* **86,** 5188–5191 (2001).

Acknowledgements

We thank W. Zwerger, T. Esslinger, A. Görlitz, H. Briegel, E. Wright and I. Cirac for discussions, and A. Altmeyer for help in the final stages of the experiment. This work was supported by the DFG.

Competing interests statement

The authors declare that they have no competing financial interests.

Correspondence and requests for materials should be addressed to I.B.
(e-mail: imb@mpq.mpg.de).